

# **Development of Photonic Integrated Circuits for Terahertz Beam Steering**

Von der Fakultät für Ingenieurwissenschaften,  
Abteilung Elektrotechnik und Informationstechnik  
der Universität Duisburg-Essen

zur Erlangung des akademischen Grades

Doktor der Ingenieurwissenschaft

genehmigte Dissertation

von

Peng Lu  
aus  
Tianjin

Gutachter: Prof. Dr.-Ing. Andreas Stöhr  
Gutachter: Prof. Stavros Iezekiel, PhD  
Tag der mündlichen Prüfung: 24. Juli 2024

# DuEPublico

Duisburg-Essen Publications online

UNIVERSITÄT  
DUISBURG  
ESSEN

*Offen im Denken*

ub | universitäts  
bibliothek

This dissertation is made available via DuEPublico, the institutional repository of the University of Duisburg-Essen and is also available as printed version.

**DOI:** 10.17185/duepublico/82660

**URN:** urn:nbn:de:hbz:465-20241211-092745-5



This work may be used under a Creative Commons Attribution 4.0 License (CC BY 4.0).

## Acknowledgement

First and foremost, I extend my sincerest thanks to my advisor, Prof. Dr.-Ing. Andreas Stöhr, for the opportunity to work as a PhD candidate in the Optoelectronics department. His daily guidance, patient explanations, frequent encouragement and inspiration were invaluable throughout my PhD study. I am particularly grateful for his time spent reviewing and correcting this thesis.

I am deeply appreciative of Prof. Stavros Iezekiel for his willingness to review my thesis.

My gratitude also extends to all committee members who invested time in reviewing my thesis and provided valuable feedback.

I would like to thank very much my current and former colleges from Optoelectronics, especially Dr. Rüdiger Buß who takes care about the IT systems in our department so that the time-consuming simulations can be successfully accomplished; José, the technological advances cannot be achieved in this thesis without his experiences and ideas; Thomas and Jonas for their active cooperation and contributions to this thesis; Sumer, Jörg, Matthias, Marcel, Ezgi, Vitaly, Sebastian and Beshar for their scientific and technological support. Special thanks to our group secretaries, Sandra, Anita, Irina for their assistance in administrative matters, which, at times, were more challenging than writing publications or this thesis.

I would also like to express my gratitude to Prof. Daniel Erni, Prof. Thomas Kaiser, Dr. Andreas Rennings, Benedikt Sievert and Enes Mutlu from the University of Duisburg-Essen, as well as Prof. Ullrich Pfeiffer, Dr. Robin Zatta and Thomas Bücher from the University of Wuppertal, for their support during my studies.

I am thankful to Dr. Chris Roeloffzen, Marcel Hoekman, Dr. Dimitri Geskus, Dr. Jörn Epping, Dr. Cateriana Taddei, Robert Grootjans, Ilka Visscher, Dr. René Heideman, Ronald Dekker and Dr. Roelof Bernardus Timens from LioniX International BV for their support during my stay there.

Last but not least, I owe all I have achieved today to my beloved family, especially my parents, Baorong Lu, Rong Wang, and my wife, Sihui. Without their unconditional support and love, I could not have achieved so much. In my easy and hard, they are always with me.



## Abstract

The unique advantages offered by terahertz (THz) waves have stimulated the emergence and advancement of novel THz systems for imaging, spectroscopy, communication, and radar applications. Currently, photonic-assisted THz technologies are on the rise due to the wide bandwidth and minimal loss of optical fibers. Additionally, their compatibility with C-band fiber-optic components in the microwave frequency region, not available for electrical technologies, further drives their development. However, because of the high free-space path loss, existing THz systems typically utilize high-gain antennas for fixed point-to-point applications. To expand their applicability in mobile environments, compact integrated transceivers with beam steering capabilities are indispensable. Therefore, this thesis focuses on developing and fabricating photonic integrated circuits (PICs) for photonic-assisted THz beam steering.

This thesis reports on the first indium phosphide (InP)-based THz leaky-wave antenna (LWA), supporting low-loss and monolithic integration with THz photodiodes (PDs). By adjusting the antenna's operating frequency from 230 to 330 GHz, quasi-linear beam steering from  $-46^\circ$  to  $42^\circ$  can be achieved. Experimental results demonstrate an average realized gain of  $\sim 11$  dBi and a 3-dB beam width of  $\sim 10^\circ$ .

Using a photonic THz transmitter based on this fabricated LWA, a mobile THz communication system that supports both single and multi-users is reported for the first time. Within the whole beam steering range, a data rate of 24 Gbit/s is achieved for a single mobile user at a wireless distance of 6 cm without using a THz amplifier for the transmitter. At longer wireless distances of up to 32 cm, data rates of up to 4 Gbit/s are achieved. Furthermore, this THz communication system could simultaneously support up to twelve users with a total wireless data capacity of 48 Gbit/s.

The thesis also reports on an optical beam forming network (OBFN) chip designed for a  $1 \times 4$  photonic-assisted phased array operating at 300 GHz. Four optical phase shifters (OPSs), each consisting of two cascaded optical ring resonators (ORRs), are used to adjust the phase shift of THz waves in the optical domain. A phase shift range of  $2\pi$  with a tuning efficiency of  $0.058 \text{ W}/\pi$  is experimentally characterized. Furthermore, a beam steering range of  $\sim 62^\circ$  is successfully demonstrated.

The thesis also delves into the design, concept, and technological advancements of 2D THz beam steering approaches. A PIC concept based on an LWA array configuration is proposed. By incorporating an additionally integrated OBFN chip, a THz beam steering range of  $60^\circ$  in the E-plane of the antenna array can be achieved. Suppose this PIC is used instead of the single LWA for the mobile THz communication system, the wireless distance can be extended from 6 cm to 4.5 m for a data rate of 24 Gbit/s. Furthermore, a heterogeneous integrated III-V/Si platform is developed to enable vertical integration of a PD matrix on an OBFN chip for achieving a 2D photonic-assisted phased array. The optical modes are coupled from the waveguides of the OBFN chip into PDs through prism coupling without requiring any additional optical couplers. For fabrication purposes, an epitaxial-layer-transfer technology has been developed to transfer the only  $\sim 1.2 \mu\text{m}$  thick PD epitaxial layers from the original InP substrate onto the surface of an OBFN chip.



## Zusammenfassung

Die einzigartigen Vorteile von Terahertz-(THz)-Wellen haben die Entstehung und Fortentwicklung von innovativen THz-Systemen für Bildgebung, Spektroskopie, Kommunikation und Radar-Anwendungen angeregt. Derzeit sind photonisch unterstützte THz-Technologien aufgrund der großen Bandbreite und des minimalen Verlusts von optischen Fasern im Aufstieg. Außerdem fördert ihre Kompatibilität mit C-Band-Glasfaserkomponenten in der Mikrowellen-Frequenzregion, die für elektrische Technologien nicht verfügbar sind, ihre Entwicklung weiter. Aufgrund der hohen Freiraumdämpfung nutzen bestehende THz-Systeme jedoch typischerweise Antennen mit hohem Gewinn für feste Punkt-zu-Punkt-Anwendungen. Um ihre Anwendbarkeit in mobilen Umgebungen zu erweitern, sind kompakte integrierte Transceiver mit Strahlenkungsfähigkeiten unerlässlich. Daher konzentriert sich diese Arbeit auf die Entwicklung und Fertigung von photonisch integrierten Schaltkreisen (PICs) für photonisch unterstützte THz-Strahlenkung.

Zunächst berichtet diese Arbeit über die erste auf Indiumphosphid (InP) hergestellte THz-Leckwellenantenne (LWA), die eine verlustarme und monolithische Integration mit THz-Photodioden (PDs) unterstützt. Durch Einstellung der Antennenfrequenz von 230 bis 330 GHz ist eine quasi-lineare Strahlenkung von  $-46^\circ$  bis  $42^\circ$  zu erreichen. Experimentelle Ergebnisse zeigen einen durchschnittlichen realisierten Gewinn von ca. 11 dBi und eine 3-dB-Strahlbreite von etwa  $10^\circ$ .

Mit einem auf dieser gefertigten LWA basierenden photonischen THz-Sender wird erstmals ein mobiles THz-Kommunikationssystem vorgestellt, das sowohl Einzel- als auch Multi-Benutzer unterstützt. Innerhalb des gesamten Strahlenkungsbereichs wird eine Datenrate von 24 Gbit/s für einen einzelnen mobilen Benutzer über eine drahtlose Strecke von 6 cm ohne Verwendung eines THz-Verstärkers für den Sender erreicht. Bei längeren drahtlosen Entfernungen von bis zu 32 cm werden Datenraten von bis zu 4 Gbit/s erzielt. Darüber hinaus kann dieses THz-Kommunikationssystem gleichzeitig bis zu zwölf Benutzer mit einer gesamten drahtlosen Datenkapazität von 48 Gbit/s unterstützen.

Die Arbeit berichtet auch über einen für ein  $1 \times 4$  photonisch unterstütztes Phased-Array entwickelten optischen Strahlformungsnetzwerk (OBFN)-Chip, der bei 300 GHz arbeitet. Vier optische Phasenschieber (OPSs), die jeweils aus zwei kaskadierten optischen Ringresonatoren (ORRs) bestehen, werden verwendet, um die Phasenverschiebung von THz-Wellen im optischen Bereich anzupassen. Ein Phasenverschiebungsbereich von  $2\pi$  mit einer Abstimmungseffizienz von  $0,058 \text{ W}/\pi$  wird experimentell charakterisiert. Darüber hinaus wird ein Strahlenkungsbereich von  $\sim 62^\circ$  erfolgreich demonstriert.

Die Arbeit geht auch auf das Design, das Konzept und die technologischen Fortschritte von 2D-Strahlenkungsansätzen ein. Ein PIC-Konzept basierend auf einer LWA-Array-Konfiguration wird vorgeschlagen. Durch die Integration eines zusätzlichen OBFN-Chips kann ein THz-Strahlenkungsbereich von  $60^\circ$  in der E-Ebene des Antennen-Arrays erreicht werden. Wird dieser PIC anstelle der einzelnen LWA für das mobile THz-Kommunikationssystem verwendet, kann die drahtlose Entfernung

von 6 cm auf 4,5 m für eine Datenrate von 24 Gbit/s verlängert werden. Darüber hinaus wird eine heterogen integrierte III-V/Si-Plattform entwickelt, um die vertikale Integration einer PD-Matrix auf einem OBFN-Chip für ein 2D photonisch unterstütztes Phased-Array zu ermöglichen. Die optischen Signale werden von den Wellenleitern des OBFN-Chips durch Prismenkopplung in PDs ohne zusätzliche optische Koppler eingekoppelt. Für Fertigungszwecke wird eine Epitaxie-Schichttransfer-Technologie entwickelt, um die nur  $\sim 1,2 \mu\text{m}$  dicken PD-Epitaxieschichten vom ursprünglichen InP-Substrat auf die Oberfläche eines OBFN-Chips zu übertragen.

# Table of Contents

<b>1</b>	<b>Introduction.....</b>	<b>1</b>
1.1	THz beam steering approaches .....	2
1.1.1	Metasurface.....	2
1.1.2	Leaky-wave antenna .....	3
1.1.3	Phased array .....	4
1.2	Development of photonic integrated circuits for THz beam steering.....	5
1.2.1	Motivation and objectives.....	5
1.2.2	Challenges.....	6
1.3	Thesis organization .....	7
<b>2</b>	<b>InP-based THz beam steering leaky-wave antenna.....</b>	<b>9</b>
2.1	THz LWA and GCPW-MSL transition design.....	9
2.1.1	LWA design .....	10
2.1.2	GCPW-MSL transition design.....	11
2.2	LWA fabrication .....	13
2.3	Numerical analysis and experimental characterization.....	15
2.3.1	Scattering parameter .....	15
2.3.2	Far-field radiation pattern .....	16
<b>3</b>	<b>Mobile THz communications using InP-based leaky-wave antenna.....</b>	<b>21</b>
3.1	LWA transmitter chip with Teflon lens .....	21
3.2	THz communication system setup.....	22
3.3	Single-user mobile THz communications.....	24
3.4	Multi-user THz communications .....	25
<b>4</b>	<b>Optical beam forming network chip for THz phased array .....</b>	<b>27</b>
4.1	OBFN chip design.....	27
4.2	OBFN chip characterization .....	30
4.3	THz beam steering using a 1×4 phased array .....	35
<b>5</b>	<b>Towards 2D THz beam steering .....</b>	<b>39</b>
5.1	PIC based on THz LWA array.....	39
5.1.1	PIC design.....	39
5.1.2	Expected performance .....	40
5.2	Heterogeneous integrated III-V/Si platform for phased array .....	42
5.2.1	Optical prism coupling.....	43
5.2.2	PD epitaxial layers optimization.....	43

5.2.3	Epitaxial-layer-transfer technology .....	46
<b>6</b>	<b>Discussion.....</b>	<b>51</b>
<b>7</b>	<b>Conclusion and future work .....</b>	<b>59</b>
	<b>Abbreviations and symbols .....</b>	<b>61</b>
	Abbreviations .....	61
	Latin symbols .....	65
	Greek symbols.....	67
	<b>List of figures .....</b>	<b>69</b>
	<b>List of tables.....</b>	<b>72</b>
	<b>References .....</b>	<b>73</b>
	<b>List of publications.....</b>	<b>87</b>
	<b>Self-declaration.....</b>	<b>91</b>
	<b>Co-authorship statement .....</b>	<b>93</b>

# 1 Introduction

Over the past century, significant advancements in microwave and visible light technologies have profoundly transformed our daily lives. Positioned between these spectrums is the terahertz (THz) gap, a frequency range that remained underutilized for a considerable duration. This was primarily due to the absence of appropriate emitters for THz signal generation and efficient sensors for its detection [1]. Nevertheless, diverse THz transmitters utilizing both photonic [2-12] and electronic technologies [13-17] have been developed recently. Moreover, THz devices such as detectors [18-20], amplifiers [21-23], absorbers [24-26], filters [27, 28] and polarizers [29-31] have emerged to detect and manipulate THz waves.

Numerous efforts have been made to fill this THz gap, because THz waves present several distinct advantages over adjacent spectra. Unlike X-rays, the lower wave energy of THz waves doesn't pose an ionization hazard to biological tissues, making it suitable for medical applications [32-35]. Different from visible light, THz waves penetrate most dry dielectric materials but are absorbed or reflected by materials with large static dipoles or high electrical conductivity (e.g., water, metals). Coupled with higher resolution than microwaves, THz waves have found applications in imaging systems [36-40]. Additionally, the unique fingerprint spectra of diverse chemical compounds have significantly increased interest in THz spectroscopy systems [41-47]. Last but not least, the THz spectrum offers a broader bandwidth than the limited spectrum in the microwave region, which is crucial for future high data-rate wireless communications [48-55]. Reflecting this potential, IEEE and ITU-R have recently initiated the first standards (IEEE 802.15.3d and ITU-R F.2416-0 [56, 57]).

Despite the promise held by THz technology, its development faces specific challenges. A significant concern is the increased free-space path loss (FSPL) in the THz domain compared to microwave frequency bands [58]. This necessitates the use of high-gain antennas radiating directional beams in existing THz systems, irrespective of whether they employ photonic or electronic transmitters. Consequently, the utility of THz technologies has predominantly been in fixed point-to-point applications. To overcome these limitations and implement THz systems for mobile applications, beam steering technologies are essential. The publication trend related to THz beam steering from 2012 to 2022 is illustrated in Fig. 1-1. As observed, this research area remained relatively marginal until 2017 with annual publication numbers below twenty. However, there has been a surge in interest not just from universities, but also from renowned research institutes and global enterprises, e.g., Fraunhofer (Germany) [59], National Institute of Information and Communications Technology (Japan) [60], and Samsung [61]. Although the number of publications in 2022 was still under one hundred, the upward trend highlights the significance of THz beam steering technologies. This indicates potential expansions of THz applications into areas like mobile 6G communications, AR/VR applications, and dynamic sensing.

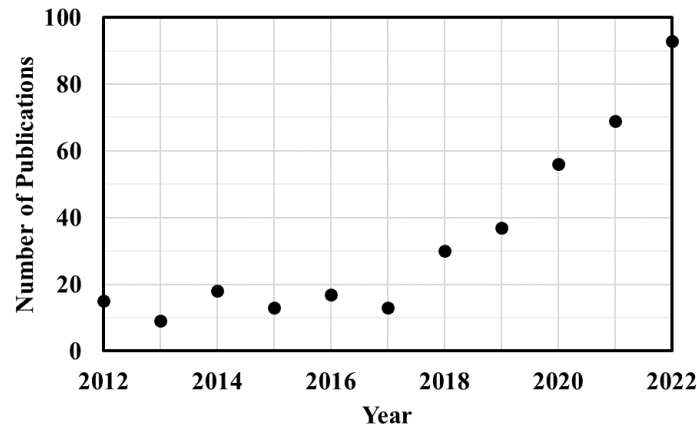


Fig. 1-1 Publication trends over the past decade on THz beam steering.

## 1.1 THz beam steering approaches

An overview of the state-of-the-art THz beam steering approaches is illustrated in Fig. 1-2. These approaches can generally be classified into three categories: metasurface, leaky-wave antenna (LWA), and phased array.

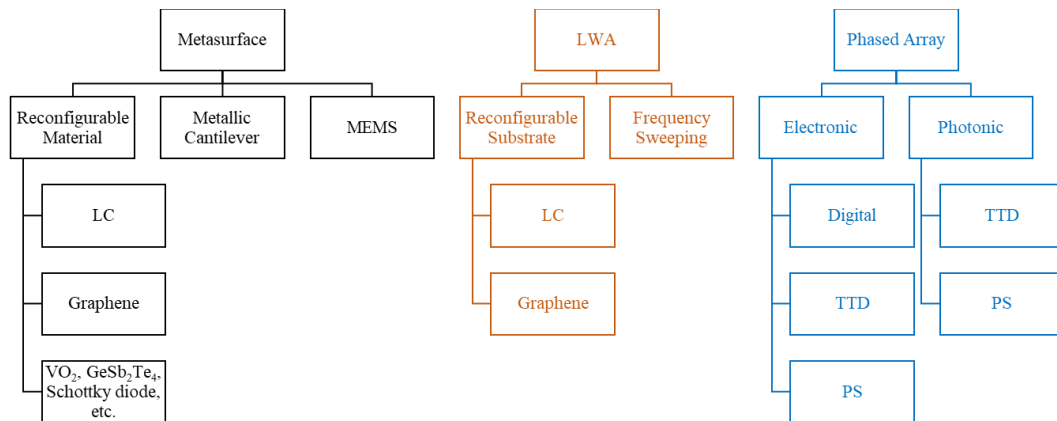


Fig. 1-2 Classification of THz beam steering approaches.

### 1.1.1 Metasurface

A metasurface is a two-dimensional (2D) artificial metamaterial, characterized by discrete subwavelength unit cells situated at the interface. For THz beam steering, these metasurfaces are spatially separated from either the photonic or electronic THz transmitters. By superimposing the local THz phase shifts introduced by each unit cell, the direction of reflected or transmitted THz beams can be manipulated [62-64].

Due to the electrically switchable anisotropy for electromagnetic waves, liquid crystals (LCs) have been employed in designing reconfigurable metasurfaces. In [65], a metasurface was reported consisting of a silicon (Si) wafer with metalized ground plane and multi-resonant cells printed on the lower surface of a quartz wafer. In between, a 70  $\mu\text{m}$  thick LC layer was inserted to actively switch the state of the cells. Consequently, an electronically controlled one-dimensional (1D) beam steering over  $55^\circ$  was realized at 100 GHz. In the 630 to 650 GHz range, a programmable metasurface based on metallic back plate-LC-complementary split ring resonators was

published [66]. Measurement results verified a 1D beam steering range of  $40^\circ$ .

Graphene, due to its tunable conductivity via chemical potential modulation by bias voltages, emerges as a promising candidate for active THz reconfigurable metasurfaces. Following the debut of a graphene-based fixed-beam reflectarray in the THz band [67], a reconfigurable reflectarray composed of  $80 \times 400$  cells was crafted for THz beam steering [68]. Each cell utilizes a bow tie (BT) antenna which concentrates the received THz energy within a  $3 \mu\text{m}$  narrow gap between two triangular elements where graphene is placed. By modulating the graphene with a bias voltage, a phase shift of  $\pi$  was achieved. With proper voltage patterning of the reflectarray, a 1D angular steering range of  $25^\circ$  at 0.98 THz was accomplished. Other materials, such as vanadium dioxide ( $\text{VO}_2$ ) [69, 70], germanium-antimony-telluride ( $\text{GeSb}_2\text{Te}_4$ , GST) [71, 72] and hybrid metal-semiconductors featuring Schottky diode effect [73], have also shown the ability to modulate phase in the THz domain. Consequently, they are promising for future THz beam steering applications.

Beyond actively tunable materials, mechanical structures have been explored for THz beam steering. In [74], a freely programmable THz spatial phase modulator based on a diffraction grating was reported. This comprised an electrostatically actuated and computer-controlled array of sub-wavelength metallic cantilevers. The adjustable displacement of each cantilever dynamically altered the period of the diffraction grating. As a result, a beam steering range exceeding  $40^\circ$  was demonstrated at 300 GHz. Using microelectromechanical systems (MEMS) based reflectors, a mechanical THz reflectarray was proposed based on a 5-bit stepwise electrostatic actuator system [75]. Here, eighty identical rectangular reflectors were sequentially placed adjacent to each other along their elongated sides to form the reflectarray. The periodic arrangement of these reflectors was designed to eliminate the grating lobes and facilitate a broader beam steering range with improved angular precision. Numerical evaluations showed a  $180^\circ$  beam steering range at 300 GHz, which still awaits experimental validation.

### 1.1.2 Leaky-wave antenna

The foundational element of an LWA is a guided-wave structure. By introducing geometric or electromagnetic variations to the structure, the guided wave can be allowed to leak along the antenna length and radiate into free space [76]. The first attempt was reported in the late 1930s by cutting a longitudinal slit along the side of a rectangular waveguide [77]. Subsequent designs replaced the slit with a series of holes to achieve a narrower beam [78]. These designs are termed uniform or quasi-uniform LWAs, characterized by closed guided-wave structures and dominant fast-wave modes. However, as frequencies increase, the miniaturized dimensions of closed guided-wave structures make mechanical slits or other geometrical deformations challenging. Thus, periodic LWAs with open guided-wave structures become more appealing due to their simpler mechanical design and reduced transmission loss [79]. Examples include microstrip lines (MSLs) [80, 81], substrate integrated waveguides (SIWs) [82-85], coplanar waveguides (CPWs) [86, 87], and dielectric waveguides [88, 89]. Since the dominant modes of these LWAs are slow waves, periodic modulations of the structure are required for leakage.

There are generally two methods to achieve beam steering with LWAs. One can

alter the antenna properties at a fixed frequency using reconfigurable structures. Alternatively, the beam direction can be adjusted by varying the operating frequency. While several reconfigurable LWAs have been showcased in the microwave range [90-93], only a few concepts are available for THz frequencies. For instance, one proposed design is a LWA based on a graphene sheet attached to a back-metallized substrate [94]. By sinusoidally modulating the graphene's surface reactance via applying appropriate DC bias voltages to different polysilicon gating pads beneath the graphene sheet, the beam direction can be steered at a consistent operating frequency. Simulations indicate a beam steering range of  $82.9^\circ$  at 2 THz using a silicon dioxide ( $\text{SiO}_2$ ) antenna substrate. Other concepts involve the use of graphene [95-97] and LC [98, 99]. A more straightforward approach to realize beam steering is to adjust the operating frequency of the LWAs, negating the need for intricate control circuits. One study demonstrated a THz LWA with a relatively simple design based on a metal parallel-plate waveguide (PPWG) [100]. The metal waveguide is 5 cm long and features two open sides to minimize ohmic losses. A single slit, measuring 4.2 cm in length and 1 mm in width, is cut into one metal plate to enable leaky radiation. By modulating the plate separation, the LWA's operating frequency range can be varied. With a plate separation of 1 mm, the beam direction is adjustable from  $17^\circ$  to  $85^\circ$  as the frequency shifts from 151 to 512 GHz. In this setup, THz waves are focused by an external lens system and then channeled into the LWA. Thus, this method requires meticulous and time-consuming adjustments. A more compact solution was demonstrated in [101], where a  $\sim 2.6$  cm long microstrip periodic LWA was fabricated on a cyclin olefin polymer (COP) substrate and powered by a vector network analyzer (VNA). Here, sweeping the frequency from 235 to 325 GHz results in beam steering from  $-23^\circ$  to  $15^\circ$ .

### 1.1.3 Phased array

As the most well-known technology, phased arrays can steer the beam by controlling the relative time or phase difference between adjacent radiating elements using either electronic or photonic technologies [102, 103]. In the realm of electronic technology, the time delay and phase shift of signals can be processed digitally, for example, through field-programmable gate arrays (FPGAs). For each antenna or sub-array of antennas, a digital-to-analog converter (DAC) and an RF chain are essential. Consequently, such digital beam steering techniques can be costly and power-intensive [104], and only few studies have been demonstrated in the THz domain. For instance, a beam steering range of  $80^\circ$  was achieved at 140 GHz employing an electronic-assisted phased array that consists of eight dual-channel 45 nm complementary metal-oxide semiconductor (CMOS) radio-frequency integrated circuits (RFICs) and 128 antennas [61]. Analog processing of signals is more prevalent to control time and phase through true time delays (TTDs) or phase shifters (PSs). In [105, 106], phased arrays utilizing electronic TTDs and the 65 nm CMOS technology, were demonstrated. The first integrated phased array based on electronic PSs at THz frequencies was reported in [107]. A phase resolution of  $9^\circ$  and a beam steering over  $80^\circ$  were achieved at 280 GHz. Subsequent designs of PS-based phased arrays have been realized in both CMOS [108-110] and silicon germanium (SiGe) bipolar complementary metal-oxide semiconductor (BiCMOS) [111] technologies.

In photonic assisted phased arrays, adjustments in time delay and phase shift are

made optically, subsequently transferring to the THz domain through photomixers. A straightforward method to implement optical TTDs involves fiber-based optical delay lines [112], which however prevent a compact integration. Therefore, chip integrated delay lines, switched by Mach-Zehnder-interferometers (MZIs), have been developed for a  $1 \times 4$  photonic assisted phased array at 94 GHz [113]. This design achieved discrete time delays with a resolution of 1.5 ps. Additionally, phased arrays utilizing optical phase shifters (OPSs) have been demonstrated. One such innovative study reported on-chip integrated OPSs using thermo-optically controlled straight waveguides [114]. This configuration resulted in a  $50^\circ$  continuous beam steering of a 300 GHz radiation.

## 1.2 Development of photonic integrated circuits for THz beam steering

### 1.2.1 Motivation and objectives

Photonic-assisted THz systems possess inherent advantages over those that utilize electronic transmitters for THz signal generation. One notable benefit is their extremely broad and tunable bandwidth, which ranges from GHz to a few THz. Furthermore, mature and cost-effective C-band (wavelength: 1530 to 1565 nm) fiber-optic components in the microwave frequency region are readily compatible with photonic THz transmitters. The existing low-loss optical fiber infrastructure allows THz signals to be transmitted over long distances, thereby enabling centralized radio access networks [39, 51, 115].

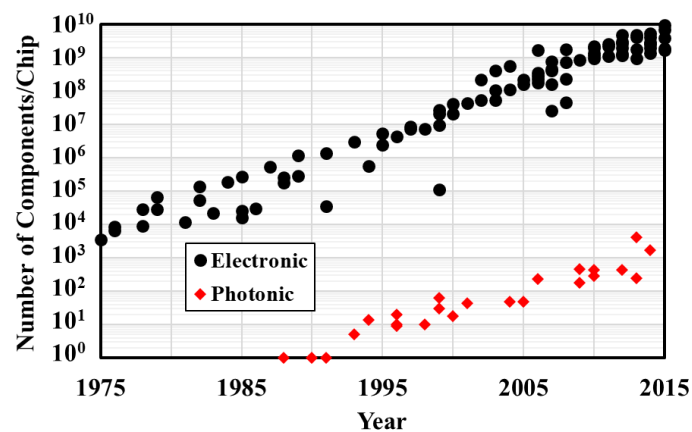


Fig. 1-3 A comparative study of the evolution in complexity between electronic and photonic chips. Adapted from [116] (licensed under [Creative Commons Attribution 4.0 International license](#)) and [117] (licensed under a [Creative Commons License](#)).

However, the development of photonic integrated circuits (PICs) has trailed electronic development by approximately thirty years [117], when considering milestone inventions, e.g., transistor (1947, [118]) / semiconductor laser (1962, [119, 120]), transistor integration (1958, [121]) / laser integration (1987, [122]) and electronic multi-project wafer (MPW) (1979, [123]) / photonic MPW (2008, [124]). The discrepancy in component integration on chips further highlights this gap, as depicted in Fig. 1-3. Such differences can be attributed to the larger footprints and heat production of photonic components compared to transistors [117]. Additionally, while CMOS technology is predominant for electronic devices, state-of-the-art photonic components often rely on diverse material systems, each with unique advantages and

challenges [2-12, 125-133]. Nonetheless, significant efforts are underway to develop compact and functional PICs by integrating various material platforms [117, 134-137]. Yet, there remain limited compact and integrated photonic solutions specifically tailored for THz beam steering.

The objectives of this thesis are to advance the development of PICs for photonic-assisted THz beam steering, a field that is still in its early stages, and to utilize the merits of photonic technologies in mobile THz systems. This thesis initially explores LWAs due to their potential for mobile THz joint communication and sensing systems, a concept already proven in microwave frequencies [138, 139]. Additionally, phased arrays are investigated owing to the demand for frequency-independent beam steering techniques in THz imaging applications as necessitated by project C07 within Collaborative Research Center/Transregio SFB/TRR 196 "Mobile material characterization and localization by electromagnetic sensing" (MARIE), on which I have actively worked. Both methodologies exhibit promising potential for integration with THz PDs, enabling the continuous-wave (CW) THz signal generation using mature and cost-effective C-band fiber-optic components at room temperature with high output power. This makes them favorable in comparison to other photonic THz sources, such as photoconductive antennas (PCAs) [8, 140-143] and quantum-cascade lasers (QCLs) [3, 9, 11]. Recently, modified uni-traveling carrier photodiodes (MUTC-PDs) with milliwatt-level output power in the WR-3 band have been reported [12].

### 1.2.2 Challenges

LWAs with hybrid integrated PDs through wire bonding have been previously demonstrated within the microwave frequency spectrum [144-146]. However, to the best of our knowledge, wire bonding has only been reported for frequencies up to 220 GHz [147], and it is expected to result in high losses at THz frequencies [148, 149]. Therefore, THz LWAs based on an indium phosphide (InP) substrate are essential to allow low-loss and monolithic integration with InP-based THz PDs. Another challenge is the increasing number of surface wave modes in the antenna substrate as the operating frequency rises. These modes cannot be radiated, compromising antenna radiation efficiency. This phenomenon is especially pronounced for InP due to its high permittivity [76, 150]. Consequently, thin InP substrates are required for LWAs to reduce the number of these undesired surface wave modes [150]. However, the inherent brittleness of InP complicates clean-room fabrication processes, especially when its thickness is reduced below 100  $\mu\text{m}$ . Thus, the research area of PD-integrated THz LWAs remains largely uncharted. Furthermore, LWAs' beam steering remains inherently one-dimensional through antenna frequency modulations. This underscores the importance of exploring strategies for 2D THz beam steering.

To date, optical beam forming network (OBFN) chips based on TriPleX waveguides [133] targeting THz phased arrays have been reported with some limitations. Switched delay lines for time delay adjustment [113] demands numerous thermo-optical switches to ensure fine-tuned beam angle resolution, which in return leads to significant power consumption. For OPSs based on straight waveguides [114], phase tuning is feasible only for a single optical carrier in an optical heterodyne configuration. The second optical heterodyne signal needs to be combined after each OPS with additional optical

waveguides. Therefore, two optical inputs are required for the OBFN chip. This leads to inevitable waveguide intersections on the chip and higher optical losses, especially in large-scale phased arrays. Another method, employing cascaded optical ring resonators (ORRs) to realize TTDs for photonic-assisted phased arrays at microwave frequencies [151-153], becomes increasingly challenging when scaled to THz frequencies. This is mainly because of the increased sensitivity of the phased array's beam angle to time delay fluctuations. For instance, even a minor 0.3 ps time delay adjustment can change the beam angle by approximately  $10^\circ$  for a phased array with a radiating element pitch of  $500\ \mu\text{m}$  operating at 300 GHz. This necessitates more cascaded ORRs in each TTD to maintain femtosecond ripples in magnitude, requiring a more intricate control circuitry to support precise tuning. Therefore, there is an urgent need to develop an OBFN chip which supports continuous beam steering, has a compact design, and ensures both efficient tuning and minimal optical loss. Moreover, with existing OBFN chips, only linear PD arrays can be integrated through butt coupling, whereas a PD matrix is essential to be vertically integrated for 2D beam steering. The prevalent evanescent coupling techniques between Si waveguides and InP PDs [154-156] are not suitable for the vertical integration of TriPleX waveguides with InP PDs due to pronounced refractive index disparities leading to an infeasible propagation constant matching of the optical modes. While other methodologies, such as grating couplers [157-159] and mirror couplers [160], require complicated and time-consuming fabrication processes. Therefore, it is crucial to explore alternative integration strategies.

### 1.3 Thesis organization

The predominant theme of this cumulative thesis is the development of PICs for 1D THz beam steering and the investigation of their utility in THz mobile systems. This part is based on three publications featured in international peer-reviewed journals ([Lu I], [Lu II], and [Lu III]). The latter section of the thesis focuses on advancing from 1D to 2D beam steering capabilities.

[Lu I]: P. Lu, T. Haddad, B. Sievert, B. Khani, S. Makhlouf, S. Dülme, J. F. Estévez, A. Rennings, D. Erni, U. Pfeiffer, and A. Stöhr, "InP-based THz Beam Steering Leaky-wave Antenna," *IEEE Transactions on Terahertz Science and Technology*, vol. 11, no. 2, pp. 218-230, March 2021, doi: [10.1109/TTHZ.2020.3039460](https://doi.org/10.1109/TTHZ.2020.3039460). (This work is licensed under a [Creative Commons License](https://creativecommons.org/licenses/by/4.0/))

[Lu II]: P. Lu, T. Haddad, J. Tebart, M. Steeg, B. Sievert, J. Lackmann, A. Rennings, and A. Stöhr, "Mobile THz Communications using Photonic Assisted Beam Steering Leaky-wave Antennas," *Optics Express*, vol. 29, no. 14, pp. 21629-21638, July 2021, doi: [10.1364/OE.427575](https://doi.org/10.1364/OE.427575). (© 2021 Optical Society of America under the terms of the [OSA Open Access Publishing Agreement](https://openaccess.osa.org/))

[Lu III]: P. Lu, T. Haddad, J. Tebart, C. Roeloffzen, and A. Stöhr, "Photonic Integrated Circuit for Optical Phase Control of  $1 \times 4$  Terahertz Phased Arrays," *Photonics*, vol. 9, no. 12: 902, November 2022, doi: [10.3390/photonics9120902](https://doi.org/10.3390/photonics9120902). (© 2022 by the authors. Licensee MDPI, Basel, Switzerland. This article is an open access article distributed under the terms and conditions of the Creative Commons Attribution (CC BY) license (<https://creativecommons.org/licenses/by/4.0/>).

Chapter 2 presents the development of the first InP-based THz LWA designed for monolithic integration with THz PDs. This LWA enables a 1D beam steering when varying the frequency from 230 to 330 GHz. To verify its performance, scattering parameters and beam profiles of the fabricated THz LWAs are experimentally determined and compared with the simulated results.

Using this LWA, a mobile THz communication system is introduced in chapter 3. To the best of our knowledge, this is the first experimental demonstration of THz communications using beam steering antennas. Specifically, the wireless data rate for a single mobile user is experimentally investigated across varied transmission angles and ranges. Additionally, the guard bands required for multi-user operations are measured to ascertain the maximum number of users and the overall data capacity the system can support.

In chapter 4, a  $1\times 4$  OBFN chip with 4 OPSs based on TriPleX waveguides for 1D beam steering at 300 GHz, is developed and experimentally characterized. Furthermore, the beam steering capability of a  $1\times 4$  phased array employing THz BT antennas, is numerically analyzed when this OBFN chip is used for phase control.

Chapter 5 focuses on the exploration of extending the beam steering capabilities of the developed approaches from one dimension to two dimensions. A PIC concept, based on a  $1\times 4$  LWA array with monolithically integrated PDs, is proposed, and its expected performance is systematically discussed. For phased arrays, a heterogeneously integrated III-V/Si platform is developed to fabricate a 2D PD array on an OBFN chip. Concurrently, the PD's epitaxial layers are optimized to maximize the effective absorption efficiency.

Chapter 6 discusses the attributes and limitations of state-of-the-art THz beam steering approaches. It offers a comprehensive analysis from multiple perspectives, including integrability, THz output power, antenna gain, beam steering range, bandwidth, as well as the complexity of control circuits, scalability for 2D beam steering, and potential application domains.

This final chapter offers a conclusion of the thesis, along with an outlook on the subject matter.

## 2 InP-based THz beam steering leaky-wave antenna

For the first time, an InP-based THz LWA is developed for monolithic integration with InP-based THz PDs. This proposed PIC is designed to generate signals within the frequency range of 230 to 330 GHz via optical heterodyning. Fig. 2-1 illustrates the conceptual design of this PIC. To minimize the number of surface wave modes and consequently enhance the associated antenna radiation efficiency, the THz LWA is fabricated on an ultra-thin InP substrate with a thickness of 50  $\mu\text{m}$ . This substrate is bonded to a Si substrate using the thermocompression bonding (TCB) technique. At this interface, a gold (Au) layer serves both as the bonding layer and as the ground plane for the MSL-based THz LWA. For the transmission of THz signals from the PD to the LWA, a grounded coplanar waveguide to microstrip line (GCPW-MSL) transition is employed. To prevent short circuits between the p- and n-contacts of the PD, layers of Benzocyclobutene (BCB) are utilized. These layers also protect the fragile metallic signal and ground transmission lines from potential damage. To introduce the leak mode, i.e., fast wave, periodic rectangular stubs are attached on both sides of the MSL. In this chapter, numerical analysis of the THz LWAs and GCPW-MSL transitions is presented, accompanied by a detailed exploration of the fabrication process and experimental characterizations results.

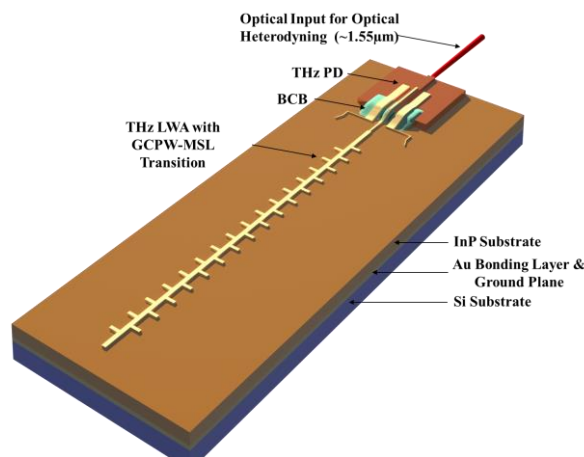


Fig. 2-1 Conceptual view of the proposed PIC for signal generation from 230 to 330 GHz using optical heterodyning. Beam steering is achieved by a THz MSL periodic LWA with an on-chip monolithically integrated THz PD on a 50  $\mu\text{m}$  thick InP substrate bonded on a Si mechanical carrier. Adapted from [Lu 1].

### 2.1 THz LWA and GCPW-MSL transition design

As discussed in chapter 1.1.2, open guided-wave structures have demonstrated superiority over closed guided-wave structures for THz LWAs due to their simpler topology and reduced transmission loss [79]. Another important characteristic of these structures is that the phase constant of the leaky mode can possess both positive and negative values. This enables beam steering from backfire to endfire of the LWAs [161]. Thereof, MSLs are especially inspired due to their straightforward fabrication process and compatibility of integration with active sources [101, 162, 163]. Given these advantages, MSLs are selected for the design of the InP-based THz LWA in this thesis. Furthermore, a GCPW-MSL transition is developed for the experimental

characterization of LWAs and the future monolithic integration with PDs. A visual representation of this design can be observed in Fig. 2-2, which presents the layout for both the GCPW-MSL transition and a segment of the THz LWA.

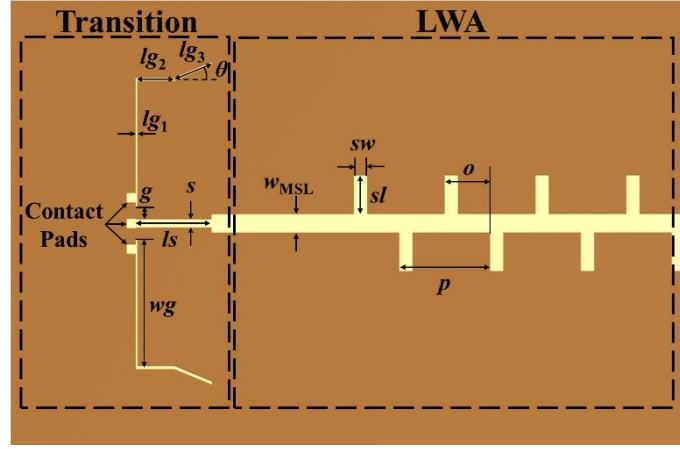


Fig. 2-2 Top view of the GCPW-MSL transition and a segment of the MSL periodic LWA. Adapted from [Lu 1].

### 2.1.1 LWA design

To simplify the design requirements of the GCPW-MSL transition, the input impedance of the LWA is tailored to be  $\sim 35 \Omega$  for impedance matching with the in-house fabricated THz PDs. The MSL width  $w_{\text{MSL}}$  can be described as a function of the InP substrate thickness  $h_{\text{sub}}$ , the relative permittivity of the InP  $\epsilon_{r,\text{InP}}$  ( $\epsilon_{r,\text{InP}} \approx 12.4$  [164]), and MSL characteristic impedance  $Z_0$  [165]:

$$w_{\text{MSL}} = h_{\text{sub}} \cdot \frac{8 \cdot \exp(A)}{\exp(2A) - 2} \quad \text{for } w_{\text{MSL}} < 2 \cdot h_{\text{sub}} \quad (2.1)$$

with the parameter  $A$  being:

$$A = \frac{Z_0}{60} \cdot \sqrt{\frac{\epsilon_{r,\text{InP}} + 1}{2} + \frac{\epsilon_{r,\text{InP}} - 1}{\epsilon_{r,\text{InP}} + 1} \left( 0.23 + \frac{0.11}{\epsilon_{r,\text{InP}}} \right)}. \quad (2.2)$$

For a  $35 \Omega$  impedance, the MSL width is calculated to be  $73.46 \mu\text{m}$  using Eq. (2.1) and Eq. (2.2). This width is then optimized to  $70 \mu\text{m}$  using CST Studio Suite.

The dominant mode of the guided-waves in an MSL is a slow wave and cannot be radiated, i.e., the phase constant  $\beta$  of the dominant mode is larger than the free-space wavenumber  $k_0$ . To generate leaky modes, thirty-two periodic rectangular stubs are symmetrically attached to both sides of the MSL, enabling the introduction of fast waves. In this way, an infinite number of space harmonics with the phase constants  $\beta_n$  is created [76]:

$$\beta_n = \beta_0 + \frac{2 \cdot n \cdot \pi}{p}, \quad (2.3)$$

where  $n$  is the harmonic order,  $p$  is the unit cell period and  $\beta_0$  is the phase constant of the fundamental space harmonic.

Eq. (2.3) can be rewritten as:

$$\frac{\beta_n}{k_0} = \frac{\beta_0}{k_0} + \frac{2 \cdot n \cdot \pi}{k_0 \cdot p} = \frac{\beta_0}{k_0} + \frac{n \cdot \lambda_0}{p}, \quad (2.4)$$

where  $\lambda_0$  is wavelength in vacuum.

From this equation, it can be observed that the harmonic order  $n$  must be negative to enable a radiated space harmonic ( $\beta_n/k_0 < 1$ ), because the fundamental space harmonic is a slow wave ( $\beta_0/k_0 > 1$ ) as discussed above. Generally, LWAs are designed to ensure a unitary fast space harmonic ( $n = -1$ ) to achieve a single-beam radiation [76]. In this case, the period  $p$  is equal to the guided wavelength  $\lambda_g$  [163], which can be calculated through [165]:

$$\lambda_g = \frac{c_0}{f_{\text{LWA}} \cdot \sqrt{\epsilon_{\text{eff}}}}, \quad (2.5)$$

where  $f_{\text{LWA}}$  is the LWA operating frequency. The effective permittivity of the MSL  $\epsilon_{\text{eff,MSL}}$  on the 50  $\mu\text{m}$  thick InP substrate can be calculated using [165]:

$$\epsilon_{\text{eff,MSL}} = \frac{\epsilon_{\text{r,InP}} + 1}{2} + \frac{\epsilon_{\text{r,InP}} - 1}{2 \cdot \sqrt{1 + \frac{12 \cdot h_{\text{sub}}}{w_{\text{MSL}}}}}. \quad (2.6)$$

The calculated period should be 366  $\mu\text{m}$  using Eq. (2.5) and Eq. (2.6), given that the LWA is designed for a frequency range from 230 to 330 GHz with a center frequency of 280 GHz. By means of CST Studio Suite, the period is further optimized to 353  $\mu\text{m}$  for improved realized gain.

The stub length and width are set to 150  $\mu\text{m}$  and 50  $\mu\text{m}$  respectively to maximize the realized gain and optimize the 3-dB beam width.

All key parameters of the finalized THz MSL periodic LWA design are summarized in Table 2-1. The total antenna length is  $\sim 6$  mm.

Table 2-1 Parameters of THz MSL periodic LWA. Adapted from [Lu I].

Symbol	Value ( $\mu\text{m}$ )	Description
$w_{\text{MSL}}$	70	MSL width
$p$	353	Period
$sw$	50	Stub width
$sl$	150	Stub length
$o$	176.5	Stub offset

### 2.1.2 GCPW-MSL transition design

GCPW-MSL transitions in the microwave region typically rely on a limited ground plane width to suppress the excitation of undesired parasitic substrate modes [166-169]. However, simulation results for THz frequencies reveal that such designs cannot offer optimal performance. An alternative solution is the employment of vertical interconnect access (VIA) holes [170], which requires extremely time-intensive sequential processes

in InP, e.g., focused ion beam (FIB) etching. Therefore, a THz GCPW-MSL transition without VIA holes is designed featuring short-length ground planes instead of narrow-width ground planes to limit parasitic substrate modes. The layout of this transition is shown in Fig. 2-2. In this thesis, the LWA is experimentally characterized utilizing a commercial WR-3 GSG-probe for proof-of-concept measurements. Consequently, the contact pad pitch at the start of the transition structure is designed to be  $100\ \mu\text{m}$ , and the width of the signal line  $s$  is set at  $30\ \mu\text{m}$  for impedance matching. The parameters of the GCPW-MSL transition are listed in Table 2-2.

Table 2-2 Parameters of GCPW-MSL transition. Adapted from [Lu I].

Parameter	Value ( $\mu\text{m}$ )	Description
$s$	30	Signal line width
$g$	50	Gap
$l_s$	295	Signal line length
$w_g$	500	Ground-plate width
$lg_1$	5	Ground-strip length 01
$lg_2$	150	Ground-strip length 02
$lg_3$	157	Ground-strip length 03
$\theta$	$22^\circ$	Angle of ground-strip 03

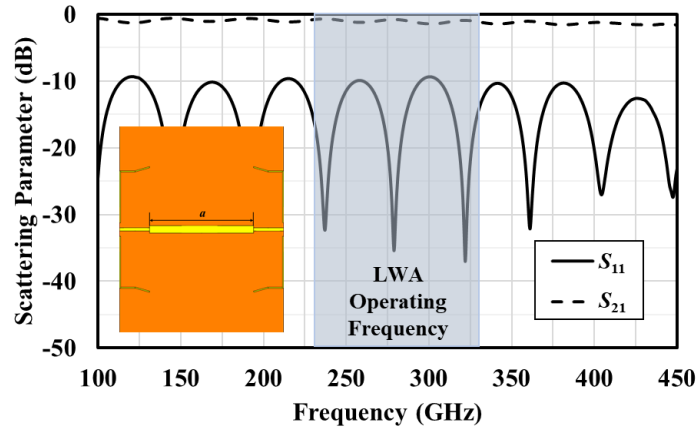


Fig. 2-3 Simulated scattering parameters of the back-to-back GCPW-MSL transition from 100 to 450 GHz. The inset shows the simulated layout of the GCPW-MSL transition with an MSL length of  $a = 1\ \text{mm}$  [Lu I].

The scattering parameters of the developed GCPW-MSL transition are numerically analyzed in a back-to-back transition configuration with a 1 mm long MSL without stubs ( $w_{\text{MSL}} = 70\ \mu\text{m}$ ). The results are plotted in Fig. 2-3. As can be seen,  $S_{11}$  remains below  $-10\ \text{dB}$  over a frequency span from 100 to 450 GHz, presenting a good impedance matching with the LWA throughout its operating frequency range. A periodic fluctuation is observed, which can be attributed to different widths between the transition signal pad and the MSL. This can be optimized using a taper structure at the interface in future designs. Additionally, the maximum insertion loss remains under 1.6 dB over the entire frequency range and below 1.4 dB for the operating frequency of

the LWA. Excluding the simulated average insertion loss of the 1 mm long MSL (~0.5 dB), the derived insertion loss for each GCPW-MSL transition is maximum 0.5 dB in the frequency range of 100 to 450 GHz.

A survey of state-of-the-art GCPW-MSL transitions is provided in Table 2-3. As can be seen, the transition developed in this thesis offers the highest operating frequency and the largest bandwidth without sacrificing insertion loss or return loss.

Table 2-3 Comparison of GCPW-MSL transitions [Lu 1].

Freq. (GHz)	$S_{11}$ (dB)	$S_{21}$ (dB)	Substrate Material	Ref.
10-40	< -10	> -1	High-resistivity silicon	[166]
50-75	< -10	> -1.5	PET	[167]
DC-77	< -10	-0.2	BCB	[168]
75-110	< -18	-0.3	High-resistivity silicon	[169]
100-450	< -10	> -0.5	InP	This work

## 2.2 LWA fabrication

A metallic ground layer is indispensable for MSL periodic LWAs. Generally, there are two methods to bond the InP-based antenna substrate onto the Si carrier: eutectic bonding and TCB. The eutectic bonding process commonly employs alloys, such as Au-tin (Sn), Au-Ge, Au-Si and aluminum (Al)-Ge, requiring temperatures ranging between 300°C and 500°C [171]. However, the intense heat can induce considerable mechanical stress between the bonded InP and Si wafers due to the discrepancy in their thermal expansion coefficients ( $\alpha_{\text{InP}} = 4.8 \times 10^{-6} \text{ K}^{-1}$ ,  $\alpha_{\text{Si}} = 2.6 \times 10^{-6} \text{ K}^{-1}$ ) [172]. Additionally, such temperatures can alter the doping profile of PD epitaxial layers. Therefore, this thesis employs TCB, which is based on interfacial atom diffusion and operates at a lower bonding temperature. Au is selected as the bonding layer material due to its low resistivity, oxidation resistance, low diffusion temperature and high bonding accuracy [173-175].

The fabrication procedure for the THz LWA integrated with the GCPW-MSL transition using the developed substrate-transfer technology, is outlined in Fig. 2-4. Initially, layers of titanium (Ti), platinum (Pt) and Au with thicknesses of 30 nm, 20 nm and 1000 nm respectively, are deposited onto both InP and Si substrate surfaces. After cleaning both wafers with acetone and isopropanol, they are bonded using a flip-chip bonder (SET FC150). The bonding parameters are detailed in Fig. 2-5. A bonding pressure of ~3 MPa is maintained for around 4 hours with an annealing temperature of 250°C. This relatively low temperature helps mitigate mechanical stress between the InP and Si wafers. Notably, temperature adjustments are only initiated once the optimal bonding pressure is reached. This ensures minimal displacement and deformation of the wafers. After bonding, the InP substrate is ground, followed by a chemical mechanical polishing (CMP) process. This results in a uniformly 50  $\mu\text{m}$  thick InP substrate with a smooth surface. Finally, THz LWAs integrated with GCPW-MSL transitions are fabricated using contact lithography. Photographs of the fabricated THz LWAs and transitions are presented in Fig. 2-4. As observed, the 50  $\mu\text{m}$  thick InP

substrate exhibits minimal edge breakages and a visually glazed surface. This denotes both the robustness of the TCB bond and the excellence of the CMP procedure.

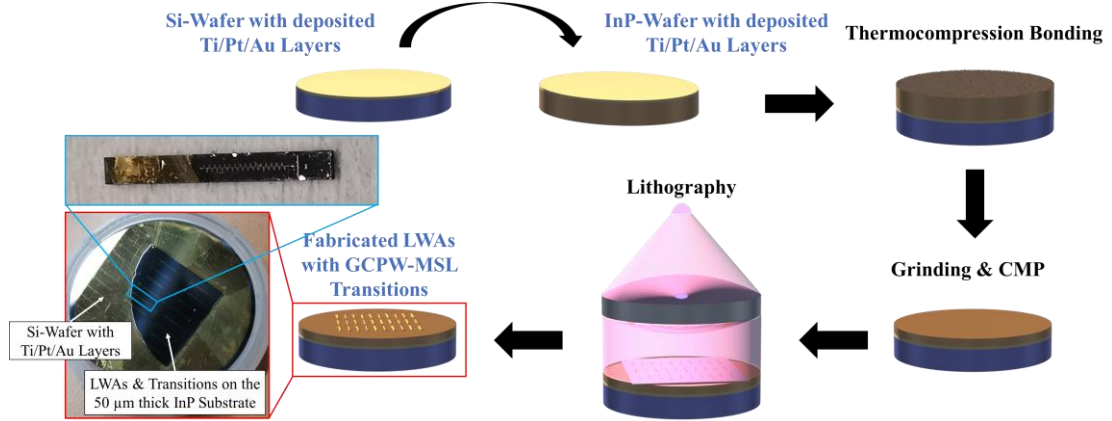


Fig. 2-4 Fabrication process flow of the designed THz MSL periodic LWAs with GCPW-MSL transitions based on substrate-transfer technology. The photographs show the fabricated LWAs with GCPW-MSL transitions on an intact and a cleaved 1.5 mm wide InP substrate. Adapted from [Lu I].

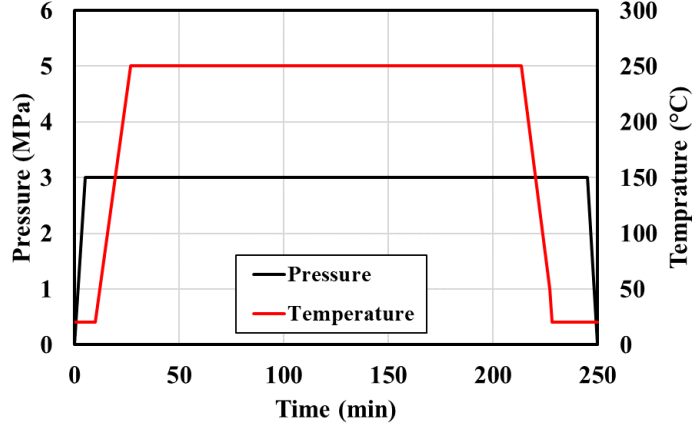


Fig. 2-5 Bonding parameters of the developed substrate-transfer technology.

For high-frequency electronic components, the skin effect cannot be ignored which leads to an elevated electric current density near the outer conductor surface. The depth, at which the current density drops to 1/e of the surface value, is called skin depth and given by [176]:

$$\delta = \frac{c_0}{\sqrt{2\pi\sigma_0 f}} \text{ for } l_{\text{MFP}} \ll \delta, l_{\text{MFP}} \ll \frac{v_F}{f}, \quad (2.7)$$

where  $c_0$  is the speed of light in vacuum,  $f$  is frequency and  $T$  is temperature. For Au at room temperature, the static electric conductivity  $\sigma_0$  is  $3 \times 10^{17} \text{ s}^{-1}$  [176], the mean free path of a conduction electron  $l_{\text{MFP}}$  is 37.7 nm [177] and the Fermi velocity  $v_F$  is  $13.82 \times 10^5 \text{ m/s}$  [177]. Using these values, the skin depth is calculated to be 398.9 nm at 300 GHz.

The Au surface roughness of the fabricated THz LWA is experimentally characterized using a DektakXT stylus profiler. In total, five thousand data points are recorded over a measurement length of 500  $\mu\text{m}$ , as shown in Fig. 2-6. The surface height predominantly fluctuates within the range of  $\pm 12 \text{ nm}$ . According to the model presented

in [178], the root-mean-square (RMS) roughness is determined to be  $\sim 8.3$  nm. This level of roughness indicates a minimal influence from the skin effect. The RMS roughness value is also incorporated into the LWA performance simulations executed using CST Studio Suite. The simulation results will be elaborated in the following subchapter and compared with measurement values.

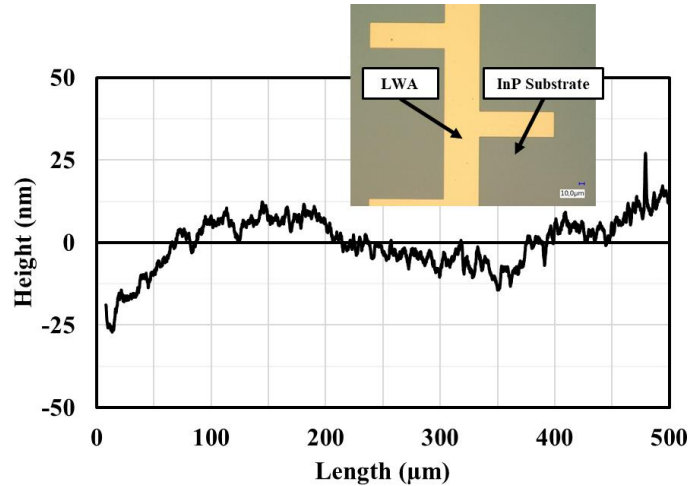


Fig. 2-6 Measured roughness of the fabricated LWA surface using a DektakXT stylus profiler. Insert shows a microscopic image of the fabricated LWA section [Lu I].

## 2.3 Numerical analysis and experimental characterization

### 2.3.1 Scattering parameter

In Fig. 2-7, the simulated  $S_{11}$  of the developed THz LWA integrated with the GCPW-MSL transition is plotted by a black solid line. It can be observed that the return loss predominantly exceeds 10 dB except near 273 GHz due to the open-stopband (OSB) effect [76, 93, 161]. In periodic LWAs, when the beam radiates to broadside, all the reflections of guided waves at radiating elements add in phase back to the antenna input and lead to a contra-directional coupling of space harmonics. This results in a reactive input impedance and a large mismatch.

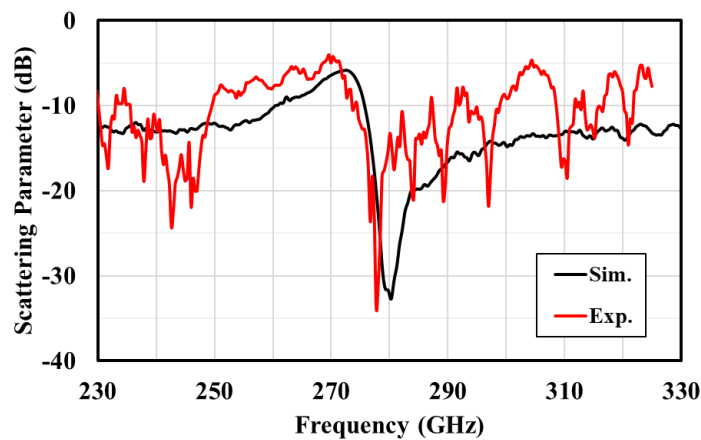


Fig. 2-7 Simulated and measured  $S_{11}$  parameters of the fabricated THz LWA with the GCPW-MSL transition [Lu I].

To validate these simulated outcomes, the  $S_{11}$  is experimentally characterized using

a VNA (Agilent Technologies 8361A) with a millimeter wave VNA extender (OML V03VNA2-T/R). These results are also plotted in Fig. 2-7 as a red solid line. A good agreement is yielded between the simulation results and the experimental data. It needs to be mentioned that in our recent publication [179], the OSB effect in this developed LWA has been effectively mitigated by adding matching stubs to form an asymmetric unit cell.

### 2.3.2 Far-field radiation pattern

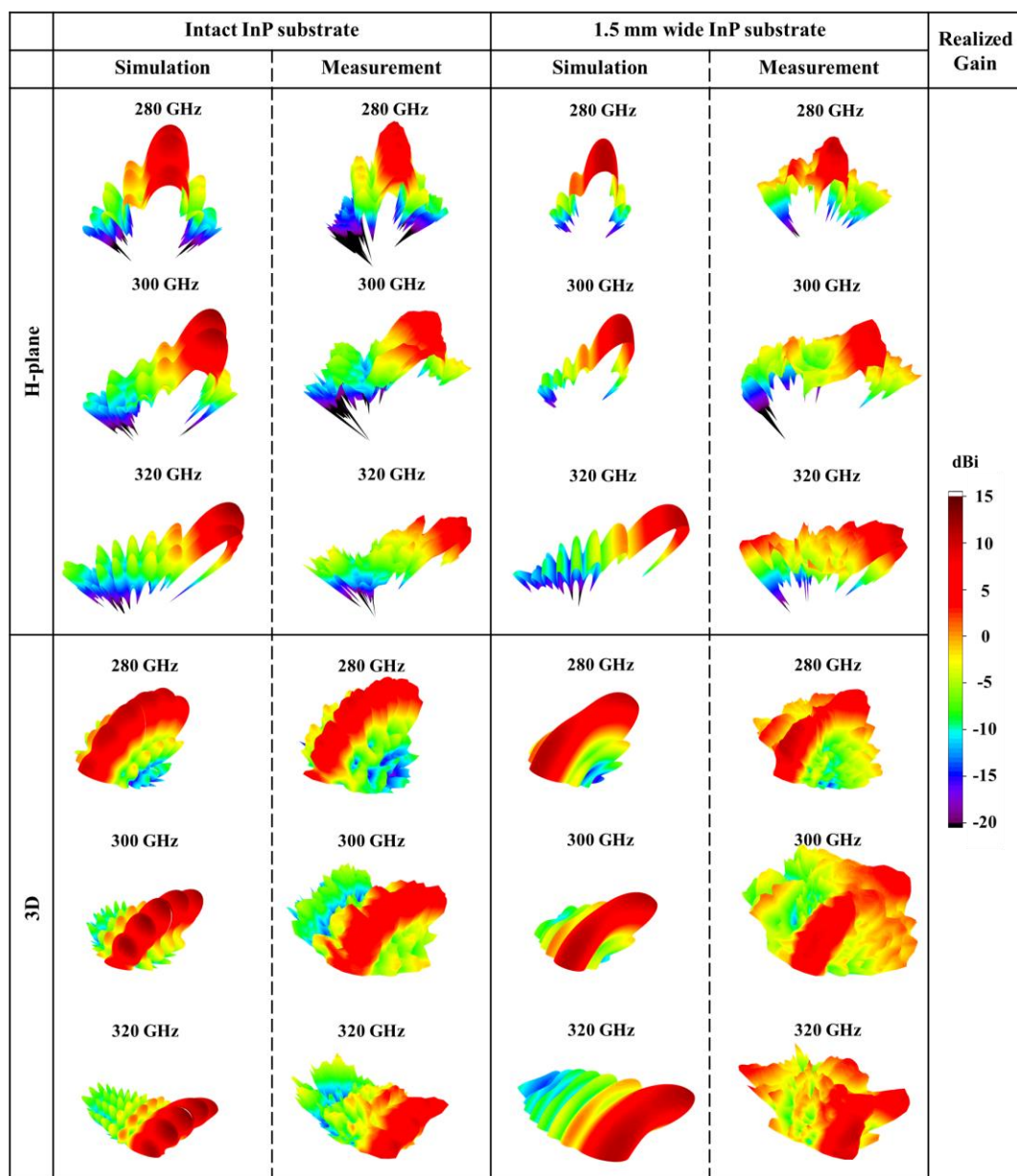


Fig. 2-8 Simulated and experimentally determined far-field radiation patterns of the THz LWA with the GCPW-MSL transition on an intact InP substrate and a cleaved InP substrate with a width of 1.5 mm at 280 GHz, 300 GHz and 320 GHz. Adapted from [Lu 1].

The far-field radiation patterns of the developed THz LWA integrated with the GCPW-MSL transition are simulated and experimentally characterized on an intact InP substrate as well as a cleaved InP substrate with a 1.5 mm width, respectively. It can be seen from Fig. 2-8 that the simulated radiation patterns of the LWA on the intact

substrate exhibit multiple finger-like lobes caused by surface wave modes. In contrast, a fan-like beam can be achieved by narrowing InP substrate.

The experimental characterization of the LWA radiation patterns is executed using a THz on-wafer antenna measurement system as shown in Fig. 2-9 [180]. For THz signal generation, an extender (Rohde & Schwarz ZC330) is connected to the VNA (Rohde & Schwarz ZVA-40), while another extender (Rohde & Schwarz ZRX330) is used for signal detection. The receiver with a high-gain horn antenna is installed on an automatic hemispherical goniometer system which enables a measurable inclination angle from  $0^\circ$  to  $51^\circ$  and an azimuthal angle of  $360^\circ$ . THz signal from the VNA is fed to the THz LWA using a GSG-probe contacted with the GCPW-MSL transition. It needs to be mentioned that this measurement system can correctly measure the far-field radiation patterns only from broadside to endfire of the LWA, because the radiation towards backfire is partially reflected by the GSG-probe. Experimentally characterized far-field patterns in steps of  $2^\circ$  over an inclination range from  $0^\circ$  to  $50^\circ$  and in steps of  $5^\circ$  over the full azimuthal plane are presented in Fig. 2-8 as well. These results show an excellent agreement with the simulated beam patterns. For the LWA on the intact InP substrate, not only the finger-like radiation patterns, but also even the side lobes agree qualitatively for each frequency. Some stronger side lobes can be observed when having the 1.5 mm wide antenna substrate, which is mainly due to roughness introduced to the substrate edges during the sawing process.

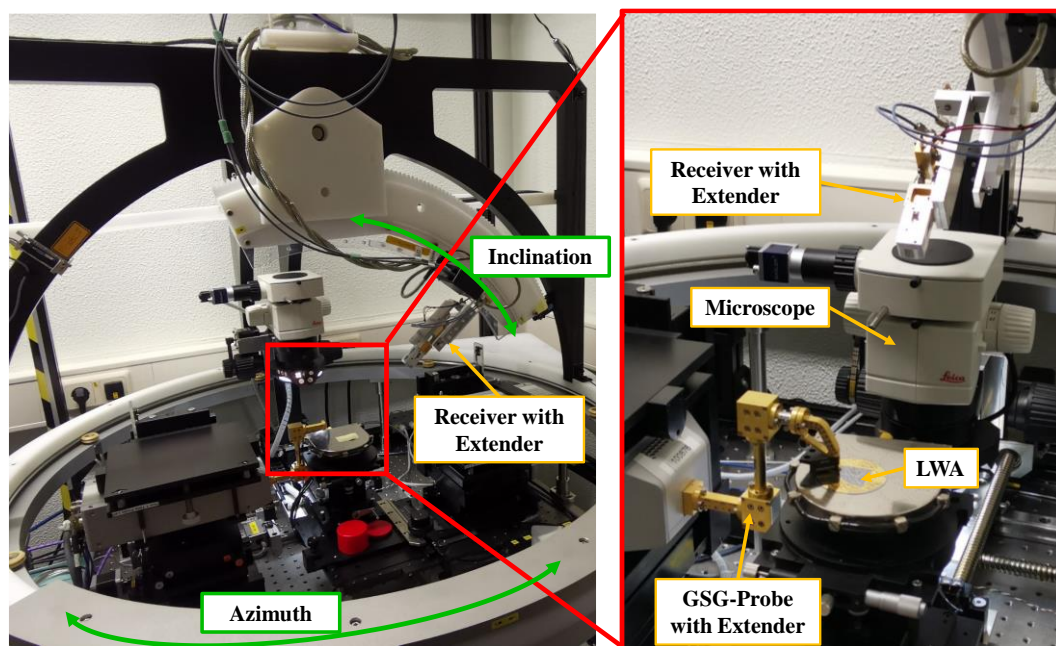


Fig. 2-9 On-wafer antenna measurement system for far-field radiation pattern measurements [Lu 1].

The quantitative evaluations of beam direction, 3-dB beam width and realized gain from both simulated and measured results are summarized in Fig. 2-10, Fig. 2-11, and Fig. 2-12, respectively.

Regardless of the substrate width of the LWA, simulation results as shown in Fig. 2-10 indicate that the beam direction is steered quasi-linearly from  $-46^\circ$  to  $42^\circ$  in the H-plane when the frequency is varied from 230 to 330 GHz. This simulation trend is verified by the measurement results from 280 to 330 GHz. Only a slight deviation can

be observed for the LWA on the 1.5 mm wide substrate above 320 GHz. This can be attributed to the rough substrate edges introduced during the sawing process.

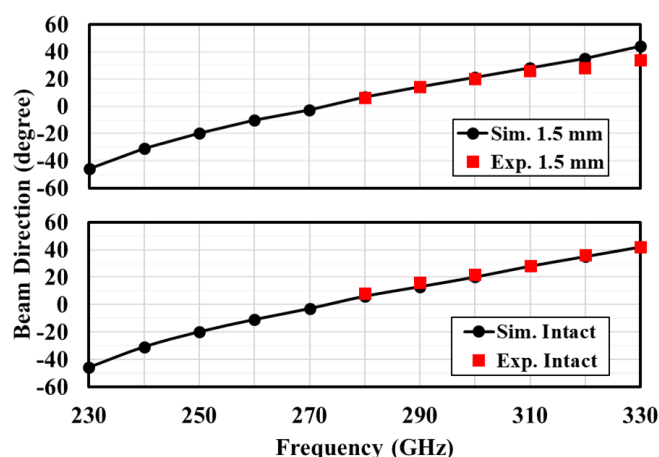


Fig. 2-10 Simulated and measured relationship between beam direction and frequency from 230 to 330 GHz of the THz LWA with the GCPW-MSL transition in the H-plane. Adapted from [Lu I].

As illustrated in Fig. 2-11, substrate width also has a minimal influence on the 3-dB beam width in the H-plane. The maximum 3-dB beam width reaches  $\sim 17^\circ$  at 230 GHz and reduces as the frequency increases. Measurement results confirm the simulated values and demonstrate the impact of the edge roughness on the cleaved InP substrate at higher frequencies. Nonetheless, the minimum 3-dB beam width is still larger than  $9^\circ$ . Given that a beam steering range of  $\sim 88^\circ$  is expected, when the LWA frequency is varied from 230 to 330 GHz with a steering rate of  $\sim 0.88^\circ/\text{GHz}$ , the coherence bandwidth of the LWA is determined to be more than 10 GHz for the entire beam steering range.

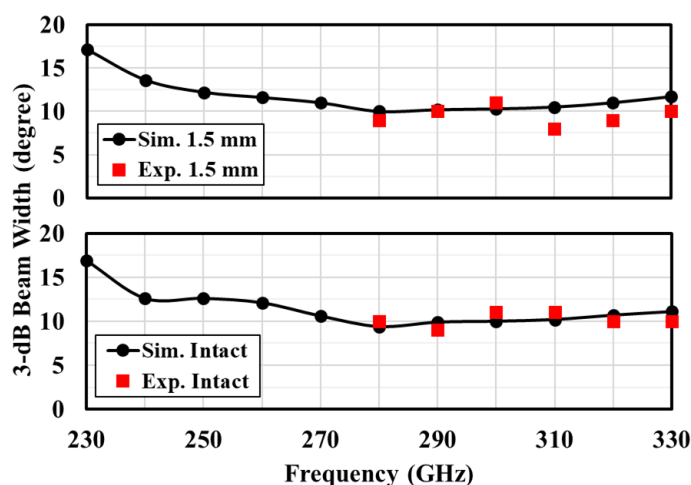


Fig. 2-11 Simulated and measured relationship between 3-dB beam width and frequency from 230 to 330 GHz of the THz LWA with the GCPW-MSL transition in the H-plane. Adapted from [Lu I].

Fig. 2-12 presents both the numerically analyzed and experimentally determined realized gains of the LWA on InP substrates with varying widths. A noticeable discrepancy exists between the simulated and measured realized gain of the LWA on the intact substrate in the 280 to 330 GHz range. This can be partially attributed to the

suboptimal pitch of the GSG-probe utilized during the experimental characterization, leading to calibration challenges. However, after employing a compatible GSG-probe for characterization of the LWA on the cleaved substrate, the experimental results show a good agreement with the simulated values.

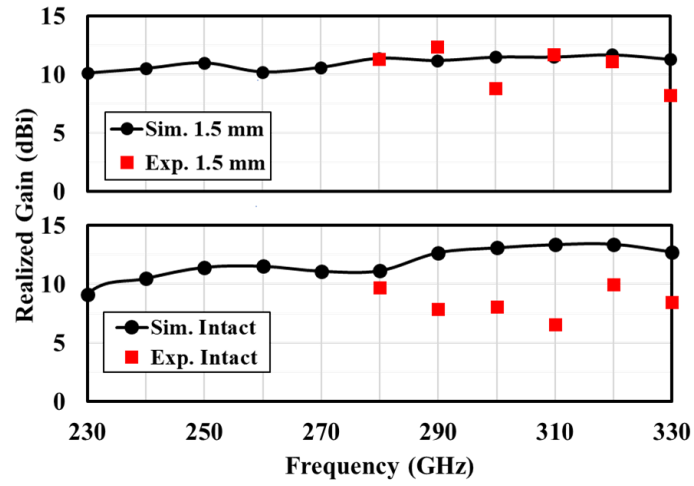


Fig. 2-12 Simulated and measured relationship between realized gain and frequency from 230 to 330 GHz of the THz LWA with the GCPW-MSL transition. Adapted from [Lu I].



### 3 Mobile THz communications using InP-based leaky-wave antenna

In this chapter, the first mobile 6G THz communication system is demonstrated. This system utilizes radio-over-fiber technology combined with an optical heterodyne setup to generate THz data signals which are then radiated by the innovative InP-based THz LWA. By adjusting the wavelength of the local oscillator (LO) laser, the beam direction can be easily steered. For detection, an envelope detector is employed. The performance of this mobile THz communication system is experimentally investigated across various wireless transmission angles and distances, in both single-user and multi-user scenarios.

#### 3.1 LWA transmitter chip with Teflon lens

To enhance the directivity of the LWA, a hemicylindrical Teflon lens is designed using CST Studio Suite. This lens has a diameter of 3.8 mm and a relative permittivity of  $\sim 2.1$ . Its impact on the LWA is evaluated using the previously mentioned THz on-wafer antenna measurement system [180]. Specifically, the far-field radiation patterns of the LWA are experimentally characterized at various angles with the lens positioned 2.7 mm above the antenna. The measured values, together with the simulation results both with and without the Teflon lens, are presented in Fig. 3-1, Fig. 3-2 and Fig. 3-3.

The simulation results in Fig. 3-1 reveal that the lens has a slight impact on the LWA's beam steering capability with a maximum deviation of  $4^\circ$ . Experimental characterization indicates that the beam scans over  $33^\circ$ , i.e., from  $6^\circ$  to  $39^\circ$ , in a quasi-linear manner with  $\sim 0.7^\circ/\text{GHz}$  when the frequency is adjusted between 280 GHz and 330 GHz.

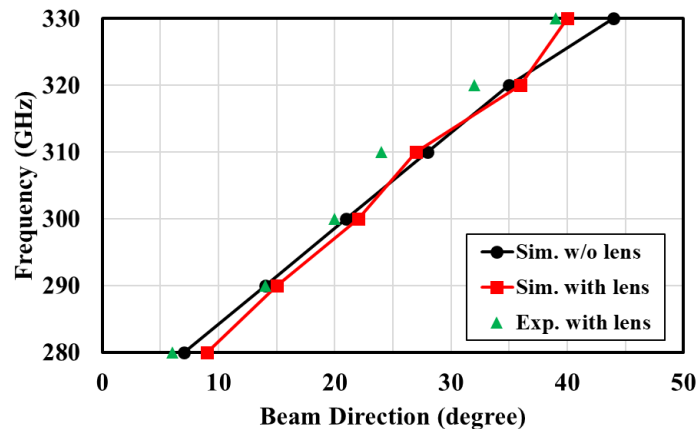


Fig. 3-1 Simulated and experimentally characterized beam direction of the THz LWA with the GCPW-MSL transition on the 1.5 mm wide InP substrate in the H-plane. Adapted from [Lu II].

It can be observed from Fig. 3-2 that the lens has a negligible influence on the simulated 3-dB beam width in the H-plane over the entire steering range as expected, since the lens is intentionally designed to focus the beam only in the E-plane. Also, a good agreement between the measured and the simulated results is achieved with a maximum deviation of  $1^\circ$ . The smallest measured 3-dB beam width is  $9^\circ$ . With the

beam steering rate of  $0.7^\circ/\text{GHz}$ , the coherence bandwidth of the antenna exceeds 12 GHz.

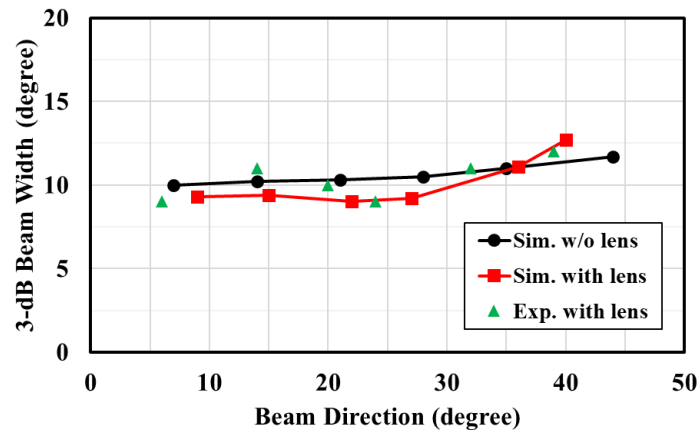


Fig. 3-2 Simulated and experimentally characterized 3-dB beam width of the THz LWA with the GCPW-MSL transition on the 1.5 mm wide InP substrate in the H-plane. Adapted from [Lu II].

As depicted in Fig. 3-3, the simulated LWA's directivity without the developed Teflon lens is around 14 dBi, which is significantly enhanced to  $\sim 23$  dBi when employing the lens. A minor discrepancy of less than 2 dB between the simulated and measured values can be observed for beam directions exceeding  $20^\circ$ , which can be attributed to imperfections in the shape of the fabricated Teflon lens and potential misalignment during the measurements.

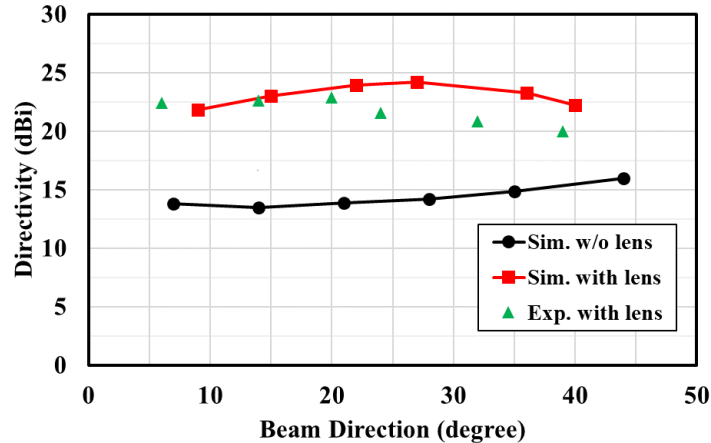


Fig. 3-3 Simulated and experimentally characterized directivity of the THz LWA with the GCPW-MSL transition on the 1.5 mm wide InP substrate. Adapted from [Lu II].

### 3.2 THz communication system setup

Fig. 3-4 presents a schematic view of the THz communication system which uses the photonic-assisted THz LWA as a beam-steering transmitter. The system employs an optical heterodyne setup for THz data signal generation and an envelope detector. In this setup, an arbitrary waveform generator (AWG, Keysight M9505A) generates an intermediate frequency (IF) orthogonal frequency-division multiplexing (OFDM) waveform in the digital domain and then converts it to the analog domain. After amplification using a medium power amplifier (MPA), the waveform is modulated onto

a 1.55  $\mu\text{m}$  optical carrier by means of a Mach-Zehnder modulator (MZM) and then optically amplified by an erbium-doped fiber amplifier (EDFA). A second laser (laser 2) with a tunable beat frequency relative to laser 1 in the THz range is employed for optical heterodyning in the UTC-PD (NTT Electronics J-band photomixer module) and consequently, the OFDM waveform can be transferred to the THz domain. To investigate multi-user scenarios using the LWA, a third laser is added to generate a second THz carrier. Through the GSG-probe (FormFactor I325-T-GSG-100BT), the THz OFDM waveform generated by the UTC-PD is transmitted to the LWA. The beam direction can be manipulated by adjusting the wavelengths of laser 2 or laser 3. The Teflon lens is placed 2.7 mm above the LWA. For reception, a WR-2.8 diagonal horn antenna is used to receive the wireless transmitted THz waveform which is then amplified by the THz low noise amplifier (LNA, Radiometer Physics LNA 250-350 25 8). The subsequent down-conversion to IF is executed using an envelope detector, i.e., the zero-biased Schottky-barrier diode (SBD, Virginia Diodes WR-2.8 ZBD-F40). In contrast to a heterodyne detection approach, the performance of an envelope receiver is independent of the frequency difference between the data carrier and the LO signal [53, 181]. Thus, the envelop detection approach is suitable for LWA-based transmitters with variable THz carrier frequencies. After that, the waveform is digitized by the high-frequency digital signal analyzer (DSA, Keysight DSA-Z 634A) and then analyzed using the off-line digital signal processing. The maximum data bandwidth of this mobile THz communication system is expected to be  $\sim 12$  GHz which is only limited by the coherence bandwidth of the LWA. The photograph in Fig. 3-4 shows the wireless frontend and receiver setup. The receiver is mounted on a goniometer to support angular-dependent measurements and emulate a mobile user scenario.

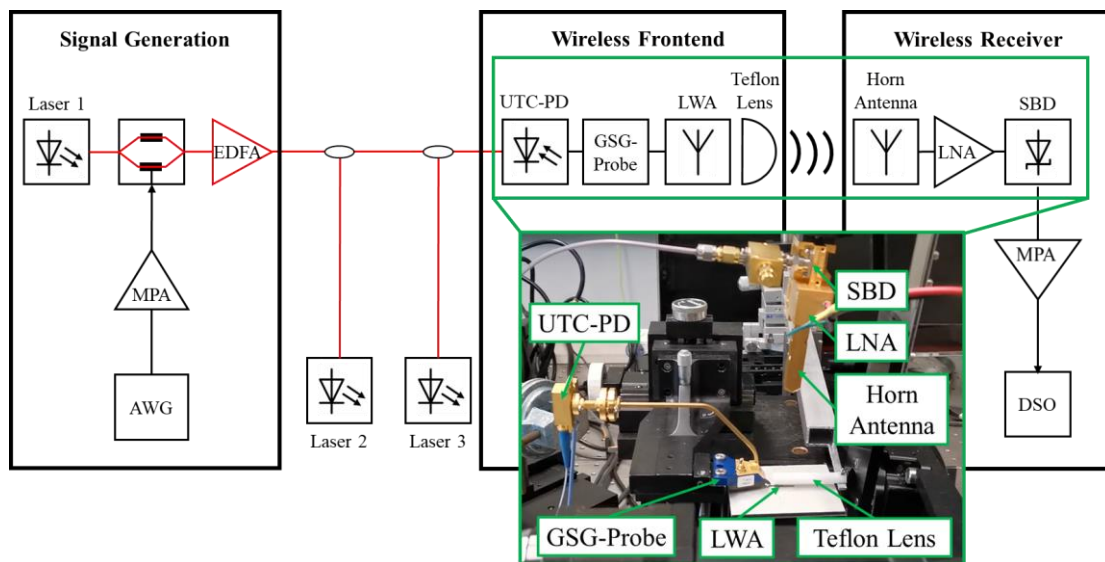


Fig. 3-4 Schematic view of the mobile THz communication system using the photonic-assisted THz LWA with the Teflon lens. The photograph shows the wireless frontend and receiver.

The link budget of the system is estimated in Table 3-1 for beam directions of  $6^\circ$ ,  $20^\circ$  and  $32^\circ$ . As intended, the system performance remains largely consistent regardless of the beam direction or the corresponding THz wireless carrier frequency. This leads to a quasi-uniform input power to the SBD of around  $-9.6$  dBm for all beam directions.

It needs to be mentioned that while though the Teflon lens enhances the LWA directivity by about 9 dB, the measured realized gains are around 14.3 dBi, as shown in Table 3-1. This is only an improvement of ~3 dB compared to the results (without the lens) presented in Fig. 2-12. The primary reason for this discrepancy is that repeated characterizations of the fabricated LWA damaged the contact pads of the GCPW-MSL transition, resulting in increased losses. Therefore, a ~6 dB higher input power to the SBD is expected when a freshly fabricated LWA is used in this communication system.

Table 3-1 Link budget for beam directions of 6°, 20° and 32° for a wireless distance of 6 cm. Adapted from [Lu II].

Beam direction (degree)	6	20	32
Wireless carrier frequency (GHz)	280	300	320
PD output power (dBm)	-14.27	-13.64	-14.46
Probe insertion loss (dB)	4.73	5.11	5.79
LWA realized gain (dBi)	14.08	14.01	14.76
FSPL (dB) @ 6 cm	56.95	57.55	58.11
Horn antenna realized gain (dBi)	23.63	24.03	24.56
THz LNA gain (dB)	27.95	28.82	29.92
SBD input power (dBm)	-10.29	-9.46	-9.12

### 3.3 Single-user mobile THz communications

The performance of the mobile THz communication system is first verified by measuring the bit error rate (BER) over a wireless distance of 6 cm and with beam angles from 6° to 39°. The measured signals have bandwidths of 8 GHz and 12 GHz at an IF of 6 GHz using a 4-QAM IF-OFDM modulation. The MZM is biased at ~2 V to minimize the effects of signal-signal beating interference (SSBI) [181]. Of the 512 subcarriers, 16 are used as pilots to compensate for the carrier-frequency offset. Since the input power of the SBD receiver is nearly independent of the beam direction as detailed in Table 3-1, a consistent BER is expected and has been confirmed by the measurement results plotted in Fig. 3-5.

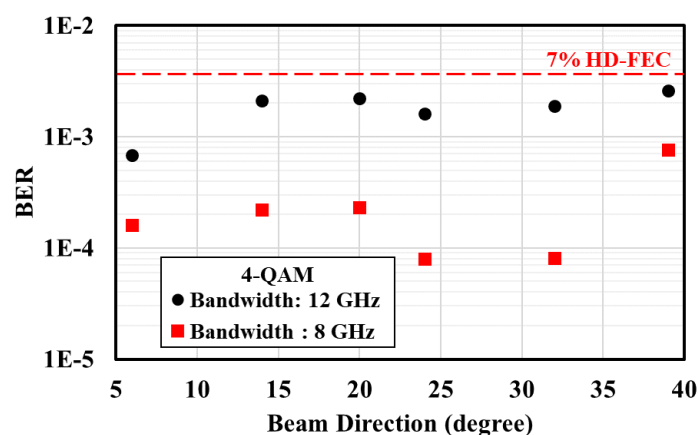


Fig. 3-5 Measured BER of 4-QAM IF OFDM data signals with bandwidths of 8 GHz and 12 GHz from 6° to 39° over a wireless distance of 6 cm. The IF is 6 GHz. Adapted from [Lu II].

For both bandwidths, the BERs are below  $3.8 \times 10^{-3}$  which is the threshold for 7% overhead hard decision forward error correction (HD-FEC) [182]. Based on these

results, it can be concluded that a minimum net data rate of 20.46 Gbit/s is achieved for all beam directions using a 12 GHz bandwidth.

To evaluate the system performance for extended wireless distances, the BER is measured again for 4-QAM IF OFDM waveforms with bandwidths of 6 GHz, 4 GHz and 2 GHz (IF at 3 GHz), while progressively moving the receiver away from the transmitter at a beam direction of  $6^\circ$ . The results are depicted in Fig. 3-6. For a bandwidth of 6 GHz (data rate: 12 Gbit/s), a wireless transmission distance is achieved up to 16 cm for below the HD-FEC level. When the bandwidth is reduced to 4 GHz, the wireless link can be expanded up to 20 cm, while a data rate of 4 Gbit/s (bandwidth: 2 GHz) is accomplished for a wireless distance of 32 cm.

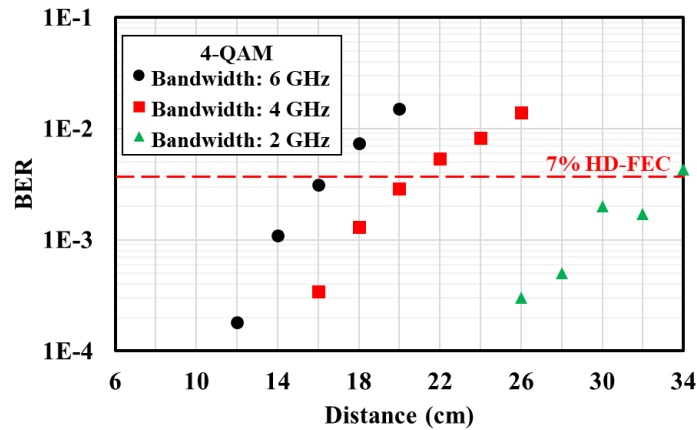


Fig. 3-6 Measured BER of 4-QAM IF OFDM data signals for wireless transmission distances from 6 to 34 cm. The IF is 3 GHz, and the beam direction is  $6^\circ$ . Adapted from [Lu II].

### 3.4 Multi-user THz communications

For multi-user scenarios, the proposed THz LWA can be used to simultaneously generate multiple beams pointing in different directions by assigning a different carrier frequency to each user waveform. In the proposed mobile THz communication system based on optical heterodyning, multiple carriers can be generated by using additional LO lasers. To survey the number of users and the total data capacity that this system can support, it is necessary to experimentally determine the minimum angular difference between beams assigned to different users. For this reason, an additional LO laser (laser 3) is added to simultaneously generate and radiate two THz waveforms targeting different directions (see Fig. 3-7).

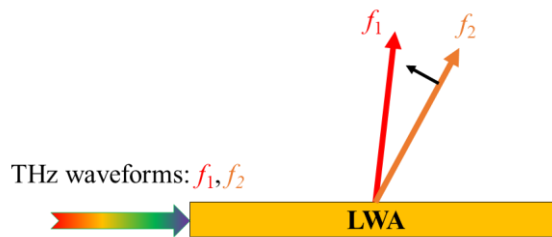


Fig. 3-7 Schematic view of the LWA in multi-beam operation.

One beam with frequency  $f_1$  is fixed at a direction of  $6^\circ$ , while the second beam is steered closer to the first one by reducing its frequency  $f_2$ . The BER is measured for a

wireless distance of 6 cm until the values for one user reach the HD-FEC threshold of  $3.8 \times 10^{-3}$  due to the interference between the two OFDM waveforms. Systematic experiments are executed for data signals with different modulation parameters and the yielded results are summarized in Table 3-2.

It is found that regardless of bandwidth, the guard band between two waveforms must be larger than 1 GHz to ensure transmission below the HD-FEC threshold. The number of users that the system can potentially support is linked to the available bandwidth for each user. In detail, with a wireless data rate of 12 Gbit/s per user, a minimum user separation of  $10^\circ$  allows the fabricated LWA to simultaneously support up to four users within its  $33^\circ$  scanning range. This results in a total data capacity of 48 Gbit/s, assuming that the spectral power density of the beams satisfies the below HD-FEC requirements. By reducing the bandwidth, the signal-to-noise ratio (SNR) is increased which enables the use of more complex QAM modulations, such as 16-QAM. Consequently, a data rate of 4 Gbit/s is achieved with a narrow bandwidth of 1 GHz. Here, users can be located closer to each other. This increases the potential user count to 12, while maintaining a total data capacity at 48 Gbit/s.

Table 3-2 Measurement parameters and results for multi-user scenarios [Lu II].

QAM	IF (GHz)	Data Bandwidth (GHz)	Data Rate (Gbit/s)	BER	Guard Band (GHz)	User Separation (degree)	User Number	Total Data Capacity (Gbit/s)
16	1	1	4	$3.2 \times 10^{-3}$	1	3	12	48
16	3	2	8	$7.8 \times 10^{-4}$	1	6	6	48
4	4	6	12	$1.3 \times 10^{-3}$	1	10	4	48

## 4 Optical beam forming network chip for THz phased array

For certain THz applications, such as imaging, frequency-independent photonic-assisted THz beam steering approaches are required. As discussed in chapter 1.2.2, it is quite challenging to implement easy-to-use optical TTDs for THz phased arrays. Due to the reduced influence of the beam squint effect in the THz domain, OPSs are deemed as an attractive alternative. This chapter reports on the design and experimental characterization of a  $1 \times 4$  OBFN chip based on four OPSs consisting of ORRs for continuous beam steering at 300 GHz. Compared to OPSs relying on straight waveguides [114], this OBFN chip avoids waveguide intersections and allows a higher phase tuning efficiency. The fabrication of this OBFN chip employs TriPleX waveguides with an extremely low optical propagation loss and a high optical confinement factor, leading to a compact chip design [133]. Additionally, this chip can be monolithically integrated with diverse photonic components, e.g., reconfigurable photonic RF filters [183], high-granularity wavelength division multiplexers [184], high-order ring resonators [185] and programmable optical signal processors [186]. Thus, it becomes feasible to develop a single PIC that incorporates multiple complex functions, including the capability for beam steering.

### 4.1 OBFN chip design

The concept of the  $1 \times 4$  OBFN chip with integrated THz PDs for 1D beam steering at 300 GHz is shown in Fig. 4-1. Two laser signals (@  $1.55 \mu\text{m}$ ) with a beat frequency of 300 GHz are coupled into the OBFN chip and then divided into four waveguides by three MZIs with tunable power distribution capabilities. Each OPS consists of two cascaded and identical ORRs based on TriPleX waveguides. Using coupler heaters, the power coupling coefficients of the ORRs can be adjusted, while their resonance frequencies are modified by the biases of the ring heaters. Four butt-coupled PDs with integrated antennas having a half-wavelength pitch are used to transfer the optical phase shift to the THz domain by optical heterodyning, allowing control of the THz beam direction through the OBFN chip.

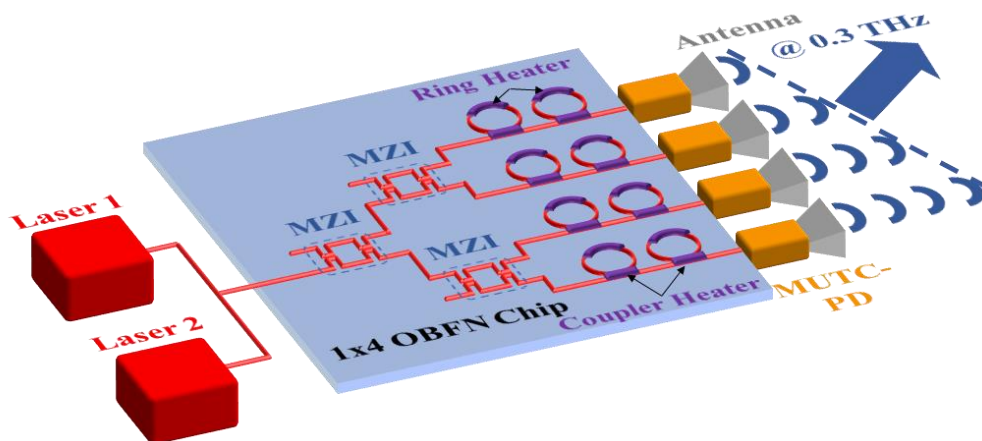


Fig. 4-1 Concept of the  $1 \times 4$  OBFN chip with integrated MUTC-PDs for 1D beam steering at 300 GHz [Lu III].

To understand the operating principle of OPSs based on ORRs, the phase response

of a single ORR must be investigated. Under the condition of over-coupling range (the power coupling coefficient  $k$  is larger than the round-trip loss  $P_L$ ), the phase response is given by [187]:

$$\varphi(\Omega) = \pi - (2\Omega + \varphi_{\text{ring}}) - \arctan \left[ \frac{\sqrt{1-k} \cdot \sin(\Omega + \varphi_{\text{ring}})}{q - \sqrt{1-k} \cdot \cos(\Omega + \varphi_{\text{ring}})} \right] - \arctan \left[ \frac{q \cdot \sqrt{1-k} \cdot \sin(\Omega + \varphi_{\text{ring}})}{1 - q \cdot \sqrt{1-k} \cdot \cos(\Omega + \varphi_{\text{ring}})} \right], \quad (4.1)$$

where  $\Omega$  is the normalized angular frequency to the free spectral range (FSR) of an ORR ( $\Omega = 2 \cdot \pi \cdot f / f_{\text{FSR}}$ ) and  $\varphi_{\text{ring}}$  is the normalized round-trip phase shift which indicates the resonance frequency offset of the ORR ( $\varphi_{\text{ring}} = 2 \cdot \pi \cdot f_{\text{res,offset}} / f_{\text{FSR}}$ ). The amplitude loss factor  $q$  is a function of the round-trip loss  $P_L$ :

$$q = 10^{-\frac{P_L}{20}}. \quad (4.2)$$

For a lossless ORR ( $q = 1$ ) with a power coupling coefficient of 0.5, the calculated phase response of a single ORR ( $\varphi_{\text{ring}} = 0$ ) over one FSR (red line) is shown in Fig. 4-2. By changing  $\varphi_{\text{ring}}$  using the ring heater, the phase response can be shifted as illustrated by the purple and yellow lines. When one laser signal ( $f_{\text{LD1}}$ ) is set at the ring's resonance frequency and the other optical heterodyne signal ( $f_{\text{LD2}}$ ) is set at the off-resonance frequency, different optical phase shifts are applied to the two laser signals, which are subsequently transferred to the THz domain using the PDs described by  $\Delta\varphi_{\text{THz}} = \Delta\varphi_{\text{LD1}} - \Delta\varphi_{\text{LD2}}$  [188].

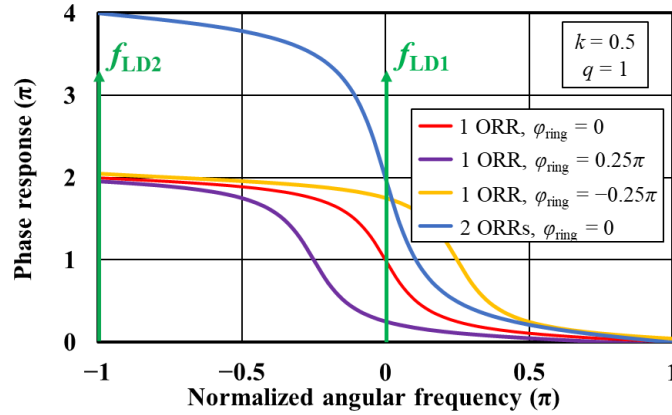


Fig. 4-2 Calculated phase responses over one FSR for a single ORR with different round-trip phase shifts  $\varphi_{\text{ring}}$  and for two cascaded ORRs with the same resonance frequency. The power coupling coefficient  $k$  is 0.5 and the amplitude loss factor  $q$  is 1 [Lu III].

The maximum phase tunable range of the laser signal 1 is  $2\pi$  ( $\Delta\varphi_{\text{LD1,max}} = 2\pi$ ) and its phase adjustment concurrently leads to the phase variation of laser signal 2 ( $\Delta\varphi_{\text{LD2}} \neq 0$ ). Therefore, two cascaded ORRs are used for each OPS to achieve a THz phase shift  $\Delta\varphi_{\text{THz}}$  of at least  $2\pi$ . The related phase response is depicted by the blue line in Fig. 4-2. Furthermore, it can be observed that the FSR of the ORRs should be twice the THz frequency, i.e., 600 GHz. The corresponding ORR round-trip length  $L$  should be 0.282 mm which can be calculated using:

$$L = \frac{c_0}{n_g \cdot f_{\text{FSR}}}, \quad (4.3)$$

where  $n_g$  is the group index of TriPleX waveguides and equal to 1.777. However, the minimum round-trip length of a fabricated ORR must exceed 7 mm due to the required heater length for thermo-optical control. This leads to a maximum FSR of 24.1 GHz which is smaller than the optimum value. However, thanks to the periodicity of ORRs, it is possible to satisfy the conditions, i.e.,  $f_{LD2}$  at the off-resonance frequency and  $f_{LD1}$  at the resonance frequency, if the FSR meets the following criteria:

$$|f_{LD1} - f_{LD2}| = (m + \frac{1}{2}) \cdot f_{FSR}, \quad (4.4)$$

where  $m$  is a natural number.

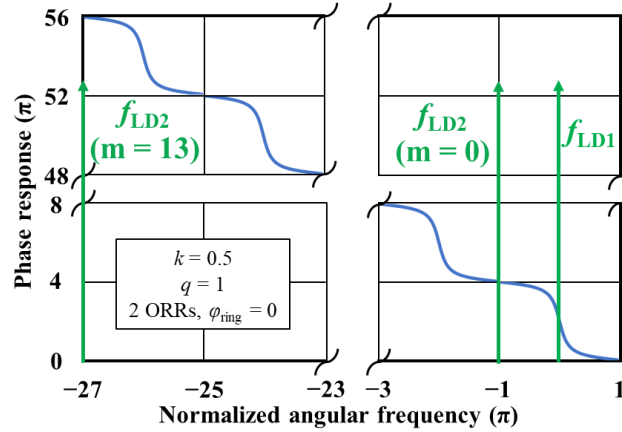


Fig. 4-3 Calculated phase response over fourteen FSRs for two cascaded ORRs with the same resonance frequency. The power coupling coefficient  $k$  is 0.5 and the amplitude loss factor  $q$  is 1 [Lu III].

As can be seen from Fig. 4-3, the phase shift of the laser signal with  $f_{LD2}$  ( $m = 13$ ) is the same as that with  $f_{LD2}$  ( $m = 0$ ) when adjusting  $\phi_{ring}$ , i.e., the resonance frequency of the ORRs. Consequently, all ORRs in the OBFN chip are designed with an FSR of 22.22 GHz.

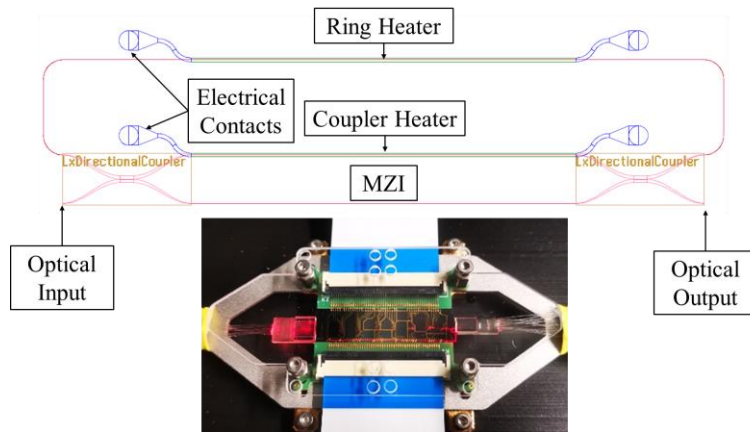


Fig. 4-4 Mask design of an ORR. The inset shows the fabricated OBFN chip.

The OBFN chip is designed using the Synopsys OptoDesigner software and fabricated by LioniX International BV. The mask design for an ORR is illustrated in Fig. 4-4. The TriPleX waveguides are represented by red lines, and heaters are indicated by green lines. The MZI consists of two directional couplers and a coupler heater. The

inset shows the fabricated OBFN chip under visible light test.

## 4.2 OBFN chip characterization

To use the fabricated OBFN chip for beam steering applications, the thermo-optically controlled power coupling coefficient  $k$  and the resonance frequency offset  $f_{\text{res,offset}}$  of each ORR must be experimentally characterized as functions of the voltages applied to the coupler and ring heaters, respectively. The power coupling coefficient  $k$  can be derived from the measured ORR group delay  $\tau_g$  using [187]

$$\tau_g = T_{\text{RT}} + \frac{q\sqrt{1-k}\cos(\Omega+\varphi_{\text{ring}})-(1-k)}{(1-k)-2q\sqrt{1-k}\cos(\Omega+\varphi_{\text{ring}})+q^2} \cdot T_{\text{RT}} + \frac{q\sqrt{1-k}\cos(\Omega+\varphi_{\text{ring}})-q^2(1-k)}{1-2q\sqrt{1-k}\cos(\Omega+\varphi_{\text{ring}})+q^2(1-k)} \cdot T_{\text{RT}}. \quad (4.5)$$

The group delay of each ORR is experimentally determined using a wavelength-sweeping approach [189] (see Fig. 4-5). For an optimal trade-off between measurement resolution and noise, a RF signal at 200 MHz ( $f_{\text{RF}} < 1\% \cdot f_{\text{FSR}}$ ) is generated by a VNA (Anritsu-360) and then modulated onto an optical carrier with a tunable wavelength using an MZM. As the laser wavelength and the coupler heater voltage for the ORR are adjusted, the phase shift of the RF signal  $\Delta\varphi_{\text{RF}}$  is measured by the VNA and the associate group delay can be calculated using  $\tau_g \approx \Delta\varphi_{\text{RF}} / (2\pi \cdot f_{\text{RF}})$ . Finally, the power coupling coefficient for each ORR can be determined using Eq. (4.5). For the fabricated OBFN chip, the experimentally determined optical propagation loss is  $\sim 0.7$  dB/cm. Considering the round-trip length of 7.59 mm, the round-trip loss  $P_L$  is calculated to be 0.5 dB, which translates to an amplitude loss factor  $q$  of 0.944. The round-trip time can be calculated using  $T_{\text{RT}} = 1 / f_{\text{FSR}}$ . It needs to be mentioned that the temperature changes caused by the heaters can alter the optical characteristics of the entire OBFN chip during measurements. Therefore, the chip is mounted on a heat sink equipped with a thermoelectric cooler (TEC) which is regulated by a temperature controller (Thorlabs TED4015) at 20 °C.

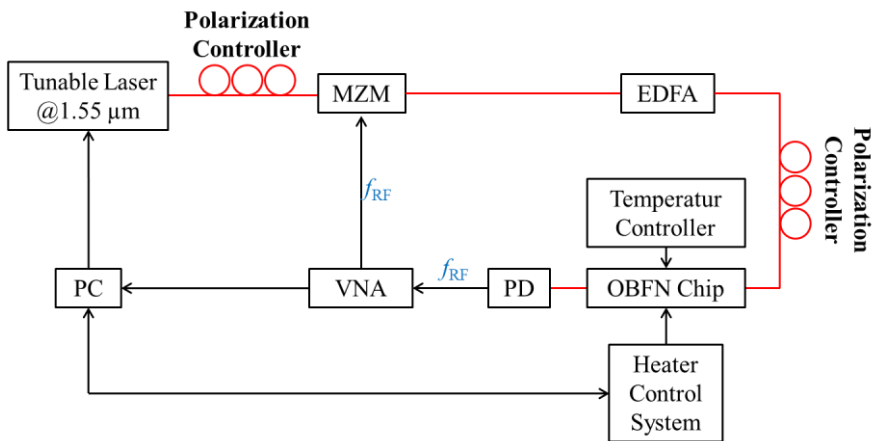


Fig. 4-5 Measurement setup for group delay characterization.

The measured power coupling coefficient  $k$  as a function of the coupler heater bias is presented in Fig. 4-6. As observed, the power coupling coefficient increases from  $\sim 0.19$  to  $\sim 1$  as the bias voltage is adjusted from 4 to 12 V. The power coupling

coefficient of 0.5 can be achieved with a bias setting of 8.3 V.

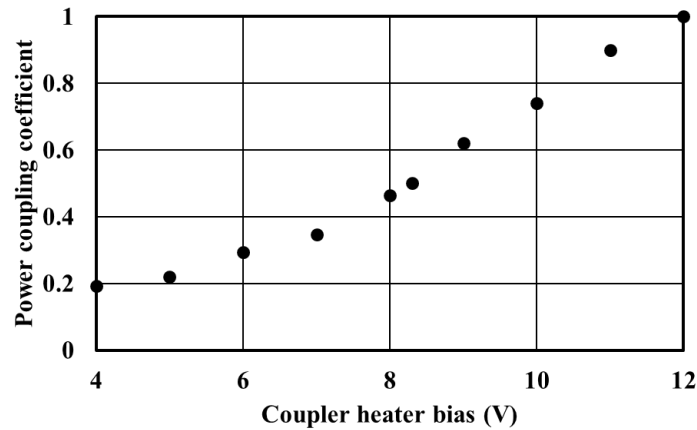


Fig. 4-6 Measured power coupling coefficient as a function of the coupler heater bias of an ORR [Lu III].

The resonance frequency offsets of the ORRs are experimentally determined using a high-resolution optical spectrum analyzer (OSA, APEX Technologies AP2060A) and the results are depicted in Fig. 4-7. As can be seen, to shift the resonance frequency over one FSR, a bias voltage of  $\sim 17$  V is required.

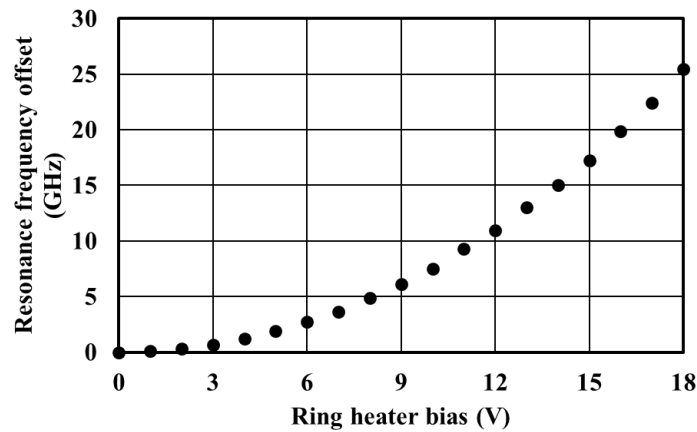


Fig. 4-7 Measured resonance frequency offset as a function of the ring heater bias of an ORR [Lu III].

Using these measurement results, the power coupling coefficients of all ORRs are set to be 0.5 and the ring heaters are tuned to ensure that each ORR possesses an identical resonance frequency. This configuration, in which the phase shifts of all four OPSs are identical, is defined as the initial state of the OBFN chip. Fig. 4-8 shows the optical frequency response of one OPS in this initial state. As can be seen, the two resonance frequencies are at 193.4001 THz and 193.4220 THz, indicating an FSR of  $\sim 21.9$  GHz. Due to this minor deviation from the initially designed FSR of 22.22 GHz ( $< 1.5\%$ ), the fabricated OBFN chip is optimally suited for beam steering at 295.65 GHz instead of the intended 300 GHz according to Eq. (4.4).

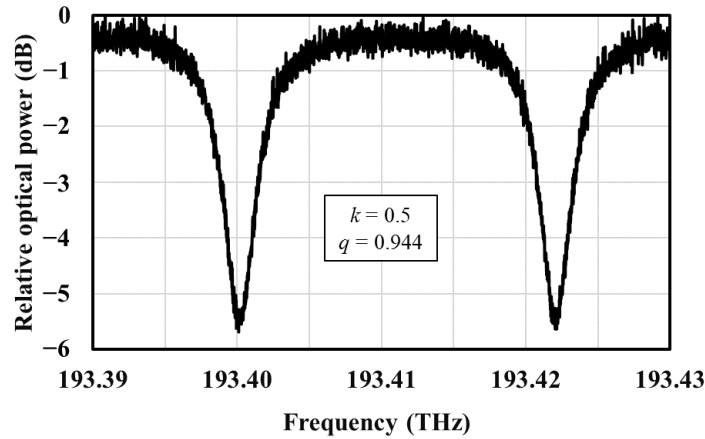


Fig. 4-8 Measured optical frequency response of one OPS with two cascaded ORRs having the same resonance frequency [Lu III].

To measure the THz phase shift controlled by the OPSs, the measurement setup illustrated in Fig. 4-9 is used. Two optical heterodyne signals (@ 1.55  $\mu\text{m}$ ) are generated using two free-running integrable tunable laser assemblies (Pure Photonics PPCL200). After amplification by the EDFA (Thorlabs EDFA100P), an optical polarization controller is employed to mitigate potential optical losses in the OBFN chip caused by the large polarization birefringence of TriPleX waveguides [132]. To precisely regulate the bias of each heater, a heater control system is developed and implemented. The temperature of the OBFN chip is maintained at 20  $^{\circ}\text{C}$  by the temperature controller. To measure the phase difference between two waveguide ports (WPs), two PDs are interfaced with WP1 and WP2 through fiber-chip coupling. Optical delay lines (ODLs, Newport MDL-002-I-15-56-PP-FC/APC) are used to compensate for the fiber length difference from the OBFN chip to the PDs. A DSA (Keysight DSA-Z 634A) is employed to measure the amplitudes of the RF signals generated by the PDs.

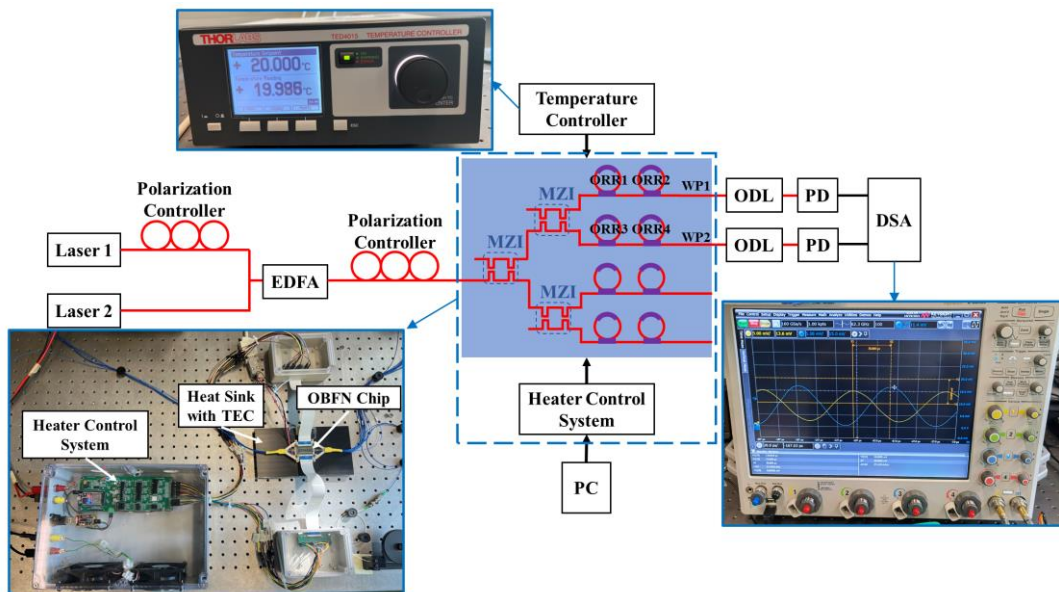


Fig. 4-9 Measurement setup for phase shift characterization [Lu III].

Before executing the experimental characterization, all ORRs are set their initial

state using the heater control system, i.e., with a power coupling coefficient of 0.5 and a resonance frequency of 193.4001 THz. Since the maximum analog bandwidth of the DSA is 63 GHz, the phase shift between the two WPs cannot be directly measured in the THz domain. However, the periodicity of the ORRs allows THz phase shift measurement using lower microwave frequencies. As explained in chapter 4.1, any frequencies  $f_{LD1}$  and  $f_{LD2}$  that satisfied Eq. (4.4) will demonstrate the same phase shift. This means when  $f_{LD1}$  is fixed at 193.4001 THz (resonance frequency of the ORRs), the phase shift for  $f_{LD2} = 193.41105$  THz ( $m = 0$ ) is same as for  $f_{LD2} = 193.69575$  THz ( $m = 13$ ), as shown in Fig. 4-3. Therefore, an RF signal with a frequency of 10.95 GHz mirrors the phase shift of a signal at 295.65 GHz. This method effectively circumvents the bandwidth limitation of the DSA and allows for accurate phase shift measurements.

During the measurements, the RF signal at 10.95 GHz generated by the PD at WP1 serves as the trigger reference for the DSA. The RF signal from WP2 is then measured when tuning the OPS, i.e., the ring heater biases of the two cascaded ORRs (ORR3 and ORR4), and the results are plotted in Fig. 4-10. As observed, the amplitude with a peak at the normalized time of 0 ps (black solid line) corresponds to the initial state of the OBFN chip. By increasing the ring heater biases, the time delay of the measured RF signal is tuned to 15.2 ps (blue solid line), 30.5 ps (red solid line) and 45.7 ps (green solid line). These are equal to phase shifts of  $60^\circ$ ,  $120^\circ$  and  $180^\circ$ , respectively. Inverse phase shifts down to  $-180^\circ$  can be achieved by reducing the ring heater biases, as illustrated by the dashed lines. Overall, a phase tuning of  $2\pi$  is achieved.

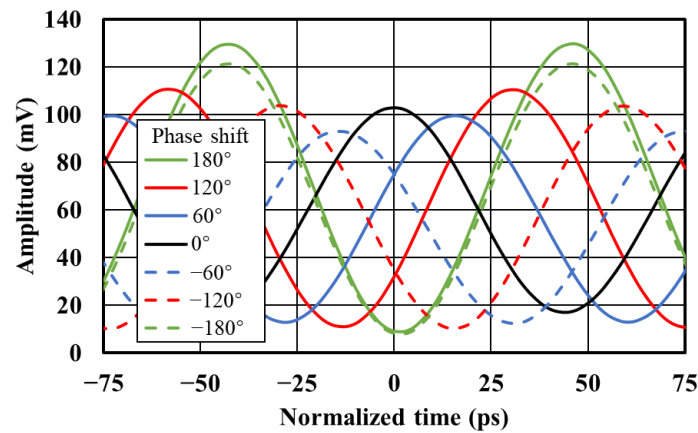


Fig. 4-10 Measured amplitudes of the 10.95 GHz RF signal (WP2) for various ring heater biases [Lu III].

The corresponding ring heater bias settings for ORR3 and OOR4 are plotted in Fig. 4-11. A slight difference can be observed due to fabrication tolerances. To achieve a  $2\pi$  phase shift, the ring heater bias of the ORR3 is changed from 3.42 to 6.52 V, and the bias of the ORR4 is increased from 3.72 to 6.79 V.

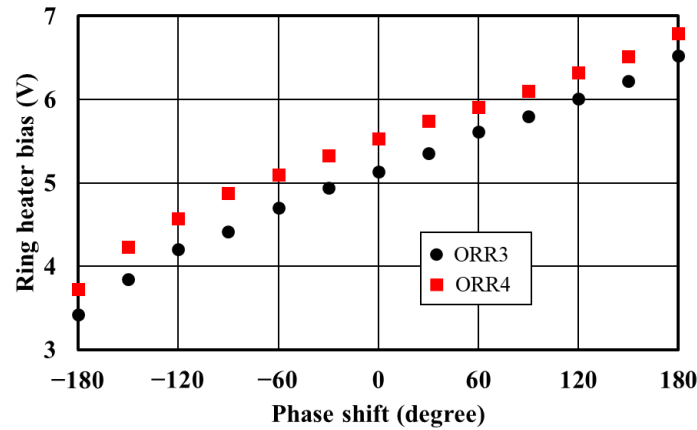


Fig. 4-11 Measured ring heater biases of the ORR3 and ORR4 for phase shifts from  $-180^\circ$  to  $180^\circ$  [Lu III].

The dissipative power of the heaters is calculated based on the measured heater resistance of  $540 \Omega$  and presented in Fig. 4-12, which indicates a phase tuning efficiency of  $0.058 \text{ W}/\pi$ .

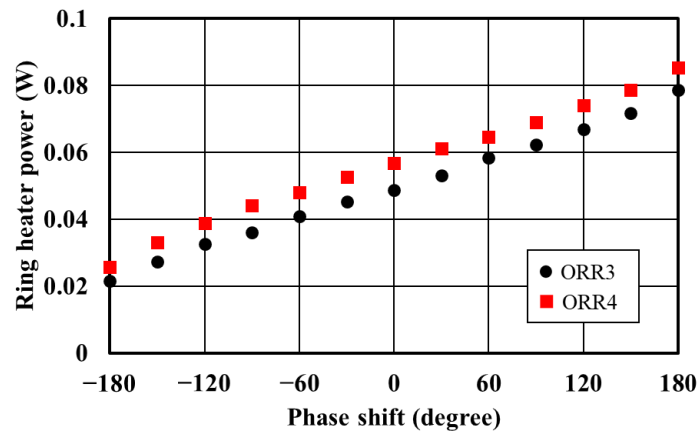


Fig. 4-12 Calculated dissipative ring heater power of ORR3 and ORR4 for phase shifts from  $-180^\circ$  to  $180^\circ$  [Lu III].

From Fig. 4-10, it can be observed that the amplitude of the 10.95 GHz signal varies for different phase shifts. This is because the dispersive power transmission loss of the ORRs leads to a fluctuation in the transmitted optical power, especially for the laser signal near the resonance frequency. As can be seen, the largest amplitude deviation reaches  $\sim 40.15 \text{ mV}$  when comparing the amplitudes corresponding to phase shifts of  $180^\circ$  and  $-60^\circ$ . To systematically analyze the impact of this inherent power variation on the THz beam steering performance of a  $1 \times 4$  phased array, the output power of a UTC-PD (NTT Electronics J-band photomixer module) is measured at 295 GHz for different phase shifts using an SBD (Virginia Diodes WR-3.4 ZBD) as the power detector. The results are presented in Fig. 4-13. The minimum relative power is found at a phase shift of  $-30^\circ$ , not at  $0^\circ$  as one might expect. This is traced back to a slight mismatch between the laser wavelength and the ORR's resonance frequency during the experiments. When considering the entire phase tuning range of  $2\pi$ , the maximum deviation in detected THz output power is about 3.8 dB.

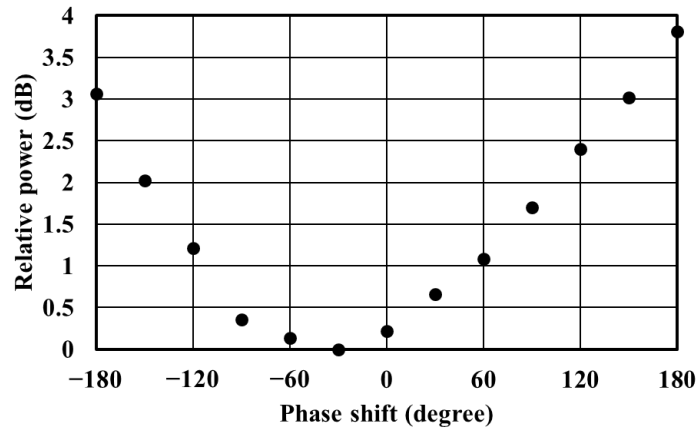


Fig. 4-13 Measured relative output power of the UTC-PD at 0.295 THz for phase shifts from  $-180^\circ$  to  $180^\circ$  [Lu III].

### 4.3 THz beam steering using a $1 \times 4$ phased array

The impact of the measured THz power variation on beam steering performance is numerically analyzed using CST Studio Suite. This is carried out for a  $1 \times 4$  phased array that comprises four BT antennas with a pitch of  $500 \mu\text{m}$  placed on a  $100 \mu\text{m}$  thick InP substrate. To enhance directivity, InP-based dielectric rod waveguide (DRW) antennas are positioned beneath the BT antennas, as depicted in the inset in Fig. 4-14. Each DRW antennas has a thickness  $d$  of  $150 \mu\text{m}$ , a length  $l$  of  $3500 \mu\text{m}$ , and a width  $w$  of  $500 \mu\text{m}$ .

The beam steering behavior of the  $1 \times 4$  phased array is explored under two scenarios: (a) with a constant power applied to each BT antenna, and (b) incorporating the measured power variations. In both scenarios, the phase difference between adjacent antennas  $\Delta\phi$  is adjusted between  $-120^\circ$  and  $120^\circ$ , with a step size of  $30^\circ$ . While phase differences exceeding  $120^\circ$  are attainable using the fabricated OBFN chip, they result in significantly increased side lobes, and thus lower directivity and gain. Table 4-1 summarizes the parameters assigned to each antenna for simulations. In the constant power scenario, each antenna receives a uniform input power of  $0.21 \text{ dBm}$ , independent of the phase difference. This power level is determined based on the  $0^\circ$  phase shift when the power level at  $-30^\circ$  is assumed to be  $0 \text{ dBm}$  (see Fig. 4-13). The phase of the BT1 remains constant, while the phases of the other antennas are adjusted accordingly. For instance, with a phase difference  $\Delta\phi$  of  $30^\circ$ , the phases for BT1 to BT4 are set at  $0^\circ$ ,  $30^\circ$ ,  $60^\circ$  and  $90^\circ$ , respectively.

Fig. 4-14 (a) to (h) present the polar diagrams of the absolute radiation power of the phased array for all phase differences (blue lines). This power is the sum of the total input power in  $\text{dBm}$  of the four BT antennas combined with the simulated realized gain. As can be seen, the beam is steered to  $31^\circ$  with a phase difference of  $120^\circ$  between adjacent antennas. The maximum absolute radiation power consistently exceeds  $15.2 \text{ dBm}$  that is independent of the phase difference. Negative phase shifts result in the beam steering in the opposite direction. Consequently, the maximum beam steering range is  $62^\circ$ .

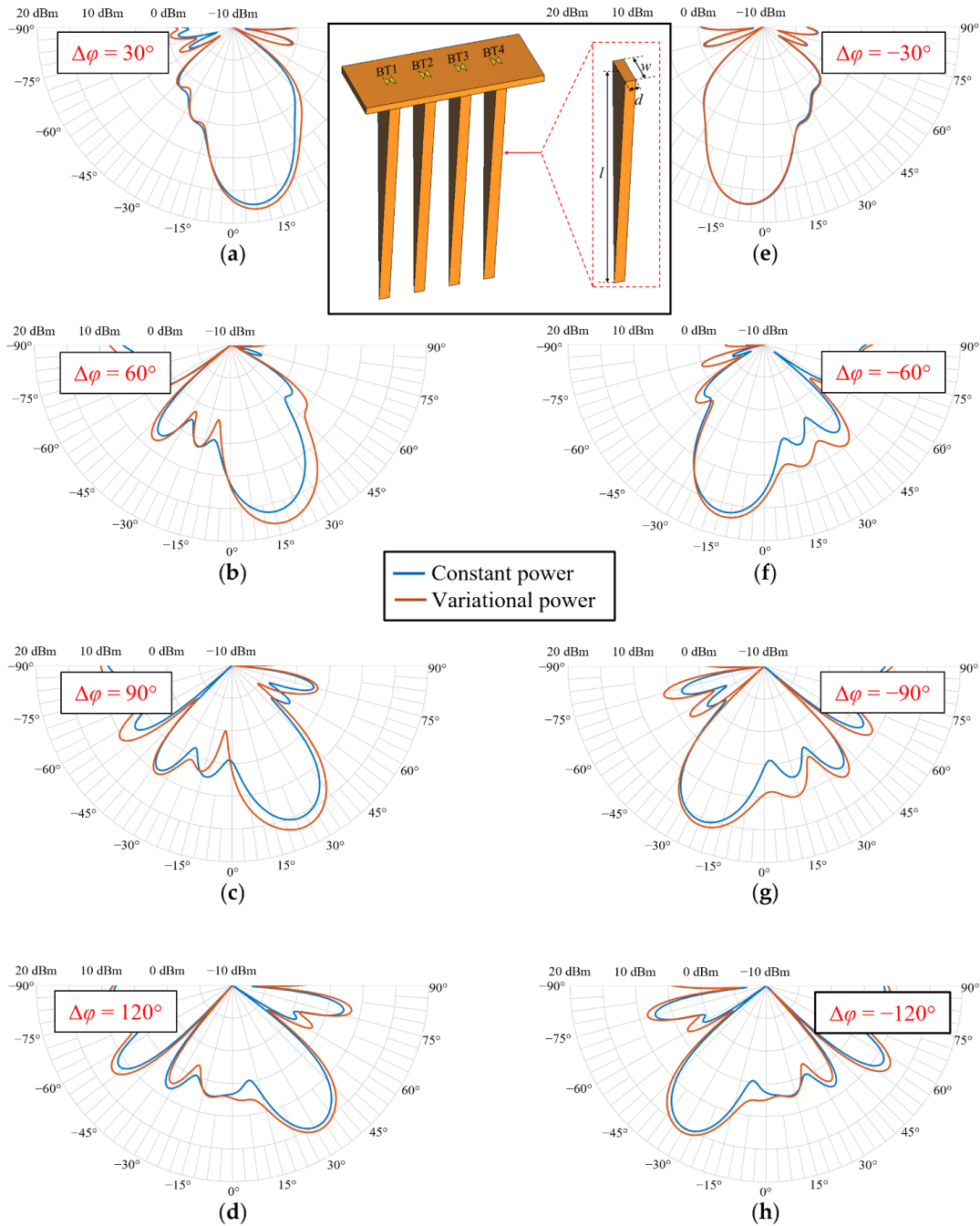


Fig. 4-14 Simulated polar diagrams of the absolute radiation power of the  $1 \times 4$  phased array with constant (blue lines) and variational (red lines) power at 295 GHz for phase differences between adjacent antennas of (a)  $30^\circ$ , (b)  $60^\circ$ , (c)  $90^\circ$ , (d)  $120^\circ$ , (e)  $-30^\circ$ , (f)  $-60^\circ$ , (g)  $-90^\circ$  and (h)  $-120^\circ$ . The inset shows a schematic drawing of the  $1 \times 4$  phased array with DRW antennas [Lu III].

In the variational antenna input power scenario, the simulated phase settings are identical to those for the constant power scenario. Only the input power for each antenna is adjusted according to the measurement results presented in Fig. 4-13. For these simulations, the power level at  $-30^\circ$  is also assumed to be 0 dBm. It needs to be mentioned that due to the phase periodicity, the power levels at negative phases (from  $0^\circ$  to  $-180^\circ$ ) can be used for phases between  $180^\circ$  and  $360^\circ$ , e.g., the measured value at

$-120^\circ$  is employed for the power level at  $240^\circ$ . The power levels for phases within the  $-180^\circ$  to  $-360^\circ$  range are determined using the same methodology. The resulting polar diagrams of the absolute radiation power (red lines) are presented in Fig. 4-14 (a) to (h) as well. As can be seen, the radiation patterns, including the power variations, show a good agreement with the patterns where antenna power levels remain constant. In general, the observed deviations in the beam direction and absolute radiation power are lower than  $1^\circ$  and 0.8 dB, respectively. Only for the phase differences of  $60^\circ$  and  $90^\circ$ , a slightly larger power mismatch of less than 2 dB can be noticed, which is still within acceptable limits. Thus, it is concluded that the inherent power variations caused by the OBFN chip only have a minor impact on the beam steering performance of the phased array.

Table 4-1 Parameters for numerical analyses of constant power and variational power scenarios at 295 GHz [Lu III].

Phase Difference between Adjacent Antennas	Antenna												Figure
	BT1			BT2			BT3			BT4			
	Phase	Input Power (dBm)		Phase	Input Power (dBm)		Phase	Input Power (dBm)		Phase	Input Power (dBm)		
		Constant Power	Variational Power		Constant Power	Variational Power		Constant Power	Variational Power		Constant Power	Variational Power	
30°	0°	0.21	0.21	30°	0.21	0.66	60°	0.21	1.09	90°	0.21	1.70	Fig. 4-14 (a)
60°	0°	0.21	0.21	60°	0.21	1.09	120°	0.21	2.40	180°	0.21	3.81	Fig. 4-14 (b)
90°	0°	0.21	0.21	90°	0.21	1.70	180°	0.21	3.81	270°	0.21	0.36	Fig. 4-14 (c)
120°	0°	0.21	0.21	120°	0.21	2.40	240°	0.21	1.22	360°	0.21	0.21	Fig. 4-14 (d)
-30°	0°	0.21	0.21	-30°	0.21	0	-60°	0.21	0.13	-90°	0.21	0.36	Fig. 4-14 (e)
-60°	0°	0.21	0.21	-60°	0.21	0.13	-120°	0.21	1.22	-180°	0.21	3.06	Fig. 4-14 (f)
-90°	0°	0.21	0.21	-90°	0.21	0.36	-180°	0.21	3.06	-270°	0.21	1.70	Fig. 4-14 (g)
-120°	0°	0.21	0.21	-120°	0.21	1.22	-240°	0.21	2.40	-360°	0.21	0.21	Fig. 4-14 (h)

## 5 Towards 2D THz beam steering

The capability to steer THz beams in two dimensions is necessary for daily applications. Although preliminary attempts using electronic technologies have been reported [107, 108], photonic approaches remain comparatively underexplored. This chapter will investigate methods to extend the beam steering capabilities of the developed InP-based THz LWA and the photonic-assisted THz phased array to two dimensions.

### 5.1 PIC based on THz LWA array

To facilitate 2D beam steering with the InP-based THz LWA, a PIC using an array configuration is proposed. Implementing this PIC in the mobile THz 6G communication system presented in chapter 3, will significantly extend the wireless range and enable 2D tracking of mobile users. The expected performance of this system will be discussed in detail in the following sections.

#### 5.1.1 PIC design

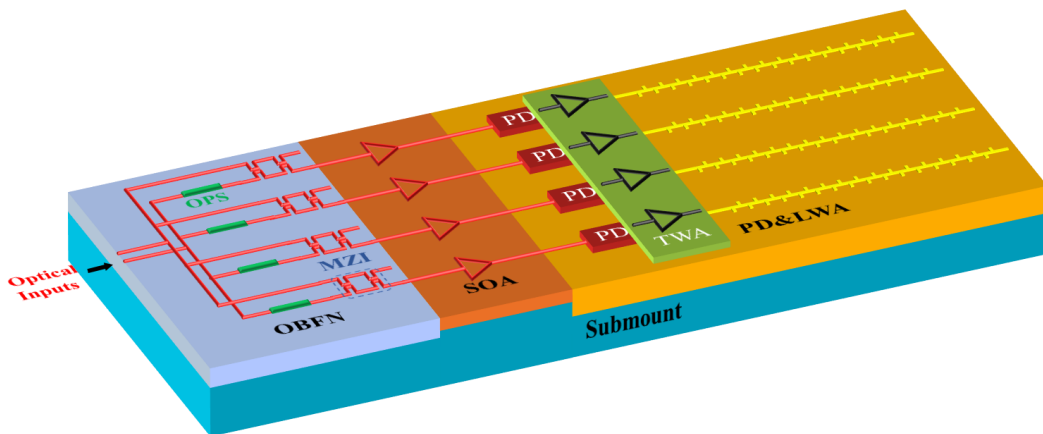


Fig. 5-1 Concept of the PIC featuring 2D THz beam steering.

The concept of the PIC supporting optical heterodyning for THz signal generation and 2D beam steering is illustrated in Fig. 5-1. In contrast to the configuration of a single THz LWA integrated with a PD, this  $1 \times 4$  array design significantly improves the realized gain of the transmitter and enhances the transmitted power by coherently combining the output power of multiple PDs in free space. The LWA pitch is set at  $535 \mu\text{m}$ , corresponding to half wavelength at 280 GHz signals (the median operating frequency of LWAs). Further improvement of the THz output power is achieved by integrating THz traveling-wave amplifiers (TWAs) with the LWAs and PDs via flip-chip bonding. Semiconductor optical amplifiers (SOAs) are butt-coupled to the PDs to provide sufficient optical power. An OBFN chip, designed to modify the phase shifts between adjacent PDs, enables beam steering in the E-plane of the LWAs and is integrated with the SOAs also using butt coupling. Due to the limited FSR of ORRs and their dispersive phase response, four OPSs based on straight waveguides are employed in the OBFN chip to provide the 100 GHz bandwidth required for LWA frequency sweeping. To avoid the 3 dB optical loss caused by directional couplers, MZIs are utilized to combine the optical heterodyne signals. The mask layout for the

OBFN chip is shown in Fig. 5-2. The inset presents the fabricated chip, where the golden lines indicate electrical leads and heaters. To align the optical waveguides of the OBFN, SOA, and PD & LWA chips at a uniform height for butt coupling, a submount is employed to compensate for any chip thickness differences. This innovative PIC design enables 2D beam steering with only one control unit for frequency tuning and four for phase adjustments, resulting in a relatively simple and feasible control circuit.

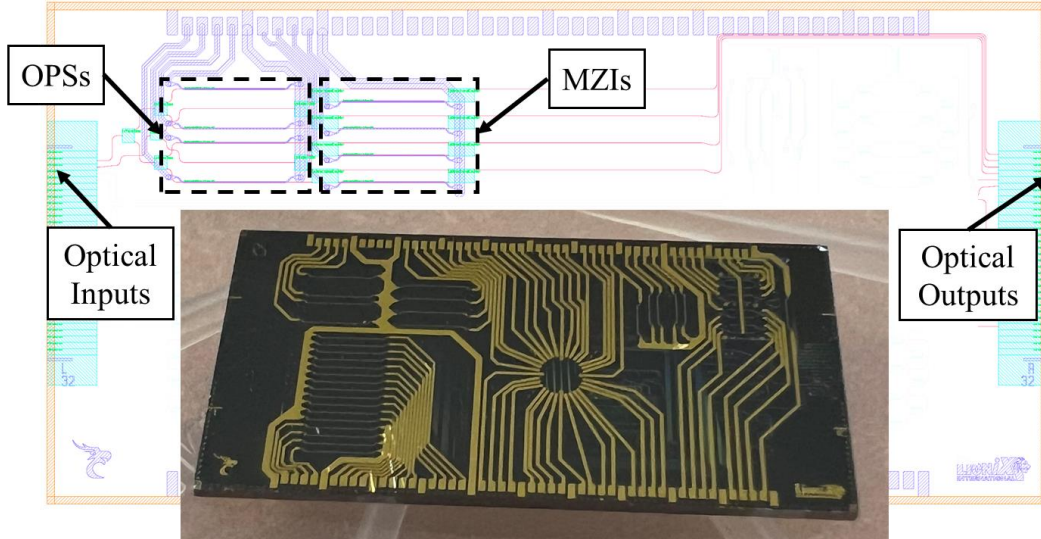


Fig. 5-2 Mask design of the OBFN chip with four OPSs based on straight waveguides. The inset shows the fabricated OBFN chip.

### 5.1.2 Expected performance

To evaluate the performance of the PIC in the THz domain, it is crucial to determine the output power of the THz PDs, which largely depends on the optical power supplied by the SOAs. A single SOA can generate an optical output power of around 15 dBm, provided its input power exceeds 5 dBm [190]. To meet this requirement, each optical input of the OBFN chip should receive an optical power of 12.5 dBm, considering fiber-chip coupling loss ( $\sim 0.5$  dB), power division loss into four waveguides (6 dB), optical propagation loss in waveguides ( $< 3$  dB) [133],  $\sim 3$  dB gain from combining two heterodyning signals using MZIs, and optical coupling loss ( $\sim 1$  dB) between the OBFN and SOA chips. This power level can be achieved with commercial tunable lasers and EDFAs. Due to the additional butt-coupling loss from an SOA to a PD ( $\sim 1$  dB) and optical propagation losses in a PD waveguide ( $\sim 0.5$  dB), the expected optical input power of each PD  $P_{\text{PD,input}}$  is estimated to be  $\sim 13.5$  dBm. Using Ansys Lumerical, the simulated absorption efficiency is  $\sim 63\%$  for a THz PD with a footprint of  $3 \times 16 \mu\text{m}^2$  [12]. Then, the PD responsivity can be calculated using [191]

$$S_{i,\text{PD}} = \eta_{\text{abs}} \cdot \frac{e \cdot \lambda_{\text{laser}}}{h \cdot c_0}, \quad (5.1)$$

where  $e$  is the electron charge,  $\lambda_{\text{laser}}$  is the laser wavelength and  $h$  is the Planck constant. The calculated responsivity of the PD is 0.79 A/W at a laser wavelength of  $1.55 \mu\text{m}$ . Multiplying this value by the optical input power of the PD results in a photocurrent  $I_{\text{ph}}$  of 17.6 mA, which is lower than the saturation photocurrent of 20 mA [12]. Assuming a modulation depth of 100% (two optical heterodyne signals with the equal optical

power), the ideal output power of the PD with a 50  $\Omega$  load is estimated to be 8.9 dBm [192]. The frequency response of the PD demonstrates a decrease with a  $1/f^{-2}$  slope from the calculated RC limited 3-dB frequency ( $\sim 80$  GHz) and a  $1/f^{-4}$  slope from transit time limited cutoff frequency ( $\sim 254$  GHz) [12]. Consequently, based on these characteristics, the PD output powers are calculated from 230 to 330 GHz and presented in Table 5-1.

Table 5-1 Link budget calculation of the mobile THz 6G communication system using the proposed PIC as the transmitter.

Frequency (GHz)	230	240	250	260	270	280	290	300	310	320	330
Beam direction in the H-plane (degree)	-48	-33	-21	-12	-3	6	13	20	27	35	43
Single PD output power (dBm)	-3.3	-3.6	-4.0	-4.7	-5.3	-6.0	-6.6	-7.2	-7.7	-8.3	-8.8
Single TWA output power (dBm)	12.5	13.1	13.2	12.6	11.0	10.8	10.1	10.0	9.5	5.9	N.A.
Single LWA input power (dBm)	11.6	12.4	12.5	11.9	10.3	10.1	9.4	9.3	8.8	5.2	N.A.
LWA array input power (dBm)	17.8	18.4	18.5	17.9	16.3	16.1	15.4	15.3	14.8	11.2	N.A.
LWA array realized gain (dBi)	14.2	16.3	16.8	17.8	17.6	17.7	18.5	18.8	18.7	18.6	17.8
FSPL (dB) @ 4.5 m	92.7	93.1	93.5	93.8	94.1	94.4	94.8	95.0	95.3	95.6	95.9
Horn antenna realized gain (dBi)	22.8	23.1	23.5	23.8	24.1	24.4	24.7	25.0	25.3	25.5	25.8
THz LNA gain (dB)	N.A.	5.9	17.7	28.7	26.6	28.0	29.5	28.8	31.0	29.8	28.5
SBD input power (dBm) @ 4.5 m	N.A.	-29.4	-17.0	-5.6	-9.5	-8.2	-6.7	-7.1	-5.5	-10.5	N.A.

Next, the THz signals generated by the PDs will be amplified using flip-chip bonded TWAs [193]. With carefully designed transitions, a bonding insertion loss of less than 0.7 dB can be obtained for the entire WR-3 band [194]. This ensures that the TWAs operate in a saturated condition across all operating frequencies, because their input powers exceed  $-9$  dBm. The output power of a single TWA is summarized in Table 5-1. Assuming a bonding insertion loss of 0.7 dB from TWAs to LWAs, the total input power of the  $1 \times 4$  LWA array is calculated and presented in Table 5-1 along with the simulated realized gain of the array determined using CST Studio Suite. Employing the same receiver setup as reported in chapter 3, the input power for the SBD is calculated for a wireless distance of 4.5 m. As shown, this mobile THz communication system allows beam steering within an H-plane range from  $-33^\circ$  to  $35^\circ$  over a frequency spectrum from 240 to 320 GHz, limited by the bandwidths of the TWAs and LNAs. A

data rate of 24 Gbit/s can be achieved for a single user between  $-12^\circ$  and  $+35^\circ$  up to 4.5 m due to equivalent SBD input power levels compared with those in Table 3-1. Additionally, the E-plane beam steering capability of the PIC is numerically analyzed using CST Studio Suite. Fig. 5-3 illustrates the simulated far-field radiation patterns at the broadside of the LWA array. By adjusting the phase difference between adjacent LWAs from  $0^\circ$  to  $120^\circ$ , a beam steering range of  $30^\circ$  is achieved with only a minor decrease of 1.7 dB in realized gain. Therefore, changing the phase difference from  $-120^\circ$  to  $120^\circ$  enables a total beam steering range of  $60^\circ$  in the E-plane with negligible impact on the realized gain. The rapid tunability of thermally-controlled OPSs based on TriPleX waveguides and high wavelength sweep speed lasers such as Santec TSL-570 allows for scanning both E- and H-plane ranges within several milliseconds [195].

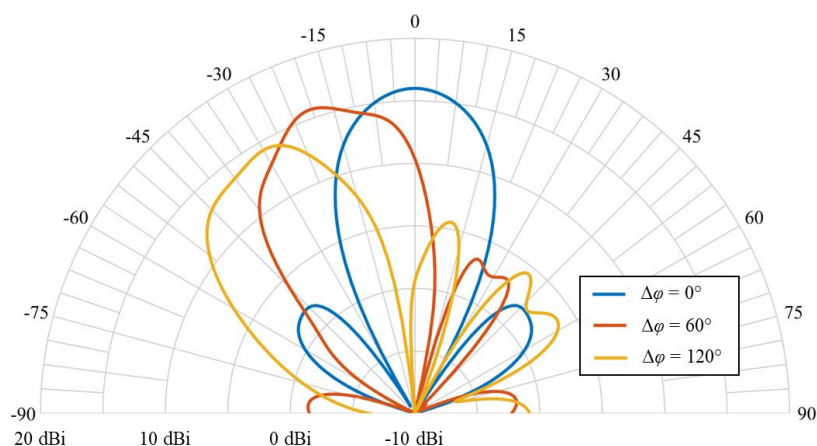


Fig. 5-3 Simulated polar diagrams of realized gain in the E-plane and at broadside of the LWA array for phase differences between adjacent antennas of  $0^\circ$ ,  $60^\circ$  and  $120^\circ$ .

## 5.2 Heterogeneous integrated III-V/Si platform for phased array

To date, the integration of OBFN chips based on TriPleX waveguides with PDs has predominantly relied on optical butt coupling [133]. However, this approach restricts the integration to linear PD arrays for 1D beam steering since it is limited to the chip's edge. To enable 2D beam steering, a vertical integration approach is essential, allowing the integration of a PD matrix onto the surface of an OBFN chip. In this subchapter, a heterogeneous integrated III-V/Si platform is demonstrated where precise lithography can be employed for aligning PDs to TriPleX waveguides instead of relying on high precision bonding in hybrid integration technologies. This technology eliminates the need for complex bonding processes and facilitates large-scale integration of PDs [196].

A key step in this process is the successful transfer of epitaxial layers of THz PDs from the InP substrate onto the TriPleX chip using the developed epitaxial-layer-transfer procedure. Aluminum oxide ( $\text{Al}_2\text{O}_3$ ) layers are utilized as bonding layers due to their transparency and intermediate refractive index at a wavelength of  $1.55 \mu\text{m}$  [197]. These  $\text{Al}_2\text{O}_3$  layers are deposited on both the InP PD chip and TriPleX chip through the atomic layer deposition (ALD) process that offers conformal and uniform interlayers along with precise thickness control [198-200]. Furthermore,  $\text{Al}_2\text{O}_3$  layers have a relatively high hydroxyl group density ( $\sim 18 \text{ OH/nm}^2$ ), which is four times higher than that of Si [201]. This facilitates strong bonds at a low annealing temperature without altering the doping profile of PD epitaxial layers and compromising the high-frequency

performance characteristics of PDs. Moreover, the overall thickness of these  $\text{Al}_2\text{O}_3$  layers is only  $\sim 20$  nm, resulting in an increased overlap area between the evanescent fields of modes in the TriPleX waveguides and the InP PDs. This integration approach enables prism coupling for efficient optical coupling without requiring additional couplers for TriPleX waveguides.

### 5.2.1 Optical prism coupling

A schematic view of the prism coupling approach is illustrated in Fig. 5-4. This method employs a prism placed on top of an optical waveguide with a sufficiently thin top cladding layer. The evanescent tails of the incident light field within the prism and the guided wave within the waveguide can interact. By carefully choosing the incident light angle  $\theta_{\text{prism}}$ , phase matching between the two light waves can be achieved. This results in the efficient coupling of light into the waveguide. The incident light angle is given by [202]:

$$\theta_{\text{prism}} = \arcsin\left(\frac{n_{\text{eff,wg}}}{n_{\text{prism}}}\right). \quad (5.2)$$

As can be seen, the effective refractive index of the waveguide  $n_{\text{eff,wg}}$  must be smaller than the refractive index of the prism material  $n_{\text{prism}}$  to enable optical coupling.

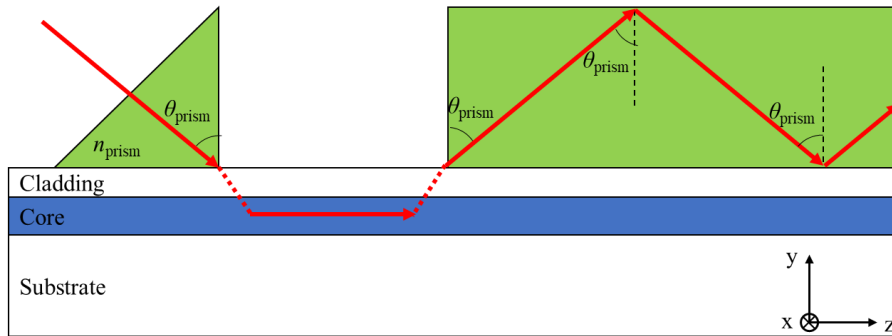


Fig. 5-4 Schematic illustration of prism coupling.

By utilizing the reciprocity principle of prism coupling, a second prism can be employed to couple light out of the waveguide. If a rectangular structure, instead of a prism, is placed on top of the waveguide and  $\theta_{\text{prism}}$  exceeds the critical angle for internal total reflection, the light field will propagate within the rectangle. This concept is applied in the optical coupling from TriPleX waveguides to InP PDs. Using Ansys Lumerical FDTD Solver, the effective refractive indices for a TriPleX waveguide and an InP PD are determined to be 1.52 and 3.23, respectively. This results in a calculated  $\theta_{\text{prism}}$  of  $28.1^\circ$  according to Eq. (5.2), which exceeds both critical angles for total reflection at the InP/air interface ( $18.0^\circ$ ) and the InP/ $\text{SiO}_2$  interface ( $26.5^\circ$ ). Therefore, this approach ensures efficient light coupling and propagation in InP PDs.

### 5.2.2 PD epitaxial layers optimization

The integration of an InP PD with a TriPleX waveguide, utilizing  $\text{Al}_2\text{O}_3$  as the bonding layer, is schematically illustrated in Fig. 5-5. The PD design, detailed in the previous publication [203], includes several key features to optimize its performance.

The p-doped quaternary indium gallium arsenide phosphide (InGaAsP) spacer reduces hole trapping at the InP/absorber heterojunction. To minimize the carrier transit time, a non-intentionally doped (n.i.d.) InGaAs absorber is employed. Another n.i.d. InP spacer is used to smooth the energy band discontinuities at the absorber/collector interface, facilitating accelerated electron injection into the collector region. The TriPleX waveguide consists of two Si<sub>3</sub>N<sub>4</sub> layers forming the waveguide core with a width of 1.1 μm, enclosed by SiO<sub>2</sub> cladding. To ensure the overlap of evanescent fields between the waveguide and the PD for efficient optical coupling, the SiO<sub>2</sub> cladding is partially removed.

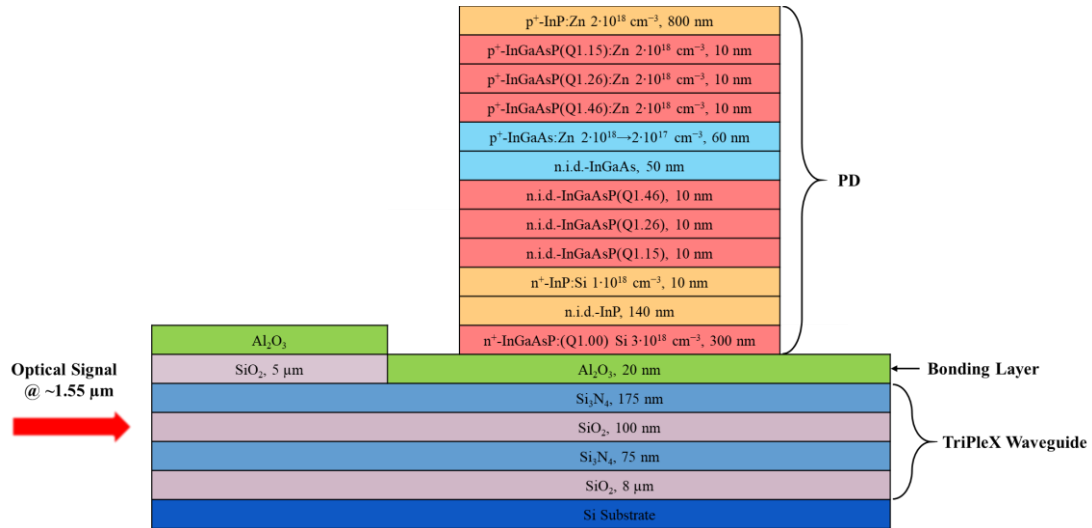


Fig. 5-5 Schematic side view of the InP PD with the integrated TriPleX waveguide using Al<sub>2</sub>O<sub>3</sub> as bonding layer.

The PD epitaxial layers are intentionally doped to achieve the required high-frequency properties, which simultaneously results in changes in optical properties. This phenomenon, known as free carrier absorption (FCA) [204], occurs due to the excitation of free carriers (holes and electrons) within the subbands of valence and conduction bands through photon absorption. Consequently, not only the absorption coefficients, but also the refractive indices of semiconductors undergo changes. Therefore, it is essential to investigate the resulting optical variations before optimizing the PD layer structure to maximize the effective absorption efficiency.

For n-doped InGaAsP and InP, the absorption coefficient caused by FCA can be calculated using [205]:

$$\alpha_{n,FCA} = \frac{Ne^3\lambda_0^2}{4\pi^2n_0(m_e^*m_e)^2c_0^3\mu_e\epsilon_0}. \quad (5.3)$$

Here,  $N$  is the doping concentration,  $n_0$  is the refractive index without doping,  $m_e^*$  is the effective mass of electron,  $m_e$  is the mass of electron,  $\mu_e$  is the electron mobility and  $\epsilon_0$  is the vacuum permittivity.

The FCA coefficient for p-doped InGaAsP and InP is given by [206]:

$$\alpha_{p,FCA} = 4.252 \cdot 10^{-20} \cdot \exp\left(\frac{-4.535}{\lambda_0}\right) \cdot P, \quad (5.4)$$

where  $P$  is the doping concentration.

The changes in the refractive indices of n- and p-doped InGaAsP and InP materials induced by FCA are [207]:

$$\Delta n_{n,FCA} = -\frac{Ne^2\lambda_0^2}{8\pi^2\varepsilon_0c_0^2n_0m_e^*m_e} \quad (5.5)$$

$$\Delta n_{p,FCA} = -\frac{Pe^2\lambda_0^2}{8\pi^2\varepsilon_0c_0^2n_0} \cdot \frac{m_{hh}^{1/2} + m_{lh}^{1/2}}{m_{hh}^{3/2} + m_{lh}^{3/2}}. \quad (5.6)$$

where  $m_{hh}$  and  $m_{lh}$  are the effective masses of heavy holes and light holes, respectively.

Taking these changes in optical properties into consideration, the design depicted in Fig. 5-5 is simulated using Ansys Lumerical FDTD Solver. The PD width is set at 3  $\mu\text{m}$ . It should be noted that absorption coefficients in all layers are assumed to be zero in the simulation for an intuitive observation of the prism coupling. As shown in Fig. 5-6, the amplitude distribution of the simulated optical field demonstrates the successful coupling of light from the TriPleX waveguide into the InP PD and the expected reflection between interfaces. The striated pattern appears due to the interference of reflected light.

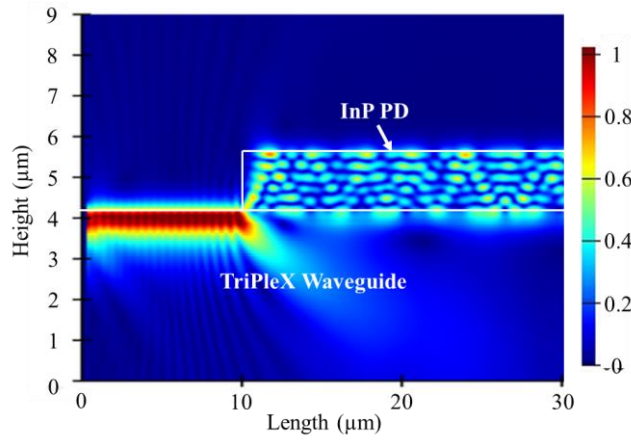


Fig. 5-6 Simulated optical amplitude distribution in the InP PD with the integrated TriPleX waveguide.

Absorption within a PD occurs both in the absorber, contributing to photocurrent generation, and in the doped layers, where FCA leads to losses. To accurately determine the PD's effective absorption efficiency, numerical analyses are carried out utilizing Ansys Lumerical FDTD Solver. The absorption efficiency in absorber  $\eta_{abs}$  is firstly simulated by only considering the absorber's absorption coefficient while setting those of the doped layers to zero. Similarly, the absorption efficiency in doped layers  $\eta_{FCA}$  is obtained by specifically focusing on the absorption within the doped layers. Finally, the absorption efficiency in all layers  $\eta_{all}$  is determined by considering the absorption coefficients in all layers of the PD. The effective absorption efficiency is then calculated using the formula  $\eta_{eff} = \eta_{all} \cdot \eta_{abs} / (\eta_{abs} + \eta_{FCA})$ . In these analyses, the thickness of the p-

doped InP layer (InP blocker) is varied while the design of other epitaxial layers remains unchanged, ensuring no degradation in the PD's high-frequency characteristics. The results for PDs with a constant width of 3  $\mu\text{m}$  and varied lengths from 4 to 16  $\mu\text{m}$  are presented in Fig. 5-7.

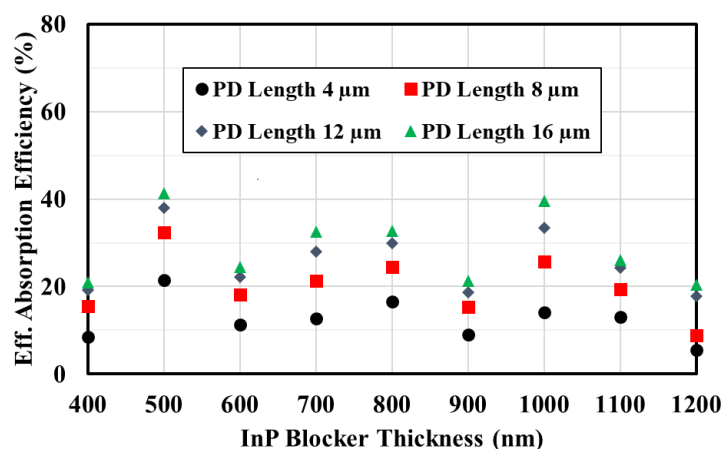


Fig. 5-7 Simulated effective absorption efficiency of InP PDs with lengths from 4 to 16  $\mu\text{m}$  and InP blocker thicknesses from 400 to 1200 nm.

The analyses revealed that a longer PD length results in a higher effective absorption efficiency  $\eta_{\text{eff}}$ . For PDs with a length of 16  $\mu\text{m}$ , two peaks of  $\eta_{\text{eff}}$  are observed at InP blocker thicknesses of 500 nm and 1000 nm. A thickness of 500 nm is chosen primarily due to the slightly higher  $\eta_{\text{eff}}$  of 41.3%, combined with the shorter processing time and reduced cost. To minimize the p-contact resistance, a p-doped InGaAsP layer with a thickness of 30 nm is added on top, resulting in the corresponding reduction of the InP blocker thickness to 470 nm to maintain the optimized effective absorption efficiency. The final design of the epitaxial layers for the PD is illustrated in Fig. 5-8.

p <sup>+</sup> -InGaAsP(Q1.30):Zn $>5 \cdot 10^{18} \text{ cm}^{-3}$ , 30 nm
p <sup>+</sup> -InP:Zn $1.5 \cdot 10^{18} \text{ cm}^{-3}$ , 470 nm
p <sup>+</sup> -InGaAsP(Q1.15):Zn $2 \cdot 10^{18} \text{ cm}^{-3}$ , 10 nm
p <sup>+</sup> -InGaAsP(Q1.26):Zn $2 \cdot 10^{18} \text{ cm}^{-3}$ , 10 nm
p <sup>+</sup> -InGaAsP(Q1.46):Zn $2 \cdot 10^{18} \text{ cm}^{-3}$ , 10 nm
p <sup>+</sup> -InGaAs:Zn $2 \cdot 10^{18} \rightarrow 2 \cdot 10^{17} \text{ cm}^{-3}$ , 60 nm
n.i.d.-InGaAs, 50 nm
n.i.d.-InGaAsP(Q1.46), 10 nm
n.i.d.-InGaAsP(Q1.26), 10 nm
n.i.d.-InGaAsP(Q1.15), 10 nm
n <sup>+</sup> -InP:Si $1 \cdot 10^{18} \text{ cm}^{-3}$ , 10 nm
n.i.d.-InP, 140 nm
n <sup>+</sup> -InGaAsP:(Q1.00) Si $3 \cdot 10^{18} \text{ cm}^{-3}$ , 300 nm

Fig. 5-8 Final design of epitaxial layers for the heterogenous integration with TriPleX waveguides.

### 5.2.3 Epitaxial-layer-transfer technology

As previously discussed, achieving optical coupling between TriPleX waveguides and InP PDs through prism coupling requires the transfer of PD epitaxial layers from the InP substrate onto the TriPleX chip. To accomplish this, an epitaxial-layer-transfer

technology based on surface active bonding (SAB) has been developed. The process flow is illustrated in Fig. 5-9. A TriPleX chip with a bonding window in its central region is employed to enable the overlapping of evanescent fields from modes within both TriPleX waveguides and InP PDs after the subsequent bonding process. This window is created by removing the top  $\text{SiO}_2$  cladding layer of waveguides. Using ALD process,  $\text{Al}_2\text{O}_3$  layers are deposited on both the InP PD chip and the TriPleX chip. To enhance the bonding strength, both chips are then treated with an  $\text{O}_2$  plasma activation process. After successful bonding, grinding and wet chemical etching processes are employed to remove the InP substrate. A detailed description of the epitaxial-layer-transfer technology is provided as follows.

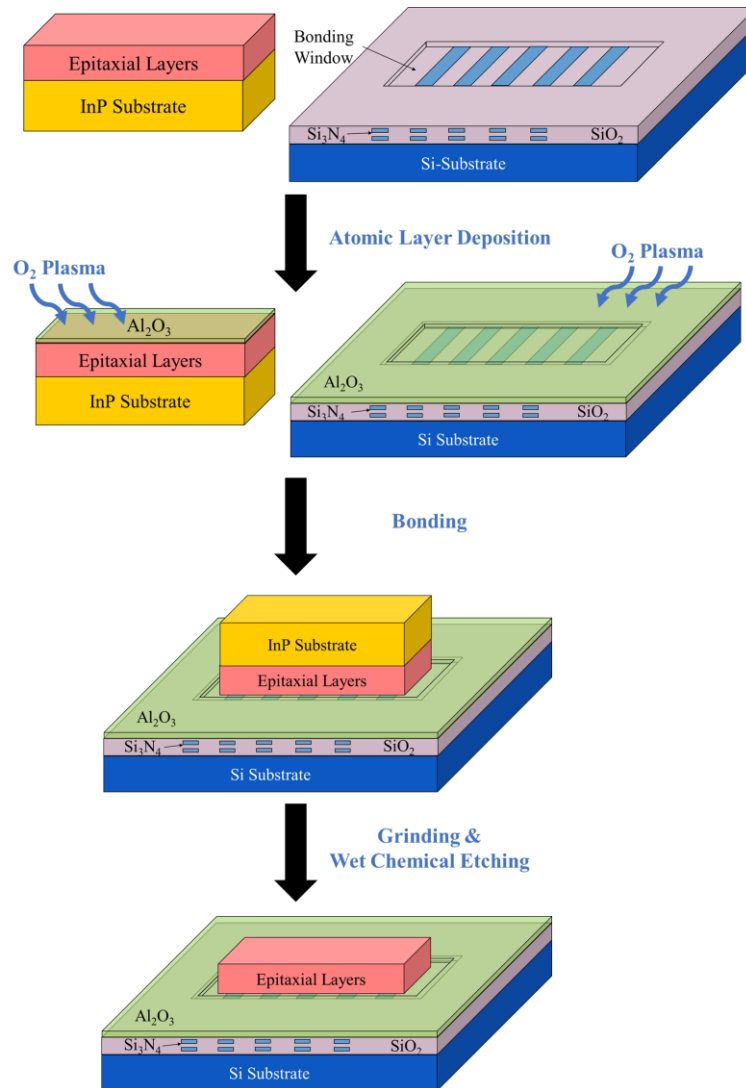


Fig. 5-9 Process flow of the epitaxial-layer-transfer technology for the heterogenous integration of InP PDs with TriPleX waveguides.

### Atomic layer deposition

ALD is a gas phase thin film deposition technology repeated in a cyclic manner that relies on sequential surface reactions [208]. Typically, one ALD cycle consists of four steps: (a) exposure to the first precursor, (b) purge or evacuation to remove non-reacted precursor molecules and gaseous reaction by-products, (c) exposure to the second

precursor, and (d) further purge or evacuation to remove non-reacted precursor molecules and gaseous reaction by-products [209]. In an ideal ALD process, the precursor molecules do not tend to react with each other, so chemisorption stops when all active surface sites are occupied. This self-terminating nature ensures highly conformal material layers with sub-angstrom or monolayer thickness control [210].

The in-house atomic layer deposition system (Sentech SI ALD LL) offers two different processes for depositing  $\text{Al}_2\text{O}_3$  bonding layers, i.e., plasma-enhanced atomic layer deposition (PEALD) and thermal atomic layer deposition (TALD). Both processes utilize trimethylaluminum (TMA,  $\text{Al}_2(\text{CH}_3)_6$ ) as the aluminum precursor and nitrogen gas of 5N purity (99.999%) as the carrier and purge gas. Initially, TMA is introduced into the reaction chamber to react with surface radicals on the substrate. Subsequently, the residual precursor and reaction by-products, such as methane, are purged using  $\text{N}_2$ . Thereafter, the two ALD processes differ in their oxygen precursors. In PEALD,  $\text{O}_2$  plasma is excited to replace the methyl groups ( $-\text{CH}_3$ ) bonded with Al atoms by O-radicals. The by-products are carbon monoxide (CO), carbon dioxide ( $\text{CO}_2$ ) and water ( $\text{H}_2\text{O}$ ) vapor [211]. In TALD, water vapor replaces  $\text{O}_2$  plasma, leading to  $\text{CH}_4$  production as a by-product [212]. As the last ALD cycle step, the reaction chamber is purged by  $\text{N}_2$ . After these four steps, i.e., one cycle, a monolayer of  $\text{Al}_2\text{O}_3$  is deposited. The desired film thickness can be achieved by repeating the cycles.

To determine the optimal ALD process for depositing bonding layers,  $\text{Al}_2\text{O}_3$  layers with a thickness of 10 nm are deposited on InP and Si wafers at 150 °C using PEALD (84 cycles) and TALD (170 cycles), respectively. The PEALD process lasts approximately 6 minutes, while the TALD process takes around 23 minutes.

### **Surface active bonding**

Before the bonding process,  $\text{Al}_2\text{O}_3$  layers deposited on the InP and Si wafers are treated with  $\text{O}_2$  plasma and subsequently rinsed with deionized (DI) water. This procedure effectively breaks the surface bonds of  $\text{Al}_2\text{O}_3$ , enhancing the density of hydroxyl groups and leading to an improved bonding strength [213, 214]. However, it is important to note that excessive plasma exposure can result in increased surface roughness, which may adversely affect the bonding strength [215].

To investigate the optimal plasma activation duration, InP and Si wafers with PEALD- or TALD- $\text{Al}_2\text{O}_3$  layers are cleaved into small chips measuring  $1 \times 1 \text{ cm}^2$ , which are activated for different durations of 10 s, 20 s, 30 s, and 40 s using the Sentech SI 500 inductive coupled plasma reactive ion etching (ICP-RIE) plasma etcher. In the reaction chamber, the plasma conditions are kept with an  $\text{O}_2$  flow rate of 28 sccm and a pressure of 10 Pa. The plasma power is set to be constant at 100 W. Following the activation processes, the chips are rinsed with DI water. To emulate the integration of InP PDs with TriPleX chips, the InP chips are bonded with the Si chips that possess identical ALD layers and activation durations. For instance, an InP chip with a PEALD- $\text{Al}_2\text{O}_3$  layer activated for 20 s is bonded with a Si chip undergoing PEALD- $\text{Al}_2\text{O}_3$  layer activation also lasting for exactly 20 seconds. The bonding procedures for different pairs of chips are executed using the consistent parameters as illustrated in Fig. 5-10 by means of the flip-chip bonder (SET FC150). The bonding pressure is increased to 2.5 MPa within 100 s and maintains for more than 5 hours. Similar to the substrate-

transfer technology demonstrated in chapter 2.2, the bonding temperature (maximum 270 °C) is regulated only after reaching the desired bonding pressure to minimize any potential displacement and deformation between the chips.

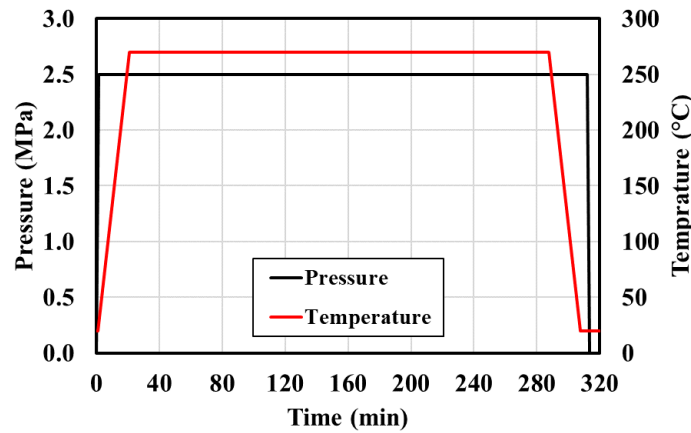


Fig. 5-10 Bonding parameters of the developed epitaxial-layer-transfer technology.

The bonded chips then undergo tensile tests to evaluate the bonding strength [216]. In these tests, bonded InP/Si chips are mounted on glass plates and then pulled perpendicularly to the bonded interface. The force required to break the bonding interface is divided by the bonding area to determine the bonding strength. The results are presented in Fig. 5-11 for chips bonded with PEALD- and TALD- $\text{Al}_2\text{O}_3$  layers. Overall, chips bonded with PEALD- $\text{Al}_2\text{O}_3$  layers exhibited a higher bonding strength and activation duration indeed influences the bonding strength. The PEALD- $\text{Al}_2\text{O}_3$  layers activated for 30 s exhibit the highest bonding strength of 6.1 MPa, compared to 1.8 MPa for TALD- $\text{Al}_2\text{O}_3$  layers activated for 20 s. Consequently, for the integration of the PD chip with the TriPleX chip, PEALD- $\text{Al}_2\text{O}_3$  layers activated for 30 s are employed, following the bonding parameters shown in Fig. 5-10.

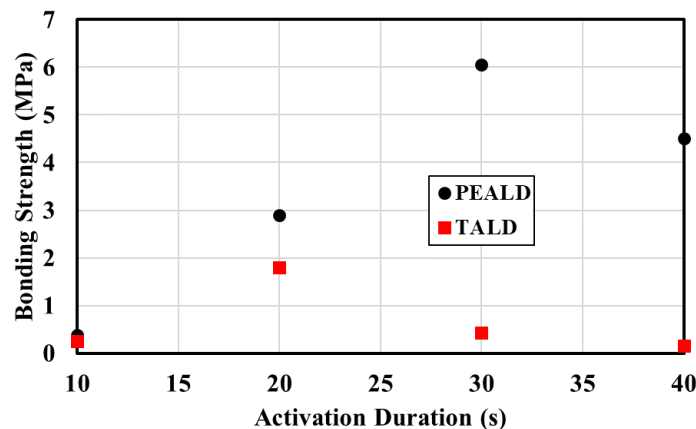


Fig. 5-11 Measured bonding strength for InP/Si chips bonded using PEALD- and TALD- $\text{Al}_2\text{O}_3$  layers.

### **Grinding and wet chemical etching**

By employing a selective wet etching process, the InP substrate of the PD chip can be removed using 37% hydrochloric acid (HCl) while the p-contact layer ( $\text{p}^+$ -InGaAsP, Q1.30) acting as a stop layer. Due to the substantial thickness of the InP substrate

(~290  $\mu\text{m}$ ), an etch duration exceeding 24 minutes is required based on the experimentally determined etch rate of ~12  $\mu\text{m}/\text{min}$ . However, the isotropic nature of wet etching leads to lateral etching of the InP layers within the PD epitaxial structure. To mitigate this, the thickness of the InP substrate is first ground to approximately 15  $\mu\text{m}$ . Multiple short immersions in HCl are then performed on the bonded PD/TriPleX chip, each lasting no longer than 30 s, until the InP substrate is completely removed. Fig. 5-12 illustrates the resultant TriPleX chip with the transferred PD epitaxial layers (thickness: ~1.2  $\mu\text{m}$ ) from its original InP substrate. It can be observed that some edge areas exhibit a partial absence of the epitaxial layers. This may be attributed to non-bonded regions resulting from voids or bubbles during the bonding process or stress induced during the grinding process. Nevertheless, most of the epitaxial layers are successfully transferred onto the TriPleX chip for future PD fabrication.

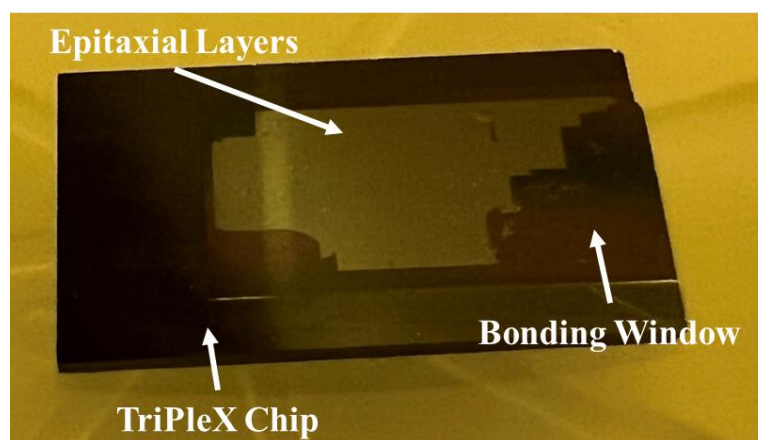


Fig. 5-12 TriPleX chip with the transferred PD epitaxial layers from the InP substrate.

## 6 Discussion

This chapter aims to provide a detailed analysis of the characteristics, limitations and key performance indicators (KPIs) of state-of-the-art THz beam steering technologies. The focus is primarily on LWAs and phased arrays, including the InP-based THz LWA and the OBFN chip based on OPSs, which were successfully developed in this thesis. A comprehensive summary of these technologies can be found in Table 6-1.

The main objective of this discussion is to provide guidelines for selecting the optimal THz beam steering technologies based on specific application requirements. The discussion is focused on the following aspects: integrability, THz output power, antenna gain, beam steering range, bandwidth, the complexity of control circuits, scalability for 2D beam steering and potential application domains.

### Integrability

Previous works on THz LWAs utilizing graphene [94, 96], PPWG [100] and COP [101] faced integration challenges with both electronic and photonic THz sources due to differing material bases. This thesis has addressed these challenges with the development of the InP-based THz LWA. The novel substrate-transfer technology, combined with the innovative GCPW-MSL transition featuring a broad bandwidth exceeding 350 GHz, facilitates the monolithic integration of LWAs with THz PDs on an InP substrate.

Regarding phased arrays, electronic technologies currently surpass photonic ones in terms of integrability, primarily due to the dominance of CMOS technology in electronic device fabrication. In contrast, state-of-the-art photonic components typically rely on diverse material systems. Consequently, photonic integration often requires the invention of novel hybrid or heterogeneous methods to enable efficient inter-chip optical and electrical coupling.

### THz output power

Phased arrays typically provide substantially higher THz output power compared to LWAs. In 1D beam steering configurations, each LWA is driven by a single THz source, whereas a phased array with  $N$  antennas requires  $N$  THz sources, one for each antenna. This disparity becomes even more pronounced in 2D beam steering setups, where the number of THz sources for phased arrays increases quadratically, but only linearly for LWA arrays.

Regarding the output power of individual THz sources, electronic technologies used in phased arrays exhibit a range from  $-12.9$  to  $2.5$  dBm at  $\sim 300$  GHz [106, 108, 111]. Competitive THz powers can be produced by photonic technologies as well [12]. By integrating these sources with additional THz amplifiers, significant increases in output power are achievable. Specifically, devices leveraging metamorphic high-electron-mobility transistor (mHEMT) technology can offer gains around 20 dB and a saturated output power exceeding 10 dBm up to nearly 330 GHz [22, 193]. However, such enhancements necessitate the development of complex integration processes due to the

disparate material systems and fabrication technologies used for THz amplifiers and THz sources in both electronic and photonic systems.

### **Antenna gain**

The gain of a single LWA is significantly affected by the substrate's permittivity on which it is fabricated [217]. For instance, the InP-based THz LWA developed in this thesis exhibits a gain  $\sim 7$  dB lower than that fabricated on a COP substrate [101]. To increase the gain, one can use antenna array configurations and increase the antenna's quantity. Fig. 6-1 illustrates the simulated realized gain of an array consisting of InP-based THz LWAs as a function of the antenna quantity at 300 GHz. The antenna's pitch is set at  $500 \mu\text{m}$ . An increase from one to twenty elements in the LWA array corresponds to a gain enhancement of about 20 dB. A similar effect is observed in phased arrays.

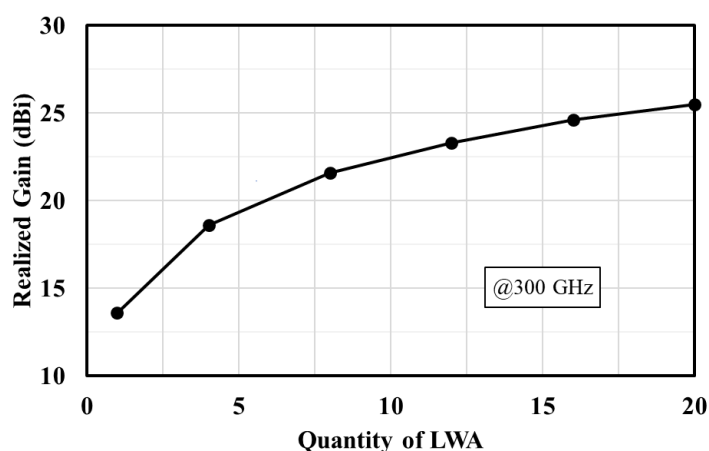


Fig. 6-1 Simulated realized gain as a function of InP-based THz LWA quantity at 300 GHz. Adapted from [Lu III].

### **Beam steering range**

Although a higher permittivity of the LWA substrate results in reduced gain, it also enables an extended beam steering range. Consequently, the InP-based THz LWA, a novel contribution of this thesis, enables a beam steering range of  $88^\circ$ . This achievement marks the widest beam steering range within the WR-3 band, as illustrated in Fig. 6-2.

The beam steering range of phased arrays is generally comparable to that of LWAs. Table 6-1 details beam steering ranges from  $30^\circ$  to  $91^\circ$  for various photonic and electronic phased arrays. The  $1 \times 4$  OBFN chip developed in this thesis allows a beam steering range over  $60^\circ$ . This performance is above the average of existing technologies within the WR-3 band, as substantiated in Fig. 6-2.

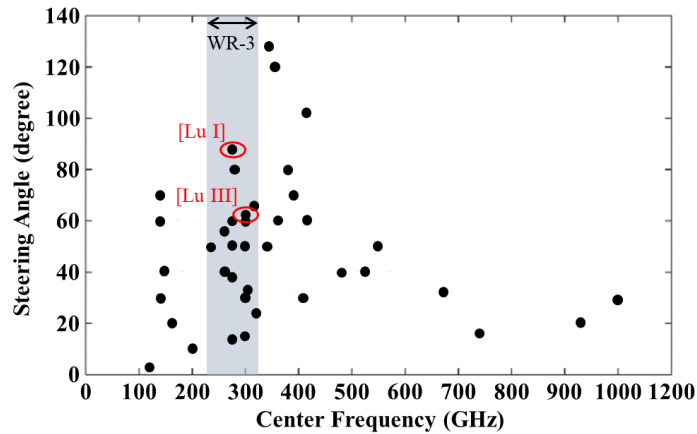


Fig. 6-2 Beam steering range for the state-of-the-art THz beam steering approaches. Adapted from [218] (licensed under a [Creative Commons License](#)).

### **Bandwidth**

Bandwidth is inherently constrained in LWAs due to the frequency-dependent beam direction. For instance, the InP-based THz LWA developed in this thesis provides a bandwidth of approximately 10 GHz, which is only ~10% of its entire operating frequency range.

In contrast, phased arrays can offer a broader bandwidth. In the THz domain, the beam squint effect becomes less pronounced, allowing the use of both electronic [107-111] and optical [114] PSs for THz phased arrays, also this thesis has introduced an OBFN chip with four OPSs. Nevertheless, there is still a concern about the beam squint effect, especially for a broad bandwidth. For quantitative evaluation, the variation in the calculated beam direction of a phased array, which correlates with the phase shift between adjacent antennas, is plotted in Fig. 6-3. With a 500  $\mu\text{m}$  antenna pitch and a carrier frequency of 300 GHz, the beam squint effect is accentuated with wider bandwidths and larger phase shifts. For example, the beam direction of a signal with a bandwidth of 60 GHz can deviate by more than  $10^\circ$  with a  $120^\circ$  phase shift.

Therefore, TTDs are still necessary for THz phased arrays when steering wideband signals. Electronic TTD solutions have achieved bandwidths over 1 THz with 300 fs resolution and 95 ps dynamic range [219]. Regarding photonics approaches, widely used ORR-based TTDs at microwave frequencies are challenging to be scaled to THz due to increased beam angle sensitivity to time delay variations. Furthermore, they typically offer a maximum bandwidth below 20 GHz, limited by the finite FSR determined by the length of thermo-optical control elements and the associated ORR's circumference. Although fiber-based optical delay lines offer theoretically unlimited bandwidth [112], their bulkiness prevents compact integration. A promising alternative could be the chip-integrated delay lines switched by MZIs [113], considering a balance between bandwidth and integrability.

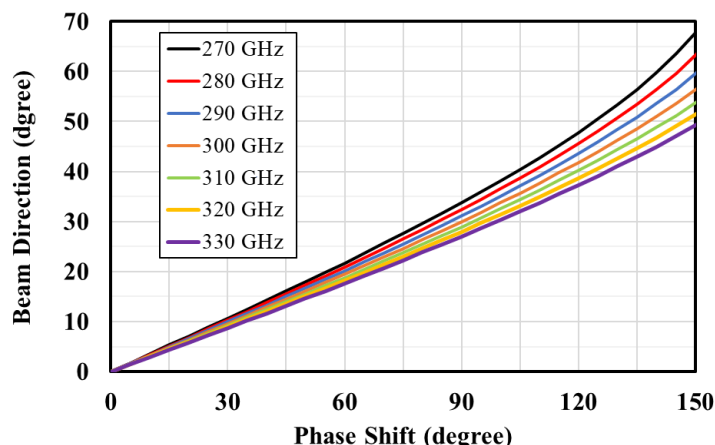


Fig. 6-3 Calculated beam directions of a phased array as a function of the phase shift between adjacent antennas with a pitch of  $500 \mu\text{m}$  for frequencies from 270 to 330 GHz.

### **Complexity of control circuits and scalability for 2D beam steering**

Similar to metasurfaces, reconfigurable LWAs require complex control systems. In contrast, THz beam steering can be more easily achieved by sweeping the operating frequency. This process is particularly straightforward with photonic-assisted LWAs by changing the wavelength of an optical heterodyne signal. For implementing 2D beam steering, an LWA array is essential, and this still necessitates integration with PSs or TTDs to modify the beam direction along the plane perpendicular to the one controlled by frequency, as presented in chapter 5.1. Nonetheless, these control circuits are less complex than those required for phased arrays.

In phased arrays, PSs or TTDs are necessary for 1D beam steering, and their complexity increases quadratically for 2D steering. Nevertheless, thanks to advances in CMOS integration technology, several initial 2D THz beam steering solutions employing electronic-assisted phased arrays have been demonstrated [107, 108]. In comparison, the existing photonic-assisted phased arrays are still limited to 1D beam steering. Among these technologies, OPSs based on straight waveguides [114] require the fewest tuning elements. The ORR-based OPSs, as discussed in this thesis, also present a relatively simple control circuitry. Optical TTDs that employ MZI-switched delay lines necessitate a significantly larger number of tuning elements, particularly to achieve fine delay resolution. The heterogeneously integrated III-V/Si platform introduced in chapter 5.2 enables the fabrication of a PD matrix on a OBFN chip, paving the way for developing photonic-assisted phased arrays in 2D THz beam steering applications.

### **Potential application domains**

The suitability of THz beam steering technologies varies depending on their distinct advantages and limitations, meaning no single approach is universally applicable.

For mobile THz communications, frequency-sweeping LWAs can be considered as a promising option, not only due to their straightforward beam steering capability but also because of their inherent frequency-dependent beam directionality. This characteristic can simultaneously support multiple users utilizing additional LO lasers, as confirmed in this thesis. Additionally, the demonstrated THz radar system based on

an LWA [101] proves the potential in the development of THz joint communication and sensing systems which have already been demonstrated at microwave frequencies [138, 139].

In the realm of spectroscopy, where photonic technologies currently dominate in generating wideband THz signals across several THz [220], it is essential to use frequency-independent beam steering technologies. In this scenario, photonic-assisted phased arrays employing MZI-based switched delay lines are ideal due to their broad bandwidth, despite the complexity of control systems.

For THz imaging systems that operate at a single frequency or within a bandwidth of several GHz, phased arrays utilizing PSs become more desirable. These systems benefit from minimal beam squint effects and simplified control circuits, making them efficient for applications with narrower bandwidth requirements.

Table 6-1 Comparison of state-of-the-art THz beam steering approaches.

Ref.	Frequency (GHz)	Type	Technology	Control Method	Integrable with THz PD	Footprint (mm <sup>2</sup> )	Array Configuration	Number of Control Units	Steering Range (degree)
[94]	2000	LWA	Graphene	Reconfigurable structure	No	N.A.	N.A.	N.A.	82.9
[96]	2000	LWA	Graphene	Reconfigurable structure	No	0.3×1.4	1×144	144	94
[100]	37 - 512	LWA	PPWG	Frequency / Mechanical	No	1×50	1×1	1	68
[101]	235 - 325	LWA	COP	Frequency (Electronic)	No	1×26	1×36	1	38
<sup>1</sup> [61]	140	Phased array	CMOS	Digital (Electronic)	No	N.A.	8×16	16	80
[105]	140	Phased array	CMOS	TTD (Electronic)	No	3×5.2	2×4	8	40
[106]	280	Phased array	CMOS	TTD (Electronic)	No	1.4×2	1×4	4	30
[109]	374 - 407	Phased array	CMOS	PS (Electronic)	No	3×3.5	1×8	8	75
[110]	531.5	Phased array	CMOS	PS (Electronic)	No	2.5	1×4	8	60
[111]	320	Phased array	SiGe BiCMOS	PS (Electronic)	No	8×4.3	1×4	4	24
[107]	280	Phased array	CMOS	PS (Electronic)	No	2.7×2.7	4×4	16	<sup>2</sup> 80/80
[108]	338	Phased array	CMOS	PS (Electronic)	No	4.1	4×4	N.A.	<sup>2</sup> 45/50
[112]	600	Phased array	Optical fiber	TTD (Photonic)	No	N.A.	1×4	4	35
[113]	94	Phased array	Si <sub>3</sub> N <sub>4</sub> / SiO <sub>2</sub>	TTD (Photonic)	Yes	8×32	1×4	20	91
[114]	300	Phased array	SiO <sub>2</sub> / Si	OPS (Photonic)	Yes	N.A.	1×4	4	50

Ref.	Frequency (GHz)	Type	Technology	Control Method	Integrable with THz PD	Footprint	Array Configuration	Number of Control Units	Steering Angle (degree)
<sup>3</sup> This work	230 - 330	LWA	InP	Frequency (Photonic)	Yes	1×7	1×32	1	88
This work	295	Phased array	Si <sub>3</sub> N <sub>4</sub> / SiO <sub>2</sub>	OPS (Photonic)	Yes	8×32	1×4	<sup>4</sup> 16 / 8	62

<sup>1</sup>This approach has been successfully employed for mobile THz 6G communications. <sup>2</sup>Two dimensional beam steering. <sup>3</sup>The world's first mobile THz 6G communication system has been demonstrated using this LWA. <sup>4</sup>The number of control units can be reduced to eight using 3 dB directional couplers or multi-mode interferometers (MMIs) instead of MZIs for ORRs.



## 7 Conclusion and future work

This thesis has reported on the successful development of two PICs supporting the integration with THz PDs for 1D THz beam steering, i.e., the InP-based THz LWA and the OBFN chip for a  $1\times 4$  photonic-assisted phased array. Additionally, it presented the first mobile THz 6G communication system and investigated the 2D photonic-assisted THz beam steering approaches.

Chapter 2 reported on the design, fabrication, and experimental characterization of the pioneering InP-based THz LWA for a frequency range from 230 to 330 GHz. This LWA incorporates a novel GCPW-MSL transition to enable monolithic integration with InP-based THz PDs. A substrate-transfer process using a Si wafer as the carrier substrate has been established to fabricate the LWAs on an only 50  $\mu\text{m}$  thick InP substrate. A good agreement between the simulated and experimentally determined antenna performance has been achieved in terms of beam direction, realized gain and 3-dB beam width. Quantitatively, the fabricated THz LWA provides the largest beam steering range of  $88^\circ$ , surpassing other existing beam steering approaches in the WR-3 band. For a 1.5 mm wide InP antenna, a 3-dB beam width of  $\sim 10^\circ$  and a realized gain of 11 dBi were achieved.

Using this fabricated LWA, the first THz communication system supporting mobile single and multi-user applications was demonstrated in chapter 3. In single user operation, a data rate of 24 Gbit/s was achieved at a wireless distance of 6 cm within the LWA's scanning range of  $33^\circ$ . The transmission range extended to 32 cm with a data rate of 4 Gbit/s. Furthermore, multi-user operation was investigated, revealing a minimum guard band of 1 GHz which indicates that the proposed approach can support up to 12 users within the antenna's coverage sector with a total capacity of 48 Gbit/s.

This thesis also introduced a THz PIC based on an array configuration of the developed InP-based THz LWAs for 2D beam steering. Compared to a single LWA, the  $1\times 4$  LWA array with four monolithically integrated THz PDs significantly enhanced the THz output power and realized gain. To further improve the THz output power, additional TWAs were proposed to be integrated with the PIC. An SOA array was suggested to be butt-coupled to the PDs to provide sufficient optical power. For beam steering in the E-plane of the LWA array, an OBFN chip has been developed to adjust phase shifts between adjacent PDs. Since beam steering in the H-plane is achieved by sweeping the antenna frequency, only four OPSs within the OBFN chip are required, enabling a simple control circuit with low power consumption. Comparing this PIC with the photonic transmitter (single LWA fed by one THz PD using a WR-3 GSG-probe) equipped with a Teflon lens for the mobile THz communication system discussed in chapter 3, it offers an average enhancement of  $\sim 30$  dB in THz output power and  $\sim 4$  dB higher realized gain without requiring any additional lens. Consequently, it enables a data rate of 24 Gbit/s for a single mobile user at wireless distances up to 4.5 m within its scanning range of  $47^\circ$  in the H-plane and  $60^\circ$  in the E-plane. This advancement makes practical deployment of THz communication systems feasible for mobile in-door applications such as AR/VR goggles.

Furthermore, chapter 4 explored a THz photonic-assisted phased array for 1D

frequency-independent beam steering. It detailed the design and experimental characterization of a  $1 \times 4$  OBFN chip for beam steering at 300 GHz. The OBFN chip based on TriPleX waveguides consists of three MZIs that control the power distribution of the optical heterodyne signals to each THz PD, and four OPSs, each incorporates two cascaded ORRs to achieve a tunable THz phase shift range of  $2\pi$ . The ORRs were designed to impose only a tunable phase shift on one of the optical heterodyne signals while leaving the second optical carrier's phase quasi-unchanged. Experimentally, a THz phase tuning range up to  $2\pi$  was demonstrated with a tuning efficiency of  $0.058 \text{ W}/\pi$  per OPS. Despite a maximum inherent power variation of 3.8 dB at 295 GHz due to the dispersive power transmission loss in the ORRs, numerical simulations using CST Studio Suite indicated minimal impact on the beam steering performance. The deviations in the beam direction and maximum absolute radiation power of the  $1 \times 4$  phased array were found to be below  $1^\circ$  and 2 dB, respectively. The observed beam steering angle at 295 GHz was  $\sim 62^\circ$  by varying the phase difference between adjacent antennas from  $-120^\circ$  to  $120^\circ$ .

To achieve 2D beam steering using THz photonic-assisted phased arrays, chapter 5 introduced a novel heterogeneous III-V/Si platform, enabling the fabrication of a PD matrix on an OBFN chip. Using prism coupling for optical coupling between TriPleX waveguides and InP PDs, this innovative approach eliminates the need for additional optical couplers and facilitates the large-scale integration of PDs. The optimized PD epitaxial layers achieved an effective absorption efficiency of  $\sim 41\%$  excluding the FCA for PDs with a footprint of  $3 \times 16 \mu\text{m}^2$ . For the fabrication of PDs, an epitaxial-transfer process was developed. Following the successful implementation of PEALD and TALD processes, the  $\text{O}_2$  plasma activation process was optimized. With an activation duration of 30 s, a bonding strength of 6.1 MPa was achieved with the PEALD  $\text{Al}_2\text{O}_3$  bonding layers. After the successful bond of a PD chip and a TriPleX chip, the InP substrate of the PD chip was removed using a combination of grinding and selective wet chemical etching. Finally, the  $\sim 1.2 \mu\text{m}$  thick PD epitaxial layers were successfully transferred from the original InP substrate onto the TriPleX chip.

For future work, the primary objective is the manufacturing of the proposed PIC based on the LWA array. Beyond the development complexities associated with each component, there are significant challenges in achieving low-loss optical and THz interconnects between them. The careful design and fabrication of transitions among PDs, TWAs and LWAs are crucial to minimize losses over a broad bandwidth in the THz domain. Additionally, the precise machining of the submount with tolerances in micrometer level is required for achieving low-loss optical butt coupling between chips. The integration of spot size converters with optical waveguides is proposed to enhance coupling efficiency.

Another crucial task, which is not completed in this thesis due to time constraints, is the fabrication and experimental characterization of THz PDs using the transferred epitaxial layers on the TriPleX chip. Moreover, the development of a new OBFN chip is necessary for effective phase/time control of the integrated PD matrix. These future endeavors aim to realize 2D THz beam steering using photonic-assisted phased arrays and to advance their deployment in mobile applications.

---

## Abbreviations and symbols

### Abbreviations

1D	one-dimensional
2D	two-dimensional
Al	aluminum
Al <sub>2</sub> O <sub>3</sub>	aluminum oxide
ALD	atomic layer deposition
Au	gold
AWG	arbitrary waveform generator
BCB	Benzocyclobutene
BER	bit error rate
BiCMOS	bipolar complementary metal-oxide semiconductor
BT	bow tie
CMOS	complementary metal-oxide semiconductor
CMP	chemical mechanical polishing
CO	carbon monoxide
CO <sub>2</sub>	carbon dioxide
COP	cyclin olefin polymer
CPW	coplanar waveguide
CW	continuous-wave
DAC	digital-to-analog converter
DI	deionized
DRW	dielectric rod waveguide
DSA	digital signal analyzer
EDFA	erbium-doped fiber amplifier
FCA	free carrier absorption
FIB	focused ion beam
FPGA	field-programmable gate array
FSPL	free-space path loss
FSR	free spectral range

GCPW	grounded coplanar waveguide
GST	germanium-antimony-telluride
H <sub>2</sub> O	water
HCl	hydrochloric acid
HD-FEC	hard decision forward error correction
ICP-RIE	inductive coupled plasma reactive ion etching
IF	intermediate frequency
InGaAsP	indium gallium arsenide phosphide
InP	indium phosphide
KPI	key performance indicator
LC	liquid crystals
LNA	low noise amplifier
LO	local oscillator
LWA	leaky-wave antenna
MARIE	mobile material characterization and localization by electromagnetic sensing
MEMS	microelectromechanical systems
mHEMT	metamorphic high-electron-mobility transistor
MMI	multi-mode interferometer
MPA	medium power amplifier
MPW	multi-project wafer
MSL	microstrip line
MUTC-PD	modified uni-traveling carrier photodiode
MZI	Mach-Zehnder-interferometer
MZM	Mach-Zehnder modulator
n.i.d.	non-intentionally doped
OBFN	optical beam forming network
ODL	Optical delay line
OFDM	orthogonal frequency-division multiplexing
OPS	optical phase shifter
ORR	optical ring resonator

OSA	optical spectrum analyzer
OSB	open-stopband
PCA	photoconductive antenna
PD	photodiode
PEALD	plasma-enhanced atomic layer deposition
PIC	photonic integrated circuit
PPWG	parallel-plate waveguide
PS	phase shifter
Pt	platinum
QCL	quantum-cascade laser
RFIC	radio-frequency integrated circuit
RMS	root-mean-square
SAB	surface active bonding
SBD	Schottky-barrier diode
Si	silicon
SiGe	silicon germanium
SiO <sub>2</sub>	silicon dioxide
SIW	substrate integrated waveguide
Sn	tin
SNR	signal-to-noise ratio
SOA	semiconductor optical amplifier
SSBI	signal-signal beating interference
TALD	thermal atomic layer deposition
TCB	thermocompression bonding
TEC	thermo-electric cooler
THz	terahertz
Ti	titanium
TMA	trimethylaluminum
TTD	true time delay
TWA	traveling-wave amplifier

VIA	vertical interconnect access
VNA	vector network analyzer
VO <sub>2</sub>	vanadium dioxide
WP	waveguide port

**Latin symbols**

$a$	microstrip line length
$c_0$	light speed in vacuum
$e$	electron charge
$f$	frequency
$f_{\text{FSR}}$	free spectral range of optical ring resonator
$f_{\text{LD}}$	frequency of laser signal
$f_{\text{LWA}}$	operating frequency of leaky-wave antenna
$f_{\text{res,offset}}$	resonance frequency offset of optical ring resonator
$f_{\text{RF}}$	frequency of RF signal
$g$	gap
$h$	Planck constant
$h_{\text{sub}}$	substrate thickness
$I_{\text{ph}}$	photocurrent
$k$	power coupling coefficient
$k_0$	free-space wavenumber
$lg$	ground-strip length
$l_{\text{MFP}}$	mean free path of conduction electron
$ls$	signal line length
$L$	round-trip length of optical ring resonator
$m_e$	mass of electron
$m_e^*$	effective mass of electron
$m_{\text{hh}}$	effective mass of heavy hole
$m_{\text{lh}}$	effective mass of light hole
$n$	harmonic order
$n_0$	refractive index without doping
$n_{\text{eff,wg}}$	effective refractive index of waveguide
$n_g$	group index of TriPleX waveguide
$n_{\text{prism}}$	refractive index of prism material
$N$	doping concentration for n-doped materials

$o$	stub offset
$p$	unit cell period
$P$	doping concentration for n-doped materials
$P_L$	round-trip loss
$q$	amplitude loss factor
$s$	signal line width
$sl$	stub length
$sw$	stub width
$S_{i,PD}$	responsivity of photodiode
$T$	temperature
$T_{RT}$	round-trip time of optical ring resonator
$v_F$	fermi velocity
$w_g$	ground-plate width
$w_{MSL}$	microstrip line width
$Z_0$	characteristic impedance

**Greek symbols**

$\alpha_{\text{InP}}$	thermal expansion coefficient of indium phosphide
$\alpha_{\text{n,FCA}}$	free carrier absorption coefficient of n-doped materials
$\alpha_{\text{p,FCA}}$	free carrier absorption coefficient of p-doped materials
$\alpha_{\text{Si}}$	thermal expansion coefficient of silicon
$\beta$	phase constant of dominant mode
$\beta_0$	phase constant of fundamental space harmonic
$\beta_n$	phase constants of space harmonics
$\delta$	skin depth
$\Delta\varphi_{\text{LD}}$	phase shift of laser signal
$\Delta\varphi_{\text{RF}}$	phase shift of RF signal
$\Delta\varphi_{\text{THz}}$	phase shift in the THz domain
$\Delta n_{\text{n,FCA}}$	refractive index change of n-doped materials
$\Delta n_{\text{p,FCA}}$	refractive index change of p-doped materials
$\epsilon_0$	vacuum permittivity
$\epsilon_{\text{eff,MSL}}$	effective permittivity of microstrip line
$\epsilon_{\text{r,InP}}$	relative permittivity of indium phosphide
$\eta_{\text{abs}}$	absorption efficiency in absorber
$\eta_{\text{all}}$	absorption efficiency in all layers
$\eta_{\text{eff}}$	effective absorption efficiency
$\eta_{\text{FCA}}$	absorption efficiency in doped layers
$\theta$	angle of ground-strip
$\theta_{\text{prism}}$	incident light angle in prism
$\lambda_0$	wavelength in vacuum
$\lambda_{\text{g}}$	guided wavelength
$\lambda_{\text{laser}}$	laser wavelength
$\mu_{\text{e}}$	electron mobility
$\sigma_0$	static electric conductivity
$\tau_{\text{g}}$	group delay
$\varphi_{\text{ring}}$	normalized round-trip phase shift

$\Omega$  normalized angular frequency to the free spectral range

## List of figures

Fig. 1-1 Publication trends over the past decade on THz beam steering. ....	2
Fig. 1-2 Classification of THz beam steering approaches. ....	2
Fig. 1-3 A comparative study of the evolution in complexity between electronic and photonic chips. Adapted from [116] (licensed under Creative Commons Attribution 4.0 International license) and [117] (licensed under a Creative Commons License). ....	5
Fig. 2-1 Conceptual view of the proposed PIC for signal generation from 230 to 330 GHz using optical heterodyning. Beam steering is achieved by a THz MSL periodic LWA with an on-chip monolithically integrated THz PD on a 50 $\mu\text{m}$ thick InP substrate bonded on a Si mechanical carrier. Adapted from [Lu I]. ....	9
Fig. 2-2 Top view of the GCPW-MSL transition and a segment of the MSL periodic LWA. Adapted from [Lu I]. ....	10
Fig. 2-3 Simulated scattering parameters of the back-to-back GCPW-MSL transition from 100 to 450 GHz. The inset shows the simulated layout of the GCPW-MSL transition with an MSL length of $a = 1$ mm [Lu I]. ....	12
Fig. 2-4 Fabrication process flow of the designed THz MSL periodic LWAs with GCPW-MSL transitions based on substrate-transfer technology. The photographs show the fabricated LWAs with GCPW-MSL transitions on an intact and a cleaved 1.5 mm wide InP substrate. Adapted from [Lu I]. ....	14
Fig. 2-5 Bonding parameters of the developed substrate-transfer technology. ....	14
Fig. 2-6 Measured roughness of the fabricated LWA surface using a DektakXT stylus profiler. Insert shows a microscopic image of the fabricated LWA section [Lu I]. ....	15
Fig. 2-7 Simulated and measured $S_{11}$ parameters of the fabricated THz LWA with the GCPW-MSL transition [Lu I]. ....	15
Fig. 2-8 Simulated and experimentally determined far-field radiation patterns of the THz LWA with the GCPW-MSL transition on an intact InP substrate and a cleaved InP substrate with a width of 1.5 mm at 280 GHz, 300 GHz and 320 GHz. Adapted from [Lu I]. ....	16
Fig. 2-9 On-wafer antenna measurement system for far-field radiation pattern measurements [Lu I]. ....	17
Fig. 2-10 Simulated and measured relationship between beam direction and frequency from 230 to 330 GHz of the THz LWA with the GCPW-MSL transition in the H-plane. Adapted from [Lu I]. ....	18
Fig. 2-11 Simulated and measured relationship between 3-dB beam width and frequency from 230 to 330 GHz of the THz LWA with the GCPW-MSL transition in the H-plane. Adapted from [Lu I]. ....	18
Fig. 2-12 Simulated and measured relationship between realized gain and frequency from 230 to 330 GHz of the THz LWA with the GCPW-MSL transition. Adapted from [Lu I]. ....	19
Fig. 3-1 Simulated and experimentally characterized beam direction of the THz LWA	

with the GCPW-MSL transition on the 1.5 mm wide InP substrate in the H-plane. Adapted from [Lu II].	21
Fig. 3-2 Simulated and experimentally characterized 3-dB beam width of the THz LWA with the GCPW-MSL transition on the 1.5 mm wide InP substrate in the H-plane. Adapted from [Lu II].	22
Fig. 3-3 Simulated and experimentally characterized directivity of the THz LWA with the GCPW-MSL transition on the 1.5 mm wide InP substrate. Adapted from [Lu II].	22
Fig. 3-4 Schematic view of the mobile THz communication system using the photonic-assisted THz LWA with the Teflon lens. The photograph shows the wireless frontend and receiver.	23
Fig. 3-5 Measured BER of 4-QAM IF OFDM data signals with bandwidths of 8 GHz and 12 GHz from $6^\circ$ to $39^\circ$ over a wireless distance of 6 cm. The IF is 6 GHz. Adapted from [Lu II].	24
Fig. 3-6 Measured BER of 4-QAM IF OFDM data signals for wireless transmission distances from 6 to 34 cm. The IF is 3 GHz, and the beam direction is $6^\circ$ . Adapted from [Lu II].	25
Fig. 3-7 Schematic view of the LWA in multi-beam operation.	25
Fig. 4-1 Concept of the $1 \times 4$ OBFN chip with integrated MUTC-PDs for 1D beam steering at 300 GHz [Lu III].	27
Fig. 4-2 Calculated phase responses over one FSR for a single ORR with different round-trip phase shifts $\phi_{\text{ring}}$ and for two cascaded ORRs with the same resonance frequency. The power coupling coefficient $k$ is 0.5 and the amplitude loss factor $q$ is 1 [Lu III].	28
Fig. 4-3 Calculated phase response over fourteen FSRs for two cascaded ORRs with the same resonance frequency. The power coupling coefficient $k$ is 0.5 and the amplitude loss factor $q$ is 1 [Lu III].	29
Fig. 4-4 Mask design of an ORR. The inset shows the fabricated OBFN chip.	29
Fig. 4-5 Measurement setup for group delay characterization.	30
Fig. 4-6 Measured power coupling coefficient as a function of the coupler heater bias of an ORR [Lu III].	31
Fig. 4-7 Measured resonance frequency offset as a function of the ring heater bias of an ORR [Lu III].	31
Fig. 4-8 Measured optical frequency response of one OPS with two cascaded ORRs having the same resonance frequency [Lu III].	32
Fig. 4-9 Measurement setup for phase shift characterization [Lu III].	32
Fig. 4-10 Measured amplitudes of the 10.95 GHz RF signal (WP2) for various ring heater biases [Lu III].	33
Fig. 4-11 Measured ring heater biases of the ORR3 and ORR4 for phase shifts from $-180^\circ$ to $180^\circ$ [Lu III].	34

Fig. 4-12 Calculated dissipative ring heater power of ORR3 and ORR4 for phase shifts from $-180^\circ$ to $180^\circ$ [Lu III].	34
Fig. 4-13 Measured relative output power of the UTC-PD at 0.295 THz for phase shifts from $-180^\circ$ to $180^\circ$ [Lu III].	35
<i>Fig. 4-14 Simulated polar diagrams of the absolute radiation power of the <math>1 \times 4</math> phased array with constant (blue lines) and variational (red lines) power at 295 GHz for phase differences between adjacent antennas of (a) <math>30^\circ</math>, (b) <math>60^\circ</math>, (c) <math>90^\circ</math>, (d) <math>120^\circ</math>, (e) <math>-30^\circ</math>, (f) <math>-60^\circ</math>, (g) <math>-90^\circ</math> and (h) <math>-120^\circ</math>. The inset shows a schematic drawing of the <math>1 \times 4</math> phased array with DRW antennas [Lu III].</i>	36
Fig. 5-1 Concept of the PIC featuring 2D THz beam steering.	39
Fig. 5-2 Mask design of the OBFN chip with four OPSs based on straight waveguides. The inset shows the fabricated OBFN chip.	40
Fig. 5-3 Simulated polar diagrams of realized gain in the E-plane and at broadside of the LWA array for phase differences between adjacent antennas of $0^\circ$ , $60^\circ$ and $120^\circ$ .	42
Fig. 5-4 Schematic illustration of prism coupling.	43
Fig. 5-5 Schematic side view of the InP PD with the integrated TriPleX waveguide using $\text{Al}_2\text{O}_3$ as bonding layer.	44
Fig. 5-6 Simulated optical amplitude distribution in the InP PD with the integrated TriPleX waveguide.	45
Fig. 5-7 Simulated effective absorption efficiency of InP PDs with lengths from 4 to $16 \mu\text{m}$ and InP blocker thicknesses from 400 to 1200 nm.	46
Fig. 5-8 Final design of epitaxial layers for the heterogenous integration with TriPleX waveguides.	46
Fig. 5-9 Process flow of the epitaxial-layer-transfer technology for the heterogenous integration of InP PDs with TriPleX waveguides.	47
Fig. 5-10 Bonding parameters of the developed epitaxial-layer-transfer technology.	49
Fig. 5-11 Measured bonding strength for InP/Si chips bonded using PEALD- and TALD- $\text{Al}_2\text{O}_3$ layers.	49
Fig. 5-12 TriPleX chip with the transferred PD epitaxial layers from the InP substrate.	50
Fig. 6-1 Simulated realized gain as a function of InP-based THz LWA quantity at 300 GHz. Adapted from [Lu III].	52
Fig. 6-2 Beam steering range for the state-of-the-art THz beam steering approaches. Adapted from [218] (licensed under a Creative Commons License).	53
Fig. 6-3 Calculated beam directions of a phased array as a function of the phase shift between adjacent antennas with a pitch of $500 \mu\text{m}$ for frequencies from 270 to 330 GHz.	54

**List of tables**

Table 2-1 Parameters of THz MSL periodic LWA. Adapted from [Lu I].....	11
Table 2-2 Parameters of GCPW-MSL transition. Adapted from [Lu I].....	12
Table 2-3 Comparison of GCPW-MSL transitions [Lu I]. ....	13
Table 3-1 Link budget for beam directions of 6°, 20° and 32° for a wireless distance of 6 cm. Adapted from [Lu II].....	24
Table 3-2 Measurement parameters and results for multi-user scenarios [Lu II].....	26
Table 4-1 Parameters for numerical analyses of constant power and variational power scenarios at 295 GHz [Lu III]. ....	38
Table 5-1 Link budget calculation of the mobile THz 6G communication system using the proposed PIC as the transmitter. ....	41
Table 6-1 Comparison of state-of-the-art THz beam steering approaches. ....	56

## References

- [1] X.-C. Zhang and J. Xu, *Introduction to THz wave photonics*. Springer, 2010.
- [2] T. Ishibashi, S. Kodama, N. S. N. Shimizu, and T. F. T. Furuta, "High-speed response of uni-traveling-carrier photodiodes," *Japanese journal of applied physics*, vol. 36, no. 10R, p. 6263, 1997.
- [3] B. S. Williams, "Terahertz quantum-cascade lasers," *Nature photonics*, vol. 1, no. 9, pp. 517-525, 2007.
- [4] A. Wakatsuki, T. Furuta, Y. Muramoto, T. Yoshimatsu, and H. Ito, "High-power and broadband sub-terahertz wave generation using a J-band photomixer module with rectangular-waveguide output port," in *2008 33rd International Conference on Infrared, Millimeter and Terahertz Waves*, 2008: IEEE, pp. 1-2.
- [5] T. J. I. M. m. Nagatsuma, "Generating millimeter and terahertz waves," vol. 10, no. 4, pp. 64-74, 2009.
- [6] H. Ito and T. Ishibashi, "Photonic terahertz-wave generation using slot-antenna-integrated uni-traveling-carrier photodiodes," *IEEE J. Sel. Top. Quantum Electron.*, vol. 23, no. 4, pp. 1-7, Jul.-Aug. 2017.
- [7] P. Latzel *et al.*, "Generation of mW level in the 300-GHz band using resonant-cavity-enhanced untraveling carrier photodiodes," *IEEE Transactions on Terahertz Science and Technology*, vol. 7, no. 6, pp. 800-807, 2017.
- [8] N. M. Burford and M. O. El-Shenawee, "Review of terahertz photoconductive antenna technology," *Optical Engineering*, vol. 56, no. 1, p. 010901, 2017.
- [9] K. Fujita *et al.*, "Recent progress in terahertz difference-frequency quantum cascade laser sources," *Nanophotonics*, vol. 7, no. 11, pp. 1795-1817, 2018.
- [10] J. P. Seddon, M. Natrella, X. Lin, C. Graham, C. C. Renaud, and A. J. Seeds, "Photodiodes for terahertz applications," *IEEE Journal of Selected Topics in Quantum Electronics*, vol. 28, no. 2, pp. 1-12, 2021.
- [11] B. Wen and D. Ban, "High-temperature terahertz quantum cascade lasers," *Progress in Quantum Electronics*, vol. 80, p. 100363, 2021.
- [12] M. Grzeslo *et al.*, "High saturation photocurrent THz waveguide-type MUTC-photodiodes reaching mW output power within the WR3. 4 band," *Optics Express*, vol. 31, no. 4, pp. 6484-6498, 2023.
- [13] H. Eisele, "State of the art and future of electronic sources at terahertz frequencies," *Electronics letters*, vol. 46, no. 26, pp. 8-11, 2010.
- [14] B. Heinemann *et al.*, "SiGe HBT with  $f_x/f_{max}$  of 505 GHz/720 GHz," in *2016 IEEE International Electron Devices Meeting (IEDM)*, 2016: IEEE, pp. 3.1. 1-3.1. 4.
- [15] T. Maekawa, H. Kanaya, S. Suzuki, and M. Asada, "Oscillation up to 1.92 THz in resonant tunneling diode by reduced conduction loss," *Applied physics express*, vol. 9, no. 2, p. 024101, 2016.
- [16] J. Yun, J. Kim, D. Yoon, and J. S. Rieh, "645-GHz InP heterojunction bipolar transistor harmonic oscillator," *Electronics Letters*, vol. 53, no. 22, pp. 1475-1477, 2017.
- [17] M. Hossain *et al.*, "A 0.5 thz signal source with-11 dbm peak output power based on inp dhbt," in *2019 49th European Microwave Conference (EuMC)*, 2019: IEEE, pp. 856-859.
- [18] F. Sizov and A. Rogalski, "THz detectors," *Progress in quantum electronics*, vol. 34, no. 5, pp. 278-347, 2010.
- [19] R. Lewis, "A review of terahertz detectors," *J. Phys. D: Appl. Phys.*, vol. 52, no.

- 43, p. 433001, Aug. 2019.
- [20] S. Makhlouf, J. Martinez-Gil, M. Grzeslo, D. Moro-Melgar, O. Cojocari, and A. Stöhr, "High-power UTC-photodiodes for an optically pumped subharmonic terahertz receiver," *Optics Express*, vol. 30, no. 24, pp. 43798-43814, 2022.
- [21] L. A. Samoska, "An overview of solid-state integrated circuit amplifiers in the submillimeter-wave and THz regime," *IEEE Transactions on Terahertz Science and Technology*, vol. 1, no. 1, pp. 9-24, 2011.
- [22] L. John, A. Tessmann, A. Leuther, P. Neining, T. Merkle, and T. Zwick, "Broadband 300-GHz power amplifier MMICs in InGaAs mHEMT technology," *IEEE Transactions on Terahertz Science and Technology*, vol. 10, no. 3, pp. 309-320, 2020.
- [23] X. Li *et al.*, "A 250–310 GHz power amplifier with 15-dB peak gain in 130-nm SiGe BiCMOS process for terahertz wireless system," *IEEE Transactions on Terahertz Science and Technology*, vol. 12, no. 1, pp. 1-12, 2021.
- [24] H. Chen, W. Ma, Z. Huang, Y. Zhang, Y. Huang, and Y. Chen, "Graphene-based materials toward microwave and terahertz absorbing stealth technologies," *Advanced Optical Materials*, vol. 7, no. 8, p. 1801318, 2019.
- [25] J. Pan, H. Hu, Z. Li, J. Mu, Y. Cai, and H. Zhu, "Recent progress in two-dimensional materials for terahertz protection," *Nanoscale Advances*, vol. 3, no. 6, pp. 1515-1531, 2021.
- [26] C. Chen, M. Chai, M. Jin, and T. He, "Terahertz metamaterial absorbers," *Advanced Materials Technologies*, vol. 7, no. 5, p. 2101171, 2022.
- [27] Q. Wang *et al.*, "Design, fabrication, and modulation of THz bandpass metamaterials," *Laser & Photonics Reviews*, vol. 13, no. 11, p. 1900071, 2019.
- [28] M. B. Heydari and M. H. V. Samiei, "A short review on graphene-based filters: perspectives and challenges," *arXiv preprint arXiv:2010.07176*, 2020.
- [29] F. Yan, C. Yu, H. Park, E. P. Parrott, and E. Pickwell-MacPherson, "Advances in polarizer technology for terahertz frequency applications," *Journal of infrared, millimeter, and terahertz waves*, vol. 34, no. 9, pp. 489-499, 2013.
- [30] K. Meng *et al.*, "Tunable broadband terahertz polarizer using graphene-metal hybrid metasurface," *Optics Express*, vol. 27, no. 23, pp. 33768-33778, 2019.
- [31] M. B. Johnston and H. J. Joyce, "Polarization Anisotropy in Nanowires: Fundamental Concepts and Progress Towards Terahertz-Band Polarization Devices," *Progress in Quantum Electronics*, p. 100417, 2022.
- [32] A. Fitzgerald, E. Berry, N. Zinovev, G. Walker, M. Smith, and J. Chamberlain, "An introduction to medical imaging with coherent terahertz frequency radiation," *Phys. Med. Biol.*, vol. 47, no. 7, pp. R67-R84, Mar. 2002.
- [33] C. Yu, S. Fan, Y. Sun, and E. Pickwell-MacPherson, "The potential of terahertz imaging for cancer diagnosis: A review of investigations to date," *Quant. Imaging Med. Surg.*, vol. 2, no. 1, pp. 33-45, Mar. 2012.
- [34] L. Wu *et al.*, "Study of in vivo brain glioma in a mouse model using continuous-wave terahertz reflection imaging," *Biomed. Opt. Express*, vol. 10, no. 8, pp. 3953-3962, Aug. 2019.
- [35] L. Yu *et al.*, "The medical application of terahertz technology in non-invasive detection of cells and tissues: opportunities and challenges," *RSC Adv.*, vol. 9, no. 17, pp. 9354-9363, Mar. 2019.
- [36] D. M. Mittleman, "Twenty years of terahertz imaging," *Opt. Express*, vol. 26, no. 8, pp. 9417-9431, Apr. 2018.
- [37] R. I. Stantchev, X. Yu, T. Blu, and E. Pickwell-MacPherson, "Real-time terahertz imaging with a single-pixel detector," *Nature communications*, vol. 11,

- no. 1, pp. 1-8, 2020.
- [38] E. S. Lee *et al.*, "High-speed and cost-effective reflective terahertz imaging system using a novel 2D beam scanner," *Journal of Lightwave Technology*, vol. 38, no. 16, pp. 4237-4243, 2020.
- [39] S. Dülme, M. Steeg, I. Mohammad, N. Schrinski, J. Tebart, and A. Stöhr, "Ultra-low phase-noise photonic terahertz imaging system based on two-tone square-law detection," *Optics Express*, vol. 28, no. 20, pp. 29631-29643, 2020.
- [40] Y. A. García-Jomaso, D. L. Hernández-Roa, J. Garduño-Mejía, C. G. Treviño-Palacios, O. V. Kolokoltsev, and N. Qureshi, "Sub-wavelength continuous THz imaging system based on interferometric detection," *Optics Express*, vol. 29, no. 12, pp. 19120-19125, 2021.
- [41] S. Hisatake, J.-Y. Kim, K. Ajito, and T. Nagatsuma, "Self-heterodyne spectrometer using uni-traveling-carrier photodiodes for terahertz-wave generators and optoelectronic mixers," *J. Lightwave Technol.*, vol. 32, no. 20, pp. 3683-3689, Oct. 2014.
- [42] N. Kanda, K. Konishi, N. Nemoto, K. Midorikawa, and M. Kuwata-Gonokami, "Real-time broadband terahertz spectroscopic imaging by using a high-sensitivity terahertz camera," *Scientific reports*, vol. 7, no. 1, pp. 1-10, 2017.
- [43] L. Yang, T. Guo, X. Zhang, S. Cao, and X. Ding, "Toxic chemical compound detection by terahertz spectroscopy: A review," *Reviews in Analytical Chemistry*, vol. 37, no. 3, 2018.
- [44] P. Han, X. Wang, and Y. Zhang, "Time - Resolved Terahertz Spectroscopy Studies on 2D Van der Waals Materials," *Advanced Optical Materials*, vol. 8, no. 3, p. 1900533, 2020.
- [45] J.-Y. Kim, H.-J. Song, K. Ajito, M. Yaita, and N. Kukutsu, "Continuous-wave THz homodyne spectroscopy and imaging system with electro-optical phase modulation for high dynamic range," *IEEE Transactions on Terahertz Science and Technology*, vol. 3, no. 2, pp. 158-164, 2013.
- [46] R. I. Hermans, J. Seddon, H. Shams, L. Ponnampalam, A. J. Seeds, and G. Aeppli, "Ultra-high-resolution software-defined photonic terahertz spectroscopy," *Optica*, vol. 7, no. 10, pp. 1445-1455, 2020.
- [47] K. Kolpatzek, X. Liu, L. Häring, J. C. Balzer, and A. Czylik, "Ultra-high repetition rate terahertz time-domain spectroscopy for micrometer layer thickness measurement," *Sensors*, vol. 21, no. 16, p. 5389, 2021.
- [48] T. Nagatsuma *et al.*, "Terahertz wireless communications based on photonics technologies," *Optics express*, vol. 21, no. 20, pp. 23736-23747, 2013.
- [49] A. J. Seeds, H. Shams, M. J. Fice, and C. C. Renaud, "Terahertz photonics for wireless communications," *Journal of Lightwave Technology*, vol. 33, no. 3, pp. 579-587, 2014.
- [50] J. Y. Suen, M. T. Fang, S. P. Denny, and P. Lubin, "Modeling of terabit geostationary terahertz satellite links from globally dry locations," *IEEE Trans. Terahertz Sci. Technol.*, vol. 5, no. 2, pp. 299-313, Mar. 2015.
- [51] T. Nagatsuma, G. Ducournau, and C. C. Renaud, "Advances in terahertz communications accelerated by photonics," *Nat. Photonics*, vol. 10, no. 6, pp. 371-379, Jun. 2016.
- [52] V. Petrov, A. Pyattaev, D. Moltchanov, and Y. Koucheryavy, "Terahertz band communications: Applications, research challenges, and standardization activities," in *2016 8th international congress on ultra modern telecommunications and control systems and workshops (ICUMT)*, 2016: IEEE, pp. 183-190.

- [53] M. F. Hermelo, P.-T. Shih, M. Steeg, A. Ng'oma, and A. Stöhr, "Spectral efficient 64-QAM-OFDM terahertz communication link," *Opti. Express*, vol. 25, no. 16, pp. 19360-19370, Aug. 2017.
- [54] T. Harter *et al.*, "Generalized Kramers–Kronig receiver for coherent terahertz communications," *Nature Photonics*, vol. 14, no. 10, pp. 601-606, 2020.
- [55] I. F. Akyildiz, C. Han, Z. Hu, S. Nie, and J. M. Jornet, "Terahertz band communication: An old problem revisited and research directions for the next decade," *IEEE Transactions on Communications*, vol. 70, no. 6, pp. 4250-4285, 2022.
- [56] IEEE. "IEEE Standard for High Data Rate Wireless Multi-Media Networks Amendment 2: 100 Gb/s Wireless Switched Point-to-Point Physical Layer." <https://standards.ieee.org/ieee/802.15.3d/6648/> (accessed on 27. Dec. 2022).
- [57] I. T. Union. "Technical and operational characteristics and applications of the point-to-point fixed service applications operating in the frequency band 275-450 GHz." [https://www.itu.int/dms\\_pub/itu-r/opb/rep/R-REP-F.2416-2018-PDF-E.pdf](https://www.itu.int/dms_pub/itu-r/opb/rep/R-REP-F.2416-2018-PDF-E.pdf) (accessed on 27. Dec. 2022).
- [58] M. El-Absi, A. A. Abbas, A. Abuelhaija, F. Zheng, K. Solbach, and T. Kaiser, "High-accuracy indoor localization based on chipless RFID systems at THz band," *IEEE access*, vol. 6, pp. 54355-54368, 2018.
- [59] S. Nellen *et al.*, "Photonic-enabled beam steering at 300 GHz using a photodiode-based antenna array and a polymer-based optical phased array," *Optics Express*, vol. 30, no. 25, pp. 44701-44716, 2022.
- [60] M. Che, K. Kondo, H. Kanaya, and K. Kato, "Arrayed photomixers for THz beam-combining and beam-steering," *Journal of Lightwave Technology*, vol. 40, no. 20, pp. 6657-6665, 2022.
- [61] S. Abu-Surra *et al.*, "End-to-end 140 GHz wireless link demonstration with fully-digital beamformed system," in *2021 IEEE International Conference on Communications Workshops (ICC Workshops)*, 2021: IEEE, pp. 1-6.
- [62] A. Nemati, Q. Wang, M. Hong, and J. Teng, "Tunable and reconfigurable metasurfaces and metadevices," *Opto-Electronic Advances*, vol. 1, no. 5, p. 180009, 2018.
- [63] S. E. Hosseinijad, K. Rouhi, M. Neshat, A. Cabellos-Aparicio, S. Abadal, and E. Alarcón, "Digital metasurface based on graphene: An application to beam steering in terahertz plasmonic antennas," *IEEE Transactions on Nanotechnology*, vol. 18, pp. 734-746, 2019.
- [64] X. Fu, F. Yang, C. Liu, X. Wu, and T. J. Cui, "Terahertz Beam Steering Technologies: From Phased Arrays to Field-Programmable Metasurfaces," *Advanced optical materials*, vol. 8, no. 3, p. 1900628, 2020.
- [65] G. Perez-Palomino *et al.*, "Design and demonstration of an electronically scanned reflectarray antenna at 100 GHz using multiresonant cells based on liquid crystals," *IEEE Transactions on Antennas and Propagation*, vol. 63, no. 8, pp. 3722-3727, 2015.
- [66] X. Fu *et al.*, "Flexible Terahertz Beam Manipulations Based on Liquid-Crystal-Integrated Programmable Metasurfaces," *ACS Applied Materials & Interfaces*, 2022.
- [67] E. Carrasco and J. Perruisseau-Carrier, "Reflectarray antenna at terahertz using graphene," *IEEE Antennas and Wireless Propagation Letters*, vol. 12, pp. 253-256, 2013.
- [68] M. Tamagnone *et al.*, "Graphene reflectarray metasurface for terahertz beam steering and phase modulation," *arXiv preprint arXiv:1806.02202*, pp. 1-15,

- 2018.
- [69] M. Liu *et al.*, "Terahertz-field-induced insulator-to-metal transition in vanadium dioxide metamaterial," *Nature*, vol. 487, no. 7407, pp. 345-348, 2012.
- [70] H. Liu, J. Lu, and X. R. Wang, "Metamaterials based on the phase transition of VO<sub>2</sub>," *Nanotechnology*, vol. 29, no. 2, p. 024002, 2017.
- [71] M. Shu, I. Chatzakis, Y. Kuo, P. Zalden, and A. Lindenberg, "Ultrafast sub-threshold photo-induced response in crystalline and amorphous GeSbTe thin films," *Applied Physics Letters*, vol. 102, no. 20, p. 201903, 2013.
- [72] P. Pitchappa *et al.*, "Volatile ultrafast switching at multilevel nonvolatile states of phase change material for active flexible terahertz metadevices," *Advanced Functional Materials*, vol. 31, no. 17, p. 2100200, 2021.
- [73] X. Su *et al.*, "Active metasurface terahertz deflector with phase discontinuities," *Optics express*, vol. 23, no. 21, pp. 27152-27158, 2015.
- [74] Y. Monnai, K. Altmann, C. Jansen, H. Hillmer, M. Koch, and H. Shinoda, "Terahertz beam steering and variable focusing using programmable diffraction gratings," *Opt. Express*, vol. 21, no. 2, pp. 2347-2354, Jan. 2013.
- [75] X. Liu *et al.*, "Terahertz Beam Steering Using a MEMS-Based Reflectarray Configured by a Genetic Algorithm," *IEEE Access*, vol. 10, pp. 84458-84472, 2022.
- [76] A. A. Oliner, D. R. Jackson, and J. Volakis, "Leaky-wave antennas," in *Antenna engineering handbook*, 4th ed. New York, NY, USA: McGraw-Hill, 2007, ch. 11.
- [77] W. Hansen, "Radiating electromagnetic waveguide," *Patent, 1940, US Patent No. 2.402. 622*, 1940.
- [78] J. Hines and J. J. O. S. U. R. F. Upson, "A wide aperture tapered-depth scanning antenna," pp. 667-7, 1957.
- [79] F. Xu and K. Wu, "Understanding leaky-wave structures: A special form of guided-wave structure," *IEEE Microw. Mag.*, vol. 14, no. 5, pp. 87-96, Jul.-Aug. 2013.
- [80] Y. Li, Q. Xue, E. K.-N. Yung, and Y. Long, "Dual-beam steering microstrip leaky wave antenna with fixed operating frequency," *IEEE Transactions on Antennas and Propagation*, vol. 56, no. 1, pp. 248-252, 2008.
- [81] W. Menzel, "A new travelling-wave antenna in microstrip," 1979.
- [82] J. Liu, D. R. Jackson, and Y. Long, "Substrate integrated waveguide (SIW) leaky-wave antenna with transverse slots," *IEEE Trans. Antennas Propag.*, vol. 60, no. 1, pp. 20-29, Jan. 2012.
- [83] M. Steeg, B. Khani, V. Rymanov, and A. Stöhr, "Novel 50–70 GHz compact PCB leaky-wave antenna with high broadside efficiency and low return loss," in *IRMMW-THz*, Copenhagen, Denmark, Sept. 25-30, 2016, pp. 1-2.
- [84] M. Steeg, N. Yonemoto, J. Tebart, and A. Stöhr, "Substrate-integrated waveguide PCB leaky-wave antenna design providing multiple steerable beams in the V-band," *Electronics*, vol. 6, no. 4, Dec. 2017, Art no. 107.
- [85] R. Agrawal, P. Belwal, and S. Gupta, "Asymmetric substrate integrated waveguide leaky wave antenna with open stop band suppression and radiation efficiency equalization through broadside," *Radioengineering*, vol. 27, no. 2, pp. 409-416, Jun. 2018.
- [86] A. Grbic and G. V. Eleftheriades, "Leaky CPW-based slot antenna arrays for millimeter-wave applications," *IEEE Trans. Antennas Propag.*, vol. 50, no. 11, pp. 1494-1504, Nov. 2002.
- [87] S. Xiao, B.-Z. Wang, X.-S. Yang, and G. Wang, "A Novel Reconfiguration

- CPW Leaky-Wave Antenna for Millimeter-Wave Application," *Int. J. Infrared Millimeter Waves*, vol. 23, no. 11, pp. 1637-1648, Nov. 2002.
- [88] J. L. Gómez-Tornero, F. D. Quesada-Pereira, and A. Álvarez-Melcón, "Analysis and design of periodic leaky-wave antennas for the millimeter waveband in hybrid waveguide-planar technology," *IEEE transactions on antennas and propagation*, vol. 53, no. 9, pp. 2834-2842, 2005.
- [89] X. Bai, S.-W. Qu, K.-B. Ng, and C. H. Chan, "Sinusoidally modulated leaky-wave antenna for millimeter-wave application," *IEEE Transactions on Antennas and Propagation*, vol. 64, no. 3, pp. 849-855, 2015.
- [90] S. Lim, C. Caloz, T. J. I. M. Itoh, and W. C. Letters, "Electronically scanned composite right/left handed microstrip leaky-wave antenna," vol. 14, no. 6, pp. 277-279, 2004.
- [91] D. K. Karmokar, K. P. Esselle, and S. G. Hay, "Fixed-frequency beam steering of microstrip leaky-wave antennas using binary switches," *IEEE transactions on antennas and propagation*, vol. 64, no. 6, pp. 2146-2154, 2016.
- [92] Z. Li, Y. J. Guo, S.-L. Chen, and J. Wang, "A period-reconfigurable leaky-wave antenna with fixed-frequency and wide-angle beam scanning," *IEEE Transactions on Antennas and Propagation*, vol. 67, no. 6, pp. 3720-3732, 2019.
- [93] B. Xi, Y. Li, Z. Liang, S. Zheng, Z. Chen, and Y. Long, "Periodic Fixed-Frequency Staggered Line Leaky Wave Antenna With Wide-Range Beam Scanning Capacity," *IEEE Access*, vol. 7, pp. 146693-146701, 2019.
- [94] M. Esquius-Morote, J. S. Gómez-Dí, and J. Perruisseau-Carrier, "Sinusoidally modulated graphene leaky-wave antenna for electronic beamscanning at THz," *IEEE Transactions on Terahertz Science and Technology*, vol. 4, no. 1, pp. 116-122, 2014.
- [95] X.-C. Wang, W.-S. Zhao, J. Hu, and W.-Y. Yin, "Reconfigurable terahertz leaky-wave antenna using graphene-based high-impedance surface," *IEEE Transactions on nanotechnology*, vol. 14, no. 1, pp. 62-69, 2014.
- [96] N. A. Al-Shalaby, A. S. Elhenawy, S. H. Zainud-Deen, and H. A. Malhat, "Electronic beam-scanning strip-coded graphene leaky-wave antenna using single structure," *Plasmonics*, vol. 16, pp. 1427-1438, 2021.
- [97] Y. Cheng, L.-S. Wu, M. Tang, Y.-P. Zhang, and J.-F. Mao, "A sinusoidally-modulated leaky-wave antenna with gapped graphene ribbons," *IEEE Antennas and Wireless Propagation Letters*, vol. 16, pp. 3000-3004, 2017.
- [98] W. Fuscaldo, D. C. Zografopoulos, F. Imperato, P. Burghignoli, R. Beccherelli, and A. Galli, "Analysis and Design of Tunable THz 1-D Leaky-Wave Antennas Based on Nematic Liquid Crystals," *Applied Sciences*, vol. 12, no. 22, p. 11770, 2022.
- [99] W. Fuscaldo *et al.*, "Tunable Fabry–Perot cavity THz antenna based on leaky-wave propagation in nematic liquid crystals," *IEEE Antennas and Wireless Propagation Letters*, vol. 16, pp. 2046-2049, 2017.
- [100] N. J. Karl, R. W. McKinney, Y. Monnai, R. Mendis, and D. M. Mittleman, "Frequency-division multiplexing in the terahertz range using a leaky-wave antenna," *Nature Photonics*, vol. 9, no. 11, pp. 717-720, 2015.
- [101] K. Murano *et al.*, "Low-profile terahertz radar based on broadband leaky-wave beam steering," *IEEE Trans. Terahertz Sci. Technol.*, vol. 7, no. 1, pp. 60-69, Jan. 2017.
- [102] D. Headland, Y. Monnai, D. Abbott, C. Fumeaux, and W. Withayachumnankul, "Tutorial: Terahertz beamforming, from concepts to realizations," *Appl Photonics*, vol. 3, no. 5, p. 051101, 2018.

- 
- [103] J. Capmany and D. Novak, "Microwave photonics combines two worlds," *Nature photonics*, vol. 1, no. 6, p. 319, 2007.
- [104] B. Ning *et al.*, "Beamforming technologies for ultra-massive MIMO in terahertz communications," *IEEE Open Journal of the Communications Society*, vol. 4, pp. 614-658, 2023.
- [105] A. Tang *et al.*, "A 65nm CMOS 140 GHz 27.3 dBm EIRP transmit array with membrane antenna for highly scalable multi-chip phase arrays," in *2014 IEEE MTT-S International Microwave Symposium (IMS2014)*, 2014: IEEE, pp. 1-3.
- [106] N. Buadana, S. Jameson, and E. Socher, "A 280-GHz digitally controlled four port chip-scale dielectric resonator antenna transmitter with DiCAD true time delay," *IEEE Solid-State Circuits Letters*, vol. 3, pp. 454-457, 2020.
- [107] K. Sengupta and A. Hajimiri, "A 0.28 THz power-generation and beam-steering array in CMOS based on distributed active radiators," *IEEE Journal of Solid-State Circuits*, vol. 47, no. 12, pp. 3013-3031, 2012.
- [108] Y. Tousei and E. Afshari, "A high-power and scalable 2-D phased array for terahertz CMOS integrated systems," *IEEE Journal of Solid-State Circuits*, vol. 50, no. 2, pp. 597-609, 2014.
- [109] Y. Yang, O. D. Gurbuz, and G. M. Rebeiz, "An eight-element 370–410-GHz phased-array transmitter in 45-nm CMOS SOI with peak EIRP of 8–8.5 dBm," *IEEE Trans. Microw. Theory Tech.*, vol. 64, no. 12, pp. 4241-4249, Dec. 2016.
- [110] K. Guo, Y. Zhang, and P. Reynaert, "A 0.53-THz subharmonic injection-locked phased array with 63- $\mu$ W radiated power in 40-nm CMOS," *IEEE Journal of Solid-State Circuits*, vol. 54, no. 2, pp. 380-391, 2018.
- [111] X.-D. Deng, Y. Li, J. Li, C. Liu, W. Wu, and Y.-Z. Xiong, "A 320-GHz 1x4 Fully Integrated Phased Array Transmitter Using 0.13- $\mu$ m SiGe BiCMOS Technology," *IEEE Transactions on Terahertz Science and Technology*, vol. 5, no. 6, pp. 930-940, 2015.
- [112] Y. Zhou, G. Sakano, Y. Yamanaka, H. Ito, T. Ishibashi, and K. Kato, "600-GHz-Wave Beam Steering by Terahertz-Wave Combiner," in *OFC*, San Diego, California, USA, Mar. 11-15, 2018, pp. 1-3.
- [113] Y. Liu, B. Isaac, J. Kalkavage, E. Adles, T. Clark, and J. Klamkin, "True Time Delay Millimeter Wave Beam Steering with Integrated Optical Beamforming Network," in *CLEO: Science and Innovations*, 2019: Optical Society of America, p. SF3N. 6.
- [114] M. Che, Y. Matsuo, H. Kanaya, H. Ito, T. Ishibashi, and K. Kato, "Optoelectronic THz-Wave Beam Steering by Arrayed Photomixers With Integrated Antennas," *IEEE Photonics Technology Letters*, vol. 32, no. 16, pp. 979-982, 2020.
- [115] M. Sung *et al.*, "Design considerations of photonic THz communications for 6G networks," *IEEE Wireless Communications*, vol. 28, no. 5, pp. 185-191, 2021.
- [116] H. R. Max Roser. "A logarithmic graph showing the timeline of how transistor counts in microchips are almost doubling every two years from 1970 to 2020; Moore's Law." <https://assets.ourworldindata.org/uploads/2020/11/Transistor-Count-over-time.png> (accessed on 21. Nov. 2023).
- [117] M. Smit, K. Williams, and J. Van Der Tol, "Past, present, and future of InP-based photonic integration," *APL Photonics*, vol. 4, no. 5, p. 050901, 2019.
- [118] J. Bardeen and W. H. Brattain, "The transistor, a semi-conductor triode," *Physical Review*, vol. 74, no. 2, p. 230, 1948.
- [119] R. N. Hall, G. E. Fenner, J. Kingsley, T. Soltys, and R. Carlson, "Coherent light emission from GaAs junctions," *Physical Review Letters*, vol. 9, no. 9, p. 366,

- 1962.
- [120] M. I. Nathan, W. P. Dumke, G. Burns, F. H. Dill Jr, and G. Lasher, "Stimulated emission of radiation from GaAs p-n junctions," *Applied Physics Letters*, vol. 1, no. 3, pp. 62-64, 1962.
- [121] C. A. Harper, *Electronic materials and processes handbook*. McGraw-Hill Education, 2004.
- [122] M. Suzuki, Y. Noda, H. Tanaka, S. Akiba, Y. Kushiuro, and H. Isshiki, "Monolithic integration of InGaAsP/InP distributed feedback laser and electroabsorption modulator by vapor phase epitaxy," *Journal of lightwave technology*, vol. 5, no. 9, pp. 1277-1285, 1987.
- [123] C. Mead and L. Conway, "Introduction to VLSI systems," ed: Addison-wesley Reading, MA, 1980.
- [124] ePIXnet. "Towards a foundry model for micro- and nanophotonic ICs." <https://www.jeppix.eu/wp-content/jeppix/Vision+Document+Photonic+Foundry+Model+-+ePIXnet+Steering+Committee.pdf> (accessed on 07. July 2023).
- [125] H. J. Eichler and J. Eichler, *Laser: Bauformen, Strahlführung, Anwendungen*. Springer-Verlag, 2015.
- [126] M. Moehrle *et al.*, "Tunable short cavity 10-gb/s 1550-nm DFB-laser with integrated optical amplifier and taper," *IEEE Photonics Technology Letters*, vol. 23, no. 16, pp. 1157-1159, 2011.
- [127] N. K. Dutta and Q. Wang, *Semiconductor optical amplifiers*. World scientific, 2013.
- [128] B. Howley, X. Wang, M. Chen, and R. T. Chen, "Reconfigurable delay time polymer planar lightwave circuit for an X-band phased-array antenna demonstration," *Journal of Lightwave Technology*, vol. 25, no. 3, pp. 883-890, 2007.
- [129] H. Ma, A. Y. Jen, and L. R. Dalton, "Polymer-based optical waveguides: materials, processing, and devices," *Advanced materials*, vol. 14, no. 19, pp. 1339-1365, 2002.
- [130] G. Li *et al.*, "Ultralow-loss, high-density SOI optical waveguide routing for macrochip interconnects," *Optics express*, vol. 20, no. 11, pp. 12035-12039, 2012.
- [131] W. Zhang and J. Yao, "A fully reconfigurable waveguide Bragg grating for programmable photonic signal processing," *Nature communications*, vol. 9, no. 1, p. 1396, 2018.
- [132] K. Wörhoff, R. G. Heideman, A. Leinse, and M. Hoekman, "TriPleX: a versatile dielectric photonic platform," *Advanced Optical Technologies*, vol. 4, no. 2, pp. 189-207, 2015.
- [133] C. G. Roeloffzen *et al.*, "Low-loss Si<sub>3</sub>N<sub>4</sub> TriPleX optical waveguides: Technology and applications overview," *IEEE journal of selected topics in quantum electronics*, vol. 24, no. 4, pp. 1-21, 2018.
- [134] Z. Zhang *et al.*, "Hybrid photonic integration on a polymer platform," in *Photonics*, 2015, vol. 2, no. 3: MDPI, pp. 1005-1026.
- [135] A. Y. Liu and J. Bowers, "Photonic integration with epitaxial III-V on silicon," *IEEE Journal of Selected Topics in Quantum Electronics*, vol. 24, no. 6, pp. 1-12, 2018.
- [136] J. M. Ramirez *et al.*, "III-V-on-silicon integration: from hybrid devices to heterogeneous photonic integrated circuits," *IEEE Journal of Selected Topics in Quantum Electronics*, vol. 26, no. 2, pp. 1-13, 2019.

- 
- [137] P. Kaur, A. Boes, G. Ren, T. G. Nguyen, G. Roelkens, and A. Mitchell, "Hybrid and heterogeneous photonic integration," *APL Photonics*, vol. 6, no. 6, p. 061102, 2021.
- [138] M. Steeg, J. Tebart, K. Neophytou, M. A. Antoniadou, S. Iezekiel, and A. Stöhr, "3D radar localization via photonic chirp leaky-wave antenna beam scanning," in *2019 International Topical Meeting on Microwave Photonics (MWP)*, 2019: IEEE, pp. 1-4.
- [139] M. Steeg, F. Exner, J. Tebart, A. Czulwik, and A. Stöhr, "OFDM joint communication–radar with leaky-wave antennas," *Electronics Letters*, vol. 56, no. 21, pp. 1139-1141, 2020.
- [140] M. Suzuki and M. Tonouchi, "Fe-implanted InGaAs terahertz emitters for 1.56  $\mu$  m wavelength excitation," *Applied Physics Letters*, vol. 86, no. 5, p. 051104, 2005.
- [141] C. Wood *et al.*, "Terahertz emission from metal-organic chemical vapor deposition grown Fe: InGaAs using 830 nm to 1.55  $\mu$  m excitation," *Applied Physics Letters*, vol. 96, no. 19, p. 194104, 2010.
- [142] B. Sartorius *et al.*, "All-fiber terahertz time-domain spectrometer operating at 1.5  $\mu$ m telecom wavelengths," *Optics express*, vol. 16, no. 13, pp. 9565-9570, 2008.
- [143] R. J. Dietz *et al.*, "64  $\mu$  w pulsed terahertz emission from growth optimized InGaAs/InAlAs heterostructures with separated photoconductive and trapping regions," *Applied Physics Letters*, vol. 103, no. 6, p. 061103, 2013.
- [144] M. Steeg, S. Dülme, J. Tebart, T. Neerfeld, V. Rymanov, and A. Stöhr, "Polarization Diversity Photoreceiver Integration on 26 GHz PCB Leaky-Wave Antenna for Photonic Beam Steering Transmitter," in *2019 International Topical Meeting on Microwave Photonics (MWP)*, 2019: IEEE, pp. 1-4.
- [145] A. Pascual *et al.*, "A scalable photomixing array for increased emitted power," in *2019 44th International Conference on Infrared, Millimeter, and Terahertz Waves (IRMMW-THz)*, 2019: IEEE, pp. 1-2.
- [146] A. J. Pascual-Gracia *et al.*, "A Photonically-Excited Leaky-Wave Antenna Array at E-Band for 1-D Beam Steering," *Applied Sciences*, vol. 10, no. 10, p. 3474, 2020.
- [147] P. Stärke, C. Carta, and F. Ellinger, "Direct chip-to-waveguide transition realized with wire bonding for 140–220 GHz G-band," *IEEE Transactions on Terahertz Science and Technology*, vol. 10, no. 3, pp. 302-308, 2020.
- [148] K. M. Leong *et al.*, "A 340–380 GHz integrated CB-CPW-to-waveguide transition for sub millimeter-wave MMIC packaging," vol. 19, no. 6, pp. 413-415, 2009.
- [149] D. Torres, A. Kopa, M. Meinhold, P. Lewis, J. Delisio, and C. Gray, "Microcoaxial Interconnects for Signals, Bias, and Supply of MMICs," in *2019 IEEE MTT-S International Microwave Symposium (IMS)*, 2019: IEEE, pp. 1046-1049.
- [150] D. Pozar, "Considerations for millimeter wave printed antennas," *IEEE Trans. Antennas Propag.*, vol. 31, no. 5, pp. 740-747, Sept. 1983.
- [151] M. Burla *et al.*, "Multiwavelength-integrated optical beamformer based on wavelength division multiplexing for 2-D phased array antennas," *Journal of lightwave technology*, vol. 32, no. 20, pp. 3509-3520, 2014.
- [152] Y. Liu *et al.*, "Ultra-low-loss silicon nitride optical beamforming network for wideband wireless applications," *IEEE Journal of Selected Topics in Quantum Electronics*, vol. 24, no. 4, pp. 1-10, 2018.

- [153] N. Tessema *et al.*, "A tunable Si<sub>3</sub>N<sub>4</sub> integrated true time delay circuit for optically-controlled K-band radio beamformer in satellite communication," *Journal of Lightwave Technology*, vol. 34, no. 20, pp. 4736-4743, 2016.
- [154] P. R. Binetti *et al.*, "InP-based membrane couplers for optical interconnects on Si," *IEEE Photonics Technology Letters*, vol. 21, no. 5, pp. 337-339, 2009.
- [155] X. Xie *et al.*, "High-power and high-speed heterogeneously integrated waveguide-coupled photodiodes on silicon-on-insulator," *Journal of Lightwave Technology*, vol. 34, no. 1, pp. 73-78, 2015.
- [156] H. Park *et al.*, "A hybrid AlGaInAs-silicon evanescent waveguide photodetector," *Optics express*, vol. 15, no. 10, pp. 6044-6052, 2007.
- [157] L. Gounaridis *et al.*, "Design of grating couplers and MMI couplers on the TriPleX platform enabling ultra-compact photonic-based biosensors," *Sensors and Actuators B: Chemical*, vol. 209, pp. 1057-1063, 2015.
- [158] E. Ryckeboer *et al.*, "Silicon-on-insulator spectrometers with integrated GaInAsSb photodiodes for wide-band spectroscopy from 1510 to 2300 nm," *Optics express*, vol. 21, no. 5, pp. 6101-6108, 2013.
- [159] H. Li *et al.*, "Investigation of the chip to photodetector coupler with subwavelength grating on SOI," *Optics & Laser Technology*, vol. 76, pp. 79-84, 2016.
- [160] Y. Shen *et al.*, "Hybrid integration of modified uni-traveling carrier photodiodes on a multi-layer silicon nitride platform using total reflection mirrors," *Optics express*, vol. 25, no. 9, pp. 9521-9527, 2017.
- [161] F. Monticone and A. Alu, "Leaky-wave theory, techniques, and applications: from microwaves to visible frequencies," *Proceedings of the IEEE*, vol. 103, no. 5, pp. 793-821, 2015.
- [162] P. Baccarelli, P. Burghignoli, F. Frezza, A. Galli, and P. Lampariello, "Novel modal properties and relevant scanning behaviors of phased arrays of microstrip leaky-wave antennas," *IEEE Transactions on Antennas and Propagation*, vol. 51, no. 12, pp. 3228-3238, 2003.
- [163] J. James and P. Hall, "Microstrip antennas and arrays. Part 2: New array-design technique," *IEE J. Microwaves, Opt. Acoust.*, vol. 1, no. 5, pp. 175-181, Sept. 1977.
- [164] J. A. Hejase, P. R. Paladhi, and P. P. Chahal, "Terahertz characterization of dielectric substrates for component design and nondestructive evaluation of packages," *IEEE Trans. Compon., Packag., Manuf. Technol.*, vol. 1, no. 11, pp. 1685-1694, Nov. 2011.
- [165] D. M. Pozar, *Microwave Engineering, 3Rd Ed.* Hoboken, NJ, USA: J. WileyS, 2005.
- [166] G. Zheng, J. Papapolymerou, and M. M. Tentzeris, "Wideband coplanar waveguide RF probe pad to microstrip transitions without via holes," *IEEE Microwave and Wireless Components Letters*, vol. 13, no. 12, pp. 544-546, Dec. 2003.
- [167] A. Chahadih, P. Y. Cresson, C. Mismar, and T. Lasri, "V-band via-less GCPW-to-microstrip transition designed on PET flexible substrate using inkjet printing technology," *IEEE Microwave and Wireless Components Letters*, vol. 25, no. 7, pp. 436-438, 2015.
- [168] M. El-Gibari, D. Averty, C. Lupi, M. Brunet, H. Li, and S. Toutain, "Ultra-broad bandwidth and low-loss GCPW-MS transitions on low-k substrates," *Electronics Letters*, vol. 46, no. 13, pp. 931-933, 2010.
- [169] J.-P. Raskin, G. Gauthier, L. P. Katehi, and G. M. Rebeiz, "Mode conversion at

- GCPW-to-microstrip-line transitions," *IEEE Trans. Microwave Theory Tech.*, vol. 48, no. 1, pp. 158-161, Jan. 2000.
- [170] R. Simons, *Coplanar waveguide circuits, components, and systems*. New York, NY, USA: John Wiley & Sons, 2001.
- [171] V. Dragoi, E. Cakmak, and E. Pabo, "Wafer bonding with metal layers for MEMS applications," in *2009 International Semiconductor Conference*, 2009, vol. 1: IEEE, pp. 215-218.
- [172] A. W. Fang *et al.*, "Hybrid silicon evanescent devices," *Mater. Today*, vol. 10, no. 7-8, pp. 28-35, Jul-Aug. 2007.
- [173] M. Taklo, P. Storås, K. Schjølberg-Henriksen, H. Hasting, and H. Jakobsen, "Strong, high-yield and low-temperature thermocompression silicon wafer-level bonding with gold," *Journal of Micromechanics and Microengineering*, vol. 14, no. 7, p. 884, 2004.
- [174] G. Zhang, X. Ang, Z. Chen, C. C. Wong, and J. Wei, "Critical temperatures in thermocompression gold stud bonding," *Journal of Applied Physics*, vol. 102, no. 6, p. 063519, 2007.
- [175] E. Higurashi and T. Suga, "Review of low-temperature bonding technologies and their application in optoelectronic devices," *Electronics and Communications in Japan*, vol. 99, no. 3, pp. 63-71, 2016.
- [176] V. Bezerra, G. Bimonte, G. Klimchitskaya, V. Mostepanenko, and C. Romero, "Thermal correction to the Casimir force, radiative heat transfer, and an experiment," *The European Physical Journal C*, vol. 52, no. 3, pp. 701-720, 2007.
- [177] D. Gall, "Electron mean free path in elemental metals," *Journal of Applied Physics*, vol. 119, no. 8, p. 085101, 2016.
- [178] E. Gadelmawla, M. Koura, T. Maksoud, I. Elewa, and H. Soliman, "Roughness parameters," *J. Mater. Process. Technol.*, vol. 123, no. 1, pp. 133-145, Apr. 2002.
- [179] T. Haddad, C. Biurrun-Quel, P. Lu, H. Kaya, I. Mohammad, and A. Stöhr, "Suppressing Open Stopband for Terahertz Periodic Microstrip Leaky-Wave Antennas," in *2023 17th European Conference on Antennas and Propagation (EuCAP)*, Florence, Italy, 2023, pp. 1-5.
- [180] B. Sievert, J. T. Svejda, D. Erni, and A. Rennings, "Spherical mm-Wave/THz Antenna Measurement System," *IEEE Access*, vol. 8, pp. 89680-89691, 2020.
- [181] M. Steeg, F. Exner, J. Tebart, A. Czyliwik, and A. Stöhr, "100 Gbit/s V-band Transmission Enabled by Coherent Radio-over-Fiber System with IF-OFDM Envelope Detection and SSBI Suppression."
- [182] Z. Li *et al.*, "Direct-detection 16-QAM Nyquist-shaped subcarrier modulation with SSBI mitigation," in *2015 IEEE International Conference on Communications (ICC)*, 2015: IEEE, pp. 5204-5209.
- [183] L. Zhuang, "Flexible RF filter using a nonuniform SCISSOR," *Optics letters*, vol. 41, no. 6, pp. 1118-1121, 2016.
- [184] L. Zhuang *et al.*, "Sub-GHz-resolution C-band Nyquist-filtering interleaver on a high-index-contrast photonic integrated circuit," *Optics express*, vol. 24, no. 6, pp. 5715-5727, 2016.
- [185] C. Taddei *et al.*, "Fully reconfigurable coupled ring resonator-based bandpass filter for microwave signal processing," in *Microwave Photonics (MWP) and the 2014 9th Asia-Pacific Microwave Photonics Conference (APMP) 2014 International Topical Meeting on*, 2014: IEEE, pp. 44-47.
- [186] L. Zhuang, C. G. Roeloffzen, M. Hoekman, K.-J. Boller, and A. J. Lowery,

- "Programmable photonic signal processor chip for radiofrequency applications," *Optica*, vol. 2, no. 10, pp. 854-859, 2015.
- [187] X. Han *et al.*, "Influence of coupling conditions on the time delay characteristics of parallel-cascaded optical waveguide ring resonators," *Optik*, vol. 124, no. 5, pp. 377-384, 2013.
- [188] K. Kolpatzeck, L. Haring, and A. Czyliw, "Phase control in photonicly steered phased array transmitters by optical homodyne detection," in *2016 46th European Microwave Conference (EuMC)*, 2016: IEEE, pp. 1095-1098.
- [189] L. Zhuang *et al.*, "Novel ring resonator-based integrated photonic beamformer for broadband phased array receive antennas—Part II: Experimental prototype," *Journal of lightwave technology*, vol. 28, no. 1, pp. 19-31, 2009.
- [190] <https://www.lumerical.com/customer-success/fraunhofer-hhi/> (accessed on 13. Feb. 2023).
- [191] R. Hui and M. O'Sullivan, "Fundamentals of Optical Devices," in *Fiber-Optic Measurement Techniques*: Academic Press, 2022, ch. 1.
- [192] Y. Shen *et al.*, "Near 100% external quantum efficiency 1550-nm broad spectrum photodetector," *Optics Express*, vol. 30, no. 2, pp. 3047-3054, 2022.
- [193] F. Thome and A. Leuther, "A 75–305-GHz Power Amplifier MMIC With 10–14.9-dBm P out in a 35-nm InGaAs mHEMT Technology," *IEEE Microwave and Wireless Components Letters*, vol. 31, no. 6, pp. 741-743, 2021.
- [194] S. Sinha *et al.*, "Flip-chip approach for 500 GHz broadband interconnects," *IEEE Transactions on Microwave Theory and Techniques*, vol. 65, no. 4, pp. 1215-1225, 2017.
- [195] SANTEC. <https://santec.imgix.net/Files/Datasheets/TSL-570-Datasheet.pdf> (accessed on 17. Juli 2023).
- [196] M. R. Billah *et al.*, "Hybrid integration of silicon photonics circuits and InP lasers by photonic wire bonding," *Optica*, vol. 5, no. 7, pp. 876-883, 2018.
- [197] P. Kumar, M. K. Wiedmann, C. H. Winter, and I. Avrutsky, "Optical properties of Al<sub>2</sub>O<sub>3</sub> thin films grown by atomic layer deposition," *Applied Optics*, vol. 48, no. 28, pp. 5407-5412, 2009.
- [198] Y. Ikku *et al.*, "Al<sub>2</sub>O<sub>3</sub> activated direct wafer bonding for iii–v cmos photonics platform," in *IPRM 2011-23rd International Conference on Indium Phosphide and Related Materials*, 2011: IEEE, pp. 1-4.
- [199] M. Yokoyama *et al.*, "Formation of III–V-on-insulator structures on Si by direct wafer bonding," *Semiconductor science and technology*, vol. 28, no. 9, p. 094009, 2013.
- [200] Y. Li *et al.*, "Room temperature wafer bonding by surface activated ALD-Al<sub>2</sub>O<sub>3</sub>," *ECS Transactions*, vol. 50, no. 7, p. 303, 2013.
- [201] H. K. Sahoo, L. Ottaviano, Y. Zheng, O. Hansen, and K. Yvind, "Low temperature bonding of heterogeneous materials using Al<sub>2</sub>O<sub>3</sub> as an intermediate layer," *Journal of Vacuum Science & Technology B, Nanotechnology and Microelectronics: Materials, Processing, Measurement, and Phenomena*, vol. 36, no. 1, p. 011202, 2018.
- [202] O. Solgaard, *Photonic microsystems: Micro and nanotechnology applied to optical devices and systems*. Springer Science & Business Media, 2009.
- [203] S. Dülme *et al.*, "300 GHz photonic self-mixing imaging-system with vertical illuminated triple-transit-region photodiode terahertz emitters," in *MWP*, Ottawa, Canada, Oct. 7-10, 2019, pp. 1-4.
- [204] S. Krishnamurthy, Z. G. Yu, L. P. Gonzalez, and S. Guha, "Temperature-and wavelength-dependent two-photon and free-carrier absorption in GaAs, InP,

- GaInAs, and InAsP," *Journal of Applied Physics*, vol. 109, no. 3, p. 033102, 2011.
- [205] R. G. Hunsperger, *Integrated optics*. Springer, 1995.
- [206] J.-P. Weber, "Optimization of the carrier-induced effective index change in InGaAsP waveguides-application to tunable Bragg filters," *IEEE Journal of Quantum Electronics*, vol. 30, no. 8, pp. 1801-1816, 1994.
- [207] B. R. Bennett, R. A. Soref, and J. A. Del Alamo, "Carrier-induced change in refractive index of InP, GaAs and InGaAsP," *IEEE Journal of Quantum Electronics*, vol. 26, no. 1, pp. 113-122, 1990.
- [208] T. Suntola and J. Antson, "Method for producing compound thin films," ed: Google Patents, 1977.
- [209] R. L. Puurunen, "Surface chemistry of atomic layer deposition: A case study for the trimethylaluminum/water process," *Journal of applied physics*, vol. 97, no. 12, p. 9, 2005.
- [210] S. M. George, "Atomic layer deposition: an overview," *Chemical reviews*, vol. 110, no. 1, pp. 111-131, 2010.
- [211] S. Heil, J. Van Hemmen, M. Van De Sanden, and W. Kessels, "Reaction mechanisms during plasma-assisted atomic layer deposition of metal oxides: A case study for Al<sub>2</sub>O<sub>3</sub>," *Journal of Applied Physics*, vol. 103, no. 10, p. 103302, 2008.
- [212] T. Weckman and K. Laasonen, "First principles study of the atomic layer deposition of alumina by TMA-H<sub>2</sub>O-process," *Physical Chemistry Chemical Physics*, vol. 17, no. 26, pp. 17322-17334, 2015.
- [213] C. Tan and G. Chong, "Low Temperature Wafer Bonding of Low-κ Carbon-Doped Oxide for Application in 3D Integration," *Electrochemical and Solid-State Letters*, vol. 13, no. 2, p. H27, 2009.
- [214] J. Fan, P. Anantha, C. Liu, M. Bergkvist, H. Wang, and C. S. Tan, "Thermal characteristics of inp-al<sub>2</sub>o<sub>3</sub>/si low temperature heterogeneous direct bonding for photonic device integration," *ECS Journal of Solid State Science and Technology*, vol. 2, no. 9, p. N169, 2013.
- [215] D. Pasquariello and K. Hjort, "Plasma-assisted InP-to-Si low temperature wafer bonding," *IEEE Journal of Selected Topics in Quantum Electronics*, vol. 8, no. 1, pp. 118-131, 2002.
- [216] B. Muller and A. Stoffel, "Tensile strength characterization of low-temperature fusion-bonded silicon wafers," *Journal of Micromechanics and Microengineering*, vol. 1, no. 3, p. 161, 1991.
- [217] K. Neophytou, S. Iezekiel, M. Steeg, and A. Stöhr, "Design of PCB leaky-wave antennas for wide angle beam steering," in *2018 11th German Microwave Conference (GeMiC)*, 2018: IEEE, pp. 152-155.
- [218] Y. Monnai, X. Lu, and K. Sengupta, "Terahertz Beam Steering: from Fundamentals to Applications," *Journal of Infrared, Millimeter, and Terahertz Waves*, vol. 44, no. 3-4, pp. 169-211, 2023.
- [219] M. M. Assefzadeh and A. Babakhani, "Broadband 0.03–1.032 THz signal generation and radiation based on a fully-integrated 4×2 impulse radiating array in 90nm SiGe BiCMOS," in *2016 41st International Conference on Infrared, Millimeter, and Terahertz waves (IRMMW-THz)*, 2016: IEEE, pp. 1-2.
- [220] P. U. Jepsen, D. G. Cooke, and M. Koch, "Terahertz spectroscopy and imaging—Modern techniques and applications," *Laser & Photonics Reviews*, vol. 5, no. 1, pp. 124-166, 2011.



## List of publications

### Journal publications

1. A. Bhutani, M. Kretschmann, J. Dittmer, **P. Lu**, A. Stöhr, and T. Zwick, "A 220 GHz to 325 GHz Grounded Coplanar Waveguide Based Periodic Leaky-Wave Beam-Steering Antenna in Indium Phosphide Process," *Electronics*, vol. 12, no. 6, pp 3482, 2023.
2. M. Grzeslo, S. Dülme, S. Clochiatti, T. Neerfeld, T. Haddad, **P. Lu**, J. Tebart, S. Makhlof, C. Biurrun-quel, J. L. Fernández Estévez, J. Lackmann, N. Weimann, and A. Stöhr, "High saturation photocurrent THz waveguide type MUTC-photodiodes reaching mW output power within the WR3.4 band," *Optics Express*, vol. 31, no. 4, pp. 6484-6498, 2023.
3. **P. Lu**, T. Haddad, J. Tebart, C. Roeloffzen, and A. Stöhr, "Photonic Integrated Circuit for Optical Phase Control of  $1 \times 4$  Terahertz Phased Arrays," *Photonics*, vol. 9, no. 12: 902, November 2022.
4. T. Haddad, C. Biurrun-Quel, **P. Lu**, J. Tebart, B. Sievert, S. Makhlof, M. Grzeslo, J. Teniente, C. Del-Río, and A. Stöhr, "Photonic-assisted 2-D Terahertz Beam Steering Enabled by a LWA Array Monolithically Integrated with a BFN," *Optics Express*, vol. 30, no. 21, pp. 38596-38612, October 2022.
5. **P. Lu**, T. Haddad, J. Tebart, M. Steeg, B. Sievert, J. Lackmann, A. Rennings, and A. Stöhr, "Mobile THz Communications using Photonic Assisted Beam Steering Leaky-wave Antennas," *Optics Express*, vol. 29, no. 14, pp. 21629-21638, July 2021.
6. **P. Lu**, T. Haddad, B. Sievert, B. Khani, S. Makhlof, S. Dülme, J. F. Estévez, A. Rennings, D. Erni, U. Pfeiffer, and A. Stöhr, "InP-based THz Beam Steering Leaky-wave Antenna," *IEEE Transactions on Terahertz Science and Technology*, vol. 11, no. 2, pp. 218-230, March 2021.
7. S. Makhlof, M. Steeg, T. Haddad, J. Tebart, S. Dülme, M. Grzeslo, **P. Lu**, J. L. F. Estevez, S. Malz, U. R. Pfeiffer, and A. Stöhr, "Novel 3-D Multilayer Terahertz Packaging Technology for Integrating Photodiodes Arrays and Rectangular Waveguide-Power Combiners," *IEEE Transactions on Microwave Theory and Techniques*, vol. 68, no. 11, pp. 4611-4619, September 2020.
8. V. Rymanov, B. Khani, S. Dülme, **P. Lu**, and A. Stöhr, "InP-based Waveguide Triple Transit Region Photodiodes for Hybrid Integration with Passive Optical Silica Waveguides," *Photonics*, vol. 2, no. 4, pp. 1152-1163, December 2015.

### Conference contributions

1. T. Haddad, J. Tebart, I. Mohammad, **P. Lu**, S. Makhlof, and A. Stöhr, "Recent Developments of Photonic Integrated Chips for THz Beamsteering", in *European Conference on Optical Communication (ECOC) 2023*, Glasgow, UK, October, 2023, pp. 1-4. (*invited paper*)
2. M. Kretschmann, A. Bhutani, **P. Lu**, A. Stöhr, and T. Zwick, "THz Dielectric Resonator Antenna with Rectangular Waveguide Slot Feed", in *26th edition of the European Microwave Week (EuMW 2023)*, Berlin, Germany, September

- 2023, pp. 1-4.
3. J. Tebart, J. Dittmer, T. Haddad, **P. Lu**, Sebastian Randel, and A. Stöhr, "Mobile 6G Communications at THz Frequencies Enabled by Leaky-wave Antenna Beam Steering", in *26th edition of the European Microwave Week (EuMW 2023)*, Berlin, Germany, September 2023, pp. 1-4.
  4. J. Tebart, **P. Lu**, T. Haddad, S. Iwamatsu, and A. Stöhr, "Prospects and Technologies for Mobile Terahertz 6G Communications," in *Optical Fiber Communication Conference*, San Diego, USA, March 2023, pp. 1-3. (*invited paper*)
  5. T. Haddad, C. Biurrun-Quel, **P. Lu**, H. Kaya, I. Mohammad, and A. Stöhr, "Suppressing Open Stopband for Terahertz Periodic Microstrip Leaky-Wave Antennas," in *2023 17th European Conference on Antennas and Propagation (EuCAP)*, Florence, Italy, March 2023, pp. 1-5.
  6. C. Preuss, E. Mutlu, R. Kress, S. Clochiatti, **P. Lu**, A. Stöhr, W. Prost, and N. Weimann, "FR4 Test Board for Measurements on InP Resonant Tunneling Diode THz Oscillators Integrated via Flip Chip Bonding Technology," in *2022 15th UK-Europe-China Workshop on Millimetre-Waves and Terahertz Technologies (UCMMT)*, Tønsberg, Norway, December 2022, pp. 1-3.
  7. **P. Lu**, T. Haddad, J. Tebart, and A. Stöhr, "Photonic Integrated Chips for THz Beam Steering," in *Asia Communications and Photonics Conference 2021*, Shanghai, China, October 2021, pp. 1-3. (*invited paper*)
  8. J. Tebart, **P. Lu**, T. Haddad, S. Iwamatsu, J. Lackmann, J. L. Fernandez-Estévez, and A. Stöhr, "Mobile Terahertz 6G Communications Enabled by Integrated Photonic-Assisted Beam Steering Antennas," in *Conference proceedings of the 2021 European Conference on Optical Communication (ECOC)*, Bordeaux, France, September 2021, pp. 13-16.
  9. **P. Lu**, T. Haddad, J. Tebart, and A. Stöhr, "Integrated Photonic Front Ends for Short-Range Mobile THz Communications," in *XXXIV General Assembly and Scientific Symposium of the International Union of Radio Science*, Rome, Italy, August 2021, pp. 1.
  10. M. M. Aller, **P. Lu**, V. Rymanov, A. Stöhr, and S. Preu, "Side-illuminated Fully Ballistic p-i-n Diode-based Photomixer at 1550 nm," in *2020 45th International Conference on Infrared, Millimeter, and Terahertz Waves*, Buffalo, USA, November 2020, pp. 1-2.
  11. **P. Lu**, T. Haddad, J. Tebart, B. Sievert, A. Rennings, and A. Stöhr, "THz Beam Steering with InP-based Leaky-Wave Antenna," in *2020 45th International Conference on Infrared, Millimeter, and Terahertz Waves*, Buffalo, USA, November 2020, pp. 1-2.
  12. S. Dülme, V. Cherniak, K. Kaya, **P. Lu**, J. Tebart, M. Grzeslo, J.L. Fernández-Estévez, T. Haddad, I. Appiagyei, and A. Stöhr, "Two-port Slot Bowtie Antenna with Monolithically Integrated Photodiodes for THz Power Combining," in *2020 45th International Conference on Infrared, Millimeter, and Terahertz Waves*, Buffalo, USA, November 2020, pp. 1-2.
  13. A. Stöhr, **P. Lu**, T. Haddad, M. Steeg, J. Tebart, B. Sievert, A. Rennings, M. Hofmann, S. Dülme, K. Kolpatzek, and A. Czulwik, "Microwave Photonic mm-Wave & THz Beam Steering for Imaging, Radar and Communications," in

- 2019 *Asia Communications and Photonics Conference*, Chengdu, China, November 2019, pp. 1-3. (*invited paper*)
14. S. Dülme, M. Grzeslo, J. Morgan, M. Steeg, M. Lange, J. Tebart, N. Schriniski, I. Mohammad, T. Neerfeld, **P. Lu**, A. Beling, and A. Stöhr, "300 GHz Photonic Self-Mixing Imaging-System with vertical illuminated Triple-Transit-Region Photodiode Terahertz Emitters," in *2019 International Topical Meeting on Microwave Photonics*, Ottawa, Canada, October 2019, pp. 1-4.
  15. **P. Lu**, M. Steeg, T. Haddad, K. Neophytou, S. Makhlouf, S. Dülme, M. Grzeslo, V. Rymanov, and A. Stöhr, "Photonic Integrated Chips for Millimeter-Wave and THz Beam Steering Antennas," in *2019 21st International Conference on Transparent Optical Networks*, Angers, France, July 2019, pp. 1-4. (*invited paper*)
  16. M. Steeg, **P. Lu**, J. Tebart, and A. Stöhr, "2D mm-Wave Beam Steering via Optical True-Time Delay and Leaky-Wave Antennas," in *2019 12th German Microwave Conference*, Stuttgart, Germany, March 2019, pp. 158-161.
  17. S. Dülme, N. Schriniski, M. Steeg, **P. Lu**, B. Khani, C. Brenner, M. R. Hofmann, and A. Stöhr, "Phase Delay of Terahertz Fabry-Perot Resonator characterized by a Photonic Two-Tone Spectroscopy System with Self-Heterodyne Receiver," in *2018 43rd International Conference on Infrared, Millimeter, and Terahertz Waves*, Nagoya, Japan, September 2018, pp. 1-2.
  18. **P. Lu**, M. Steeg, K. Kolpatzck, S. Dülme, B. Khani, A. Czulwik, and A. Stöhr, "Photonic Assisted Beam Steering for Millimeter-Wave and THz Antennas," in *2018 IEEE Conference on Antenna Measurements & Applications*, Västerås, Sweden, September 2018, pp. 1-4. (*invited paper*)
  19. S. Dülme, N. Schriniski, B. Khani, **P. Lu**, V. Rymanov, A. Stöhr, C. Brenner, and M. R. Hofmann, "Compact Optoelectronic THz Frequency Domain Spectroscopy System for Refractive Index Determination based on Fabry-Perot Effect," in *2018 First International Workshop on Mobile Terahertz Systems*, Duisburg, Germany, July 2018, pp. 1-5.
  20. S. Dülme, B. Khani, V. Rymanov, **P. Lu**, and A. Stöhr, "Terahertz Near Field Coupling for Integrating III-V Photodiodes on Silicon," in *2018 11th German Microwave Conference*, Freiburg, Germany, March 2018, pp. 275-278.
  21. V. Rymanov, **P. Lu**, S. Dülme, and A. Stöhr, "Lens-assisted Quasi-optical THz Transmitter Employing Antenna-integrated Triple Transit Region Photodiodes," in *2017 International Topical Meeting on Microwave Photonics*, Beijing, China, October 2017, pp. 1-4.
  22. **P. Lu**, V. Rymanov, S. Dülme, B. Sievert, A. Rennings, and A. Stöhr, "THz Beam Forming and Beam Switching using Lens-assisted Quasi-optical THz Transmitter," in *2017 International Topical Meeting on Microwave Photonics*, Beijing, China, October 2017, pp. 1-4.



## Self-declaration

I have informed the co-authors that I have incorporated the following three publications into this cumulative dissertation. This decision does not restrict their rights to utilize the same publications in their own cumulative dissertations.

- P. Lu, T. Haddad, B. Sievert, B. Khani, S. Makhlouf, S. Dülme, J. F. Estévez, A. Rennings, D. Erni, U. Pfeiffer, and A. Stöhr, "InP-based THz Beam Steering Leaky-wave Antenna," *IEEE Transactions on Terahertz Science and Technology*, vol. 11, no. 2, pp. 218-230 March 2021, doi: [10.1109/TTHZ.2020.3039460](https://doi.org/10.1109/TTHZ.2020.3039460).
- P. Lu, T. Haddad, J. Tebart, M. Steeg, B. Sievert, J. Lackmann, A. Rennings, and A. Stöhr, "Mobile THz Communications using Photonic Assisted Beam Steering Leaky-wave Antennas," *Optics Express*, vol. 29, no. 14, pp. 21629-21638, July 2021, doi: [10.1364/OE.427575](https://doi.org/10.1364/OE.427575).
- P. Lu, T. Haddad, J. Tebart, C. Roeloffzen, and A. Stöhr, "Photonic Integrated Circuit for Optical Phase Control of  $1 \times 4$  Terahertz Phased Arrays," *Photonics*, vol. 9, no. 12: 902, November 2022, doi: [10.3390/photonics9120902](https://doi.org/10.3390/photonics9120902).



## Co-authorship statement

The co-author contributions for the three publications presented in this thesis are as follows. These publications have not been used for any other doctoral or qualification procedure.

P. Lu, T. Haddad, B. Sievert, B. Khani, S. Makhoulf, S. Dülme, J. F. Estévez, A. Rennings, D. Erni, U. Pfeiffer, and A. Stöhr, "InP-based THz Beam Steering Leaky-wave Antenna," *IEEE Transactions on Terahertz Science and Technology*, vol. 11, no. 2, pp. 218-230 March 2021, doi: [10.1109/TTHZ.2020.3039460](https://doi.org/10.1109/TTHZ.2020.3039460). (This work is licensed under a [Creative Commons License](https://creativecommons.org/licenses/by/4.0/))

Author	Affiliation and Contact Details	Contribution
M. Sc. Peng Lu	Department of Optoelectronics, University of Duisburg-Essen Lotharstr. 55, 47057 Duisburg, Germany	Conceptualization, Data curation, Formal analysis, Investigation, Methodology, Resources, Validation, Visualization, Writing - original draft, Writing - review & editing.
M. Sc. Thomas Haddad	Department of Optoelectronics, University of Duisburg-Essen Lotharstr. 55, 47057 Duisburg, Germany	Data curation, Formal analysis, Methodology, Validation, Visualization, Writing - original draft, Writing - review & editing.
M. Sc. Benedikt Sievert	Department of General and Theoretical Electrical Engineering, University of Duisburg-Essen Bismarckstraße 81, 47057 Duisburg, Germany	Data curation, Investigation, Resources, Writing - review & editing.
M. Sc. Beshar Khani	NTT Germany AG & Co. KG Horexstraße 7, 61352 Bad Homburg vor der Höhe, Germany	Writing - review & editing.
M. Sc. Sumer Makhoulf	Department of Optoelectronics, University of Duisburg-Essen Lotharstr. 55, 47057 Duisburg, Germany	Writing - review & editing.
M. Sc. Sebastian Dülme	Radiometer Physics GmbH Werner-von-Siemens-Str. 4, 53340 Meckenheim, Germany	Writing - review & editing.

José Fernández Estévez	Department of Optoelectronics, University of Duisburg-Essen Lotharstr. 55, 47057 Duisburg, Germany	Investigation.
Dr. Andreas Rennings	Department of General and Theoretical Electrical Engineering, University of Duisburg-Essen Bismarckstraße 81, 47057 Duisburg, Germany	Resources, Writing - review & editing.
Prof. Dr. Daniel Erni	Department of General and Theoretical Electrical Engineering, University of Duisburg-Essen Bismarckstraße 81, 47057 Duisburg, Germany	Resources, Writing - review & editing.
Prof. Dr. Ullrich Pfeiffer	Institute for High-frequency and Communication Technology, University of Wuppertal Rainer-Gruenter-Str. 21, 42119 Wuppertal, Germany	Resources, Writing - review & editing.
Prof. Dr. Andreas Stöhr	Department of Optoelectronics, University of Duisburg-Essen Lotharstr. 55, 47057 Duisburg, Germany	Conceptualization, Funding acquisition, Project administration, Supervision, Writing - review & editing.

P. Lu, T. Haddad, J. Tebart, M. Steeg, B. Sievert, J. Lackmann, A. Rennings, and A. Stöhr, "Mobile THz Communications using Photonic Assisted Beam Steering Leaky-wave Antennas," *Optics Express*, vol. 29, no. 14, pp. 21629-21638, July 2021, doi: [10.1364/OE.427575](https://doi.org/10.1364/OE.427575). (© 2021 Optical Society of America under the terms of the [OSA Open Access Publishing Agreement](#))

<b>Author</b>	<b>Affiliation and Contact Details</b>	<b>Contribution</b>
M. Sc. Peng Lu	Department of Optoelectronics, University of Duisburg-Essen Lotharstr. 55, 47057 Duisburg, Germany	Conceptualization, Data curation, Formal analysis, Investigation, Methodology, Resources, Validation, Visualization, Writing - original draft, Writing - review & editing.
M. Sc. Thomas Haddad	Department of Optoelectronics, University of Duisburg-Essen Lotharstr. 55, 47057 Duisburg, Germany	Investigation, Writing - review & editing.
M. Sc. Jonas Tebart	Department of Optoelectronics, University of Duisburg-Essen Lotharstr. 55, 47057 Duisburg, Germany	Conceptualization, Investigation, Resources, Validation, Writing - original draft, Writing - review & editing.
Dr. Matthias Steeg	trinamiX GmbH Industriestraße 35, 67063 Ludwigshafen am Rhein, Germany	Investigation.
M. Sc. Benedikt Sievert	Department of General and Theoretical Electrical Engineering, University of Duisburg-Essen Bismarckstraße 81, 47057 Duisburg, Germany	Data curation, Investigation, Resources.
Dr. Jörg Lackmann	Department of Optoelectronics, University of Duisburg-Essen Lotharstr. 55, 47057 Duisburg, Germany	Resources.
Dr. Andreas Rennings	Department of General and Theoretical Electrical Engineering, University of Duisburg-Essen Bismarckstraße 81, 47057 Duisburg, Germany	Resources.
Prof. Dr. Andreas Stöhr	Department of Optoelectronics, University of Duisburg-Essen	Conceptualization, Funding acquisition, Project administration,

	Lotharstr. 55, 47057 Duisburg, Germany	Supervision, Writing - review & editing.
--	---	---

P. Lu, T. Haddad, J. Tebart, C. Roeloffzen, and A. Stöhr, "Photonic Integrated Circuit for Optical Phase Control of  $1 \times 4$  Terahertz Phased Arrays," *Photonics*, vol. 9, no. 12: 902, November 2022, doi: [10.3390/photonics9120902](https://doi.org/10.3390/photonics9120902). (© 2022 by the authors. Licensee MDPI, Basel, Switzerland. This article is an open access article distributed under the terms and conditions of the Creative Commons Attribution (CC BY) license (<https://creativecommons.org/licenses/by/4.0/>.)

Author	Affiliation and Contact Details	Contribution
M. Sc. Peng Lu	Department of Optoelectronics, University of Duisburg-Essen Lotharstr. 55, 47057 Duisburg, Germany	Conceptualization, Data curation, Formal analysis, Investigation, Methodology, Resources, Validation, Visualization, Writing - original draft, Writing - review & editing.
M. Sc. Thomas Haddad	Department of Optoelectronics, University of Duisburg-Essen Lotharstr. 55, 47057 Duisburg, Germany	Data curation, Resources, Software, Visualization, Writing - review & editing.
M. Sc. Jonas Tebart	Department of Optoelectronics, University of Duisburg-Essen Lotharstr. 55, 47057 Duisburg, Germany	Resources, Writing - review & editing.
Dr. Chris Roeloffzen	LioniX International BV, Hengelosestraat 500, 7521 AN Enschede, Netherlands	Methodology, Writing - review & editing.
Prof. Dr. Andreas Stöhr	Department of Optoelectronics, University of Duisburg-Essen Lotharstr. 55, 47057 Duisburg, Germany	Conceptualization, Funding acquisition, Project administration, Supervision, Writing - review & editing.

# InP-Based THz Beam Steering Leaky-Wave Antenna

Peng Lu , Thomas Haddad , *Graduate Student Member, IEEE*, Benedikt Sievert , Beshar Khani , Sumer Makhlof , Sebastian Dülme , José Fernández Estévez, Andreas Rennings , *Member, IEEE*, Daniel Erni , *Member, IEEE*, Ullrich Pfeiffer , *Fellow, IEEE*, and Andreas Stöhr, *Senior Member, IEEE*

**Abstract**—For mobile THz applications, integrated beam steering THz transmitters are essential. Beam steering approaches using leaky-wave antennas (LWAs) are attractive in that regard since they do not require complex feeding control circuits and beam steering is simply accomplished by sweeping the operating frequency. To date, only a few THz LWAs have been reported. These LWAs are based on polymer or graphene substrates and thus, it is quite impossible to monolithically integrate these antennas with state-of-the-art indium phosphide (InP)-based photonic or electronic THz sources and receivers. Therefore, in this article, we report on an InP-based THz LWA for the first time. The developed and fabricated THz LWA consists of a periodic leaking microstrip line integrated with a grounded coplanar waveguide to microstrip line (GCPW-MSL) transition for future integration with InP-based photodiodes. For fabrication, a substrate-transfer process using silicon as carrier substrate for a 50- $\mu\text{m}$  thin InP THz antenna chip has been established. By changing the operating frequency from 230 to 330 GHz, the fabricated antenna allows to sweep the beam direction quasi-linearly from  $-46^\circ$  to  $42^\circ$ , i.e., the total scanning angle is  $88^\circ$ . The measured average realized gain and 3-dB beam width of a 1.5-mm wide InP LWA are  $\sim 11$  dBi and  $10^\circ$ . This article furthermore discusses the use of the fabricated LWA for THz interconnects.

**Index Terms**—Beam steering, indium phosphide (InP), leaky-wave antenna (LWA), monolithic integrated circuits, wafer bonding.

## I. INTRODUCTION

**T**ERAHERTZ (THz) waves feature distinct advantages compared to its neighboring spectra, making this frequency spectrum (0.1–10 THz) very attractive for several applications.

Manuscript received July 11, 2020; revised September 23, 2020; accepted October 26, 2020. Date of publication November 19, 2020; date of current version March 3, 2021. This work was supported by the Deutsche Forschungsgemeinschaft (DFG, German Research Foundation) under Project-ID 287022738 – TRR 196. (*Corresponding author: Peng Lu.*)

Peng Lu, Thomas Haddad, Sumer Makhlof, Sebastian Dülme, José Fernández Estévez, and Andreas Stöhr are with the Department of Optoelectronics, University of Duisburg-Essen, 47057 Duisburg, Germany (e-mail: peng.lu@uni-due.de; thomas.haddad@uni-due.de; sumer.makhlof@uni-due.de; sebastian.duelme@uni-due.de; jose.fernandez-estevez@uni-due.de; andreas.stoehr@uni-due.de).

Beshar Khani is with the NTT Germany AG & Co. KG, 61352 Bad Homburg vor der Höhe, Germany (e-mail: beshar.khani@uni-due.de).

Benedikt Sievert, Andreas Rennings, and Daniel Erni are with the Department of General and Theoretical Electrical Engineering, University of Duisburg-Essen, 47057 Duisburg, Germany (e-mail: benedikt.sievert@uni-due.de; andre.rennings@uni-due.de; daniel.erni@uni-due.de).

Ullrich Pfeiffer is with the Institute for High-frequency and Communication Technology, University of Wuppertal, 42119 Wuppertal, Germany (e-mail: ullrich.pfeiffer@uni-wuppertal.de).

Color versions of one or more of the figures in this article are available online at doi.org/10.1109/TTHZ.2020.3039460.

Digital Object Identifier 10.1109/TTHZ.2020.3039460

THz waves are far less energetic than X-rays, i.e., they are nonionizing for biological tissues and, consequently, are promising for several medical applications [1]–[4]. Benefiting from the shorter wavelength in contrast to microwaves, THz waves offer a much higher spatial resolution, which makes them quite intriguing for high-resolution imaging applications [5], [6]. Beyond the high spatial resolution, most dry dielectric materials are transparent for THz waves, whereas materials with high electrical conductivity or with large static dipoles (i.e., metals and water) are strong reflectors or absorbers for THz waves. This leads to high image contrasts [7], [8]. In addition, THz spectroscopy systems have received much attention, benefiting from the unique fingerprint spectra of various chemical compounds [9], [10]. Not the least, in comparison to the scarce available spectrum in the microwave region, THz waves offer a much wider available bandwidth which is crucial for future high data-rate wireless communications [11]–[13] and short-range THz interconnects [14]. Reconfigurable short-range high data rate THz interconnects would be very beneficial, e.g., for data centers and even for intramachine communications.

The above-mentioned applications have stimulated technological advances mainly focusing on the development of THz sources and THz receivers with higher transmit power levels and better sensitivities [15]–[17]. However, despite the fact that there have been great achievements in that regard, high-gain THz antennas and THz beam steering technologies are still essential for many applications, such as THz interconnects, to overcome the comparably high THz free-space path loss (FSPL). This is on the one hand to relax requirements of the employed THz transmitter and THz receiver but moreover to enable mobility and spatial multiplexing.

In the recent past, different THz beam steering approaches have been investigated, including, for instance, microelectromechanical systems (MEMS) enhancing the scanning-speed and precision compared to classical mechanical approaches [18]. Also, several electronic approaches such as phased-array transmitter [19], electronically controlled metasurfaces based on  $\text{VO}_2$  [20], or graphene reflect arrays [21] have been studied. Also, photonic beam steering approaches have attracted much attention. This is because photonics offers some key generic advantages with respect to beam steering, which include a wide operational bandwidth, the availability of low phase noise sources, and a compact chip size [22], [23]. Furthermore, it is possible to transfer phase shifts and even true time delays performed in the infrared domain to the THz regime for beam steering. By means of an  $1 \times 4$  photomixer array and fiber-optic

delay lines, 1-D beam steering within an angle of  $35^\circ$  at 600 GHz has been realized [24]. In [25], the THz beam has been steered with a maximum angle of  $29^\circ$  by using an array of photoconductive antennas (PCAs) and a free-space optical phase shifter approach. However, the complex optical phase shifters required in both cases prevent monolithic photonic integration.

Leaky-wave antennas (LWAs) do not require such complex phase shifter or true time delay feeders since here, beam steering is achieved by tuning the carrier frequency [26]. Thus, THz LWAs are envisaged to be an attractive solution for applications such as THz interconnects which necessitate robust and highly integrated THz beam steering antennas. This in turn requires that the THz LWA can be integrated with state-of-the-art photonic or electronic sources and receivers.

In previous works, some first THz LWAs have already been realized. In [27], a THz LWA based upon a metamaterial waveguide with a quantum cascade laser (QCL) is reported. A microstrip periodic LWA based on polymer substrate fed by a vector network analyzer (VNA) is shown in [28]. The disadvantage of these approaches is that the developed LWAs could not be monolithically integrated with state-of-the-art chip-sized photonic or electronic THz sources and receivers, which are typically based upon indium phosphide (InP) substrate. For photonics, this is to enable the use of mature  $1.55\ \mu\text{m}$  IR laser diodes, modulators, and amplifiers and for electronics, this is because InP transistors offer the highest maximum oscillation frequencies and transit frequencies [29], [30]. For 26 GHz 5G band and E band, several LWAs based upon low-permittivity substrates have been hybrid integrated with InP photodiodes using wire bonding [31]–[33]. However, at THz frequencies, wire bonding will lead to high losses [34], [35]. Therefore, we here propose the use of THz LWAs based upon InP substrate for future monolithic and low-loss integration with THz photodiodes.

In this work, we report on an InP-based THz beam steering LWA. The design of the fabricated InP THz LWA studied in this work is motivated by future integration with InP THz photodiodes to realize monolithically integrated robust beam steering THz transmitter chips. To our knowledge, this is the first InP-based THz beam steering LWA. The target applications we focus at are short-range THz communications, i.e., THz interconnects and THz image scanner. For THz interconnects, the targets are to achieve an antenna realized gain and a coherence bandwidth of at least 10 dBi and 10 GHz, respectively. Given the output power of THz photodiodes which is about  $-20\ \text{dBm}$  at 300 GHz and considering further the free-space path loss, atmospheric attenuation, THz envelope receiver sensitivity, and required SNR, such antennas are expected to support data rates of at least 10 Gb/s over 30 cm using QPSK modulation [13]. The maximum beam steering angle is mainly defined by the permittivity of the antenna's substrate [36]. For InP, a scanning angle around  $90^\circ$  for a full-band WR3 band THz LWA antenna is expected. This will be further discussed in Section III.

In detail, we report on a microstrip-type InP LWA for the 0.3-THz WR3 waveguide band. The THz LWA is designed using CST Studio Suite. To enable future integration with triple-transit-region photodiodes (TTR-PDs), the LWA features a grounded coplanar waveguide to microstrip line (GCPW-MSL)

THz transition whose design is also novel to our knowledge. To reduce the number of surface wave modes and thus, increase the radiation efficiency of the THz LWA, a silicon (Si) substrate-transfer process has been developed to enable fabrication of the THz LWA on a  $50\text{-}\mu\text{m}$  thin grounded InP substrate. We also created an on-wafer antenna measurement system for characterizing the radiated THz beam in the far-field.

The manuscript is organized as follows. In Section II, the motivation for developing integrated InP-based photonic THz beam steering transmitter chips is discussed. Section III reports on the designs of the InP THz LWA and the InP GCPW-MSL THz transition. The developed substrate-transfer fabrication process is described in Section IV. Section V presents the experimentally determined THz scattering parameters, the measured THz beam profiles, and the THz scanning angles. The experimental findings are also compared with the simulated performances. Finally, in Section VI, we discuss the potential of using the developed LWA for THz interconnects.

## II. CONCEPT OF A PHOTONIC INTEGRATED THz TRANSMITTER

As mentioned above, first THz LWAs were demonstrated in [27] and [28]. However, these approaches required liquid-nitrogen cooling or used bulky VNAs with THz extenders as signal sources. An InP-based THz LWA is quite attractive because it would enable monolithic integration with InP-based THz photodiodes and room temperature operation. Today, THz photodiodes offer reasonably high output power, typically reaching several  $10\ \mu\text{W}$  @ 0.3 THz [37], [38]. This opens the potential for a photonic integrated circuit (PIC) consisting of an InP-based photodiode monolithically integrated with a THz LWA to create a THz beam steering transmitter chip. Even monolithic integration of  $1.55\ \mu\text{m}$  laser diodes can be envisaged.

The high permittivity and low loss tangent of InP contribute to reducing the overall antenna dimensions and losses in the InP substrate [39], [40]. In addition, the higher permittivity of InP as compared to low-permittivity substrates such as polymers, leads to a smaller period of LWA unit cells, which results in an increase of the beam-scanning angle [36].

When using InP as substrate material for the antenna, the substrate thickness becomes one of the most crucial design parameters as it defines the number of surface wave modes in the substrate which have a strong impact on the LWA performance [41]. A thick substrate would lead to more bounded surface wave modes which cannot be radiated along the LWA and thus, cause a degradation of the radiation efficiency [42]. Here, a  $50\text{-}\mu\text{m}$  thin InP substrate is used for antenna fabrication. This in turn necessitates the use of a mechanical carrier substrate.

A schematic view of the proposed photonic THz beam steering transmitter chip based upon the above considerations is illustrated in Fig. 1. A Si substrate is used as the carrier for the InP-based THz photodiode and LWA. An Au layer is utilized as bonding layer and functions as ground plane for the THz LWA. For fabrication, the InP substrate is bonded on the Si substrate using thermocompression bonding (TCB). Epitaxial layers of photodiodes will be grown on the grinded and polished InP substrate. After that, photodiodes and antennas will be

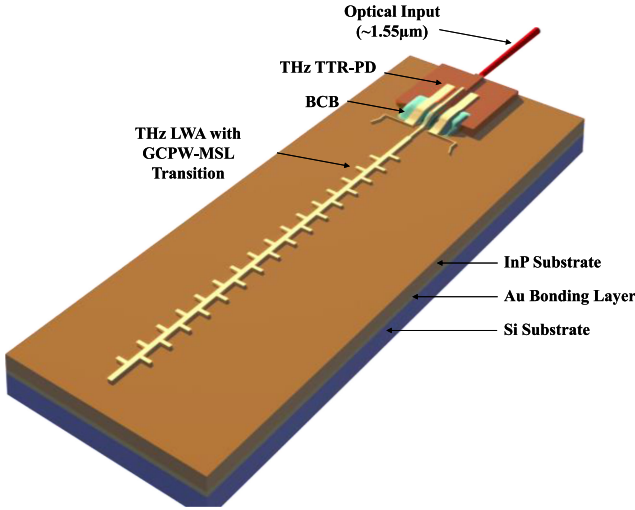


Fig. 1. Conceptual image of a THz microstrip periodic LWA with an on-chip integrated TTR-PD on an InP-to-Si bonded wafer.

fabricated using standard lithography technology. For connecting the photodiode with the LWA, a GCPW-MSL transition is required and BCB is used as a passivation layer to avoid short circuits between the p- and n-contacts of the PD (see also Fig. 1). BCB also functions as a planarization layer, helping to avoid breakage of the metallic signal and ground transmission lines.

### III. THZ LWA AND GCPW-MSL TRANSITION DESIGN

#### A. LWA Design

For the microwave frequency region, different LWA topologies have been studied, including rectangular waveguides [43], [44], substrate integrated waveguides (SIWs) [26], [45]–[47], or coplanar waveguides (CPWs) [48], [49]. However, for the THz frequency region, open guided-wave structures are preferred because of the lower transmission loss [50]. Microstrip LWAs featuring open guided-wave structures have been intensively investigated due to the simple fabrication process, lightweight, and better integration with active sources [28], [51], [52]. Therefore, we develop a THz LWA based on microstrip line in this work. To facilitate the integration with THz photodiodes that usually feature a GCPW output, an additional GCPW-MSL transition is needed. The resulting layout of the developed THz LWA with the integrated GCPW-MSL transition is shown in Fig. 2.

For future monolithic integration of the microstrip LWA with our InP-based 300 GHz TTR-PDs, the LWA's input impedance is designed to be similar to the impedance of the TTR-PDs, which is around  $35 \Omega$ . There are several models to mathematically analyze the input impedance of a microstrip [53]–[55]. In this work, we use the model described in [55], where the characteristic impedance  $Z_0$  is a function of microstrip width  $w$ , relative permittivity of InP substrate  $\epsilon_r$  ( $\epsilon_r \approx 12.4$  [40]), and substrate thickness  $h$  as defined in (1) and (2) in the following:

$$\frac{w}{h} = \frac{8e^A}{e^{2A} - 2} \text{ for } \frac{w}{h} < 2 \quad (1)$$

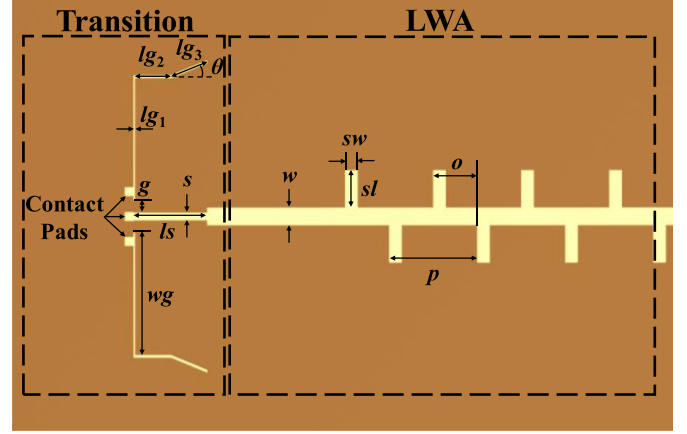


Fig. 2. Schematic top view of the microstrip periodic LWA with a GCPW-MSL transition on an InP-to-Si bonded wafer.

with the parameter  $A$

$$A = \frac{Z_0}{60} \sqrt{\frac{\epsilon_r + 1}{2}} + \frac{\epsilon_r - 1}{\epsilon_r + 1} \left( 0.23 + \frac{0.11}{\epsilon_r} \right). \quad (2)$$

Here,  $w/h$  is equal to 1.4691, i.e.,  $w/h < 2$ , and thus, according to the model, the width of the microstrip should be  $w = 73.46 \mu\text{m}$ . By computational electromagnetics simulations using CST Studio Suite, we finally found the optimum width to be  $w = 70 \mu\text{m}$ .

In a simple straight MSL, the quasi-TEM mode would not be radiated, because the phase constant  $\beta$  of the quasi-TEM mode is larger than the free-space wavenumber  $k_0$ . In other words, the dominant mode in a straight MSL is a slow wave. To make the dominant mode a fast wave, i.e., a mode that is radiated, we utilize 32 periodic rectangular stubs as comb-lines on both sides of the microstrip. This design creates an infinite number of space harmonics with the phase constants  $\beta_n$  [42]

$$\beta_n = \beta_0 + \frac{2n\pi}{p} \quad (3)$$

where  $p$  is the period and  $\beta_0$  is phase constant of the fundamental space harmonic. To achieve a single beam radiation, LWAs are designed to ensure a unitary fast space harmonic ( $n = -1$ ) [42]. The period  $p$  between stubs is equal to the guided wavelength  $\lambda_g$  [52], which can be calculated through [55]

$$\lambda_g = \frac{c_0}{f\sqrt{\epsilon_{\text{eff}}}} \quad (4)$$

where  $f$  is the operating frequency of the antennas. In this work, the LWA is designed for 230 to 330 GHz operation with a center frequency  $f = 280$  GHz. The effective permittivity of the microstrip line on the  $50\text{-}\mu\text{m}$  thick InP-substrate can be calculated using [55]

$$\epsilon_{\text{eff}} = \frac{\epsilon_r + 1}{2} + \frac{\epsilon_r - 1}{2\sqrt{1 + \frac{12h}{w}}} \text{ for } w/h > 1. \quad (5)$$

This results in an effective permittivity of  $\epsilon_{\text{eff}} = 8.56$ . Thus, according to the model and (5), the period should be  $p = 366 \mu\text{m}$ . By means of CST Studio Suite, we then found the

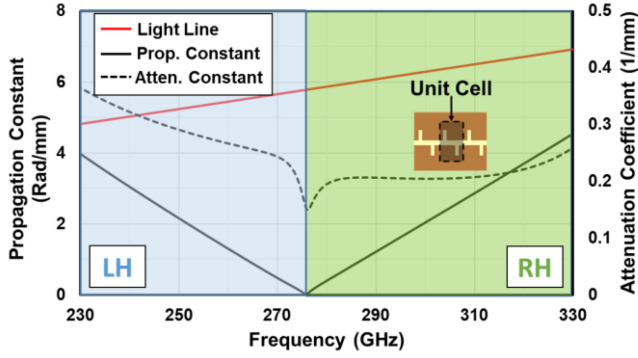


Fig. 3. Simulated dispersion diagram of a single LWA unit cell.

optimum period to be  $p = 353 \mu\text{m}$ , where the simulated effective permittivity of the antenna changes from 9.74 to 10.14 as the frequency varies from 230 to 330 GHz.

To determine the beam steering angle and the 3-dB beam width of the LWA, the simulated dispersion diagram is provided for a single unit cell. As can be observed from Fig. 3, the phase constant of the first space harmonic ( $n = -1$ ) is smaller than the free-space propagation constant (light line) from 230 to 330 GHz, i.e., a fast wave is generated and radiates from the LWA. In the left-handed (LH) region, the beam is steered toward backfire for decreasing frequency. In the right-handed (RH) region, the beam is steered toward endfire as the frequency increases. The beam direction from broadside is given by [42]

$$\sin \theta_m \approx \frac{\beta_{-1}}{k_0}. \quad (6)$$

Therefore, a beam steering range of  $\sim 95^\circ$  is expected from 230 to 330 GHz with  $\sim 0.95^\circ/\text{GHz}$ . To achieve a coherence bandwidth of 10 GHz for THz interconnects, the 3-dB beam width of LWA radiations at all frequencies must be larger than  $9.5^\circ$ , so that a fixed receiver can detect the spatially disperse THz signals. The 3-dB beam width of an infinite LWA can be calculated using [28]

$$\theta_w = \frac{2\alpha c_0}{2\pi f \cos \theta_{-1}} \quad (7)$$

where  $\alpha$  is the attenuation coefficient of an LWA and  $c_0$  is the speed of light in vacuum. As can be seen from Fig. 3, the minimum  $\alpha$  is  $\sim 0.15 \text{ mm}^{-1}$  at broadside with  $sl = 150 \mu\text{m}$  and  $sw = 50 \mu\text{m}$ . Therefore, a 3-dB beam width larger than  $10^\circ$  is expected even for broadside.

It is well known that for periodic LWAs, the open-stop band (OSB) effect causes a nonnegligible decrease of the antenna's gain of broadside radiation. This is caused by contradirectional coupling of space harmonics, which leads to a very high VSWR and a significantly suppressed radiation power in periodic LWAs with open structures [42], [56]. The presence of the OSB effect is represented on the attenuation curve in Fig. 3 as a small subsidence located at broadside. Fig. 4 shows the simulated Bloch impedance  $Z_B$  of the microstrip periodic LWA with 16 unit cells considering the mutual coupling and the edge effects. As can be seen in Fig. 4, a real, nonzero Bloch impedance

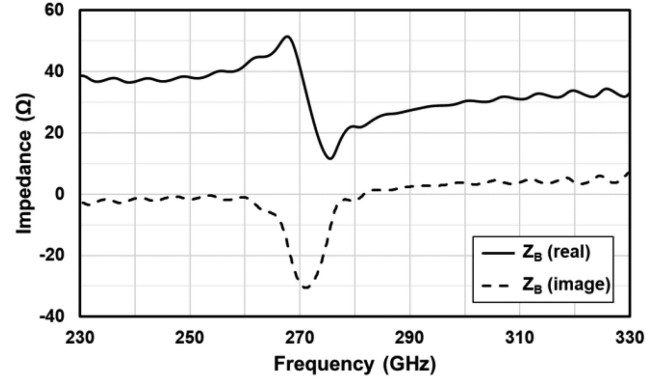


Fig. 4. Simulated Bloch impedance of the microstrip periodic LWA.

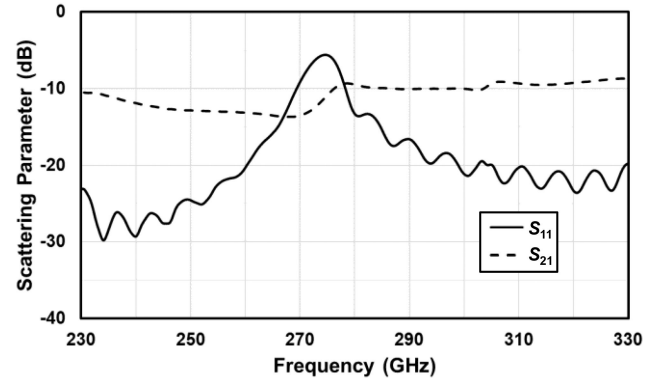


Fig. 5. Simulated scattering parameters of the microstrip periodic LWA.

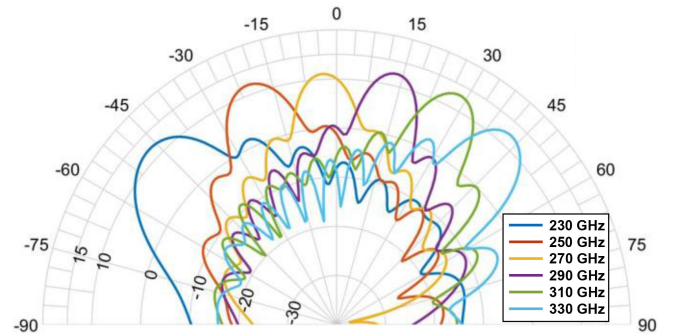


Fig. 6. Simulated far-field radiation patterns for the designed microstrip LWA at 230, 250, 270, 290, 310, and 330 GHz in the H-plane.

at broadside indicates that the OSB effect is mitigated at the broadside [57] with an accepted behavior regarding the chosen structure and the design target (realized gain larger than 10 dBi). For the further mitigation of the OSB effect, an asymmetric unit cell design could be used, as reported in [58].

As can be observed from Fig. 5, for most frequencies, the return loss is below 10 dB. At the broadside frequency, the return loss reaches a maximum of 5.6 dB. Nevertheless, as can be seen in Fig. 6, the maximum realized gain is about 12.5 dBi with a small penalty of about 2 dB for radiation at 270 GHz. The beam direction changes from backfire to endfire passing through

TABLE I  
PARAMETERS OF MICROSTRIP PERIODIC LWA

Symbol	Value	Description
$w$	70 $\mu\text{m}$	microstrip line width
$p$	353 $\mu\text{m}$	period
$sw$	50 $\mu\text{m}$	stub width
$sl$	150 $\mu\text{m}$	stub length
$o$	176.5 $\mu\text{m}$	stub offset

TABLE II  
COMPARISON OF GCPW-MSL TRANSITIONS

Freq. (GHz)	$S_{11}$ (dB)	$S_{21}$ (dB)	Substrate Material	Ref.
10-40	<-10	>-1	high-resistivity silicon	[59]
50-75	<-10	>-1.5	PET	[60]
DC-77	<-10	-0.2	BCB	[61]
75-110	<-18	-0.3	high-resistivity silicon	[62]
100-450	<-10	>-0.5	InP	This work

broadside. By increasing the frequency, the beam sweeps from  $-48^\circ$  at 230 GHz to  $43^\circ$  at 330 GHz with a minimum 3-dB beam width of  $\sim 10^\circ$ . Thus, the total beam steering angle is over  $91^\circ$  for a bandwidth of 100 GHz.

The overall radiation efficiency of the designed antenna, i.e., the ratio between the radiated power and the input power to the LWA used in CST for simulations, is around 60%, except for broadside where it is 51%.

All key parameters of the finally designed microstrip periodic LWA are summarized in Table I.

### B. GCPW-MSL Transition Design

For the microwave region, GCPW-MSL transitions can be realized as a surface-to-surface transition via electromagnetic coupling between ground conductors. As shown in Table II, several GCPW-MSL transitions have been demonstrated up to 110 GHz [59]–[62].

However, simulation results at THz frequencies reveal that the performance of such designs is far from optimum, because the excitation of parasitic substrate modes cannot be sufficiently suppressed by limiting the ground plane width of the GCPWs. This problem can be overcome by means of vertical interconnect access (VIA) holes [63]. However, the fabrication of deep VIAs in InP is not at all straightforward and substantially complicates the fabrication process. Therefore, we developed a novel GCPW-MSL transition that does not necessitate VIAs. The designed transition structure is shown in Fig. 2. Since the aim in this work is to experimentally characterize the LWA using a commercial WR-3 GSG-probe for proof-of-concept measurements, we considered a CPW pitch of 100  $\mu\text{m}$  at the beginning of the transition. The width of the signal line  $s$  was designed to be 30  $\mu\text{m}$  for impedance matching with the commercial GSG-probes. Instead of limited width ground planes, we designed short length ground planes to limit parasitic substrate modes.

The parameters of the GCPW-MSL transition are listed in Table III.

TABLE III  
PARAMETERS OF GCPW-MSL TRANSITION

Parameter	Value	Description
$s$	30 $\mu\text{m}$	Signal line width (GCPW)
$g$	50 $\mu\text{m}$	Gap (GCPW)
$ls$	295 $\mu\text{m}$	Signal line length (GCPW)
$wg$	500 $\mu\text{m}$	Ground-plate width
$lg_1$	5 $\mu\text{m}$	Ground-strip length 01
$lg_2$	150 $\mu\text{m}$	Ground-strip length 02
$lg_3$	157 $\mu\text{m}$	Ground-strip length 03
$\theta$	$22^\circ$	Angle of ground-strip 03

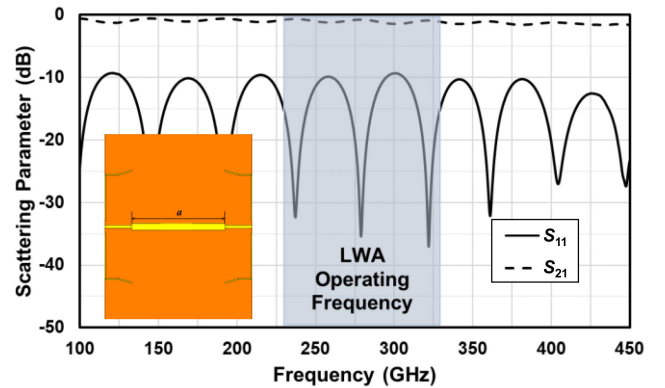


Fig. 7. Simulated scattering parameters of the back-to-back GCPW-MSL transition from 100 to 450 GHz. Inset shows the layout of the GCPW-MSL transition with a MSL length of  $a = 1$  mm.

Simulated scattering parameters of the back-to-back transition with a 1-mm long MSL ( $w = 70 \mu\text{m}$ ) are shown in Fig. 7. As can be observed, the designed transition yields a good matching over an extremely broad bandwidth which is crucial for the integration with an LWA. Simulation results show that  $S_{11}$  is lower than  $-10$  dB within a frequency range from 100 to 450 GHz. The periodic fluctuation is caused by the different signal pad widths of the transition and the MSL and can be optimized using a taper structure at the interface in the future. Furthermore, the insertion loss is reasonably small with a maximum loss below 1.6 dB over the entire frequency range and even below 1.4 dB for the operating frequency of the LWA. The simulated average loss of the 1000  $\mu\text{m}$  MSL is  $\sim 0.5$  dB, and therefore, the extracted insertion loss per transition is maximum 0.5 dB from 100 to 450 GHz.

## IV. FABRICATION

As discussed above, the development of InP-based beam steering LWAs requires  $\sim 50\text{-}\mu\text{m}$  thin InP layers. However, such thin InP substrates are extremely fragile and thus, difficult to be handled during the clean-room fabrication process. Therefore, we developed a substrate-transfer technology using a thick Si substrate to mechanically stabilize the thin InP substrate layer.

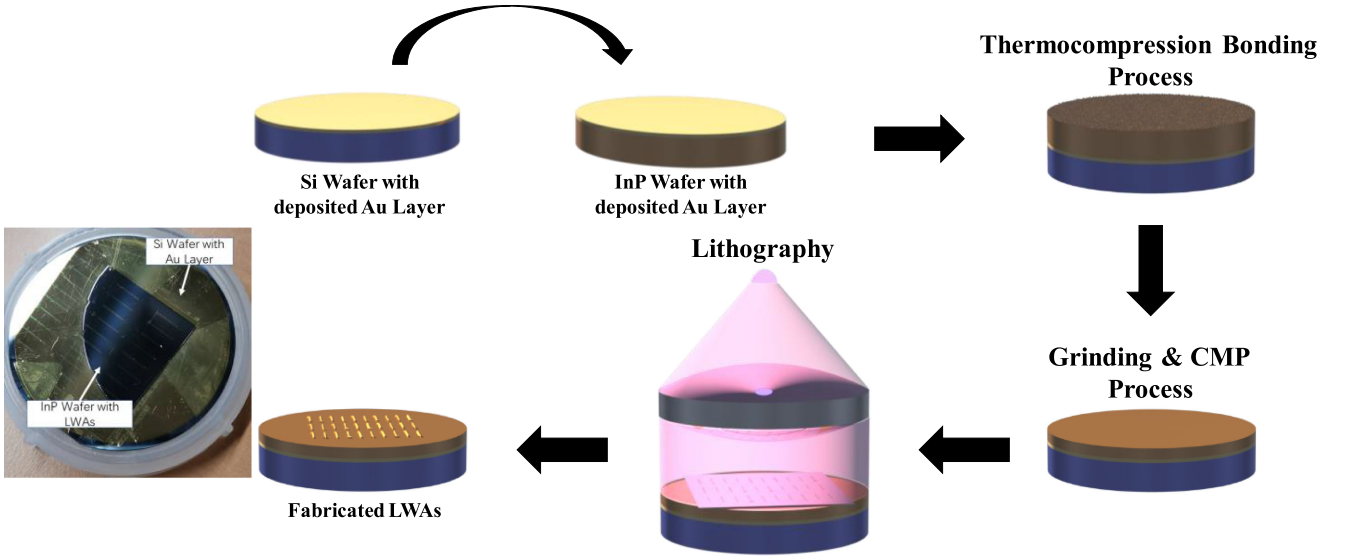


Fig. 8. Fabrication process flow of designed microstrip periodic LWAs with GCPW-MSL transitions based on substrate-transfer technology. The photograph shows the fabricated LWAs.

Fig. 8 sketches the entire fabrication process flow of the designed microstrip periodic LWA with the integrated GCPW-MSL transition. At first, 1- $\mu\text{m}$  thick Ti/Pt/Au layers were deposited on both sides, the surfaces of the InP and the Si substrate. Next, the InP and Si wafers were cleaned using acetone and isopropanol before TCB using a flip-chip bonder (SET FC150) with a bonding pressure of  $\sim 3$  MPa for about 4 h. Due to the mismatch of thermal expansion coefficients (TECs) between InP and Si ( $\alpha_{\text{InP}} = 4.8 \times 10^{-6} \text{ K}^{-1}$ ,  $\alpha_{\text{Si}} = 2.6 \times 10^{-6} \text{ K}^{-1}$ ) [64], the bonding temperature was limited to 250  $^{\circ}\text{C}$  in order to avoid mechanical stress between bonded wafers. The thickness of the InP substrate was reduced to 50  $\mu\text{m}$  by grinding followed by a chemical mechanical polishing (CMP) process to achieve a smooth surface, which is crucial for low-loss THz transmission. Finally, microstrip periodic LWAs with GCPW-MSL transitions were fabricated on the polished InP-wafer using contact lithography. The photograph in Fig. 8 shows the fabricated LWAs. As can be seen, the InP substrate shows a visually glazed surface with just a few breakages at the edges which is an indication for a good TCB bonding strength and high-quality CMP process.

## V. EXPERIMENTAL CHARACTERIZATION

In the THz regime, the influence of the conductor surface roughness must be considered because the electric current density peaks near the conductor surface due to the skin effect. For that reason, we measured the surface roughness of the fabricated structure by means of a DektakXT stylus profiler. For a length of 500  $\mu\text{m}$ , altogether 5000 measurement points of the Au surface of the fabricated microstrip LWA were taken. The measured roughness profile is plotted in Fig. 9. As can be seen, the surface height fluctuates only between  $\pm 12$  nm. In order to consider this surface roughness in our simulation model, we calculated the root-mean-square (rms) roughness according to [65]

$$R_q = \sqrt{\frac{1}{n} \sum_{i=1}^n y_i^2} \quad (8)$$

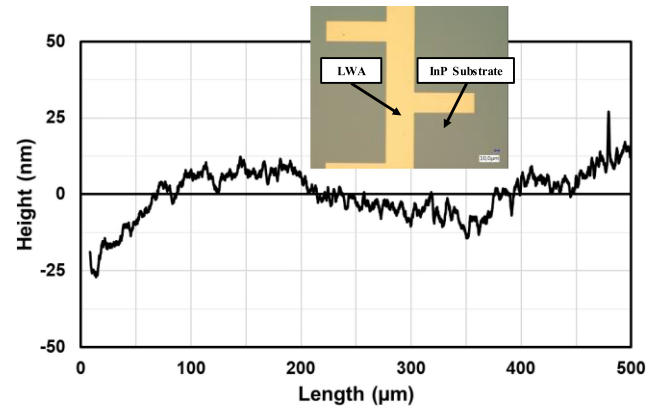


Fig. 9. Measured roughness of microstrip LWA surface by means of a DektakXT stylus profiler. Insert shows a microscopic photo of a fabricated LWA section.

where  $n$  is the number of measured samples and  $y$  is measured height. This results in an rms roughness of  $\sim 8.3$  nm.

The skin depth determines the depth at which the current density is attenuated to  $1/e$  compared to the surface value and it can be calculated using [66]

$$\delta(T) = \frac{c}{\sqrt{2\pi\sigma_0(T) f}} \text{ for } l(T) \ll \delta(T), l(T) \ll \frac{v_F}{f} \quad (9)$$

where  $\sigma_0$  is the static electric conductivity,  $l$  is the mean free path of a conduction electron, and  $v_F$  is the Fermi velocity (for Au at room temperature:  $\sigma_0 = 3 \times 10^{17} \text{ s}^{-1}$  [66],  $l = 37.7$  nm [67], and  $v_F = 13.82 \times 10^5$  m/s [67]). The skin depth for an Au conductor at 300 GHz is 398.9 nm, which indicates that the impact of the surface roughness is not significant.

The simulated  $S_{11}$  of the microstrip periodic LWA with GCPW-MSL transition (black solid line) is shown in Fig. 10. Outside the stopband at 273 GHz, the return loss is lower than 10 dB. Note that the slight change of the broadside frequency is

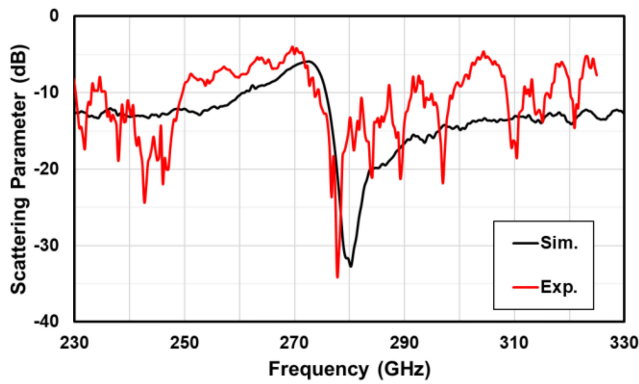


Fig. 10. Simulated and measured  $S_{11}$  parameters of the GCPW-MSL transition with the microstrip periodic LWA.

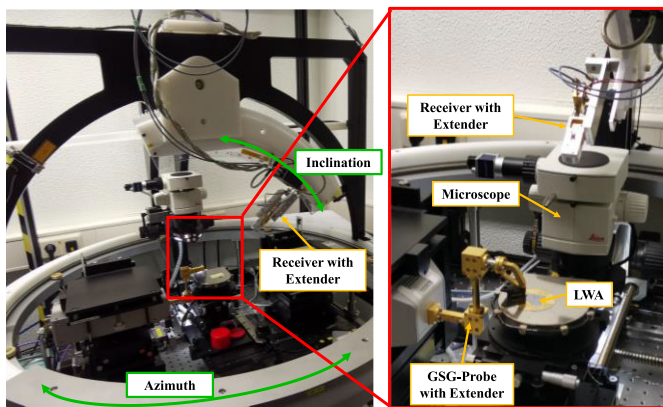


Fig. 11. On-wafer antenna measurement system for far-field radiation pattern measurements.

caused by the transition. For experimental  $S_{11}$  characterization, a VNA (Agilent Technologies 8361A) with a millimeter wave VNA extender (OML V03VNA2-T/R) were used. As can be seen in Fig. 10, the simulation results and the experimentally determined values (red solid line) are in good agreement, which is also an indication for good calibration at such high frequencies.

To experimentally verify beam steering using the fabricated LWA, a THz on-wafer antenna measurement system was developed for measuring the far-field radiation pattern [68]. Here, a VNA (Rohde & Schwarz ZVA-40) and two extenders (Rohde & Schwarz ZC330 and ZRX330), one for signal generation and the other one for signal detection, were used to characterize the beam profile between 220 and 330 GHz. As can be seen from Fig. 11, the receiver has been installed on an automatic hemispherical goniometer system. A C-shaped sliding rail enables receiver movement over an inclination range from  $0^\circ$  to  $51^\circ$ . A  $360^\circ$  rotation in the horizontal plane is carried out by another ring sliding rail. A GSG-probe was used to contact the GCPW-MSL transition of the fabricated LWA for feeding the THz signal. The whole measurement system is placed on an optical table for vibration isolation. It needs to be mentioned that the far-field radiation pattern of the antenna could only be

measured correctly between 273 and 330 GHz. This is because for frequencies lower than 273 GHz, the antenna radiates toward backfire, and the beam is then partially reflected by the GSG-probe.

Fig. 12 shows the simulated and the experimentally determined far-field radiation patterns for different frequencies and for two different antennas. In detail, results are shown for a 1.5-mm wide (a) and an uncleaved (b) InP-based THz LWA. For the measurement, the far-field patterns have been characterized for the same carrier frequencies in steps of  $2^\circ$  over an inclination range from  $0^\circ$  to  $50^\circ$  and in steps of  $5^\circ$  over the full horizontal plane ( $360^\circ$ ).

It can be observed that the radiation patterns of the thinner 1.5-mm wide LWA exhibit a fanlike beam, whereas the radiation patterns of the uncleaved LWA exhibit multiple fingerlike lobes. Note that the “finger-beams” are not grating lobes but are caused by surface wave modes excited in the wide uncleaved InP-to-Si substrate. It is worth mentioning at this point that such “fingerlike” beams can be mitigated by using an array of LWA, which is discussed for THz interconnects in Section VI.

Overall, an excellent agreement between the simulated and the experimentally determined beam patterns is found. The steering angles and even the fingerlike radiation patterns qualitatively agree very well for each frequency. Even the sidelobes for the uncleaved antenna can be clearly observed, which highlights the sensitivity of the developed measurement system. For the 1.5-mm wide antenna, one can observe some stronger sidelobes which are traced back to the impact of the nearby edge which is very rough due to the sawing process.

For a quantitative comparison, the beam direction, 3-dB beam width, and realized gain for the two antennas are shown versus the carrier frequency in Figs. 13–15. These figures also show the expected performances from simulations.

As can be seen from Fig. 13, the simulated beam directions of the designed LWA are not influenced by the width of antenna substrate and sweep from  $-46^\circ$  to  $42^\circ$  by changing the frequency from 230 to 330 GHz, which is successfully confirmed by the corresponding measured results from 280 to 330 GHz. Only around 320 GHz, measured beam angles of the LWA with a 1.5-mm wide substrate are slightly lower than the simulated values due to the rough edges. Fig. 14 shows that the maximum 3-dB beam widths in the H-plane of both LWAs are  $\sim 17^\circ$  at 230 GHz and reduce with increasing frequency. Nonetheless, the minimum value is still larger than  $9^\circ$ . Measurement results confirm the simulated values and demonstrate the impact of edge roughness on the performance of 1.5-mm wide LWA at higher frequencies again. It can be observed from Fig. 15 that the measured average realized gain of the LWA with an uncleaved substrate between 280 and 330 GHz is  $\sim 8.4$  dBi, which is about 4.3 dB lower than the simulated value within this frequency range. The somewhat lower gain of the fabricated antenna can be explained partly by calibration issues and the fact that the pitch of the GSG-probe used for experimental characterization was not perfect for the antenna design. Using a compatible GSG-probe, the LWA with a 1.5-mm wide substrate was measured and the results show a good agreement with simulated values consequently.

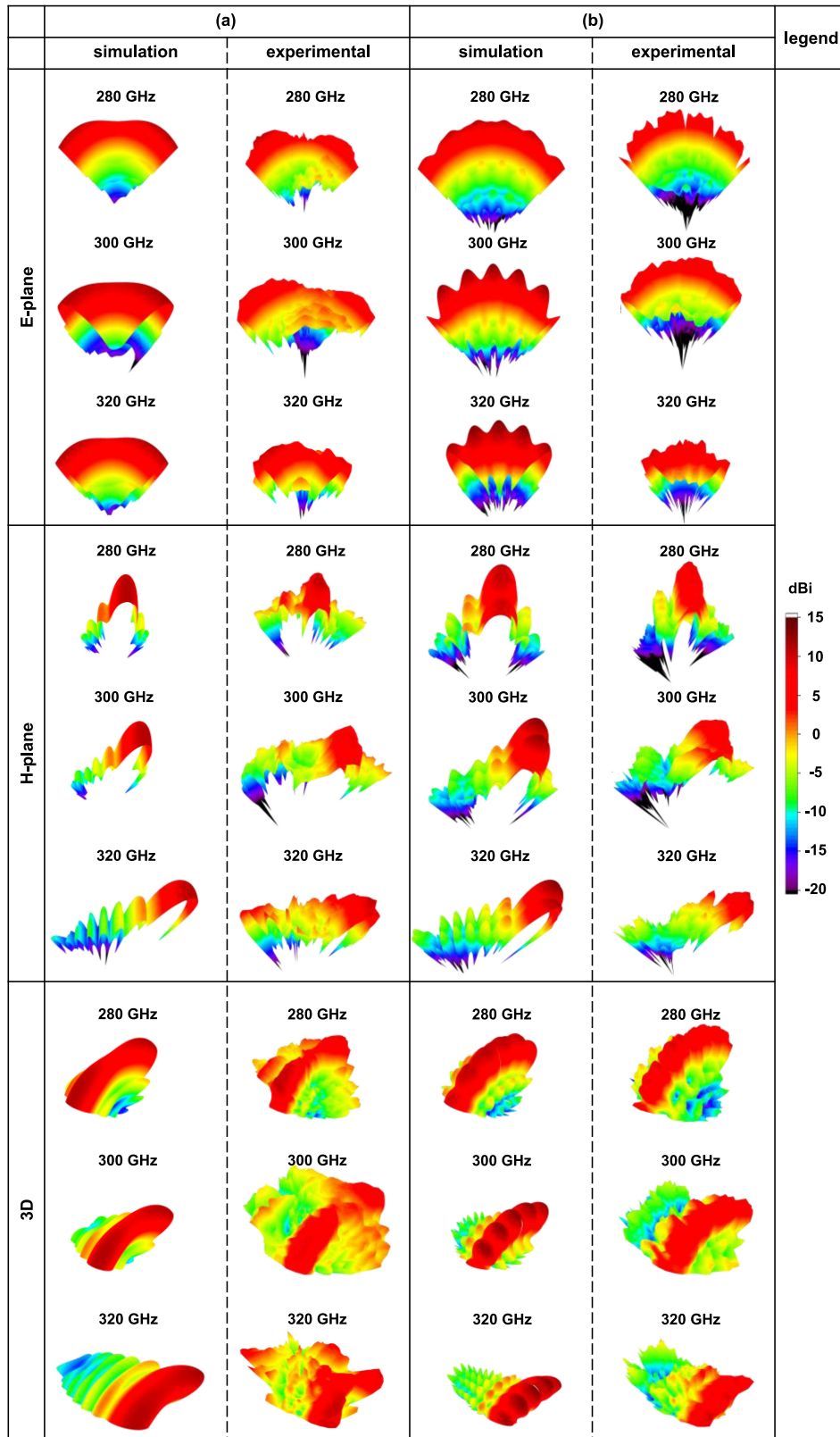


Fig. 12. Simulated and experimentally determined far-field radiation patterns of the microstrip LWA with a GCPW-MSL transition on (a) 1.5 mm wide substrate and (b) uncleaved substrate at 280, 300, and 320 GHz.

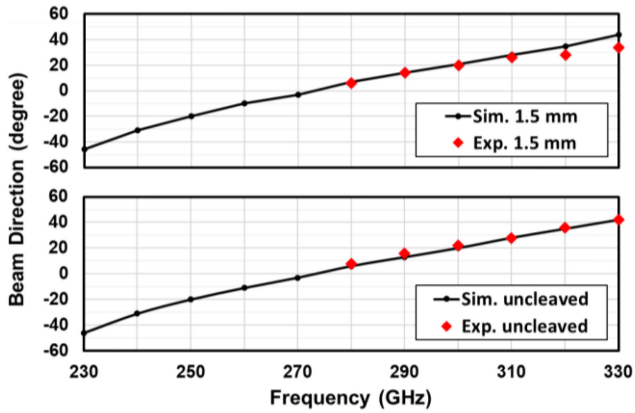


Fig. 13. Simulated and measured relationship between beam direction and frequency from 230 to 330 GHz of the microstrip periodic LWA with GCPW-MSL transition.

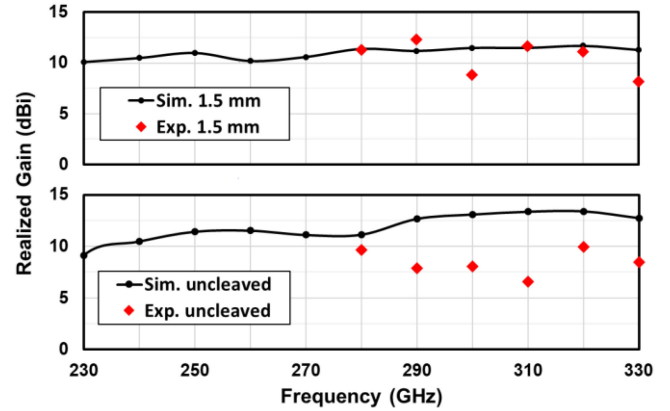


Fig. 15. Simulated and measured relationship between realized gain and frequency from 230 to 330 GHz of the microstrip periodic LWA with GCPW-MSL transition.

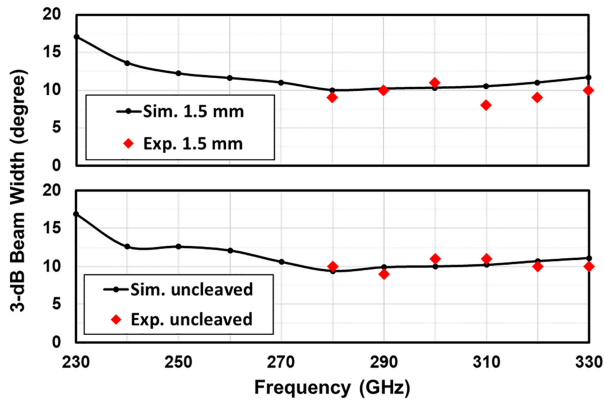


Fig. 14. Simulated and measured relationship between 3-dB beam width and frequency from 230 to 330 GHz of the microstrip periodic LWA with GCPW-MSL transition.

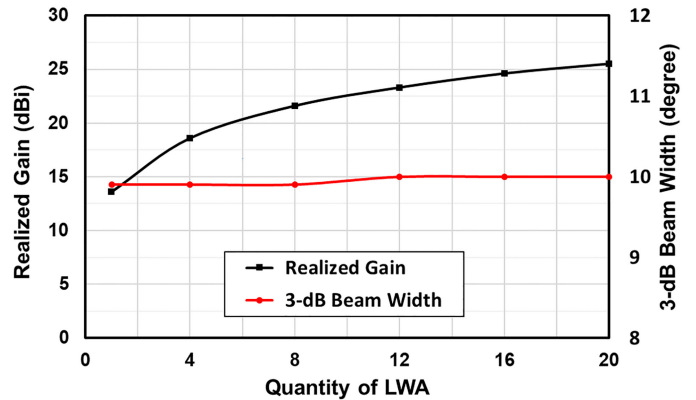


Fig. 16. Simulated realized gain and 3-dB beam width in the H-plane as a function of LWA quantity at 0.3 THz.

## VI. TWO-DIMENSIONAL LWA ARRAY FOR THZ INTERCONNECTS

The InP-based THz beam steering LWA developed in this work yields quasi-linear THz beam steering with  $\sim 0.7^\circ/\text{GHz}$  from 260 to 330 GHz. In this frequency range, the 3-dB beam width in the H-plane is approximately  $10^\circ$ , as shown in Fig. 14. Therefore, the developed LWA could provide a coherence bandwidth exceeding 10 GHz. The transmission distance using a single LWA with an integrated PD is expected to be over 30 cm, as mentioned in Section I. To extend the wireless distance, we suggest using an array of LWAs for THz interconnects. Such an array can now be fabricated in a quite straightforward manner thanks to the possibility of monolithic integration on InP. This would be beneficial in three aspects—it would allow to coherently combine the output power of multiple PDs, it would substantially increase the realized gain of the antenna and it would allow 2-D beam steering. Fig. 16 shows the simulated realized gain and the 3-dB beam width in the H-plane, both at 0.3 THz, as a function of the array size for an LWA array with an antenna pitch of  $500\ \mu\text{m}$ . It can be seen that 3-dB beam width in the H-plane is almost constant but the realized gain is

substantially increased, benefiting from a higher directivity in the orthogonal spatial dimension.

For example, when using four parallel LWAs instead of only one, the realized gain at 0.3 THz would increase by about 5 dB and in addition, the output power could be increased by up to 6 dB, when neglecting additional losses at this point. Using Friis equation, we can then estimate that the wireless transmission distance could be extended by a factor of three to around 1 m. This would be sufficient for high data rate THz interconnects between TV sets or inside cabinets used in data centers.

Moreover, it can also be seen from Fig. 17(a) that the far-field radiation pattern for four LWAs on a wide substrate is not “finger-beam” anymore as observed in Fig. 12. Thanks to the array, a focused pencil beam is radiated, i.e., there would be no antenna-related signal distortion.

Finally, 2-D beam steering is achieved when using an additional photonic true time delay which allows to tune the time delay at each of the four photodiodes individually [69]. It can be observed from Fig. 17(b) that with a time delay of 0.5 ps between each LWA, the beam is steered not only in the H-plane, but also in the E-plane with  $\varphi = 318^\circ$  and  $\theta = 28^\circ$ , respectively.

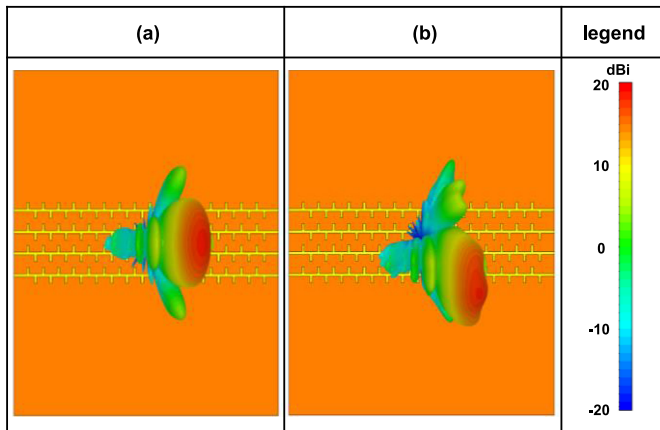


Fig. 17. Simulated far-field radiation pattern of a  $1 \times 4$  microstrip periodic LWA array with a time delay of (a) 0 ps and (b) 0.5 ps between each LWA at 0.3 THz (top view).

In the future and for 2-D steering, the LWA array thus needs to be integrated with an optical beam forming network (OBFN) chip.

## VII. CONCLUSION

This article reports on the design, fabrication, and experimental characterization of an InP-based THz beam steering LWA. To our knowledge, this is the first THz LWA based upon InP substrate, which is an important step toward future monolithic integration with active photonic or electronic THz sources and receivers. The antenna includes a novel grounded coplanar waveguide to microstrip line transition that has been integrated to facilitate future monolithic integration with InP-based THz photodiodes. For being able to fabricate the LWAs on very thin InP, a substrate-transfer process using silicon as carrier substrate has been established. The developed process allows fabrication of the THz structures with an rms roughness of only 8.3 nm. Experimental THz scattering parameter analysis and THz far-field measurements yield a good agreement between the simulated and the experimentally determined antenna performances. Quantitatively, the fabricated THz LWA provides quasi-linear THz beam steering with  $0.7^\circ/\text{GHz}$  from 260 to 330 GHz, i.e., a total steering angle of  $88^\circ$ . For a 1.5-mm wide InP antenna, the achieved 3-dB beam width and realized gain are  $\sim 10^\circ$  and 11 dBi.

Finally, we discussed the use of the developed LWAs for THz interconnects. For an array consisting of four LWAs, a pencil beam with a coherence bandwidth of 10 GHz and a maximum realized gain over 18 dBi is achieved, which is estimated to support wireless THz transmission up to 1 m.

## ACKNOWLEDGMENT

The authors would like to thank R. Zatta and T. Bücher from Bergische Universität Wuppertal, Germany, for the experimental THz  $S_{11}$  scattering parameter measurements, and E. Mutlu from Universität Duisburg-Essen, Germany, for the cleaving of LWAs.

## REFERENCES

- [1] A. Fitzgerald, E. Berry, N. Zinovev, G. Walker, M. Smith, and J. Chamberlain, "An introduction to medical imaging with coherent terahertz frequency radiation," *Phys. Med. Biol.*, vol. 47, no. 7, pp. R67–R84, Mar. 2002.
- [2] C. Yu, S. Fan, Y. Sun, and E. Pickwell-MacPherson, "The potential of terahertz imaging for cancer diagnosis: A review of investigations to date," *Quant. Imag. Med. Surg.*, vol. 2, no. 1, pp. 33–45, Mar. 2012.
- [3] L. Wu *et al.*, "Study of in vivo brain glioma in a mouse model using continuous-wave terahertz reflection imaging," *Biomed. Opt. Express*, vol. 10, no. 8, pp. 3953–3962, Aug. 2019.
- [4] L. Yu *et al.*, "The medical application of terahertz technology in non-invasive detection of cells and tissues: Opportunities and challenges," *RSC Adv.*, vol. 9, no. 17, pp. 9354–9363, Mar. 2019.
- [5] M. Koch, S. Hunsche, P. Schumacher, M. Nuss, J. Feldmann, and J. Fromm, "THz-imaging: A new method for density mapping of wood," *Wood Sci. Technol.*, vol. 32, no. 6, pp. 421–427, Dec. 1998.
- [6] M. Hu *et al.*, "A wavelet-predominant algorithm can evaluate quality of THz security image and identify its usability," *IEEE Trans. Broadcast.*, vol. 66, no. 1, pp. 140–152, Mar. 2010.
- [7] X. Zhang and J. Xu, *Introduction to THz Wave Photonics*. New York, NY, USA: Springer, 2010.
- [8] D. M. Mittleman, "Twenty years of terahertz imaging," *Opt. Express*, vol. 26, no. 8, pp. 9417–9431, Apr. 2018.
- [9] S. Hisatake, J.-Y. Kim, K. Ajito, and T. Nagatsuma, "Self-heterodyne spectrometer using uni-traveling-carrier photodiodes for terahertz-wave generators and optoelectronic mixers," *J. Lightw. Technol.*, vol. 32, no. 20, pp. 3683–3689, Oct. 2014.
- [10] A. Majeed *et al.*, "Broadband THz absorption spectrometer based on excitonic nonlinear optical effects," *Light, Sci. Appl.*, vol. 8, no. 1, pp. 1–5, Mar. 2019.
- [11] J. Y. Suen, M. T. Fang, S. P. Denny, and P. Lubin, "Modeling of terabit geostationary terahertz satellite links from globally dry locations," *IEEE Trans. THz Sci. Technol.*, vol. 5, no. 2, pp. 299–313, Mar. 2015.
- [12] T. Nagatsuma, G. Ducournau, and C. C. Renaud, "Advances in terahertz communications accelerated by photonics," *Nature Photon.*, vol. 10, no. 6, pp. 371–379, Jun. 2016.
- [13] M. F. Hermelo, P.-T. Shih, M. Steeg, A. Ng'oma, and A. Stöhr, "Spectral efficient 64-QAM-OFDM terahertz communication link," *Opt. Express*, vol. 25, no. 16, pp. 19360–19370, Aug. 2017.
- [14] J. W. Holloway, G. C. Dogiamis, and R. Han, "Innovations in terahertz interconnects: High-speed data transport over fully electrical terahertz waveguide links," *IEEE Microw. Mag.*, vol. 21, no. 1, pp. 35–50, Jan. 2020.
- [15] H. Ito and T. Ishibashi, "Photonic terahertz-wave generation using slot-antenna-integrated uni-traveling-carrier photodiodes," *IEEE J. Sel. Topics Quantum Electron.*, vol. 23, no. 4, pp. 1–7, Jul./Aug. 2017.
- [16] K. Ahi, "Review of GaN-based devices for terahertz operation," *Opt. Eng.*, vol. 56, no. 9, pp. 1–14, Sep. 2017.
- [17] R. Lewis, "A review of terahertz detectors," *J. Phys. D, Appl. Phys.*, vol. 52, no. 43, Aug. 2019, Art. no. 433001.
- [18] Y. Monnai, K. Altmann, C. Jansen, H. Hillmer, M. Koch, and H. Shinoda, "Terahertz beam steering and variable focusing using programmable diffraction gratings," *Opt. Express*, vol. 21, no. 2, pp. 2347–2354, Jan. 2013.
- [19] Y. Yang, O. D. Gurbuz, and G. M. Rebeiz, "An eight-element 370–410-GHz phased-array transmitter in 45-nm CMOS SOI with peak EIRP of 8–8.5 dBm," *IEEE Trans. Microw. Theory Techn.*, vol. 64, no. 12, pp. 4241–4249, Dec. 2016.
- [20] X. Li *et al.*, "Switchable multifunctional terahertz metasurfaces employing vanadium dioxide," *Sci. Rep.*, vol. 9, no. 1, pp. 1–13, Apr. 2019.
- [21] M. Tamagnone *et al.*, "Graphene reflectarray metasurface for terahertz beam steering and phase modulation," 2018, *arXiv:1806.02202*.
- [22] T. Nagatsuma, A. Hirata, N. Shimizu, H. Song, and N. Kukutsu, "Photonic generation of millimeter and terahertz waves and its applications," in *Proc. 19th Int. Conf. Appl. Electromagn. Commun.*, Dubrovnik, Croatia, Sep. 2007, pp. 1–4.
- [23] D. Sun *et al.*, "Photonic generation of millimeter and terahertz waves with high phase stability," *Opt. Lett.*, vol. 39, no. 6, pp. 1493–1496, Mar. 2014.
- [24] Y. Zhou, G. Sakano, Y. Yamanaka, H. Ito, T. Ishibashi, and K. Kato, "600-GHz-wave beam steering by terahertz-wave combiner," in *Proc. Opt. Fiber Commun.*, San Diego, CA, USA, Mar. 2018, pp. 1–3.
- [25] K. Maki and C. Otani, "Terahertz beam steering and frequency tuning by using the spatial dispersion of ultrafast laser pulses," *Opt. Express*, vol. 16, no. 14, pp. 10158–10169, Jul. 2008.

- [26] M. Steeg, N. Yonemoto, J. Tebart, and A. Stöhr, "Substrate-integrated waveguide PCB leaky-wave antenna design providing multiple steerable beams in the V-band," *Electronics*, vol. 6, no. 4, Dec. 2017, Art. no. 107.
- [27] P. W. Hon, A. A. Tavallae, Q. Chen, B. S. Williams, and T. Itoh, "Radiation model for terahertz transmission-line metamaterial quantum-cascade lasers," *IEEE Trans. THz Sci. Technol.*, vol. 2, no. 3, pp. 323–332, May 2012.
- [28] K. Murano *et al.*, "Low-profile terahertz radar based on broadband leaky-wave beam steering," *IEEE Trans. THz Sci. Technol.*, vol. 7, no. 1, pp. 60–69, Jan. 2017.
- [29] M. Urteaga, Z. Griffith, M. Seo, J. Hacker, and M. J. Rodwell, "InP HBT technologies for THz integrated circuits," *Proc. IEEE*, vol. 105, no. 6, pp. 1051–1067, Jun. 2017.
- [30] M. Božanić and S. Sinha, "Emerging transistor technologies capable of terahertz amplification: A way to re-engineer terahertz radar sensors," *Sensors*, vol. 19, no. 11, May 2019, Art. no. 2454.
- [31] M. Steeg *et al.*, "Polarization diversity photoreceiver integration on 26 GHz PCB leaky-wave antenna for photonic beam steering transmitter," in *Proc. Int. Topical Meeting Microw. Photon.*, 2019, pp. 1–4.
- [32] A. Pascual *et al.*, "A scalable photomixing array for increased emitted power," in *Proc. 44th Int. Conf. Infrared, Millimeter, Terahertz Waves*, 2019, pp. 1–2.
- [33] A. J. Pascual-Gracia *et al.*, "A photonically-excited leaky-wave antenna array at E-band for 1-D beam steering," *Appl. Sci.*, vol. 10, no. 10, 2020, Art. no. 3474.
- [34] K. M. Leong *et al.*, "A 340–380 GHz integrated CB-CPW-to-waveguide transition for sub millimeter-wave MMIC packaging," *IEEE Microw. Wireless Compon. Lett.*, vol. 19, no. 6, pp. 413–415, Jun. 2009.
- [35] D. Torres *et al.*, "Microcoaxial interconnects for signals, bias, and supply of MMICs," in *Proc. IEEE MTT-S Int. Microw. Symp.*, 2019, pp. 1046–1049.
- [36] K. Neophytou, S. Iezekiel, M. Steeg, and A. Stöhr, "Design of PCB leaky-wave antennas for wide angle beam steering," in *Proc. 11th German Microw. Conf.*, 2018, pp. 152–155.
- [37] S. Dülme *et al.*, "300 GHz photonic self-mixing imaging-system with vertical illuminated triple-transit-region photodiode terahertz emitters," in *Proc. Int. Top. Meeting Microw. Photon.*, Ottawa, ON, Canada, Oct. 2019, pp. 1–4.
- [38] T. Ishibashi, Y. Muramoto, T. Yoshimatsu, and H. Ito, "Unitraveling-carrier photodiodes for terahertz applications," *IEEE J. Sel. Topics Quantum Electron.*, vol. 20, no. 6, pp. 79–88, Nov./Dec. 2014.
- [39] C. A. Balanis, *Modern Antenna Handbook*. Hoboken, NJ, USA: Wiley, 2008.
- [40] J. A. Hejase, P. R. Paladhi, and P. P. Chahal, "Terahertz characterization of dielectric substrates for component design and nondestructive evaluation of packages," *IEEE Trans. Compon., Packag., Manuf. Technol.*, vol. 1, no. 11, pp. 1685–1694, Nov. 2011.
- [41] D. Pozar, "Considerations for millimeter wave printed antennas," *IEEE Trans. Antennas Propag.*, vol. AP-31, no. 5, pp. 740–747, Sep. 1983.
- [42] A. A. Oliner, D. R. Jackson, and J. Volakis, "Leaky-wave antennas," in *Antenna Engineering Handbook*, 4th ed. New York, NY, USA: McGraw-Hill, 2007, ch. 11.
- [43] L. Goldstone and A. Oliner, "Leaky-wave antennas I: Rectangular waveguides," *IRE Trans. Antennas Propag.*, vol. 7, no. 4, pp. 307–319, Oct. 1959.
- [44] P. Lampariello, F. Frezza, H. Shigesawa, M. Tsuji, and A. A. Oliner, "A versatile leaky-wave antenna based on stub-loaded rectangular waveguide. I. Theory," *IEEE Trans. Antennas Propag.*, vol. 46, no. 7, pp. 1032–1041, Jul. 1998.
- [45] J. Liu, D. R. Jackson, and Y. Long, "Substrate integrated waveguide (SIW) leaky-wave antenna with transverse slots," *IEEE Trans. Antennas Propag.*, vol. 60, no. 1, pp. 20–29, Jan. 2012.
- [46] M. Steeg, B. Khani, V. Rymanov, and A. Stöhr, "Novel 50–70 GHz compact PCB leaky-wave antenna with high broadside efficiency and low return loss," in *Proc. 41st Int. Conf. Infrared, Millimeter, Terahertz Waves*, Copenhagen, Denmark, Sep. 2016, pp. 1–2.
- [47] R. Agrawal, P. Belwal, and S. Gupta, "Asymmetric substrate integrated waveguide leaky wave antenna with open stop band suppression and radiation efficiency equalization through broadside," *Radioengineering*, vol. 27, no. 2, pp. 409–416, Jun. 2018.
- [48] A. Grbic and G. V. Eleftheriades, "Leaky CPW-based slot antenna arrays for millimeter-wave applications," *IEEE Trans. Antennas Propag.*, vol. 50, no. 11, pp. 1494–1504, Nov. 2002.
- [49] S. Xiao, B.-Z. Wang, X.-S. Yang, and G. Wang, "A novel reconfiguration CPW leaky-wave antenna for millimeter-wave application," *Int. J. Infrared Millimeter Waves*, vol. 23, no. 11, pp. 1637–1648, Nov. 2002.
- [50] F. Xu and K. Wu, "Understanding leaky-wave structures: A special form of guided-wave structure," *IEEE Microw. Mag.*, vol. 14, no. 5, pp. 87–96, Jul./Aug. 2013.
- [51] P. Baccarelli, P. Burghignoli, F. Frezza, A. Galli, and P. Lampariello, "Novel modal properties and relevant scanning behaviors of phased arrays of microstrip leaky-wave antennas," *IEEE Trans. Antennas Propag.*, vol. 51, no. 12, pp. 3228–3238, Dec. 2003.
- [52] J. James and P. Hall, "Microstrip antennas and arrays. Part 2: New array-design technique," *IEE J. Microw., Opt. Acoust.*, vol. 1, no. 5, pp. 175–181, Sep. 1977.
- [53] S. Bedair and M. Sobhy, "Accurate formulas for computer-aided design of shielded microstrip circuits," *IEE Proc. H - Microw., Opt. Antennas*, vol. 127, no. 6, pp. 305–308, Dec. 1980.
- [54] D. H. Schrauder, *Microstrip Circuit Analysis*. Upper Saddle River, NJ, USA: Prentice Hall, 1995.
- [55] D. M. Pozar, *Microwave Engineering*, 3rd ed. Hoboken, NJ, USA: Wiley, 2005.
- [56] P. Baccarelli, S. Paulotto, D. R. Jackson, and A. A. Oliner, "A new Brillouin dispersion diagram for 1-D periodic printed structures," *IEEE Trans. Microw. Theory Techn.*, vol. 55, no. 7, pp. 1484–1495, Jul. 2007.
- [57] B. Xi *et al.*, "Periodic fixed-frequency staggered line leaky wave antenna with wide-range beam scanning capacity," *IEEE Access*, vol. 7, pp. 146693–146701, 2019.
- [58] S. Paulotto, P. Baccarelli, F. Frezza, and D. R. Jackson, "A novel technique for open-stopband suppression in 1-D periodic printed leaky-wave antennas," *IEEE Trans. Antennas Propag.*, vol. 57, no. 7, pp. 1894–1906, Jul. 2009.
- [59] G. Zheng, J. Papapolymerou, and M. M. Tentzeris, "Wideband coplanar waveguide RF probe pad to microstrip transitions without via holes," *IEEE Microw. Wireless Compon. Lett.*, vol. 13, no. 12, pp. 544–546, Dec. 2003.
- [60] A. Chahadih, P. Y. Cresson, C. Mismar, and T. Lasri, "V-band via-less GCPW-to-microstrip transition designed on PET flexible substrate using inkjet printing technology," *IEEE Microw. Wireless Compon. Lett.*, vol. 25, no. 7, pp. 436–438, Jul. 2015.
- [61] M. El-Gibari *et al.*, "Ultra-broad bandwidth and low-loss GCPW-MS transitions on low-k substrates," *Electron. Lett.*, vol. 46, no. 13, pp. 931–933, 2010.
- [62] J.-P. Raskin, G. Gauthier, L. P. Katehi, and G. M. Rebeiz, "Mode conversion at GCPW-to-microstrip-line transitions," *IEEE Trans. Microw. Theory Techn.*, vol. 48, no. 1, pp. 158–161, Jan. 2000.
- [63] R. Simons, *Coplanar Waveguide Circuits, Components, and Systems*. New York, NY, USA: Wiley, 2001.
- [64] A. W. Fang *et al.*, "Hybrid silicon evanescent devices," *Mater. Today*, vol. 10, no. 7/8, pp. 28–35, Jul./Aug. 2007.
- [65] E. Gadelmawla, M. Koura, T. Maksoud, I. Elewa, and H. Soliman, "Roughness parameters," *J. Mater. Process. Technol.*, vol. 123, no. 1, pp. 133–145, Apr. 2002.
- [66] V. Bezerra, G. Bimonte, G. Klimchitskaya, V. Mostepanenko, and C. Romero, "Thermal correction to the Casimir force, radiative heat transfer, and an experiment," *Eur. Phys. J. C*, vol. 52, no. 3, pp. 701–720, 2007.
- [67] D. Gall, "Electron mean free path in elemental metals," *J. Appl. Phys.*, vol. 119, no. 8, 2016, Art. no. 085101.
- [68] B. Sievert, J. T. Svejda, D. Erni, and A. Rennings, "Spherical mm-wave/THz antenna measurement system," *IEEE Access*, vol. 8, pp. 89680–89691, 2020.
- [69] M. Steeg, P. Lu, J. Tebart, and A. Stöhr, "2D mm-wave beam steering via optical true-time delay and leaky-wave antennas," in *Proc. 12th German Microw. Conf.*, Stuttgart, Germany, Mar. 2019, pp. 158–161.



**Peng Lu** was born in Tianjin, China. He received the B.Sc. and M.Sc. degrees in nanoengineering/nano-optoelectronics from the University of Duisburg-Essen, Duisburg, Germany, in 2014 and 2016, respectively.

Since 2017, he has been a Member of the Department of Optoelectronics, Center for Semiconductor Technology and Optoelectronics (ZHO), and a Research Associate with the University of Duisburg-Essen. His current research interests include photonic integrated chips (PICs) for terahertz

beam forming, terahertz leaky-wave antenna, and 3-D hybrid integration of III-V-Si platforms.



**Thomas Haddad** (Graduate Student Member, IEEE) received the M.Sc. degree in embedded systems from the University of Duisburg-Essen, Duisburg, Germany, in 2019. His master's thesis focused on developing THz leaky wave antennas for beam steering. He is currently working toward the Ph.D. degree with the Optoelectronic Department, University of Duisburg-Essen.

His research interests include technologies of THz beam steering antennas and THz communications and applications.



**Benedikt Sievert** was born in Krefeld, Germany. He received the B.Sc. and M.Sc. degrees in electrical engineering/high frequency systems from the University of Duisburg-Essen, Duisburg, Germany, in 2017 and 2019, respectively.

Since 2017, he has been a Member of the Department of General and Theoretical Electrical Engineering, University of Duisburg-Essen. His current research interests include mm-wave on-chip antennas, electromagnetic metamaterials, and computational electromagnetics.



**Beshar Khani** received the M.Sc. degree in computer science and communications engineering from the University of Duisburg-Essen, Duisburg, Germany, in 2013.

After his study, he has gained international experience with the Department of Electronics Technology, Charles III University of Madrid, Madrid, Spain, within the Marie Curie "MITEPHO" (Microwave and TERAHERTZ PHOTONICS), focusing on the design of novel millimeter-wave circuits using the finite element method high frequency structural simulator

(HFSS). From 2014 to 2019, he was a Member of the Optoelectronics Department, University of Duisburg-Essen. His research includes III/V and RF photonic integration technologies based on high-frequency laminates. He has authored or coauthored more than 30 papers in refereed journals and conferences. His current research interests include the design and development of compact millimeter-wave and THz coherent photonic transmitters and receivers' modules for the 5G mobile communications and photonic radar applications.



**Sumer Makhlof** received the M.Sc. degree in communications engineering from the University of Duisburg-Essen, Duisburg, Germany, in 2018. His master's thesis concentrated on the 3-D printed THz photodiode packages with rectangular waveguide output. He is currently working toward the Ph.D. degree on electronic-phonic integration circuits (EPIC) for THz applications.

He is currently a Member of the Optoelectronics Department, Center for Semiconductor Technology and Optoelectronics (ZHO), and a Research Associate with the University of Duisburg-Essen.



**Sebastian Dülme** was born in Hattingen, Germany. He received the B.Sc. and M.Sc. degrees in nanoengineering/nano-optoelectronics in 2015 and 2017, respectively, from the University of Duisburg-Essen, Duisburg, Germany, where he has been working toward the Ph.D. degree with the Institute of Optoelectronics, since 2017.

His research interests include terahertz photodiodes, terahertz power combining, and terahertz spectroscopy and imaging systems.



**José Fernández Estévez** received education as a microtechnologist of semiconductor technology in 2000.

He is currently a Member of the Optoelectronics Department, Center for Semiconductor Technology and Optoelectronics (ZHO), and Technical Assistant with the University of Duisburg-Essen, Duisburg, Germany.



**Andreas Rennings** (Member, IEEE) studied electrical engineering with the University of Duisburg-Essen, Duisburg, Germany. He carried out his Diploma work with the University of California in Los Angeles, Los Angeles, CA, USA. He received the Dipl.-Ing. and Dr.-Ing. degrees from the University of Duisburg-Essen in 2000 and 2008, respectively.

From 2006 to 2008, he was an RF Engineer with IMST GmbH, Kamp-Lintfort, Germany. Since then, he has been a Senior Scientist and Principal Investigator with the Laboratory for General and Theoretical

Electrical Engineering, University of Duisburg-Essen. His general research interests include all aspects of theoretical and applied electromagnetics, currently with a focus on medical applications and on-chip millimeter-wave/THz antennas.

Dr. Rennings was the recipient of several awards, including a Student Paper Prize at the 2005 IEEE Antennas and Propagation Society International Symposium and the VDE-Promotionspreis 2009 for the dissertation.



**Daniel Erni** (Member, IEEE) received the Diploma from the University of Applied Sciences in Rapperswil (HSR), Rapperswil-Jona, Switzerland, in 1986, the Diploma from ETH Zürich, Zurich, Switzerland, in 1990, both in electrical engineering, and the Ph.D. degree in laser physics from the Laboratory for Electromagnetic Fields and Microwave Electronics, ETH Zürich, in 1996.

Since 1990, he has been with the Laboratory for Electromagnetic Fields and Microwave Electronics, ETH Zürich. From 1995 to 2006, he has been the

Founder and Head of the Communication Photonics Group, ETH Zürich. Since October 2006, he has been a Full Professor of General and Theoretical Electrical Engineering with the University of Duisburg-Essen, Duisburg, Germany. He is a Co-Founder of the spin-off company *airCode* on flexible printed RFID technology. His current research interests include optical interconnects, nanophotonics, plasmonics, advanced solar cell concepts, optical and electromagnetic metamaterials, RF, mm-wave and THz engineering, biomedical engineering, bioelectromagnetics, marine electromagnetics, computational electromagnetics, multiscale and multiphysics modeling, numerical structural optimization, and science and technology studies (STS).

Prof. Erni is a Fellow of the Electromagnetics Academy, a Member of the Center for Nanointegration Duisburg-Essen (CeNIDE), as well as a Member of the Swiss Physical Society (SPS), German Physical Society (DPG), and the Optical Society of America (OSA).



**Ullrich Pfeiffer** (Fellow, IEEE) received the Diploma and Ph.D. degree from the University of Heidelberg, Heidelberg, Germany, in 1996 and 1999, respectively, both in physics.

In 1997, he was a Research Fellow with the Rutherford Appleton Laboratory, Oxfordshire, U.K. From 1999 to 2001, he was a Postdoctoral Researcher with the University of Heidelberg on real-time electronics for particle physics experiments at the European Organization for Nuclear Research (CERN), Meyrin, Switzerland. From 2001 to 2006, he was with the

IBM T.J. Watson Research Center, where his research involved RF circuit design, power amplifier design at 60 and 77 GHz, high-frequency modeling, and packaging for millimeter-wave communication systems. Since 2008, he has been the High-frequency and Communication Technology Chair with the University of Wuppertal, Wuppertal, Germany. In 2007, he led the THz Electronics Group, Institute of High-Frequency and Quantum Electronics, University of Siegen, Siegen, Germany. His current research interests include silicon RFICs for mmWave/THz communication, radar, and imaging systems.

Prof. Pfeiffer was the co-recipient of the 2004 and 2006 Lewis Winner Award for Outstanding Paper at the IEEE International Solid-State Circuit Conference, the co-recipient of the 2006 IBM Pat Goldberg Memorial Best Paper Award, the 2007 European Young Investigator Award, the 2008 EuMIC Best Paper Award, the 2010 EuMC Microwave Prize, the 2014 EuCAP Best Paper Award, and the 2017 Microwave Prize, the 2012 and 2018 Jan Van Vessel Award for Outstanding European Paper at the IEEE International Solid-State Circuit Conference. He has been a Distinguished Lecturer for the IEEE Solid-State Circuits Society and the President of the German Association for Electrical Engineering and Information Technology e.V. (FTEI).



**Andreas Stöhr** (Senior Member, IEEE) received the Dipl.-Ing. and Dr.-Ing. degrees in electrical engineering from Gerhard-Mercator-University, Duisburg, Germany, in 1991 and 1997, respectively.

From 1987 to 1996, he was the CEO of MS Steuerungsanlagen GmbH, Germany. From 1996 to 2013, he was a Research Scientist with the University of Duisburg, Duisburg, Germany. During that period, in 1998 and 1999, he also joined the Communications Research Laboratory (CRL), Tokyo, Japan, where he worked on 60 GHz wireless systems employing radio over fiber techniques. He was also with France Telecom Orange Labs, Lannion, France, in 2009 and with Corning in 2015. He is currently also a Visiting Professor with the University of Ottawa, Ottawa, ON, Canada. Since 2011, he has been a Professor and the Head of the Optoelectronics Department, Center for Semiconductor Technology and Optoelectronics (ZHO), University of Duisburg-Essen (UDE), Duisburg, Germany. He has authored or coauthored more than 200 papers in refereed journals and conferences. His current research interests include III/V integrated microwave photonic device technology and RF photonic integration technologies for millimeter-wave and THz communications, measurement systems, as well as sensing applications.

Prof. Stöhr is a Senior Member of the IEEE Photonics and MTT Society, Committee Member and Chair of a number of international conferences, and IEEE/OSA Guest Editor.



# Mobile THz communications using photonic assisted beam steering leaky-wave antennas

PENG LU,<sup>1,\*</sup>  THOMAS HADDAD,<sup>1</sup>  JONAS TEBART,<sup>1</sup> MATTHIAS STEEG,<sup>1</sup> BENEDIKT SIEVERT,<sup>2</sup>  JÖRG LACKMANN,<sup>1</sup> ANDREAS RENNINGS,<sup>2</sup> AND ANDREAS STÖHR<sup>1</sup>

<sup>1</sup>*Optoelectronics, University of Duisburg-Essen, Duisburg, Germany*

<sup>2</sup>*General and Theoretical Electrical Engineering, University of Duisburg-Essen, Duisburg, Germany*

\*[peng.lu@uni-due.de](mailto:peng.lu@uni-due.de)

**Abstract:** THz communications is envisaged for wide bandwidth mobile communications eventually reaching data capacities exceeding 100 Gbit/s. The technology enabling compact chip-integrated transceivers with highly directive, steerable antennas is the key challenge at THz frequencies to overcome the very high free-space path losses and to support user mobility. In this article, we report on mobile and multi-user THz communications using a photonic THz transmitter chip featuring 1D beam steering for the first time. In the proposed approach, 1D THz beam steering is achieved by using a photodiode excited leaky-wave antenna (LWA) in the transmitter chip. The on-chip LWA allows to steer the directive THz beam from 6° to 39° within the upper WR3-band (0.28-0.33 THz). The antenna's directivity is 14 dBi which is further increased to 23 dBi using an additional hemicylindrical Teflon lens. The 3-dB beam width and coherence bandwidth of the fabricated THz transmitter chips with lens are 9° and 12 GHz, respectively. The proposed approach allows steering the THz beam via the beat frequency of an optical heterodyne system at a speed up to 28°/s. Without using a THz amplifier in the transmitter chip, a data rate of 24 Gbit/s is achieved for a single user for all beam directions and at short wireless distances up to 6 cm. The wireless distance is successfully increased to 32 cm for a lower data rate of 4 Gbit/s, still without using a transmitter amplifier. Also, multi-user THz communications and the overall capacity of the developed THz transmitter chip is studied revealing that up to 12 users could be supported together with a total wireless data capacity of 48 Gbit/s. Fully integrated 2D transmitter chips are expected to reach wireless distances of several meters without additional amplifiers.

© 2021 Optical Society of America under the terms of the [OSA Open Access Publishing Agreement](#)

## 1. Introduction

In the last few years, the demand of high-capacity mobile communications has been growing explosively. Upcoming applications such as augmented reality (AR), virtual reality (VR), cloud computing, 8K video broadcast, connected machines and in general real-time applications require much higher data capacities than current mobile generations can support. These can be achieved by using wider transmission bandwidths and higher spectral efficiencies [1–3]. At frequencies of up to 100 GHz, the contiguous bandwidth is limited by 14 GHz [4] and consequently, THz waves (>100 GHz) have drawn more and more attention for mobile communications due to the available broad bandwidth. For the 275-450 GHz band, a bandwidth of 68 GHz is allocated for communication purposes by the International Telecommunication Union [5]. At higher frequency beyond 1 THz, even several hundreds of GHz bandwidths are expected to be regulated. Other advantages of THz communications include the fact the much shorter wavelength allows the development of chip-integrated THz front ends. Furthermore, mobile THz communications are more difficult to be eavesdropped due to the highly directional beams and the limited propagation distance compared to legacy mobile communications using sectorial antennas [6,7].

Recently, THz communication systems featuring photonic components as transmitters [8–12] have been intensively investigated taking advantage of the developments of mature lasers, modulators, fiber amplifiers and photodiodes (PD). In contrast to electronic THz transmitters, photonic front ends benefit from the broadband performances of modern PDs used to generate the THz carriers and also from the low-loss optical fibers enabling centralized radio access networks. Most recent research works on THz communication systems focused on point-to-point transmission links and the development of ultra-high gain antennas for long-range wireless communications [9–12]. But besides backhaul links, most of the promising applications such as real-time IoT or AR/VR require mobility and multi-user support. This leads to the technological challenge of developing integrated THz transmitter and receiver chips that support THz beam steering to overcome the free-space path loss (FSPL) in the THz domain and to enable user mobility and multi-user operation. Very recently, first concepts enabling THz beam steering based on photonic phased arrays have been demonstrated by using fiber-optic delay lines [13], free-space optical phase shifter [14] or thermo-optic phase shifter [15] for the optical beam control circuitries. However, complex optical phase shifters or true time delay feeders still prevent from monolithic integration. In comparison with optical phased arrays, PD excited leaky-wave antennas (LWA) provide a less complex beam control. For LWAs, the beam direction can be simply tuned by changing the operating frequency which can be easily achieved in photonics over huge bandwidths by tuning the beat frequency of an optical heterodyne system. In the microwave region, several photonic assisted wireless communication systems using LWAs have been demonstrated. In [16], a PD integrated LWA using printed circuit board technology for E-band was developed. Using on-off keying modulation, an error-free transmission of 2.15 Gbit/s for a link distance of 25 cm was achieved using two lenses. A steerable 60 GHz band PD excited LWA with a maximum user data rate up to 6 Gbit/s was demonstrated in [17] using 64 quadrature amplitude modulation (QAM) orthogonal frequency-division multiplexing (OFDM) modulation. In addition, the inherent frequency correlative beam steering of LWAs makes them attractive not only for tracking of a single mobile user [18], but also for multi-user scenarios. In [19], a single-feed LWA was reported for simultaneous transmission to up to three users for V-band frequencies.

However, to the best of our knowledge, no THz communication systems using beam steering antennas have yet been shown. In this work, we first report on a photonic assisted beam steering THz communication system based upon a planar on-chip THz LWA. In the next section, the beam steering capabilities of the fabricated THz transmitter and the generated THz beam patterns are experimentally determined and compared to simulation results. Next, the fabricated THz transmitter chip is employed for single user mobile THz communications. Finally, guard bands required for multi-user operations are experimentally determined to study the maximum user number and total data capacity that can be supported.

## 2. 1D beam steering THz LWA transmitter chip

The planar THz LWA used in this work is intentionally fabricated on an InP substrate for future monolithic integration with InP-based photodiodes [20,21]. The fabricated LWAs utilize 32 periodic rectangular stubs on both sides of the microstrip (see inset in Fig. 1). An on-chip grounded coplanar waveguide to microstrip-line (GCPW-MSL) THz transition is integrated to allow experimental analysis of the fabricated antenna chips using ground-signal-ground (GSG)-probes. The overall length of the 0.3 THz LWA including the transition is 6.6 mm. To suppress the number of surface wave modes and increase the radiation efficiency, the LWA is fabricated on a 50- $\mu\text{m}$  thin InP substrate ( $\epsilon_r \approx 12.4$ ,  $\tan \delta \approx 0.003$ ) using a silicon substrate-transfer technology [20]. Using CST Studio Suite, an additional hemicylindrical lens is developed to further increase the directivity of the on-chip LWA. The hemicylindrical lens with a diameter of 3.8 mm is fabricated using Teflon with a permittivity of  $\epsilon_r \approx 2.1$ . Figure 1(a) shows the simulated

H-plane far-field radiation patterns of the LWA with the lens placed 2.7 mm above the antenna. As can be seen, the beam direction changes from broadside ( $0^\circ$ ) towards endfire ( $90^\circ$ ) when increasing the frequency from 0.28 to 0.33 THz. The side mode suppression is in excess of 10 dB. For experimental characterizations, a THz on-wafer antenna measurement system [22] is used to determine performances of the LWA including the lens. It should be noted that the LWA also allows to steer the THz beam towards backfire, i.e., beam directions  $<0^\circ$ . However, this could not be experimentally determined as in this case the transmitted THz beam is partly reflected by the GSG-probe. Figures 1(b)–1(d) show the simulated and measured beam direction, 3-dB H-plane beam width and the antenna's directivity. Also, the simulated LWA performances without the lens are included in these figures for comparison.

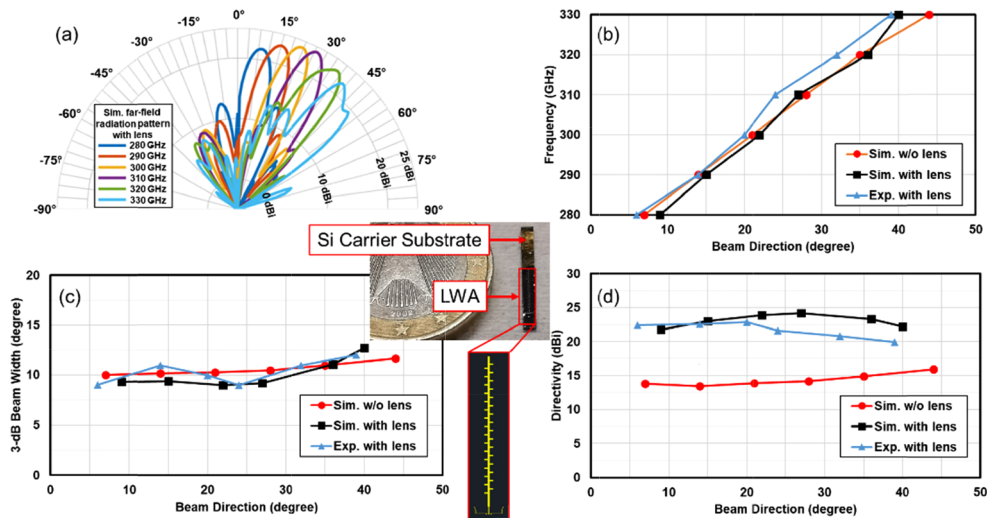


**Fig. 1.** Simulated H-plane far-field radiation patterns of the planar InP-based on-chip LWA with the hemicylindrical Teflon lens (a). Simulated and experimentally characterized beam direction (b), 3-dB H-plane beam width (c) and directivity (d) of the LWA without and with the hemicylindrical Teflon lens. The inset shows a photo of the fabricated LWA and a schematic view.

As can be seen from Fig. 1(b), the THz beam scans from  $6^\circ$  to  $39^\circ$  in a quasi-linear manner with  $\sim 0.7^\circ/\text{GHz}$  when the carrier frequency is tuned between 0.28 and 0.33 THz. Thus, the overall scanning range is  $33^\circ$ . It can also be observed that the beam direction is only barely affected by the hemicylindrical lens. Here, a maximum deviation of only  $4^\circ$  is observed at 330 GHz which is traced back to the lens. Figure 1(c) shows that the average 3-dB H-plane beam width of the on-chip antenna without the lens is  $\sim 11^\circ$  for the whole steering range. The use of the lens leads to a slightly reduced beam width for beam directions closer to broadside. For endfire, the lens widens the beam width slightly up to  $13^\circ$ . Overall, a good agreement between the measured and the simulated 3-dB beam widths is found and the beam width is rather unaffected by the lens, as it was expected. The maximum deviation is only  $\pm 1^\circ$  for the whole steering range. From the measured minimum 3-dB beam width of  $9^\circ$  and the beam steering rate of  $0.7^\circ/\text{GHz}$ , the coherence bandwidth of the antenna is determined to be in excess of 12 GHz for the whole scanning range. The simulated directivity of the on-chip LWA can be seen from Fig. 1(d), showing an antenna directivity of  $\sim 14$  dBi for the full scanning range. Using the hemicylindrical Teflon lens substantially increases the directivity up to  $\sim 23$  dBi. This is further verified by experimental measurements which agree to the simulated results for beam directions of up to  $20^\circ$ . Only above  $20^\circ$ , we observe a slightly lower directivity than expected with a maximum deviation

of  $\sim 2$  dB. This is traced back to the non-perfect shape of the manufactured Teflon lens and the misalignment during measurements.

### 3. Single-user mobile THz communications

#### 3.1. System set-up

A schematic overview of the system set-up for THz communications is shown in Fig. 2. An intermediate frequency (IF) OFDM waveform is generated in the digital domain and converted to the analog domain using an arbitrary waveform generator (AWG) (*Keysight M9505A*) with an analog bandwidth of 20 GHz. Employing IF modulation is motivated by the envelope detection approach since it enables phase recovery at the wireless receiver for complex modulation schemes such as QAM [8]. After subsequent IF amplification using a medium power amplifier (MPA) with  $\sim 30$  dB gain, the waveform is modulated onto a  $1.55\text{-}\mu\text{m}$  optical carrier (laser 1) by means of a Mach-Zehnder modulator (MZM) with 40 GHz bandwidth. Here, the optical carrier is provided by a free running integrable tunable laser assembly (ITLA) which comprises an external cavity laser diode and additional control circuits. The external cavity laser allows to tune the optical wavelength and still provides a reasonably low optical linewidth of  $\sim 25$  kHz. After optical amplification, the signal is transmitted to the wireless front end via standard single mode fiber (SMF). Then, to transfer the OFDM waveform to the THz region, a second ITLA (laser 2) with a beat frequency in the THz range w.r.t. laser 1 is employed for optical heterodyning in a uni-travelling-carrier photodiode (UTC-PD) with a high output power of  $\sim -14$  dBm at 0.3 THz. Laser 3 allows to generate a second THz carrier and is only used for the experimental characterization of multi-user scenarios (see section 4). The optically generated THz OFDM waveform is then radiated into free space using the fabricated InP LWA connected to the UTC-PD via a GSG-probe (*FormFactor I325-T-GSG-100BT*). To increase the antenna's directivity, the hemicylindrical Teflon lens is placed above the LWA as discussed above. After wireless transmission, the THz waveform is received by a standard WR2.8 diagonal horn antenna with 24 dBi gain and is further amplified via a THz low noise amplifier (*Radiometer Physics LNA 250-350 25 8*) with  $\sim 27.5$  dB gain. Down-conversion to IF is then carried out using a zero-biased Schottky-barrier diode (SBD), (*Virginia Diodes WR2.8 ZBD-F40*) with a maximum available response rate of  $\sim 40$  GHz. Frequency drifts between the data carrier and the LO can

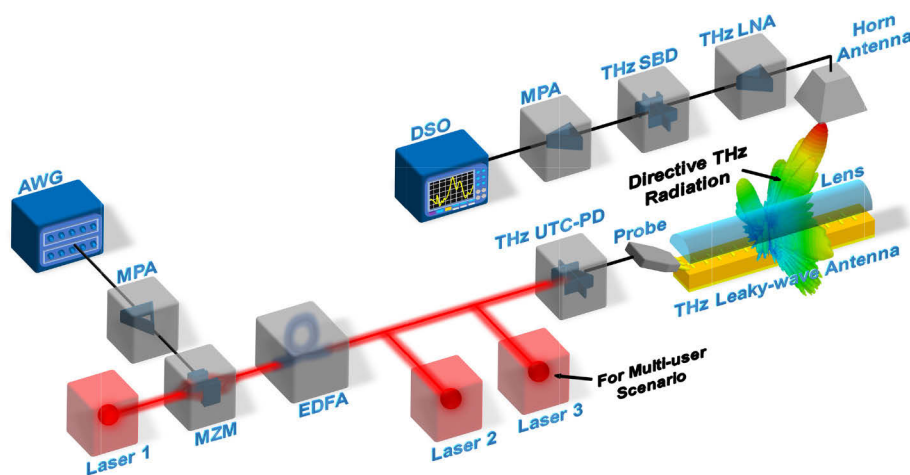


**Fig. 2.** Schematic architecture of the THz communication system set-up using the photonic LWA with the hemicylindrical Teflon lens.

be neglected for this receiver setup in comparison with a heterodyne detection approach, thus avoiding the need for locking the lasers [8,23]. For demodulating the IF-OFDM signal in the digital domain, the waveform is digitized by a high frequency digital sampling oscilloscope (DSO), (*Keysight DSA-Z 634A*) and then analyzed using off-line digital signal processing. The highest data bandwidth of this THz communication system is expected to be  $\sim 12$  GHz which is limited only by the coherence bandwidth of the LWA.

Figure 3 shows photographs of the THz communication system set-up with the Teflon lens placed  $\sim 2.7$  mm above the LWA. The wireless receiver is installed on a goniometer to support angular dependent measurements and for emulating a mobile user.

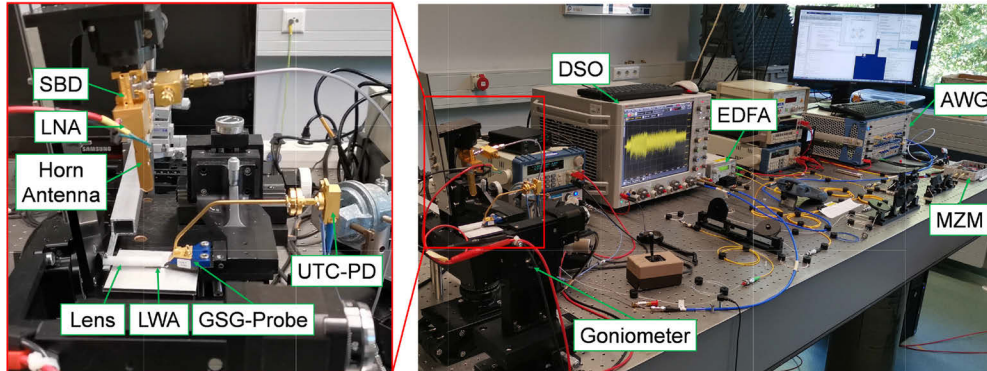


**Fig. 3.** Photographs of the THz communication system using the photonic LWA with the hemicylindrical Teflon lens.

For a wireless distance of 6 cm, the link budget of the system is estimated in Table 1 for beam directions of  $6^\circ$ ,  $20^\circ$  and  $32^\circ$ . As intended, the system performance is almost independent on the wireless carrier frequencies. Also, the FSPL is almost the same for all carrier frequencies, i.e., all beam directions. The input power to the SBD is around -9.6 dBm for all beam directions.

**Table 1.** Link budget for beam directions of  $6^\circ$ ,  $20^\circ$  and  $32^\circ$  for a wireless distance of 6 cm.

Beam Direction (degree)	6	20	32
PD Output Power (dBm)	-14.27	-13.64	-14.46
Probe Loss (dB)	4.73	5.11	5.79
LWA Gain (dBi)	14.08	14.01	14.76
FSPL (dB)	56.95	57.55	58.11
Horn Antenna Gain (dBi)	23.63	24.03	24.56
THz LNA Gain (dB)	27.95	28.82	29.92
SBD Input Power (dBm)	-10.29	-9.46	-9.12

### 3.2. Experimental results

First, the nonlinearity of the whole receiver setup including LNA, SBD and MPA is characterized. This is carried out by measuring the SNR as a function of the UTC-PD output power for a 4-QAM IF-OFDM data signal with a bandwidth (BW) of 4 GHz and an IF of 4 GHz. For this experiment, the beam direction is set to  $6^\circ$  and the wireless distance between the tip of the horn antenna and the LWA is 6 cm. The bias of MZM is set to  $\sim 2$  V to minimize signal-signal beating interference (SSBI) [23]. The number of subcarriers is 512, whereas 16 subcarriers are used as pilots to

compensate carrier-frequency offset. As can be seen in Fig. 4, the measured SNR increases from  $\sim 6.8$  dB to  $\sim 16.1$  dB quasi-linearly with the PD output power. There is a good agreement with the expected square-law response of an SBD [24] which indicates that the wireless receiver is not saturated.

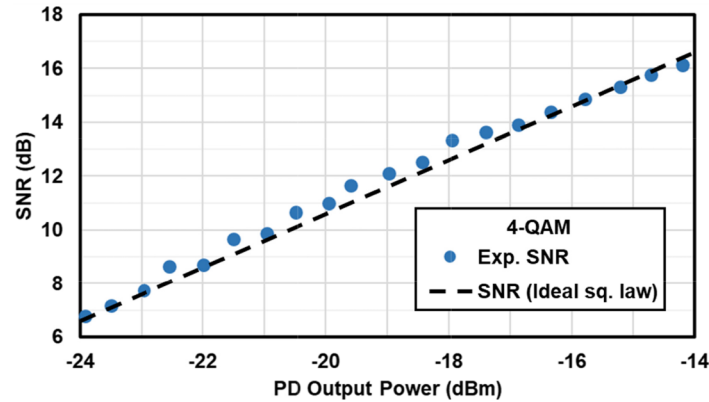


**Fig. 4.** Measured SNR of a 4-QAM IF-OFDM data signal with a bandwidth of 4 GHz at an IF of 4 GHz as a function of PD output power for a wireless transmission distance of 6 cm and a beam direction of  $6^\circ$ . The black dash line shows the SNR of an SBD as a function of PD output power assuming ideal square-law response without saturation effect after [24].

To investigate the beam steering capabilities of the THz communication system, we measured the BER as a function of the beam angles from  $6^\circ$  to  $39^\circ$ . Here, a stable BER has been found (see Fig. 5) which can be explained by the fact that the input power to the SBD receiver is nearly independent of the beam direction as detailed in Table 1. Here, 4-QAM IF-OFDM modulation and BWs of 8 GHz and 12 GHz at an IF of 6 GHz are used. For 8 GHz BW, a minimum BER of  $8 \times 10^{-5}$  is observed at angles of  $24^\circ$  and  $32^\circ$ . At  $39^\circ$ , the maximum BER is  $7.6 \times 10^{-4}$ . For 12 GHz BW, the measurement shows a similar trend with a larger BER as expected. Overall, for both bandwidths, the BER are always below  $3.8 \times 10^{-3}$  which is the limit for 7% over-head hard decision forward error correction (HD-FEC) [25]. Therefore, it can be concluded that a minimum net data rate of 20.46 Gbit/s is achieved for all beam directions using a 12 GHz BW. In the proposed system approach, the beam direction is controlled via the wavelength tuning of the LO laser. The laser allows a wavelength sweep speed of up to 40 GHz/s [26] which in turn means that the THz beam can be steered with an angular speed of  $28^\circ/\text{s}$  given the quasi-linear steering capability with  $0.7^\circ/\text{GHz}$  of the fabricated LWA.

In addition, the system performances are studied for larger wireless distances up to 34 cm using again 4-QAM IF-OFDM waveforms at a beam direction of  $6^\circ$ . The IF is fixed to 3 GHz for BWs of 2 GHz, 4 GHz and 6 GHz. As shown in Fig. 6, the BER increases for larger wireless distance due to the higher FSPL. For a BW of 6 GHz (data rate of  $\sim 12$  Gbit/s), a wireless transmission distance for below HD-FEC level BER is achieved up to 16 cm. When reducing the BW to 4 GHz, the wireless link can be extended up to 20 cm, while for a data rate of 4 Gbit/s a wireless distance of 32 cm is achieved. To further increase the wireless distance in the meter range, one option would be a monolithic integrated 2D LWA array with an array of THz PDs which will not only avoid the  $\sim 5$  dB loss of the GSG-probe, but also benefit from the array factor. This is further discussed in section 5.

The received 4-QAM constellations at a beam direction of  $6^\circ$  with a BW of 12 GHz at 6 cm and a BW of 2 GHz at 32 cm are shown in Fig. 7(a) and Fig. 7(b), respectively. As can be seen, the constellations are successfully recovered without wrapping.

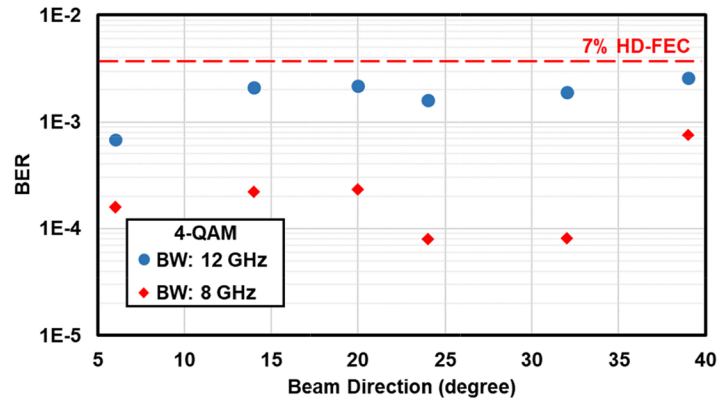


**Fig. 5.** Measured BER of 4-QAM IF-OFDM data signals with bandwidths of 8 GHz and 12 GHz from 6° to 39°. The IF frequency is 6 GHz.

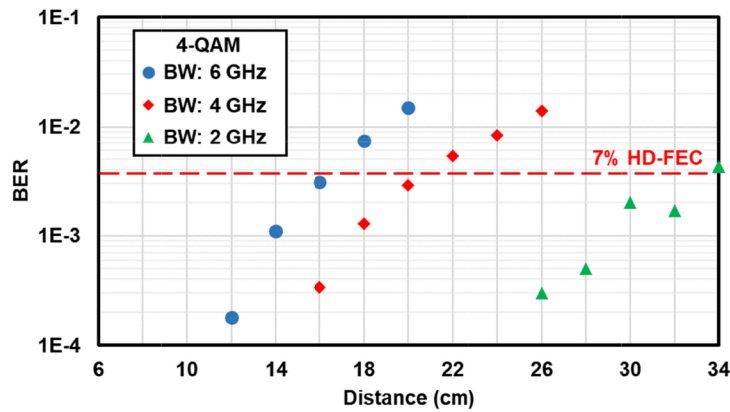


**Fig. 6.** Measured BER of 4-QAM IF-OFDM data signals for wireless transmission distances from 6 cm to 34 cm. The IF frequency is 3 GHz, and the beam direction is 6°.

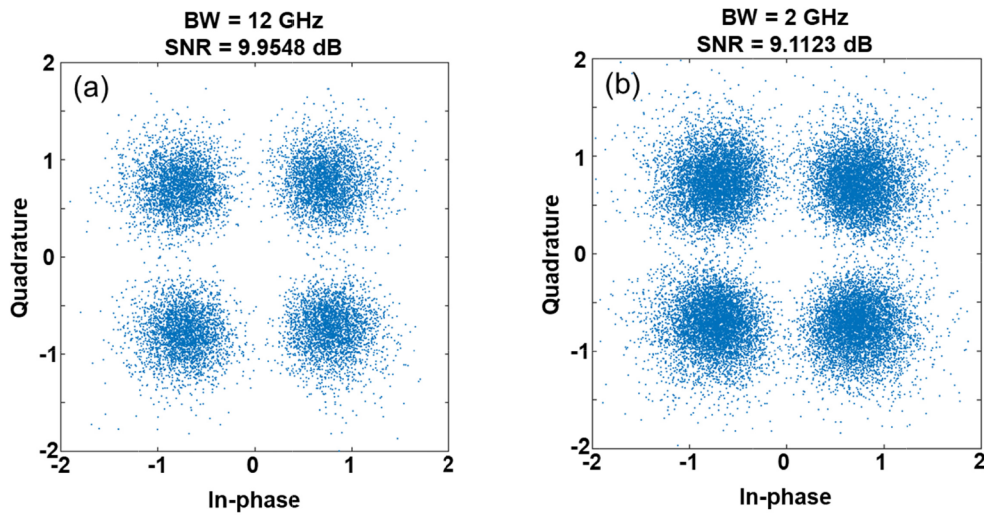


**Fig. 7.** Constellation diagrams of the received 4-QAM IF-OFDM signal with a bandwidth of 12 GHz at 6 cm (a) and a bandwidth of 2 GHz at 32 cm (b) after digital demodulation.

#### 4. Multi-user THz communications

For conventional WiFi networks, omnidirectional antennas are commonly used to cover multiple users at different angular locations w.r.t. the router. For THz communications, such omnidirectional antennas are not quite feasible due to the much higher FSPL. A solution to this problem is to use antennas providing multiple directional beams at different directions simultaneously. In that context, the proposed approach using LWAs is attractive, as it allows to generate multiple beams at different directions simply by using a different carrier frequency for each user waveform. Since the performance of the developed wireless receiver is rather independent of the carrier frequency thanks to the envelope detection approach, multiple users (wireless receivers) can be supported by only one LWA. In the proposed photonic assisted system, which is based on optical heterodyning, multiple carriers can be generated by using optical LO lasers or by using an optical comb laser.

To survey the number of users and the total data capacity that the system can support, it is necessary to investigate the interference between two neighbored beams. For this study, an additional LO laser (laser 3) is added to the system set-up (see Fig. 2) in order to simultaneously generate and radiate two THz waveforms at different beam directions. To experimentally determine the minimum beam angle difference between two users, one beam is fixed at a direction of  $6^\circ$  while the second beam is moved closer to the first one until the BER for both users reaches the HD-FEC level of  $3.8 \times 10^{-3}$  due to interference between the two OFDM waveforms. This experiment is systematically carried out for different user bandwidths.

Experimentally, it is found that independent on the BW for each user, the guard band between two waveforms must be larger than 1 GHz for below HD-FEC transmission. The measured BER for different scenarios are summarized in Table 2.

**Table 2. Measurement parameters and results for multi-user scenarios.**

QAM	IF (GHz)	Data Bandwidth (GHz)	Data Rate (Gbit/s)	BER	Guard Band (GHz)	User Separation (degree)	User Number	Total Data Capacity (Gbit/s)
16	1	1	4	$3.2 \times 10^{-3}$	1	3	12	48
16	3	2	8	$7.8 \times 10^{-4}$	1	6	6	48
4	4	6	12	$1.3 \times 10^{-3}$	1	10	4	48

Obviously, the number of users that could be potentially supported by the proposed approach is linked to the BW provided per user. For a wireless data rate of 12 Gbit/s for each single user, the minimum angular user separation must be  $10^\circ$  which results in up to 4 users that could be covered simultaneously by the fabricated LWA within the scanning range, i.e.,  $33^\circ$ . This would lead to a total data capacity of 48 Gbit/s provided the spectral power density of the radiated three beams fulfills the requirements for below HD-FEC transmission. By reducing the BW, the SNR is increased which allows to use higher order QAM modulation such as 16 QAM. This way, a data rate of 4 Gbit/s is achieved even at a narrow bandwidth of only 1 GHz. In that case, users can be located much closer to each other. The total user number would increase up to 12, while the total data capacity remains 48 Gbit/s. Note that for a monolithic integrated PD/LWA, one could also exploit the beam directions towards backfire which are currently not usable due to reflections at the GSG-probe. This would theoretically double the number of users, and the overall capacity per antenna sector would increase up to 96 Gbit/s provided sufficient output power is available.

#### 5. Conclusion

This article reports on a novel photonic assisted THz communication system supporting mobile and multi-user applications. By using a photodiode excited planar InP-based on-chip leaky-wave antenna, the direction of THz beams can be tuned via the beat frequency of an optical heterodyne

system between 0.28 and 0.33 THz. To the best of our knowledge, this is the first experimental demonstration of THz communications with beam steering antennas.

For single user operation, a data rate of 24 Gbit/s is achieved within the antenna's scanning range of  $33^\circ$ . The scanning speed of  $28^\circ/\text{s}$  allows to steer the THz beam over the full scanning range within less than 1.2 seconds. Also, multi-user operation is investigated, revealing a minimum guard band of 1 GHz which in turn indicates that the proposed approach could support up to 12 users within the antennas coverage sector and a total capacity of 48 Gbit/s.

The wireless distance for below HD-FEC mobile single-user THz communications is currently limited to short-ranges. In the experiment, the PD output power at 0.3 THz is around -14 dBm resulting in a wireless distance of 32 cm for 4 Gbit/s. Both devices, the PD and the LWA used in this experimental study are intentionally fabricated on InP-substrate to allow future monolithic integration which is expected to increase the single user link SNR by about 5 dB (insertion loss of the GSG-probe). Depending on gain and noise factor, an additional amplifier will also help to increase the wireless distance because the link SNR is typically determined by the thermal noise of the THz receiver. In addition, a great progress w.r.t. a higher SNR can be expected from monolithically integrated LWA array configurations. A 10x PD/LWA array is expected to provide 10 dB higher RF output power due to free-space power combining. As discussed in our previous work [20], a directivity enhancement of  $\sim 9$  dB is expected for such an array configuration in contrast to a single LWA. Since the hemicylindrical lens cannot be used for the 2D array, a reduction in the antenna's directivity of  $\sim 7$  dB must be considered. In total, a monolithically integrated 10x PD/LWA array is expected to increase the link SNR by at least 16 dB compared to the single LWA as presented in this work, even without the use of an additional amplifier and the hemicylindrical Teflon lens. This way, the wireless distance should be extended well into the meter range making the proposed THz approach available for mobile IoT applications such as mobile users wearing AR/VR googles in an in-door environment.

**Funding.** Bundesministerium für Bildung und Forschung(Projekt-ID 16ES0936); Deutsche Forschungsgemeinschaft (287022738 – TRR 196); NRW/EFRE Terahertz-Integrationszentrum (THzIZ).

**Disclosures.** The authors declare no conflicts of interest.

**Data availability.** Data underlying the results presented in this paper are not publicly available at this time but may be obtained from the authors upon reasonable request.

## References

1. Samsung, "6G the next hyper-connected experience for all," <https://cdn.codeground.org/nsr/downloads/researchareas/6G%20Vision.pdf>.
2. Cisco public white paper, "Cisco visual networking index: global mobile data traffic forecast update, 2017–2022," <https://cyrekdigital.com/uploads/content/files/white-paper-c11-741490.pdf>.
3. T. Kürner and S. Priebe, "Towards THz communications-status in research, standardization and regulation," *J. Infrared, Millimeter, Terahertz Waves* **35**(1), 53–62 (2014).
4. Federal Communications Commission, "Use of spectrum bands above 24 GHz for mobile radio services," <https://www.govinfo.gov/content/pkg/FR-2016-11-14/pdf/2016-25765.pdf>.
5. International Telecommunication Union, "Technical and operational characteristics and applications of the point-to-point fixed service applications operating in the frequency band 275-450 GHz," [https://www.itu.int/dms\\_pub/itu-r/opb/rep/R-REP-F.2416-2018-PDF-E.pdf](https://www.itu.int/dms_pub/itu-r/opb/rep/R-REP-F.2416-2018-PDF-E.pdf).
6. R. Singh and D. Sicker, "Beyond 5G: THz spectrum futures and implications for wireless communication," in *Proceedings of 30th European Conference of the International Telecommunications Society* (EconStor, 2019), pp. 1–30.
7. J. Ma, R. Shrestha, J. Adelberg, C.-Y. Yeh, Z. Hossain, E. Knightly, J. M. Jornet, and D. M. Mittleman, "Security and eavesdropping in terahertz wireless links," *Nature* **563**(7729), 89–93 (2018).
8. M. F. Hermelo, P.-T. Shih, M. Steeg, A. Ng'oma, and A. Stöhr, "Spectral efficient 64-QAM-OFDM terahertz communication link," *Opt. Express* **25**(16), 19360–19370 (2017).
9. G. Ducournau, P. Szriftgiser, A. Beck, D. Bacquet, F. Pavanello, E. Peytavit, M. Zaknour, T. Akalin, and J. Lampin, "Ultrawide-bandwidth single-channel 0.4-THz wireless link combining broadband quasi-optic photomixer and coherent detection," *IEEE Trans. Terahertz Sci. Technol.* **4**(3), 328–337 (2014).
10. H. Shams, M. J. Fice, K. Balakier, C. C. Renaud, F. van Dijk, and A. J. Seeds, "Photonic generation for multichannel THz wireless communication," *Opt. Express* **22**(19), 23465–23472 (2014).

11. K. Liu, S. Jia, S. Wang, X. Pang, W. Li, S. Zheng, H. Chi, X. Jin, X. Zhang, and X. Yu, "100 Gbit/s THz photonic wireless transmission in the 350-GHz band with extended reach," *IEEE Photonics Technol. Lett.* **30**(11), 1064–1067 (2018).
12. T. Harter, C. Füllner, J. N. Kemal, S. Ummethala, J. L. Steinmann, M. Brosi, J. L. Hesler, E. Bründermann, A.-S. Müller, W. Freude, S. Randel, and C. Koos, "Generalized Kramers–Kronig receiver for coherent terahertz communications," *Nat. Photonics* **14**(10), 601–606 (2020).
13. Y. Zhou, G. Sakano, Y. Yamanaka, H. Ito, T. Ishibashi, and K. Kato, "600-GHz-wave beam steering by terahertz-wave combiner," in *Proceedings of IEEE Conference on Optical Fiber Communications Conference and Exposition (IEEE, 2018)*, pp. 1–3.
14. K.-I. Maki and C. Otani, "Terahertz beam steering and frequency tuning by using the spatial dispersion of ultrafast laser pulses," *Opt. Express* **16**(14), 10158–10169 (2008).
15. M. Che, Y. Matsuo, H. Kanaya, H. Ito, T. Ishibashi, and K. Kato, "Optoelectronic THz-wave beam steering by arrayed photomixers with integrated antennas," *IEEE Photonics Technol. Lett.* **32**(16), 979–982 (2020).
16. ÁJ Pascual-Gracia, M. Ali, G. Carpintero, D. Barrio, F. Ferrero, L. Brochier, R. Sauleau, L. E. García-Muñoz, and D. González-Ovejero, "A photonic-excited leaky-wave antenna array at E-band for 1-D beam steering," *Appl. Sci.* **10**(10), 3474 (2020).
17. M. Steeg and A. Stöhr, "High data rate 6 Gbit/s steerable multibeam 60 GHz antennas for 5G hot-spot use cases," in *Proceedings of IEEE Conference on Summer Topical Meeting Series (IEEE, 2017)*, pp. 141–142.
18. M. Steeg, F. Exner, J. Tebart, A. Czulwik, and A. Stöhr, "OFDM joint communication–radar with leaky-wave antennas," *Electron. Lett.* **56**(21), 1139–1141 (2020).
19. U. Habib, M. Steeg, A. Stöhr, and N. J. Gomes, "Radio-over-fiber-supported 60 GHz multiuser transmission using leaky wave antenna," in *Proceedings of IEEE Conference on Microwave Photonics (IEEE, 2017)*, pp. 1–4.
20. P. Lu, T. Haddad, B. Sievert, B. Khani, S. Makhoulouf, S. Dülme, J. F. Estévez, A. Rennings, D. Erni, U. Pfeiffer, and A. Stöhr, "InP-based THz beam steering leaky-wave antenna," *IEEE Trans. Terahertz Sci. Technol.* **11**(2), 218–230 (2021).
21. S. Dülme, M. Steeg, I. Mohammad, N. Schriniski, J. Tebart, and A. Stöhr, "Ultra-low phase-noise photonic terahertz imaging system based on two-tone square-law detection," *Opt. Express* **28**(20), 29631–29643 (2020).
22. B. Sievert, J. T. Svejda, D. Erni, and A. Rennings, "Spherical mm-wave/THz antenna measurement system," *IEEE Access* **8**, 89680–89691 (2020).
23. M. Steeg, F. Exner, J. Tebart, A. Czulwik, and A. Stöhr, "100 Gbit/s V-band transmission enabled by coherent radio-over-fiber system with IF-OFDM envelope detection and SSBI suppression," in *Proceedings of IEEE Conference on General Assembly and Scientific Symposium of the International Union of Radio Science (IEEE, 2020)*, pp. 1–4.
24. J. L. Hesler and T. W. Crowe, "Responsivity and noise measurements of zero-bias Schottky diode detectors," in *Proceedings of International Symposium on Space Terahertz Technology (Citeseer, 2007)*, pp. 89–92.
25. Z. Li, M. S. Erkiñç, S. Pachnicke, H. Griesser, B. C. Thomsen, P. Bayvel, and R. I. Killey, "Direct-detection 16-QAM Nyquist-shaped subcarrier modulation with SSBI mitigation," in *Proceedings of IEEE International Conference on Communications (IEEE, 2015)*, pp. 5204–5209.
26. Pure Photonics, "Tunable laser products," <https://www.pure-photonics.com/product-solutions/>.

## Article

# Photonic Integrated Circuit for Optical Phase Control of $1 \times 4$ Terahertz Phased Arrays

Peng Lu <sup>1</sup>, Thomas Haddad <sup>1</sup>, Jonas Tebart <sup>1</sup>, Chris Roeloffzen <sup>2</sup> and Andreas Stöhr <sup>1,\*</sup><sup>1</sup> Department of Optoelectronics, University of Duisburg-Essen, Lotharstraße 55, 47057 Duisburg, Germany<sup>2</sup> LioniX International BV, Hengelosestraat 500, 7521 AN Enschede, The Netherlands

\* Correspondence: andreas.stoehr@uni-due.de

**Abstract:** In this manuscript, we report on a  $1 \times 4$  optical beam forming network (OBFN) chip using optical phase shifters (OPSs) based on thermo-optically controlled optical ring resonators (ORRs) for 1D beam steering at 0.3 THz. The  $1 \times 4$  OBFN chip consists of four OPSs and is fabricated using TriPleX technology. Each of the four OPSs is realized by two cascaded identical ORRs, to reach a phase shift of  $2\pi$ . To allow transfer of the optical phase shift to the THz domain by optical heterodyning in high-frequency  $1.55 \mu\text{m}$  modified uni-travelling carrier photodiodes, the ORRs are designed such that one carrier of the optical heterodyne signal is at the ORR's resonance frequency, whereas the second optical heterodyne signal is at its off-resonance. By adjusting the resonance frequencies of the two ORRs in each OPS synchronously, a relative phase variation between two optical heterodyne carriers of up to  $2\pi$  with a tuning efficiency of  $0.058 \text{ W}/\pi$ , is experimentally demonstrated. Due to the dispersive power transmission loss of the ORRs, phase tuning leads to a power variation of the optical heterodyne-generated signals up to 3.8 dB, which is experimentally characterized at 0.295 THz. It is shown numerically that this power variation only has a minor impact on the steering performance of a  $1 \times 4$  phased array. The determined beam direction deviation and maximum absolute radiation power change are smaller than  $1^\circ$  and 2 dB, respectively. By sweeping the phase difference between two adjacent THz antennas in the  $1 \times 4$  phased array, from  $-120^\circ$  to  $120^\circ$ , a beam steering range of  $\sim 62^\circ$  is demonstrated numerically at 0.295 THz.



**Citation:** Lu, P.; Haddad, T.; Tebart, J.; Roeloffzen, C.; Stöhr, A. Photonic Integrated Circuit for Optical Phase Control of  $1 \times 4$  Terahertz Phased Arrays. *Photonics* **2022**, *9*, 902. <https://doi.org/10.3390/photonics9120902>

Received: 12 October 2022  
Accepted: 23 November 2022  
Published: 25 November 2022

**Publisher's Note:** MDPI stays neutral with regard to jurisdictional claims in published maps and institutional affiliations.



**Copyright:** © 2022 by the authors. Licensee MDPI, Basel, Switzerland. This article is an open access article distributed under the terms and conditions of the Creative Commons Attribution (CC BY) license (<https://creativecommons.org/licenses/by/4.0/>).

**Keywords:** THz beam steering; optical phase shifter; optical ring resonator; TriPleX; dielectric rod waveguide; phased array

## 1. Introduction

Photonic-based THz systems have been intensively investigated for various applications, e.g., communications [1,2], spectroscopy [3,4] and imaging [5], because they offer wide operational bandwidths, superior phase noise, and low loss transmission over long distances using optical fibers. For applications such as long-range THz communications, the high free-space path loss together with the limited transmit power, necessitate the use of high-gain directional THz antennas. This, in turn, requires photonic THz beam steering technologies which can be generally classified into two categories: namely frequency-steering using leaky-wave antennas (LWAs), and frequency independent steering using phased-array antennas. LWAs offer a quite attractive approach for THz beam steering, since the beam direction can be easily adjusted by tuning the operating frequency. Especially in combination with envelope detection, first high data rate mobile THz communications have been demonstrated [6]. However, for THz spectroscopy or imaging applications, frequency independent photonic THz beam steering approaches are required. In [7], fiber-based optical delay lines are used to adjust the time delays for a  $1 \times 4$  photomixer array. This way, a maximum beam steering angle of  $35^\circ$  at 0.6 THz has been achieved. However, the fiber-based optical delay lines prevent compact integration. First, chip integrated delay

lines using Mach–Zehnder-based switched delay lines for sub-THz range, were demonstrated, e.g., in [8]. The disadvantage is that only discrete beam angles are supported, and for a high beam angle resolution, several 10 s of thermo-optical switches would be required, leading to a high-power consumption. Since the beam squint effect becomes less dominant in the THz domain [9], optical phase shifters (OPSs) for phased-array antennas have also been investigated. Using OPSs based on thermo-optically controlled straight silica waveguides [10], continuous beam steering at 0.3 THz is demonstrated, with a maximum steering angle of  $50^\circ$ . In this approach, only one heater is required for each OPS. However, the phase tuning efficiency of  $0.24 \text{ W}/\pi$  is relatively low.

Due to the low optical propagation losses,  $\text{Si}_3\text{N}_4/\text{SiO}_2$ -based TriPleX waveguides have been exploited for a number of applications, such as reconfigurable photonic RF filters [11], high-granularity wavelength division multiplexers [12], high-order ring resonators [13] and programmable optical signal processor chips [14]. Additionally, on-chip optical true time delays (TTDs) consisting of optical ring resonators (ORRs) are reported for continuous beam steering at microwave frequencies [15–17]. Using the separate carrier tuning technique, the phase shift of the optical carrier can be adjusted to compensate for the nonlinearity of the phase response of TTDs [18]. However, this approach is not easily scalable to THz frequencies, as the beam angle becomes much more sensitive to time delay variations at THz frequencies. As an example, a time delay variation of only 30 fs would lead to a beam deviation of  $\sim 1^\circ$  at 0.3 THz. Consequently, to reach a constant time delay over a reasonable bandwidth, one would need to cascade a multifold of ORRs leading to higher power consumption, and substantially more complex control circuitry.

In this manuscript, we report on the design and experimental characterization of a TriPleX-based  $1 \times 4$  OBFN chip with 4 OPSs for continuous beam steering at 0.3 THz. Each OPS consists of two cascaded ORRs. The fabricated OBFN chip enables the transfer of the optical phase shift to the THz domain, by optical heterodyne THz signal generation in high-frequency modified uni-traveling carrier photodiodes (MUTC-PDs). To support optical heterodyning, the ORRs are designed such that one laser signal is at the ORR's resonance frequency, while the other optical carrier of the heterodyne signal is at the off-resonance frequency. The manuscript demonstrates experimentally that the fabricated  $1 \times 4$  OBFN chip yields optical phase shifts up to  $2\pi$ , with a tuning efficiency of  $0.058 \text{ W}/\pi$ . Furthermore, the inherent THz power variation during phase tuning due to the dispersive power transmission loss of the ORRs, is experimentally characterized at 0.295 THz. It is shown numerically using CST Studio Suite that these power variations only have a negligible impact on the steering angle. It is furthermore determined numerically that the maximum beam steering angle for a  $1 \times 4$  phased array employing THz bow-tie antennas, is  $62^\circ$  at 0.295 THz.

## 2. Optical Beam Forming Network Chip

The concept of the  $1 \times 4$  OBFN chip with integrated MUTC-PDs for 1D beam steering at 0.3 THz, based on optical heterodyning, is shown in Figure 1a. The OBFN chip is designed and fabricated based on the  $\text{Si}_3\text{N}_4/\text{SiO}_2$  TriPleX platform [19], providing a low optical propagation loss, as well as a high optical confinement factor. Optical heterodyne laser signals ( $\sim 1.55 \mu\text{m}$ ) with a difference frequency of 0.3 THz, are combined and coupled into the OBFN chip. Three Mach–Zehnder interferometers (MZIs) are used as tunable optical splitters to adjust the power distribution into each waveguide, and to compensate for the non-uniform responsivity of the MUTC-PDs. Each OPS consists of two cascaded identical ORRs. The coupler heaters of the rings are used to change the power coupling coefficients, and thus to modify the slope of ORR's phase response. By changing the biases of the ring heaters, the ORR's resonance frequency offsets are shifted which allows it to modify the phase difference between the two optical heterodyne signals. Finally, MUTC-PDs are exploited to transfer the optical phase shift into the THz domain and by integrating the MUTC-PD array with antennas having a half-wavelength pitch, the THz beam direction can be controlled by the OBFN chip.

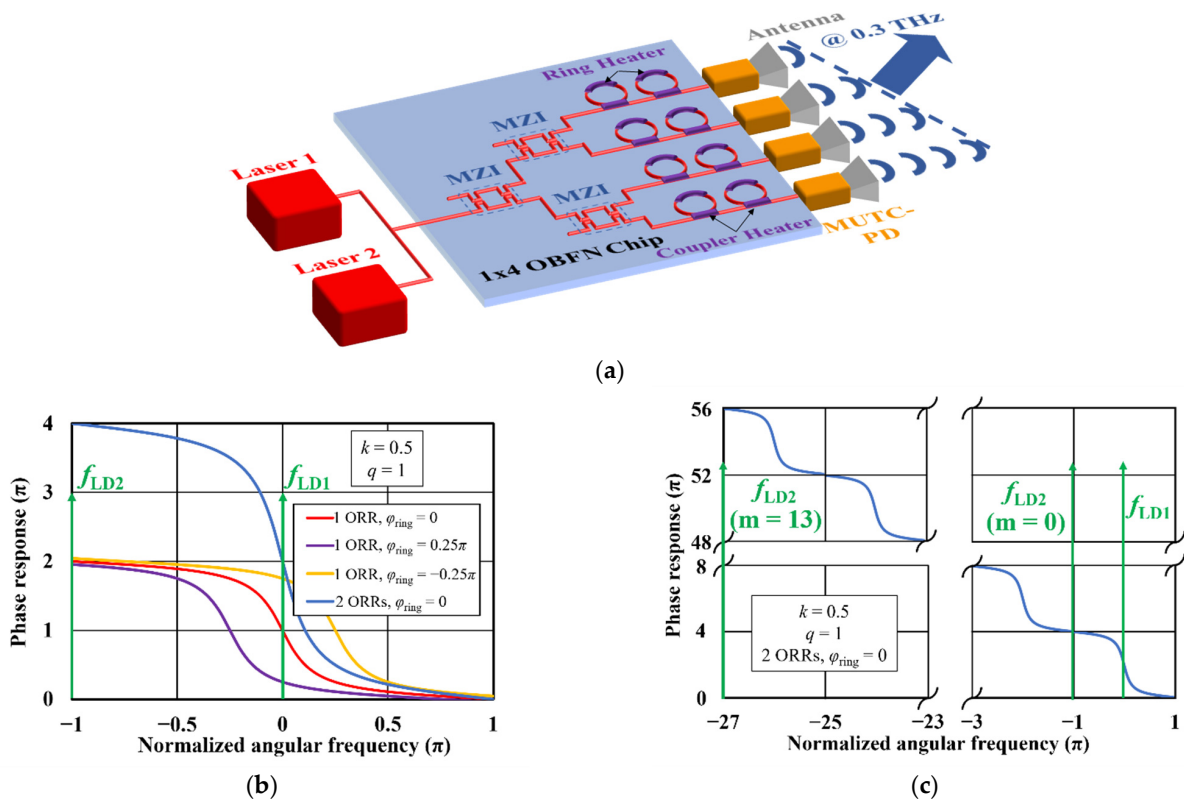


**Figure 1.** (a) Concept of the  $1 \times 4$  OBFN chip with integrated MUTC-PDs for 1D beam steering at 0.3 THz. (b) Calculated phase response within one FSR for a single ORR with different round-trip phase shifts  $\varphi_{\text{ring}}$  as well as for two cascaded ORRs with the same resonance frequency. The power coupling coefficient  $k$  is 0.5 and the amplitude loss factor  $q$  is 1. (c) Calculated phase response within fourteen FSRs for two cascaded ORRs with the same resonance frequency. The power coupling coefficient  $k$  is 0.5 and the amplitude loss factor  $q$  is 1.

In detail, the phase response of a single ORR under the condition of over-coupling range can be calculated as follows [20]:

$$\varphi(\Omega) = \pi - (2\Omega + \varphi_{\text{ring}}) - \arctan \left[ \frac{\sqrt{1-k} \cdot \sin(\Omega + \varphi_{\text{ring}})}{q - \sqrt{1-k} \cdot \cos(\Omega + \varphi_{\text{ring}})} \right] - \arctan \left[ \frac{q \cdot \sqrt{1-k} \cdot \sin(\Omega + \varphi_{\text{ring}})}{1 - q \cdot \sqrt{1-k} \cdot \cos(\Omega + \varphi_{\text{ring}})} \right], \quad (1)$$

where  $\Omega$  is the normalized angular frequency to the free spectral range (FSR) of the ORR ( $\Omega = 2 \cdot \pi \cdot f / f_{\text{FSR}}$ ),  $\varphi_{\text{ring}}$  is the round-trip phase shift which indicates the resonance frequency offset of the ORR ( $\varphi_{\text{ring}} = 2 \cdot \pi \cdot f_{\text{res,offset}} / f_{\text{FSR}}$ ), and  $k$  is the power coupling coefficient. The amplitude loss factor  $q$  is a function of the round-trip loss  $P_L$ :

$$q = 10^{-P_L/20}. \quad (2)$$

For a lossless ORR ( $q = 1$ ) with a power coupling coefficient of 0.5, the calculated phase response of a single ORR ( $\varphi_{\text{ring}} = 0$ ) over one FSR (red line), is shown in Figure 1b. As discussed before, the ORR is designed in such a way that one laser signal ( $f_{\text{LD1}}$ ) is fixed at the ring's resonance frequency, while the other heterodyne signal ( $f_{\text{LD2}}$ ) is fixed at the off-resonance frequency. By changing  $\varphi_{\text{ring}}$  through the ring heater, the phase response can be shifted, as shown in Figure 1b, by the purple and yellow lines. This allows it to impose different optical phase variations of the two laser signals, which are then transferred to the THz domain using the MUTC-PDs with  $\Delta\varphi_{\text{THz}} = \Delta\varphi_{\text{LD1}} - \Delta\varphi_{\text{LD2}}$  [21]. Since the maximum phase tunable range of the laser signal 1 ( $\Delta\varphi_{\text{LD1,max}}$ ) is  $2\pi$  when changing  $\varphi_{\text{ring}}$  from  $-\pi$  to

$\pi$  which synchronously leads to variations of  $\varphi_{LD2}$  ( $\Delta\varphi_{LD2} \neq 0$ ), it is necessary to use two cascaded ORRs for each OPS (blue line in Figure 1b) to achieve a THz phase shift  $\Delta\varphi_{THz}$  of at least  $2\pi$ . It can also be observed from Figure 1b that the FSR of the ORRs must be twice as large as the operating frequency, i.e., 0.6 THz, in order to fix one laser signal at resonance, and the one at off-resonance. The corresponding ORR round-trip length  $L$  for an FSR of 0.6 THz should be 0.282 mm in the optimum case, which can be calculated using

$$L = \frac{c_0}{n_g \cdot f_{FSR}}, \tag{3}$$

where  $n_g$  is the group index of TriPleX waveguides and equal to 1.777. However, the minimum round-trip length of a fabricated ORR must be larger than 7 mm, due to the required heater length for thermo-optical control. This leads to a maximum FSR of 24.1 GHz, which is much smaller than the optimum value. However, thanks to the periodicity of ORRs, the condition  $f_{LD2}$  at the off-resonance frequency and  $f_{LD1}$  at the resonance frequency can be satisfied, if an FSR meets the following condition:

$$|f_{LD1} - f_{LD2}| = (m + \frac{1}{2}) \cdot f_{FSR}, \tag{4}$$

where  $m$  is a natural number. As can be seen from Figure 1c, the phase shift of laser signal with  $f_{LD2}$  ( $m = 13$ ) is equal to that with  $f_{LD2}$  ( $m = 0$ ). Consequently, all ORRs in this work are designed with an FSR of 22.22 GHz.

To eventually use the fabricated OBFN chip for beam steering, the thermo-optically controlled power coupling coefficient  $k$  and the resonance frequency offset  $f_{res,offset}$  must be determined for each ORR, as a function of the coupler and ring heater voltages, respectively. To determine the power coupling coefficient, the group delay  $\tau_g$  is experimentally characterized using the wavelength-sweeping approach [22] for coupler heater voltages from 4 V to 12 V. The power coupling coefficient  $k$  can then be determined from the measured group delay using [20]

$$\tau_g(\Omega) = T + \frac{q \cdot \sqrt{1-k} \cdot \cos(\Omega + \varphi_{ring}) - (1-k)}{(1-k) - 2q \cdot \sqrt{1-k} \cdot \cos(\Omega + \varphi_{ring}) + q^2} \cdot T + \frac{q \cdot \sqrt{1-k} \cdot \cos(\Omega + \varphi_{ring}) - q^2 \cdot (1-k)}{1 - 2q \cdot \sqrt{1-k} \cdot \cos(\Omega + \varphi_{ring}) + q^2 \cdot (1-k)} \cdot T. \tag{5}$$

For the fabricated OBFN chip, the measured optical propagation loss is  $\sim 0.7$  dB/cm. By considering the round-trip length of 7.59 mm, the round-trip loss  $P_L$  can be calculated to be 0.5 dB. This leads to an amplitude loss factor  $q$  of 0.944. The round-trip time  $T$  can be calculated using  $T = 1/f_{FSR}$ . Figure 2a shows the measured power coupling coefficient  $k$  as a function of the coupler heater bias. As can be seen, the power coupling coefficient increases from  $\sim 0.19$  to  $\sim 1$  by changing the bias voltage from 4 V to 12 V. Using a coupler heater bias of  $\sim 8.3$  V, the power coupling coefficient can be set to 0.5.

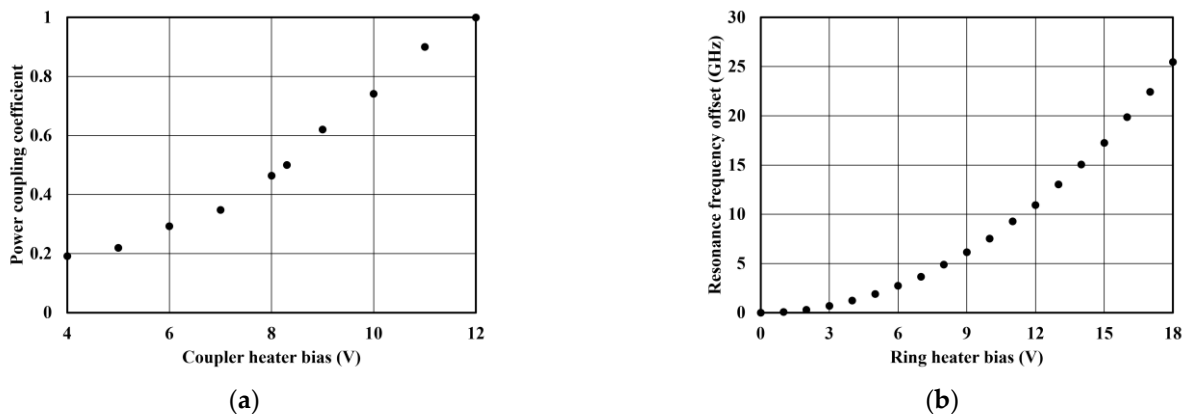


**Figure 2.** Measured power coupling coefficient as a function of coupler heater bias (a) and measured resonance frequency offset as a function of ring heater bias (b), of an ORR.

The resonance frequency offsets of ORRs are determined experimentally using a high-resolution optical spectrum analyzer (OSA, AP2060A, APEX Technologies, Marcoussis, France). Figure 2b shows the measured resonance frequency offset versus the ring heater bias. As can be seen, to shift the resonance frequency over one FSR, a bias voltage of ~17 V is required. For developing the control algorithm software, the measured resonance offset frequency is fitted using a sixth order polynomial equation

$$f_{\text{res.offset}} = 1 \cdot 10^{-6} \cdot U_r^6 - 7 \cdot 10^{-5} \cdot U_r^5 + 0.0013 \cdot U_r^4 - 0.0109 \cdot U_r^3 + 0.1147 \cdot U_r^2 - 0.0459 \cdot U_r + 0.0056, \quad (6)$$

where  $U_r$  is ring heater bias.

Based on the measurements, the power coupling coefficients of all ORRs are then set to 0.5 and the ring heaters are tuned to have the same resonance frequency in all ORRs. This is defined as the initial state for the OBFN chip, where the phase shifts of all OPSs are the same. Figure 3 shows the optical frequency response of one OPS at the initial state. As can be seen, the two resonance frequencies are at 193.4001 THz and 193.4220 THz, indicating an FSR of ~21.9 GHz. Due to this slight deviation from the designed value of 22.22 GHz (<1.5%), the fabricated OBFN chip is ideally suited for 295.65 GHz, according to Equation (4).

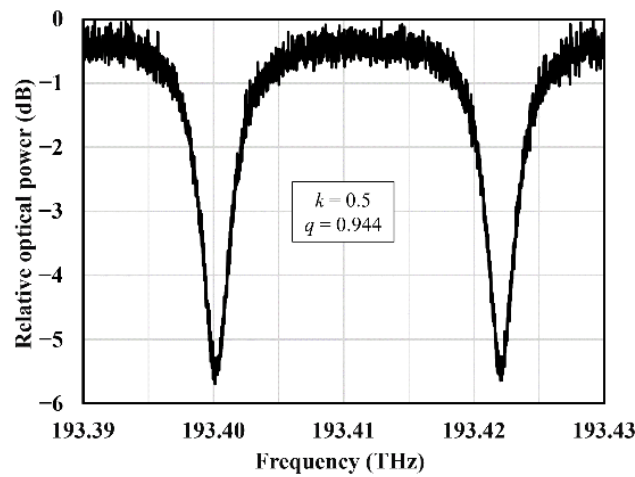


Figure 3. Measured optical frequency response of two cascaded ORRs at the same resonance frequency.

### 3. Phase Shift Characterization

To measure the phase shift between two PDs when changing the biases of ring heaters of the fabricated OBFN chip, the measurement setup shown in Figure 4 is used. Two optical heterodyne signals (@1.55 μm) are generated using two free running integrable tunable laser assemblies (PPCL200, Pure Photonics, San Jose, CA, USA). After amplification by an erbium-doped fiber amplifier (EDFA, EDFA100P, Thorlabs, Newton, NJ, USA), an optical polarization controller is used to ensure minimum optical losses due to the large polarization birefringence of TriPleX waveguides [23]. A heater control system is developed and implemented to precisely regulate the bias of each on-chip heater. The OBFN chip is mounted on a heat sink with a thermo-electric cooler (TEC) regulated by a temperature controller (TED4015, Thorlabs, Dachau/Munich, Germany) at ~20 °C. To measure the phase difference between the two waveguide ports (WPs), two PDs are fiber-chip coupled to WP1 and WP2. Optical delay lines (ODLs, Newport, Irvine, CA, USA) are used to compensate for the fiber length difference between the two PDs and the OBFN chip. A digital signal analyzer (DSA, DSA-Z 634A, Keysight, Santa Rosa, CA, USA) is used to measure the amplitudes of the PD-generated RF signals in time domain.

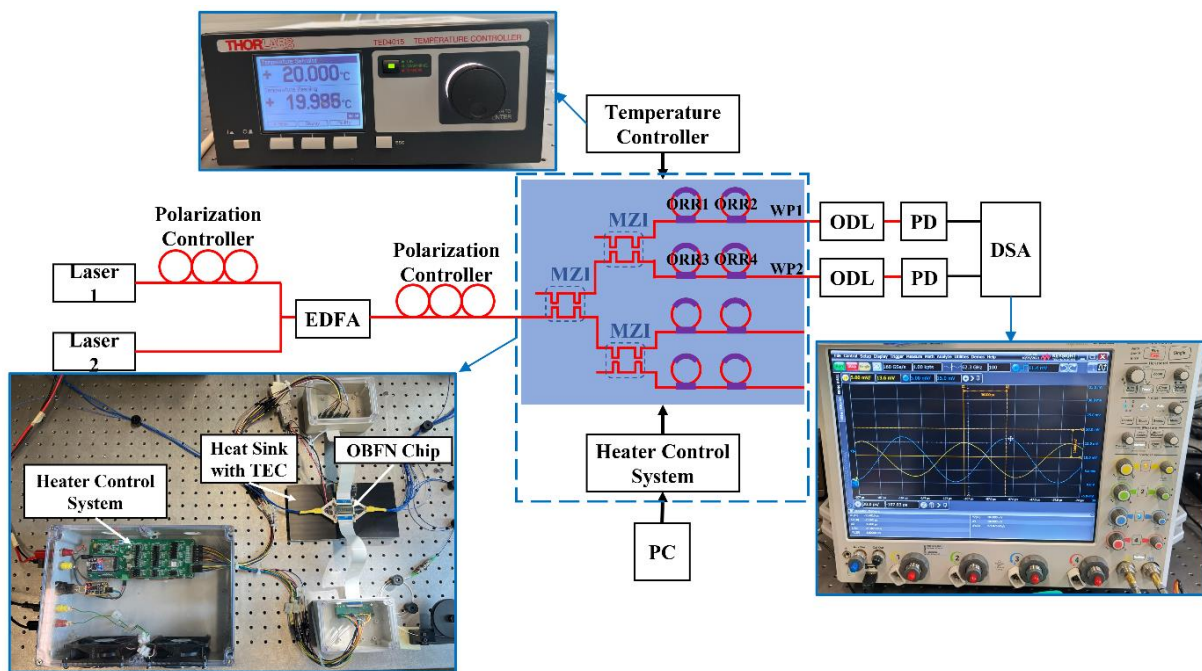
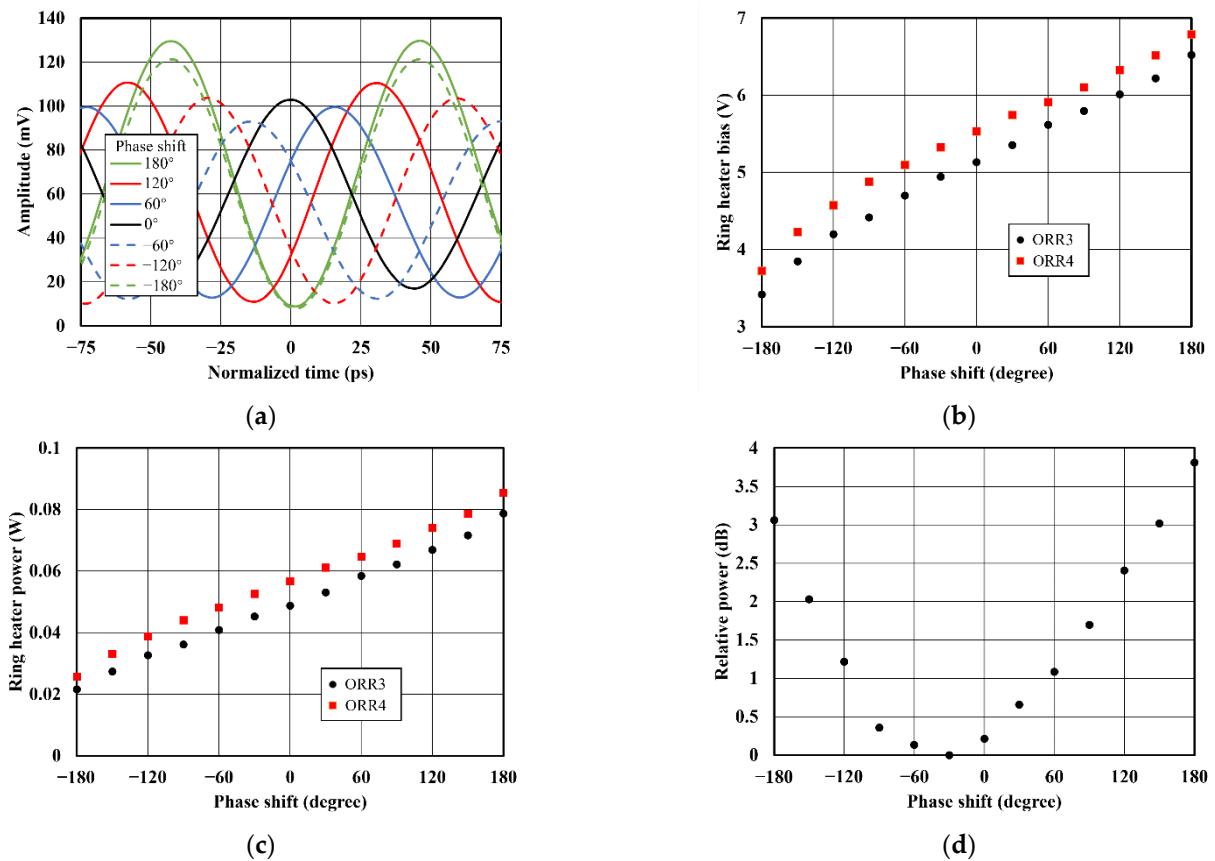


Figure 4. Measurement setup for phase shift characterization.

Before experimental characterization, all ORRs are set to be in the initial state with a power coupling coefficient of 0.5 and a resonance frequency of 193.4001 THz, using the heater control system. Since the analog bandwidth of the DSA is limited to 63 GHz, the phase shift between the two WPs cannot be measured directly in the THz domain. However, thanks to the periodicity of the ORRs, it is still possible to measure the THz phase shift using lower microwave frequencies. As explained above, all frequencies  $f_{LD1}$  and  $f_{LD2}$  that fulfill Equation (4) experience the same phase shift. This means when fixing  $f_{LD1}$  at 193.4001 THz (resonance frequency of the ORRs), the phase shift for  $f_{LD2} = 193.41105$  THz (with  $m = 0$ ) is same as for  $f_{LD2} = 193.69575$  THz (with  $m = 13$ ), as shown in Figure 1c. Therefore, the resulting phase shift for an RF signal at 10.95 GHz, is the same as for an RF frequency at 295.65 GHz.

During the measurements at an RF frequency of 10.95 GHz, the signal generated by the PD at WP1 (see Figure 4) is set as a trigger for the DSA, before tuning the two cascaded ORRs (ORR3 and ORR4) of the OPS for WP2. The RF signal measured this way is plotted in Figure 5a. As can be observed, the time delay of the 10.95 GHz signal is successfully changed when tuning the ORRs. The amplitude with a peak at the normalized time of 0 ps (black solid line) corresponds to the initial state of the OBFN chip. By increasing the ring heater biases, the time delay of the measured RF signal at 10.95 GHz is tuned to ~15.2 ps (blue solid line), ~30.5 ps (red solid line) and ~45.7 ps (green solid line). This corresponds to phase shifts of ~60°, ~120° and ~180°, respectively. Inverse phase shifts down to -180° can be achieved by reducing the ring heater biases, as shown by the dashed lines. Therefore, in total, a phase tuning of  $2\pi$  is achieved. The corresponding ring heater bias settings are plotted in Figure 5b. As can be seen, the ring heater biases of the two ORRs are slightly different due to fabrication tolerances. To achieve a  $2\pi$  phase shift, the ring heater bias of the ORR3 is changed from 3.42 V to 6.52 V, while the bias of the ORR4 is increased from 3.72 V to 6.79 V. Using the measured heater resistance of 540  $\Omega$ , the dissipative powers of the two heaters are calculated and plotted in Figure 5c. Consequently, a phase tuning efficiency of 0.058 W/ $\pi$  is achieved.



**Figure 5.** (a) Measured amplitudes of the 10.95 GHz signal (WP2) for various ring heater biases in time domain. (b) Measured ring heater biases of the ORR3 and ORR4 for phase shifts from  $-180^\circ$  to  $180^\circ$ . (c) Calculated dissipative ring heater powers of the ORR3 and ORR4 for phase shifts from  $-180^\circ$  to  $180^\circ$ . (d) Measured relative output power of a MUTC-PD at 0.295 THz for phase shifts from  $-180^\circ$  to  $180^\circ$ .

From Figure 5a, it can be also observed that the amplitudes of the 10.95 GHz signal vary for different phase shifts. This is because the dispersive power transmission loss of the ORRs causes a power variation when tuning the phase, especially for the laser signal at resonance frequency. As can be seen, the maximum amplitude deviation is  $\sim 40.15$  mV when comparing the amplitudes of the RF signals with phase shifts of  $180^\circ$  and  $-60^\circ$ . To systematically analyze the impact of this inherent power variation on THz beam steering performance of a  $1 \times 4$  phased array, we measured the output power of a MUTC-PD (J-band photomixer module, NTT Electronics, Yokohama, Japan) at 0.295 THz for different phase shifts, using a zero-biased Schottky-barrier diode (SBD, WR3.4 ZBD, Virginia Diodes, Charlottesville, VA, USA) as power detector. The results are plotted in Figure 5d. As can be seen, the minimum relative power is measured at a phase shift of  $-30^\circ$  instead of  $0^\circ$ . This is traced back to the fact that the laser wavelength did not perfectly match the ORR’s resonance frequency during the experiments. For the full phase tuning range of  $2\pi$ , the measured maximum THz output power variation is about 3.8 dB.

#### 4. THz Beam Steering

Using CST Studio Suite, we numerically analyze the impact of the measured THz power variation on the beam steering performance. This is done for a  $1 \times 4$  phased array featuring four bow-tie (BT) antennas with a pitch of  $500 \mu\text{m}$  placed on a  $100 \mu\text{m}$  thick InP substrate. To increase the directivity of this approach, InP-based dielectric rod waveguide (DRW) antennas are placed underneath the BT antennas (see inset in Figure 6). Each DRW antenna has a thickness  $d$  of  $150 \mu\text{m}$  and a length  $l$  of  $3500 \mu\text{m}$ . The width  $w$  is  $500 \mu\text{m}$ . To

fix the DRW antennas in practice, they can be mounted using a low permittivity material such as ROHACELL [24], glued on the backside of the InP substrate.

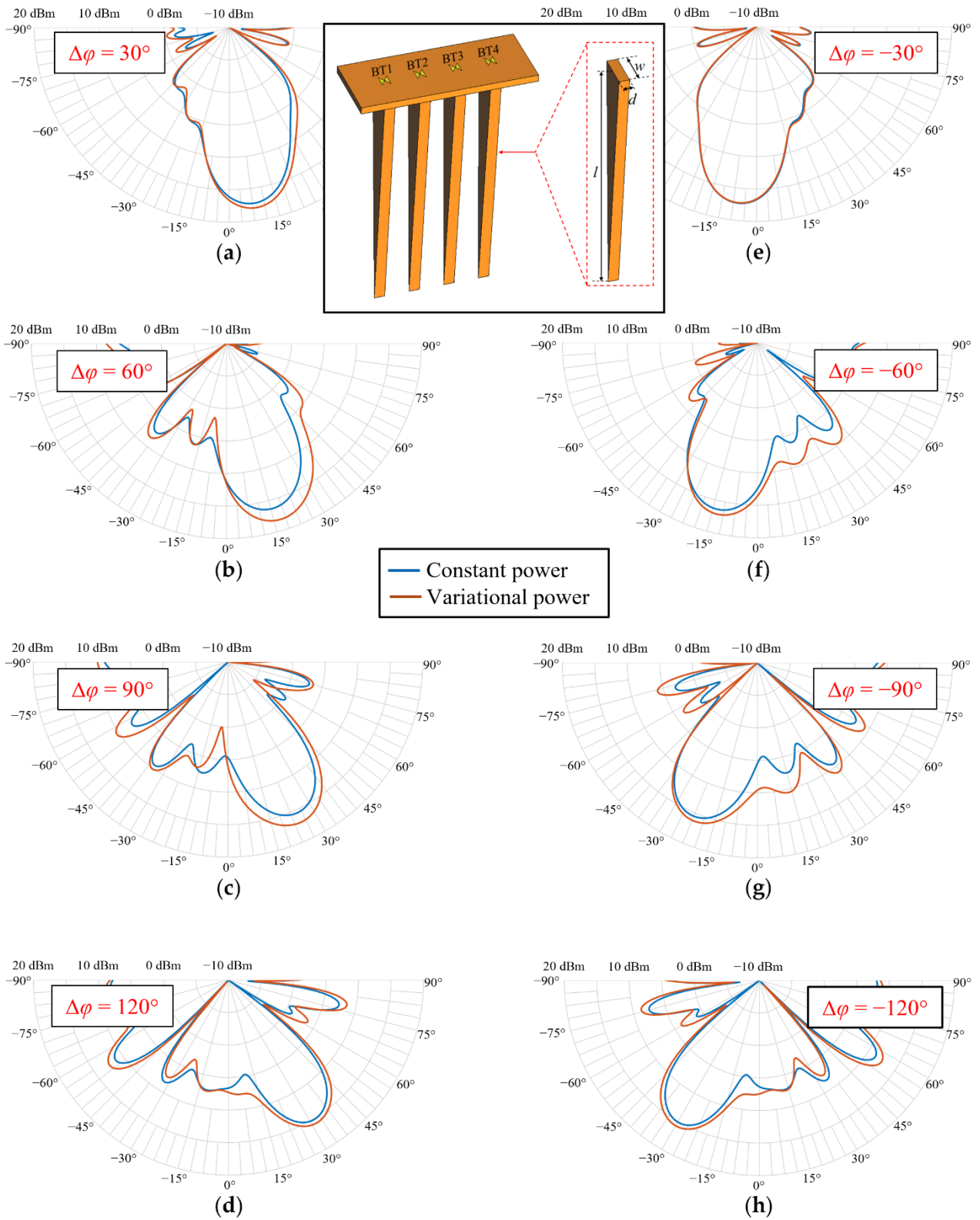


**Figure 6.** Simulated polar diagrams of absolute radiation powers of a  $1 \times 4$  phased array with constant (blue lines) and variational (red lines) powers at 0.295 THz for phase differences between two adjacent antennas of (a)  $30^\circ$ , (b)  $60^\circ$ , (c)  $90^\circ$ , (d)  $120^\circ$ , (e)  $-30^\circ$ , (f)  $-60^\circ$ , (g)  $-90^\circ$  and (h)  $-120^\circ$ . The inset shows a schematic drawing of the  $1 \times 4$  phased array with DRWs.

The beam steering behavior of the  $1 \times 4$  array is investigated for two cases: (a) for a constant power at each BT antenna, and (b) when considering the measured power variations described in Section 3. In both scenarios, the phase difference between two adjacent antennas  $\Delta\varphi$  is adjusted between  $-120^\circ$  and  $120^\circ$ , with a step size of  $30^\circ$ . Phase differences larger than  $120^\circ$  would be possible using the fabricated OBFN, but would lead to substantially higher side lobes, and thus lower directivity and gain. Table 1 summarizes the parameters for each of the four antennas used in the simulations. For the constant power scenario, all antennas have the same constant input power of 0.21 dBm, independent from the phase difference. This value is defined by the power level at the phase shift of  $0^\circ$  when the power level at  $-30^\circ$  is assumed to be 0 dBm (see Figure 5d). The phase of the BT1 maintains constant, and the phases of the other antennas are accordingly adjusted. For example, for a phase difference  $\Delta\varphi$  of  $30^\circ$ , the phases of BT1 to BT4 are set to be  $0^\circ, 30^\circ, 60^\circ$  and  $90^\circ$ . The corresponding polar diagrams of the absolute radiation power as a function of beam angle, which is the sum of the total input power of the four BT antennas in dBm and the simulated realized gain, are illustrated in Figure 6a–h for all phase differences (blue lines). As can be seen, the beam angle is  $31^\circ$  for a phase difference between two adjacent antennas of  $120^\circ$ . The maximum absolute radiation power is always in excess of 15.2 dBm, independent of the phase difference. When using negative phase shifts, the beam turns to the inverse direction. The maximum beam steering angle that can be achieved is  $\sim 62^\circ$ .

**Table 1.** Parameters for numerical analyses of constant power and variational power scenarios at 0.295 THz.

Phase Difference between Two Adjacent Antennas	Antenna												Figure
	BT1			BT2			BT3			BT4			
	Phase	Input Power (dBm)		Phase	Input Power (dBm)		Phase	Input Power (dBm)		Phase	Input Power (dBm)		
		Constant Power	Variational Power		Constant Power	Variational Power		Constant Power	Variational Power		Constant Power	Variational Power	
$30^\circ$	$0^\circ$	0.21	0.21	$30^\circ$	0.21	0.66	$60^\circ$	0.21	1.09	$90^\circ$	0.21	1.70	Figure 6a
$60^\circ$	$0^\circ$	0.21	0.21	$60^\circ$	0.21	1.09	$120^\circ$	0.21	2.40	$180^\circ$	0.21	3.81	Figure 6b
$90^\circ$	$0^\circ$	0.21	0.21	$90^\circ$	0.21	1.70	$180^\circ$	0.21	3.81	$270^\circ$	0.21	0.36	Figure 6c
$120^\circ$	$0^\circ$	0.21	0.21	$120^\circ$	0.21	2.40	$240^\circ$	0.21	1.22	$360^\circ$	0.21	0.21	Figure 6d
$-30^\circ$	$0^\circ$	0.21	0.21	$-30^\circ$	0.21	0	$-60^\circ$	0.21	0.13	$-90^\circ$	0.21	0.36	Figure 6e
$-60^\circ$	$0^\circ$	0.21	0.21	$-60^\circ$	0.21	0.13	$-120^\circ$	0.21	1.22	$-180^\circ$	0.21	3.06	Figure 6f
$-90^\circ$	$0^\circ$	0.21	0.21	$-90^\circ$	0.21	0.36	$-180^\circ$	0.21	3.06	$-270^\circ$	0.21	1.70	Figure 6g
$-120^\circ$	$0^\circ$	0.21	0.21	$-120^\circ$	0.21	1.22	$-240^\circ$	0.21	2.40	$-360^\circ$	0.21	0.21	Figure 6h

In the second scenario with varying antenna input powers, the simulated phase settings are the same as for the constant power scenario; only the input power for each antenna is set according to the measurement results, presented in Figure 5d, when the power level at  $-30^\circ$  is assumed to be 0 dBm as well. It needs to be mentioned that due to the phase periodicity, the power levels at negative phases (from  $0^\circ$  to  $-180^\circ$ ) can be used for powers at phases between  $180^\circ$  and  $360^\circ$ , e.g., the measured value at  $-120^\circ$  is used for the power level at  $240^\circ$ . The power levels for phases between  $-180^\circ$  and  $-360^\circ$  are determined in the same manner. The resulting polar diagrams of the absolute radiation power (red lines) are presented in Figure 6a–h as well. As can be seen, the radiation patterns, including the power variations, show a good agreement with those of where the power levels at each antenna are set to be constant. In general, the observed deviations of beam direction and maximum absolute radiation power are lower than  $1^\circ$  and 0.8 dB, respectively. Only for the phase differences of  $60^\circ$  and  $90^\circ$ , a larger power mismatch of  $<2$  dB can be noticed, which is still reasonable. Thus, it is concluded that the inherent power variations when using the OBFN chip only have a minor impact on the steering performance of the phased array.

## 5. Discussion

In the last decade, thermo-optically controlled ORRs have been used to realize on-chip TTDs, supporting optical heterodyning for phased array at microwave frequencies to overcome the beam squint effect. For example, using two cascaded ORRs, the time delay is tunable up to 139.7 ps for a bandwidth of 8 GHz [15]. In [16], three ORRs are used in each delay unit for 41 GHz RF signals. A delay tuning range of 208.7 ps is demonstrated with a bandwidth of 6.3 GHz. In these two approaches, the time delay is managed by individually and diversely changing the power coupling coefficients of ORRs in each delay unit. Meanwhile, the resonance frequency of each ring must be adjusted synergistically and precisely to guarantee a reasonable ripple (within several picoseconds) for microwave frequencies. Another TTD for the 20 GHz band using a single ORR was demonstrated in [17]. A delay tuning range of 26.6 ps is achieved by changing the coupler bias voltage from 12 V to 16 V, with a bandwidth of 5 GHz. Since MZIs are used as tunable couplers, delay adjustment will lead to the drift of the ORR resonance frequency which must be compensated using the ring heater voltage. The aforementioned approaches, regardless of the number of ORRs used for TTDs, require two additional ORRs for the phase shift adjustment of the optical heterodyne carrier; this compensates for the nonlinearity of the phase response of TTDs [18], which further complicates the chip control, and increases the electrical power consumption.

In the THz domain, the beam angle becomes much more sensitive to time delay variations, as discussed in Section 1. At 0.3 THz, the signal period is 3.33 ps and the beam direction can be steered of  $\sim 1^\circ$ , with a time delay variation of only 30 fs. To achieve such high required delay tuning precisely, using ORR-based TTDs while keeping the ripple in the magnitude of femtoseconds, substantially more complex control circuitry is essential.

Due to the less dominant beam squint effect in the THz domain [9], we developed the OPSs with two cascaded and identical ORRs in each, offering comparably simple control circuitry. Here, the coupler heater voltages are maintained constant after setting the power coupling coefficient of 0.5. A phase tuning range up to  $2\pi$  is achieved by uniformly adjusting the resonance frequencies of two ORRs, without the complicated and synergistic handling needed for TTDs. Compared with the OPSs based on straight waveguides, with only one heater for each control unit [10], the approach presented in this work demonstrates two inimitable merits. Firstly, the sharper phase response slope around resonance frequencies of ORRs, compared to that of straight waveguides, enables a higher phase tuning efficiency. In addition, the ORR-based OPSs are able to impose different optical phase variations on two combined optical heterodyne signals, due to the dispersive phase response of ORRs. Therefore, only one optical input is required for the OBFN chip, leading to a concise layout, as shown in Figure 1a. In contrast to that, the OPSs based on straight waveguides can be used only for the phase tuning of one optical carrier. Other passive optical waveguides are necessary to combine the second optical heterodyne signal behind each OPS. Consequently, two optical inputs are necessary for the OBFN chip. This leads to inevitable waveguide intersections on the chip and higher optical loss, especially for large phased arrays.

The OBFN chip reported in this work can be further optimized by replacing the MZIs used in each ORR as tunable couplers by 3 dB directional couplers, since the power coupling coefficients of all ORRs maintain 0.5 during the phase tuning. This way, the footprint and the power consumption of the chip can be further reduced. In Table 2, a summary of the OBFN chips discussed above is given.

**Table 2.** Comparison of OBFN chips supporting optical heterodyning for phased arrays.

Ref.	Frequency (GHz)	Control Unit	Number of Heaters in Each Control Unit	Waveguide Intersection	Tuning Efficiency	Control Circuitry
[15]	N/A (Microwaves)	TTD	8 (4 for TTD, 4 for SCT)	No	Low	Complicated
[16]	41	TTD	10 (6 for TTD, 4 for SCT)	No	Low	Complicated
[17]	20	TTD	6 (2 for TTD, 4 for SCT)	No	Low	Complicated
[10]	300	OPS	1	Yes	Intermediate (0.24 W/π)	Simple
This work	300	OPS	4/2 *	No	High (0.058 W/π)	Comparably simple

\* The heater number can be reduced to two using 3 dB directional couplers instead of MZIs for ORRs.

## 6. Conclusions

In this manuscript, we reported on the design and experimental characterization of a  $1 \times 4$  OBFN chip for continuous beam steering at 0.3 THz. The TriPleX-based OBFN chip consists of four OPSs and three MZIs, to control the phase and the power of the optical heterodyne THz signal at each transmit antenna, respectively. Two cascaded ORRs are used for each OPS to reach a maximum THz phase shift of at least  $2\pi$ . The ORRs are designed in a way to only impose a tunable phase shift on one of the optical heterodyne signals, whereas the phase of the second optical carrier remains quasi-unchanged. Experimentally, THz phase tuning up to  $2\pi$  with a tuning efficiency of only  $0.058 \text{ W}/\pi$  per OPS, is demonstrated. A maximum inherent power variation of 3.8 dB is experimentally observed at 0.295 THz, when changing the phase. This is traced back to the dispersive power transmission loss of the ORRs. It is shown numerically using CST Studio Suite that the power variations only have a minor impact on the steering performance. The deviations in beam direction and maximum absolute radiation power of a  $1 \times 4$  phased array are found to be below  $1^\circ$  and 2 dB, respectively. The manuscript also reports on the simulated far-field radiation patterns using the OBFN chip connected to the  $1 \times 4$  phased array. Each BT antenna is connected to a DRW to increase the directivity. The observed total beam steering angle at 0.295 THz is  $\sim 62^\circ$ , when changing the phase difference between two adjacent antennas from  $-120^\circ$  to  $120^\circ$ .

**Author Contributions:** Conceptualization, P.L. and A.S.; methodology, P.L. and C.R.; software, T.H.; formal analysis, P.L.; investigation, P.L.; resources, P.L., T.H. and J.T.; data curation, P.L. and T.H.; writing—original draft preparation, P.L.; writing—review and editing, P.L., T.H., J.T., C.R. and A.S.; visualization, P.L. and T.H.; supervision, A.S.; project administration, A.S.; funding acquisition, A.S. All authors have read and agreed to the published version of the manuscript.

**Funding:** This research was funded by the Federal Ministry of Education and Research within the projects “Open6GHub” (grant No.16KISK017) and “6GEM” (grant No.16KISK039 439), and by the Deutsche Forschungsgemeinschaft (DFG, German Research Foundation) under Project-ID 287022738–CRC/TRR 196 (Project C07).

**Institutional Review Board Statement:** Not applicable.

**Informed Consent Statement:** Not applicable.

**Data Availability Statement:** Not applicable.

**Acknowledgments:** The authors would like to thank Marcel Hoekman from LioniX International BV, The Netherlands, for the support in chip design and support by the Open Access Publication Fund of the University of Duisburg-Essen.

**Conflicts of Interest:** The authors declare no conflict of interest.

## References

1. Ducournau, G.; Szriftgiser, P.; Beck, A.; Bacquet, D.; Pavanello, F.; Peytavit, E.; Zaknour, M.; Akalin, T.; Lampin, J.-F. Ultrawide-bandwidth single-channel 0.4-THz wireless link combining broadband quasi-optic photomixer and coherent detection. *IEEE Trans. Terahertz Sci. Technol.* **2014**, *4*, 328–337. [CrossRef]
2. Harter, T.; Füllner, C.; Kemal, J.; Ummethala, S.; Steinmann, J.; Brosi, M.; Hesler, J.; Bründermann, E.; Müller, A.-S.; Freude, W. Generalized Kramers–Kronig receiver for coherent terahertz communications. *Nat. Photonics* **2020**, *14*, 601–606. [CrossRef]
3. Hermans, R.I.; Seddon, J.; Shams, H.; Ponnampalam, L.; Seeds, A.J.; Aeppli, G. Ultra-high-resolution software-defined photonic terahertz spectroscopy. *Optica* **2020**, *7*, 1445–1455. [CrossRef]
4. Song, H.-J.; Shimizu, N.; Furuta, T.; Suizu, K.; Ito, H.; Nagatsuma, T. Broadband-frequency-tunable sub-terahertz wave generation using an optical comb, AWGs, optical switches, and a uni-traveling carrier photodiode for spectroscopic applications. *J. Light. Technol.* **2008**, *26*, 2521–2530. [CrossRef]
5. Dülme, S.; Steeg, M.; Mohammad, I.; Schriniski, N.; Tebart, J.; Stöhr, A. Ultra-low phase-noise photonic terahertz imaging system based on two-tone square-law detection. *Opt. Express* **2020**, *28*, 29631–29643. [CrossRef] [PubMed]
6. Lu, P.; Haddad, T.; Tebart, J.; Steeg, M.; Sievert, B.; Lackmann, J.; Rennings, A.; Stöhr, A. Mobile THz communications using photonic assisted beam steering leaky-wave antennas. *Opt. Express* **2021**, *29*, 21629–21638. [CrossRef] [PubMed]
7. Zhou, Y.; Sakano, G.; Yamanaka, Y.; Ito, H.; Ishibashi, T.; Kato, K. 600-GHz-Wave Beam Steering by Terahertz-Wave Combiner. In Proceedings of the OFC, San Diego, CA, USA, 11–15 March 2018; pp. 1–3.
8. Liu, Y.; Isaac, B.; Kalkavage, J.; Adles, E.; Clark, T.; Klamkin, J. True Time Delay Millimeter Wave Beam Steering with Integrated Optical Beamforming Network. In Proceedings of the CLEO: Science and Innovations, San Jose, CA, USA, 5–10 May 2019; p. SF3N.6.
9. Lu, P.; Haddad, T.; Tebart, J.; Stöhr, A. Photonic Integrated Chips for THz Beam Steering. In Proceedings of the Asia Communications and Photonics Conference, Shanghai China, 24–27 October 2021; p. M5E.3.
10. Che, M.; Matsuo, Y.; Kanaya, H.; Ito, H.; Ishibashi, T.; Kato, K. Optoelectronic THz-wave beam steering by arrayed photomixers with integrated antennas. *IEEE Photonics Technol. Lett.* **2020**, *32*, 979–982. [CrossRef]
11. Zhuang, L. Flexible RF filter using a nonuniform SCISSOR. *Opt. Lett.* **2016**, *41*, 1118–1121. [CrossRef] [PubMed]
12. Zhuang, L.; Zhu, C.; Corcoran, B.; Burla, M.; Roeloffzen, C.G.; Leinse, A.; Schröder, J.; Lowery, A.J. Sub-GHz-resolution C-band Nyquist-filtering interleaver on a high-index-contrast photonic integrated circuit. *Opt. Express* **2016**, *24*, 5715–5727. [CrossRef] [PubMed]
13. Taddei, C.; Zhuang, L.; Hoekman, M.; Leinse, A.; Oldenbeuving, R.; van Dijk, P.; Roeloffzen, C. Fully reconfigurable coupled ring resonator-based bandpass filter for microwave signal processing. In Proceedings of the Microwave Photonics (MWP) and the 2014 9th Asia-Pacific Microwave Photonics Conference (APMP) 2014 International Topical Meeting, Hokkaido, Japan, 20–23 October 2014; pp. 44–47.
14. Zhuang, L.; Roeloffzen, C.G.; Hoekman, M.; Boller, K.-J.; Lowery, A.J. Programmable photonic signal processor chip for radiofrequency applications. *Optica* **2015**, *2*, 854–859. [CrossRef]
15. Burla, M.; Marpaung, D.A.; Zhuang, L.; Khan, M.R.; Leinse, A.; Beeker, W.; Hoekman, M.; Heideman, R.G.; Roeloffzen, C.G. Multiwavelength-integrated optical beamformer based on wavelength division multiplexing for 2-D phased array antennas. *J. Light. Technol.* **2014**, *32*, 3509–3520. [CrossRef]
16. Liu, Y.; Wichman, A.R.; Isaac, B.; Kalkavage, J.; Adles, E.J.; Clark, T.R.; Klamkin, J. Ultra-low-loss silicon nitride optical beamforming network for wideband wireless applications. *IEEE J. Sel. Top. Quantum Electron.* **2018**, *24*, 8300410. [CrossRef]
17. Tessema, N.; Cao, Z.; Van Zantvoort, J.; Mekonnen, K.; Dubok, A.; Tangdionga, E.; Smolders, A.; Koonen, A. A tunable Si<sub>3</sub>N<sub>4</sub> integrated true time delay circuit for optically-controlled K-band radio beamformer in satellite communication. *J. Lightwave Technol.* **2016**, *34*, 4736–4743. [CrossRef]
18. Burla, M.; Marpaung, D.; Zhuang, L.; Roeloffzen, C.; Khan, M.R.; Leinse, A.; Hoekman, M.; Heideman, R. On-chip CMOS compatible reconfigurable optical delay line with separate carrier tuning for microwave photonic signal processing. *Opt. Express* **2011**, *19*, 21475–21484. [CrossRef] [PubMed]
19. Roeloffzen, C.G.; Hoekman, M.; Klein, E.J.; Wevers, L.S.; Timens, R.B.; Marchenko, D.; Geskus, D.; Dekker, R.; Alippi, A.; Grootjans, R. Low-loss Si<sub>3</sub>N<sub>4</sub> TriPleX optical waveguides: Technology and applications overview. *IEEE J. Sel. Top. Quantum Electron.* **2018**, *24*, 4400321. [CrossRef]
20. Han, X.; Zhang, J.; Song, H.; Wang, L.; Teng, J.; Wu, P.; Zhao, M. Influence of coupling conditions on the time delay characteristics of parallel-cascaded optical waveguide ring resonators. *Optik* **2013**, *124*, 377–384. [CrossRef]
21. Kolpatzek, K.; Haring, L.; Czulwik, A. Phase control in photonically steered phased array transmitters by optical homodyne detection. In Proceedings of the 2016 46th European Microwave Conference (EuMC), London, UK, 4–6 October 2016; pp. 1095–1098.
22. Zhuang, L.; Roeloffzen, C.G.; Meijerink, A.; Burla, M.; Marpaung, D.A.; Leinse, A.; Hoekman, M.; Heideman, R.G.; van Etten, W. Novel ring resonator-based integrated photonic beamformer for broadband phased array receive antennas—Part II: Experimental prototype. *J. Lightwave Technol.* **2009**, *28*, 19–31. [CrossRef]
23. Wörhoff, K.; Heideman, R.G.; Leinse, A.; Hoekman, M. TriPleX: A versatile dielectric photonic platform. *Adv. Opt. Technol.* **2015**, *4*, 189–207. [CrossRef]
24. Pronat Industries. Available online: <https://pronatindustries.com/wp-content/uploads/2014/12/ROHACELL-HF-Product-Information-datasheet.pdf> (accessed on 4 October 2022).